

## N O T I C E

THIS DOCUMENT HAS BEEN REPRODUCED FROM  
MICROFICHE. ALTHOUGH IT IS RECOGNIZED THAT  
CERTAIN PORTIONS ARE ILLEGIBLE, IT IS BEING RELEASED  
IN THE INTEREST OF MAKING AVAILABLE AS MUCH  
INFORMATION AS POSSIBLE

E82-10132

JPL PUBLICATION 81-55

"Made available under NASA sponsorship  
in the interest of early and wide dis-  
semination of Earth Resources Survey  
Program information and without liability  
for any use made thereof."

CR-168514

# Geologic Application of Thermal Inertia Imaging Using HCMM Data

Anne B. Kahle  
John P. Schieltz  
Michael J. Abrams  
Ronald E. Alley  
Catherine J. LeVine

(E82-10132) GEOLOGIC APPLICATION OF THERMAL  
INERTIA IMAGING USING HCMM DATA Final  
Report (Jet Propulsion Lab.) 213 p  
HC A10/MF A01

N82-25590

CSCL 08G

Unclass

G3/43

00132

September 15, 1981



National Aeronautics and  
Space Administration

Jet Propulsion Laboratory  
California Institute of Technology  
Pasadena, California

# Geologic Application of Thermal Inertia Imaging Using HCMM Data

Anne B. Kahle  
John P. Schieldge  
Michael J. Abrams  
Ronald E. Alley  
Catherine J. LeVine

September 15, 1981

Original photography may be purchased from  
EROS Data Center

Sioux Falls, SD 57198



National Aeronautics and  
Space Administration

Jet Propulsion Laboratory  
California Institute of Technology  
Pasadena, California

The research described in this publication was carried out by the Jet Propulsion Laboratory, California Institute of Technology, under contract with the National Aeronautics and Space Administration.

## TABLE OF CONTENTS

	<i>Page</i>
I. INTRODUCTION.....	1
II. SITE SPECIFIC OBJECTIVES AND APPROACH.....	3
III. DATA ACQUISITION.....	8
A. <u>Aircraft Data</u> .....	8
B. <u>Satellite Data</u> .....	13
C. <u>Ground Measurements</u> .....	15
1. Surface and Subsurface Measurements.....	16
2. Meteorological Measurements.....	18
D. <u>Thermal Inertia Meter</u> .....	23
IV. DATA PROCESSING.....	37
A. <u>Aircraft Data Processing</u> .....	38
1. M <sup>2</sup> S Aircraft Scanner Data Processing.....	38
2. HCM and DMS Aircraft Scanner Data Processing.....	44
B. <u>HCMM Satellite Data Processing</u> .....	46
C. <u>Generation of Thermal Inertia Images</u> .....	57
V. DATA AND TECHNIQUE EVALUATION.....	59
A. <u>Atmospheric Effects</u> .....	59
B. <u>HCMR Calibration</u> .....	72
C. <u>Dependence of Thermal Inertia Calculations on Meteorological Conditions</u> .....	79
D. <u>The Effect of Soil Moisture on Thermal Inertia</u> .....	89
E. <u>Model Sensitivity Studies</u> .....	108
F. <u>Numerical Values of Thermal Inertia</u> .....	111
G. <u>Comparison of Apparent and Modeled Thermal Inertia Images</u>	117

TABLE OF CONTENTS (continued)

VI. GEOLOGICAL INTERPRETATION.....	130
A. <u>Walker Lane</u> .....	130
1. Geologic Description.....	130
2. HCMM Images.....	133
3. Aircraft Images.....	142
B. <u>Death Valley</u> .....	148
1. Geologic Description.....	148
2. HCMM Images.....	151
C. <u>Pisgah</u> .....	158
1. Geologic Description.....	158
2. HCMM Images.....	161
3. Aircraft Images.....	169
D. <u>San Rafael</u> .....	172
1. Geologic Description.....	172
2. HCMM Image.....	174
VII. SUMMARY AND CONCLUSIONS.....	190
VIII. ACKNOWLEDGEMENTS.....	195
IX. REFERENCES.....	196

FIGURES

1. Full-frame HCMM visible image of Western U.S. with test sites	4
2. HCMM visible image of Walker Lane, Nevada.....	9
3. HCMM visible image of Death Valley, California.....	10
4. HCMM visible image of Pisgah Crater, California.....	11
5. Soil temperature variation with depth and time for Death Valley.....	17

TABLE OF CONTENTS (continued)

6. Volumetric soil moisture variation with depth at Death Valley	19
7. Surface heat flux density at Stonewall Playa, Nevada.....	20
8. Schematic of the JPL micrometeorological station.....	22
9. Thermal Inertia Meter (TIM).....	27
10. Model calculation for Ottawa sand.....	31
11. Model calculation for dolomite.....	32
12. Calculated heating curves for Ottawa sand compared with observed heating.....	33
13. M <sup>2</sup> S calibration plots.....	41
14a. Example of coherent noise and severe geometric distortion.....	47
14b. Example of random noise.....	48
14c. Example of missing data segments.....	49
15a. Shaded topographic relief image of Walker Lane, Nevada.....	50
15b. Shaded topographic relief image of Death Valley, California....	51
15c. Shaded topographic relief image of Pisgah, California.....	52
16a. Death Valley March 1978 registered visible image.....	53
16b. Death Valley March 1978 registered day thermal image.....	54
16c. Death Valley March 1978 registered night thermal image.....	55

TABLE OF CONTENTS (continued)

17. Upward spectral radiance at 100 km, with surface temperature as a parameter.....	65
18. (a) transmittance, and (b) radiance spectra for a vertical path looking at the ground from space, for the six model atmospheres of LOWTRAN 5.....	67
19. Best fit curve for $T_s$ - $T_g$ data pairs for different dates.....	76
20. Best fit curve for daytime $T_s$ - $T_g$ data pairs for all dates.....	77
21. Best fit curves for all $T_s$ - $T_g$ data pairs and for daytime data pairs only.....	78
22. Sensible and latent heat flux densities calculated for Death Valley.....	84
23. Scatterplot of sensible heat flux densities.....	87
24. Sensible heat flux densities calculated from bulk aerodynamic method for two sites.....	88
25. Observed soil temperature variations at a bare field near Bakersfield, California.....	92
26. Observed soil moisture content at a bare field near Bakersfield, California.....	92
27. Calculated soil temperatures obtained from the numerical model.....	93
28. Calculated soil moisture obtained from the numerical model.....	93
29. Full-frame HCMM day IR image of part of the Western United States for May 14, 1978.....	95

TABLE OF CONTENTS (continued)

30. Full-frame HCMM day IR image of part of the Western United States for August 18, 1978.....	96
31. Full-frame HCMM day IR image of part of the Western United States for September 19, 1978.....	97
32. HCMM thermal inertia image of Death Valley for May 30, 1978....	99
33. HCMM thermal inertia image of Death Valley for July 22, 1978...	100
34. HCMM thermal inertia image of Death Valley for August 18, 1978.....	101
35. HCMM thermal inertia image of Death Valley for April 4, 1979...	102
36. M <sup>2</sup> S visible image of northern half of Death Valley.....	104
37. M <sup>2</sup> S visible image of southern half of Death Valley.....	105
38. Thermal inertia image of northern half of Death Valley.....	106
39. Thermal inertia image of southern half of Death Valley.....	107
40. Thermal inertia image of Walker Lane, Nevada obtained from HCMM data for April 4, 1979.....	118
41. Thermal inertia image of Walker Lane Nevada obtained from HCMM data for July 6, 1978.....	119
42. Shaded relief map of Walker Lane, Nevada area.....	123
43. Slope azimuth map of Walker Lane, Nevada area.....	124
44. Slope orientation map of Walker Lane, Nevada area.....	125

TABLE OF CONTENTS (continued)

45. Apparent thermal inertia image obtained from HCMM data for Walker Lane on July 6, 1978.....	127
46. Calculated thermal inertia image obtained from HCMM data for Walker Lane on July 6, 1978 without topographic corrections.....	128
47. Calculated thermal inertia image obtained from HCMM data for Walker Lane on July 6, 1978 with topographic corrections...	129
48. Location map of Walker Lane, Pissgah and Death Valley sites....	131
49. Geologic map of Goldfield, Nevada and vicinity.....	132
50. HCMM day visible image of Walker Lane site.....	134
51. HCMM day IR image of Walker Lane site.....	135
52. HCMM night IR image of Walker Lane site.....	136
53. HCMM thermal inertia image of Walker Lane site.....	137
54. HCMM color composite of Walker Lane.....	139
55. Interpretation map produced from Figure 54.....	140
56. Thermal inertia image of Goldfield, Nevada from aircraft data..	143
57. Mapped alteration zones superimposed on Figure 56.....	144
58. Geologic map of Cuprite Mining District, Nevada.....	145
59. Alteration map of Cuprite Mining District, Nevada.....	146
60. Thermal inertia image of Cuprite Mining District, Nevada from aircraft data.....	147

TABLE OF CONTENTS (continued)

61. Color ratio composite of Cuprite Mining District, Nevada from visible and near-infrared aircraft multispectral scanner data.....	149
62. Principal components composite of Cuprite Mining District, Nevada. from visible, near-infrared, and thermal inertia aircraft data.....	150
63. Geologic map of Death Valley area.....	152
64. HCMM thermal inertia image of Death Valley area.....	153
65. HCMM color composite of Death Valley.....	155
66. Interpretation map for Figure 65.....	156
67. HCMM color composite of Death Valley.....	159
68. Interpretation map for Figure 67.....	160
69. Geologic map of Pisgah, California area.....	162
70. HCMM day IR image of Pisgah area.....	163
71. HCMM night IR image of Pisgah area.....	164
72. HCMM visible image of Pisgah area.....	165
73. HCMM and Landsat color composites of Pisgah area.....	167
74. Interpretation map for Figure 73.....	168
75. Thermal inertia image of Pisgah from aircraft data.....	170
76. Interpretation map for Figure 75.....	171

TABLE OF CONTENTS (continued)

77. Location map of San Rafael Swell, Utah.....	173
78. Stratigraphic column of rocks exposed in San Rafael Swell.....	175
79. HCMM day IR image of San Rafael Swell.....	176
80. Interpretation map for Figure 79.....	177
81. Legend and explanation for Figures 80, 83, 85, 87, 89.....	178
82. HCMM night IR image of San Rafael Swell.....	179
83. Interpretation map for Figure 82.....	180
84. HCMM thermal inertia image of San Rafael Swell.....	182
85. Interpretation map for Figure 84.....	183
86. HCMM color composite of San Rafael Swell.....	184
87. Interpretation map for Figure 86.....	185
88. Landsat/Seasat composite of San Rafael Swell, Utah.....	187
89. Interpretation map for Figure 88.....	188

TABLES

1. Aircraft Flights.....	12
2. Satellite Flights.....	15
3. Thermal Inertia Standards.....	28
4. Thermal Inertia Derived from In Situ Thermal Inertia Meter Measurements.....	35

TABLE OF CONTENTS (continued)

5. M <sup>2</sup> S Wavelength Bands.....	38
6. Calibration Coefficients for M <sup>2</sup> S Scanner.....	43
7. Characteristics of U-2 Borne Scanners.....	45
8. Results from LOWTRAN Using Rawinsonde Data for Varying Surface Elevations.....	69
9. Results from LOWTRAN Using Rawinsonde Data for Varying Surface Temperatures.....	69
10. Results from LOWTRAN Using Rawinsonde Data for Various Dates.....	70
11. Results from LOWTRAN Using Midlatitude Summer Model for Varying Surface Elevations.....	71
12. Results from LOWTRAN Using Midlatitude Summer Model for Varying Surface Temperatures.....	71
13. Atmospheric Stability Parameters.....	85
14. Perturbations Upon Thermal Inertia Models.....	109
15. Thermal Intertia Values and Their Standard Deviations at Four Test Sites.....	112
16. Average Values ( $\bar{P}$ ) and Standard Deviations ( $\sigma$ ) of Thermal Inertia ( $\times 1000$ ) for 1978 HCMM Flights.....	114
17. Linear Least-Squares Fit of $P(\text{Model})$ to AP.....	121
18. Description of Symbols for Walker Lane HCMM Interpretation.....	141

TABLE OF CONTENTS (continued)

19. Description of Symbols for Death Valley HCMM Interpretation.....	157
20. Description of Symbols for Pisgah Aircraft Interpretation.....	169

## ABSTRACT

This study is part of our continuing program for the development of remote sensing for geologic applications. The main objective was to develop techniques and evaluate our ability to discriminate among surface geologic materials on the basis of their thermal properties as determined from HCMM data. Three test sites in the western U.S. were selected for study. The results of the investigation are:

- 1) Attempts to determine quantitatively accurate thermal inertia values from HCMM digital data met with only partial success due to the effects of sensor miscalibrations, radiative transfer in the atmosphere, and varying meteorology and elevation across a scene.
- 2) In most instances, apparent thermal inertia is an excellent qualitative representation of true thermal inertia. For many applications this will reduce data processing requirements with only minimal loss of information.
- 3) Computer processing of digital day and night HCMM data allowed construction of geologically useful images. At some test sites, more information was provided by Heat Capacity Mapping Mission (HCMM) data than Landsat data. Soil moisture effects and differences in spectrally dark materials were more effectively displayed using the thermal data.
- 4) Future work will extend these results, and examine the multivariate use of HCMM data with Landsat and Seasat data.

## I. INTRODUCTION

The use of middle IR thermal data represents one aspect of our development of remote sensing techniques for geologic mapping, mineral exploration and mineral assessment. Considerable success has been achieved in discriminating lithologic units, and in the separation of altered materials using various enhancement techniques with the reflected solar visible and near IR data from Landsat and aircraft multispectral scanners (Goetz et al., 1975; Abrams et al., 1977; Goetz and Rowan, 1981). These results have been verified with field data obtained with the JPL Portable Field Reflectance Spectrometer (PFRS) and lab spectra of samples from the field. Multispectral middle infrared data, acquired by aircraft scanners, have also been demonstrated to separate some geological units, in particular igneous silicate rocks (Vincent, 1975; Kahle and Rowan, 1980). However, many ambiguities in the remotely sensed data remain. The addition of thermal inertia data to the multispectral analysis will make possible the resolution of some of these problems. Some materials with similar reflective and emissive spectral characteristics will be able to be differentiated by their thermal properties. Also, since thermal properties are representative of the top several centimeters of the surface material, it will be possible to sense the characteristics of the material through a thin weathered layer or stain.

As part of this continuing program at the Jet Propulsion Laboratory, we developed a numerical model of the thermal behavior of surface materials (Kahle, 1977). Using aircraft data, we created the first thermal inertia image of a part of the Earth's surface at Pisgah Crater, California (Gillespie and Kahle, 1977), and demonstrated the utility of this image for geologic mapping (Kahle et al., 1976). Our purpose with the present study has been to

apply this technique to Heat Capacity Mapping Mission (HCMM) and aircraft data to further develop and demonstrate the use of middle IR thermal data for geologic applications.

#### II. SITE SPECIFIC OBJECTIVES AND APPROACH

Three test areas were selected at the time we proposed this study: Walker Lane, Nevada; Death Valley, California; and Plagah, California. We have concentrated our study on these areas. A fourth area, San Rafael Swell, Utah, has also been briefly examined.

The first study area is the Walker Lane (W), a major zone of NW-trending right-lateral strike-slip faulting extending from Pyramid Lake, Nevada to Las Vegas, Nevada (Figure 1). Concentration of volcanism along the northwestern and central parts of this zone during late Tertiary time has resulted in a thick sequence of extrusive and intrusive rocks ranging in composition from alkali to basaltic. The precious- and base-metal ore deposits located near Goldfield, Tonopah, and Virginia City and elsewhere along this belt are related to this intense period of volcanism. Massive Mesozoic granodiorite rocks form well-exposed erosional remnants along these parts of the zone. In the southern part of the Walker Lane, Paleozoic sedimentary rocks including limestone, dolomite, shale, and sandstone predominate. Alluvial deposits of several different types and ages occur along the zone. Thus, the proposed study area consists of rocks which have a wide compositional and textural range.

The main objective of the study of this area was to discriminate among the surface materials on the basis of their thermal properties. In particular we were to determine if it is possible to: 1) discriminate some of the extrusive volcanics, especially ash-flow and air-fall tuffs and cinders from the intrusive volcanics because of their lower density, 2) discriminate hydrothermally altered areas from unaltered rocks due to mineralogical or textural differences, 3) discriminate between sedimentary and igneous rocks, 4) dis-

ORIGINAL PAGE  
BLACK AND WHITE PHOTOGRAPH

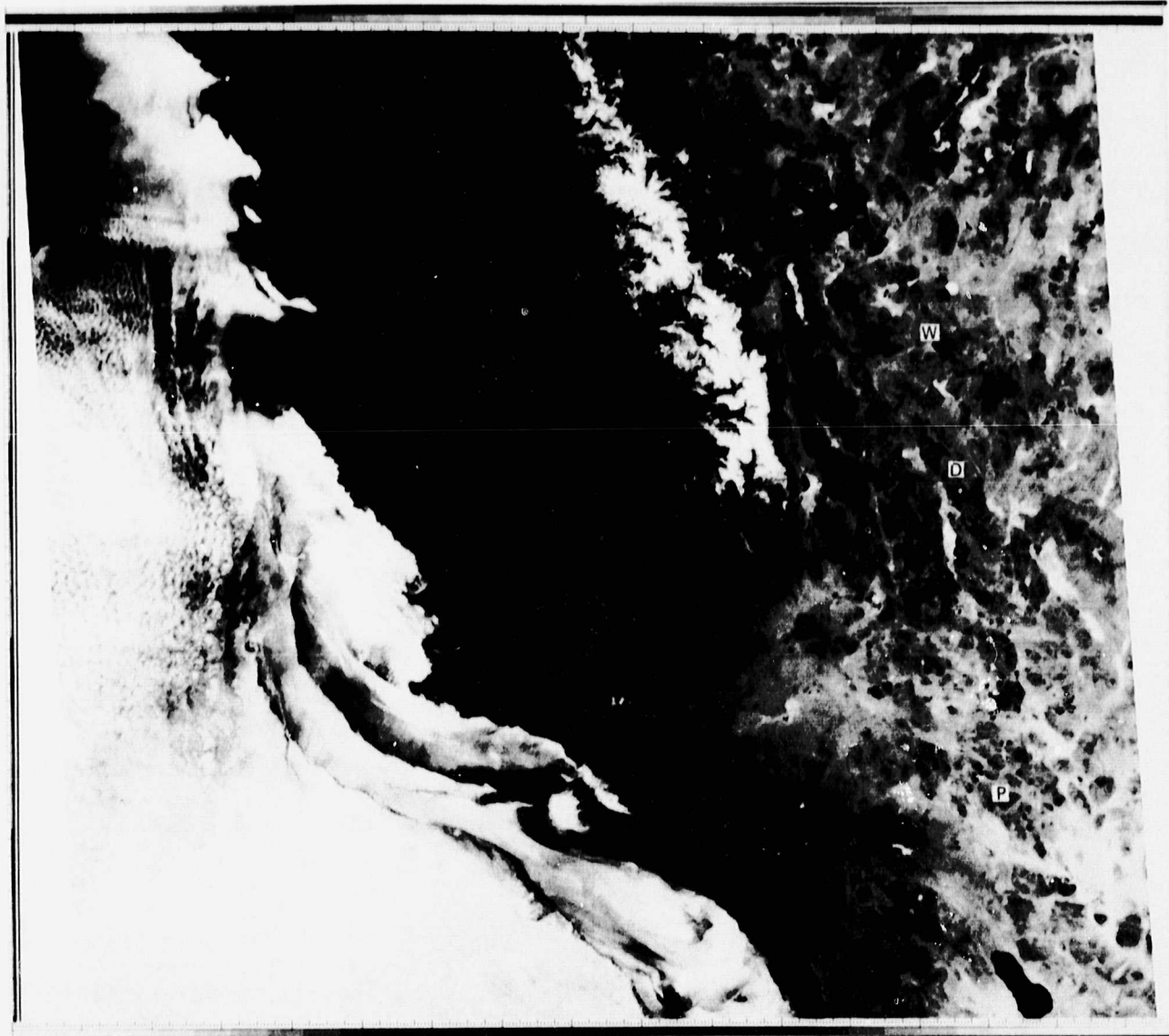


Figure 1. Full-frame HCMM visible image. Test sites are indicated by D (Death Valley), W (Walker Lane), and P (Pisgah Crater).

criminate among rock units whose compositional differences are obscured in the visible and near-infrared regions by thin surface coatings, and 5) distinguish between outcrops and alluvial areas and among alluvial deposits.

The second area of interest is Death Valley, California (D), also shown in Figure 1. Within Death Valley and the mountain ranges that border it, a great variety of rocks representing virtually every geologic period are exposed. Most of the topographic features of Death Valley can be attributed to movement along a major fault zone, the Death Valley fault zone, which approximately coincides with the valley. The valley is the drainage sump both for surface and subsurface flow for at least 23,000 square km of desert. The fill in the valley consists mainly of coarse-grained, alluvial-fan deposits on the slopes, and fine-grained alluvium and evaporite deposits at the lower elevations of the valley.

Previous study of NOAA satellite VHRR thermal infrared scanner data from the Death Valley region had shown very interesting temperature patterns at night. The mountains and valley floor are cool with the intermediate elevations being warm. This temperature pattern, which varies seasonally, appeared to be related to the evaporation from the valley floor.

The objectives of the study of this area were to: 1) develop a better understanding of the physics of the spatial and diurnal temperature variations of this region, 2) determine the utility of thermal data for ground water mapping in a desert region, and 3) examine lithologic discrimination in a complex area.

The third study area shown in Figure 1 is the Pisgah Crater - Lavic Lake region of California (P). Here, the objectives were to: 1) compare a thermal inertia map derived from HCMM data with an already existing thermal inertia map derived from aircraft data (Kahle, et al., 1976; Gillespie and Kahle,

1977), 2) determine the repeatability of the process under different meteorological conditions, and 3) determine the effects of reduced resolution in separating major lithologic units.

A fourth site, San Rafael Swell, Utah for which only one HCMM digital data set was obtained has been included primarily for future comparison with an existing Landsat-Seasat study (Blom *et al.*, 1981).

The approach taken at the three primary sites was essentially the same. Prior to the HCMM launch, day and pre-dawn aircraft scanner data were acquired at each site. These data usually consisted of several bands of multispectral visible and near-IR data and a single broadband thermal channel. Before and during the flights meteorological data were acquired at the site by field parties. The meteorological data were used in the JPL thermal model to derive tables of thermal inertia as a function of day-night temperature difference (and sometimes topography). These tables were used with the aircraft scanner data to derive thermal inertia images.

During the useful lifetime of HCMM, a similar procedure was followed. Field measurements of meteorological data were made before and during known overpass times of the satellite. These data were augmented by data from the closest National Weather Service stations. Using the thermal model and the meteorological measurements, the satellite data in digital format were reduced to thermal inertia images.

These thermal inertia images, and also the temperature and albedo images, were then evaluated for geological information. Additional field verification needs to be undertaken. Effects of varying meteorological conditions, calibration problems, topographic corrections (both aspect and elevation), and atmospheric attenuation and radiance, have been evaluated. The utility of the apparent thermal inertia as compared with the more quantitatively correct

derived thermal inertia has been studied. The methods, results and interpretation are discussed in the subsequent sections.

### III. DATA ACQUISITION

Data were collected from satellite and aircraft flights over the three test areas: Walker Lane, Nevada; Death Valley, California; and Pisgah Crater, California. The three areas are shown on images obtained from HCMM flights in Figures 1 through 4. The first image (Figure 1) contains all three areas on a single, full-frame picture of the western United States. The subsequent figures show individual areas. In the Walker Lane area we have studied two test sites, the Goldfield mining district (G) and the Cuprite mining district (C) near Stonewall Mountain; both sites are indicated in Figure 2. Death Valley is shown in Figure 3 and Pisgah in Figure 4.

#### A. Aircraft Data

Table 1 lists the digital aircraft data collected for this study. The aircraft data consist of nineteen different flights. The date of each flight, the area of coverage, the aircraft type and sensor used are given in the table. Double coverage of the Goldfield area was obtained on August 8, 1977 with data from both the NP-3A and the U-2. Numbers in parentheses indicate more than one flight over an area.

The aircraft operations consist of two flights over a test area within a 24 hour period. The two consecutive flights are necessary in order to determine the day-night temperature difference from the IR radiance data. A predawn flight is made just before sunrise to measure the minimum diurnal temperature of the ground and a mid-afternoon flight, one or two hours after local solar noon, is made to measure the temperature maximum and the surface albedo. On some flights the NP-3A and NC-130B made two runs for each flight: one at a low level ( $\sim 2.1 - 4.2$  km ASL) and one at a high level ( $\sim 7.6$  km ASL). The lengths of the flight lines are 3.7 km at Pisgah, 15-22 km at Death

ORIGINAL PAGE  
BLACK AND WHITE PHOTOGRAPH

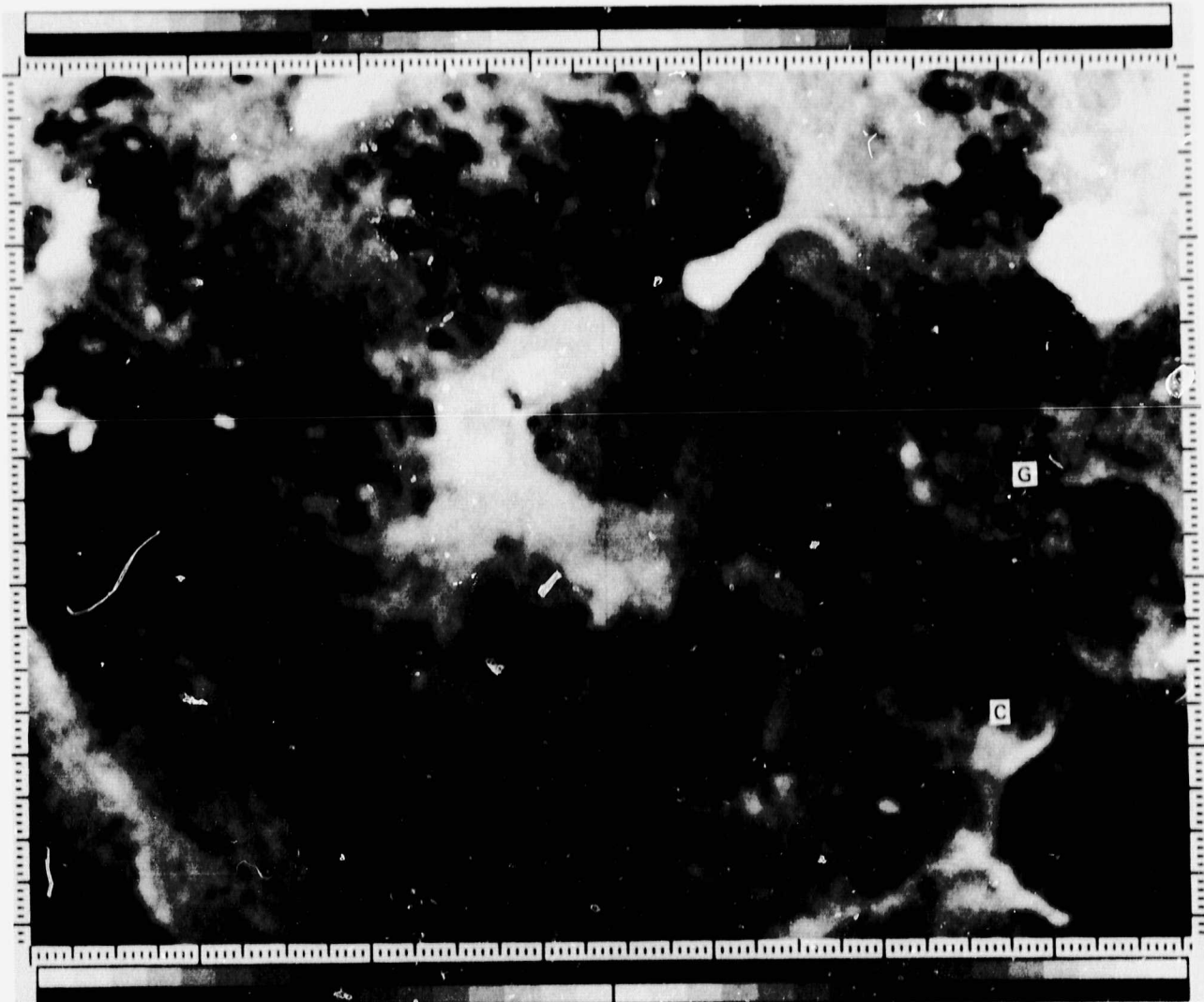


Figure 2. HCMM visible image of Walker Lane, Nevada. Test sites indicated by G (Goldfield mining district) and C (Cuprite mining district).

ORIGINAL PAGE  
BLACK AND WHITE PHOTOGRAPH



Figure 3. HCMM visible image of Death Valley, California.

ORIGINAL PAGE  
BLACK AND WHITE PHOTOGRAPH



Figure 4. HCMM visible image of Pisgah Crater, California.

TABLE 1  
AIRCRAFT FLIGHTS

<u>Date</u>	<u>Site</u>	<u>Aircraft</u>	<u>Sensor</u>
March 29-30, 1975	Pisgah (2)	NP-3A	M <sup>2</sup> S
September 3, 1975	Pisgah	U-2	HCM
June 14, 1976	Walker Lane Death Valley Pisgah	U-2	HCM
October 26-27, 1976	Goldfield Cuprite	NP-3A	M <sup>2</sup> S
March 11, 1977	Death Valley	NP-3A	M <sup>2</sup> S
July 13-14, 1977	Pisgah	NP-3A	M <sup>2</sup> S
August 8-9, 1977	Walker Lane Goldfield Cuprite	U-2 NP-3A	HCM M <sup>2</sup> S
February 2-3, 1978	Death Valley	U-2	HCM
March 14-15, 1978	Death Valley	U-2	HCM
August 18, 1978	Goldfield Cuprite	NC-130B	M <sup>2</sup> S
April 4, 1979	Death Valley (2)	U-2	DMS

Valley, and 5.5 km (for the Goldfield area) and 8.5 km (for the Cuprite area) at Walker Lane. All U-2 flights were at 19.8 km ASL. The Bendix M<sup>2</sup>S (Modular Multispectral Scanner) was used on the NP-3A and the NC-130B. This is an electro-optical scanner which measures electromagnetic radiation in ten channels between 0.33 and 1.1  $\mu$ m, and in a thermal IR channel from 7.95 to 13.5  $\mu$ m. The instrument has a scan angle of 100°, a scan rate of 20 revolutions per second, and an instantaneous field of view (IFOV) of 2.5 milliradians. At an altitude of 2.1 km, the sensor covers a ground swath of 5.0 km in width and at nadir has an IFOV of about 5 m square. The U-2 was flown with either of two sensors, the Heat Capacity Mapper (HCM) or the Daedalus Multispectral Scanner (DMS). The HCM is a scanner that was built at the Goddard Space Flight Center (GSFC). It detects the visible and near IR (0.5 - 0.7  $\mu$ m) and thermal IR (10.5 - 12.5  $\mu$ m) portions of the electromagnetic spectrum. The HCM has a 90° scan angle, a 2.8 milliradian IFOV, and a thermal resolution of 0.2°C. At an altitude of 19.8 km, the sensor scans a swath of 39.6 km, and at nadir has an IFOV of about 55 m square. The DMS is an eleven channel scanner with a scan rate of 10 revolutions per second which covers the spectrum from 0.38 to 1.1  $\mu$ m and from 10.4 to 12.5  $\mu$ m. The system uses either of two scanheads of 1.25 or 2.5 milliradians angular resolution. From an altitude of 19.8 km, the sensor covers a swath of either 15 or 36 km and has a resolution of either 25 or 50 m depending upon the scanhead.

#### B. Satellite Data

The HCMM satellite views the Earth's surface with the HCMR scanning/imaging radiometer which operates with two channels in the visible and near IR (0.55 - 1.1  $\mu$ m) and the thermal IR (10.5 - 12.5  $\mu$ m) regions. The sensor has a scan rate of 14 revolutions per second, an IFOV of 0.83 milliradians, and a

thermal resolution of  $0.4^{\circ}\text{K}$  at  $280^{\circ}\text{K}$ . At the satellite altitude of 620 km, the ground resolution is about 500 m.

Prior to what appeared might be favorable weather conditions during satellite passes over our test sites, a team of investigators was dispatched from JPL to obtain ground truth measurements; however, these measurements were only taken at one of the sites on any given occasion. These measurements are described in detail in the next section. Hourly weather observations from nearby National Weather Service stations were used as ground truth for the other two sites. Ground truth measurements at the site continued only if the weather remained clear; otherwise, the effort was abandoned. All the HCMM data of the test sites were first obtained from GSFC in image form and then examined to select only those passes when weather conditions permitted clear views of the ground. Digital HCMM images were obtained for periods when field measurements had been made and/or when the GSFC images indicated that good quality satellite data were available. The digital HCMM data used in this study are listed in Table 2.

HCMM digital data were obtained for 9 sets of overpasses from May, 1978 to April, 1979 for the Walker Lane, Death Valley, and Pisgah Crater areas. With one exception (July 21-22, 1978), each of these sets includes a night overpass (N), 24 hours later another night overpass, 12 hours later a day overpass (D), and 24 hours later another day overpass. Each NNDD set covers most of all three test sites. Included in this data set is one completely cloud-free nine-day period between July 15 and July 23, 1978, when field measurements were taken at Cuprite for the entire period and two HCMM NNDD sets of overpasses (7 total) were obtained. Simultaneous HCMM and aircraft data are available for April, 1979 flights over Death Valley.

TABLE 2  
SATELLITE FLIGHTS

Dates	Remarks
May 13-15, 1978	Pisgah missed on 5/14 night
May 29-31, 1978	Death Valley and Pisgah missed on 5/30 night
July 5-7, 1978	Pisgah missed on 7/6 night
July 16-18, 1978	Death Valley and Pisgah missed on 7/17 night
July 21-22, 1978	No second day coverage (July 23)
August 17-19, 1978	Pisgah missed on 8/18 night
August 27-28, 1978	San Rafael coverage only
September 18-20, 1978	No Death Valley coverage
September 18-20, 1978	Pisgah missed on 9/19 night
April 3-5, 1979	All sites covered

#### C. Ground Measurements

A ground truth program was established to collect supporting data for aircraft and HCMM overflights. The data consist of: 1) surface temperature measurements, 2) subsurface temperature measurements, 3) soil moisture measurements, and 4) meteorological observations. The surface and subsurface measurements were collected at various locations at each site by a team of investigators, and recorded by hand. The meteorological data were obtained in digital and analog format by automated equipment placed at a central location at each site. For convenience, we first discuss the surface and subsurface measurements - data sets (1) through (3), and then the meteorological measurements - data set (4).

## 1. Surface and subsurface measurements

The surface temperature measurements were obtained with a Barnes PRT-5 Precision Radiation Thermometer. This instrument is a portable infrared radiometer which operates in the thermal region from 8 to 14  $\mu\text{m}$ , has a field of view of about  $2^\circ$ , and is accurate to within  $0.5^\circ\text{C}$  over a temperature range from  $-20$  to  $+75^\circ\text{C}$ . The radiation emitted from the target is read directly from a scale on the PRT-5 as an equivalent blackbody temperature.

Subsurface temperature measurements were made with Yellow Springs Instrument (YSI) thermistors buried in the soil at a number of depths, usually 2 to 50 cm below the surface. These temperature sensors consist of vinyl-jacketed probes whose tips contain thermistors which can be used over a range from  $-30$  to  $+100^\circ\text{C}$ . The probes are connected to a phone jack by leads, and when the jack is inserted in the receptacle of a YSI meter, the temperature is read from a scale. Figure 5 shows a diurnal pattern for soil temperature that was obtained in March, 1978 from YSI probe measurements at Death Valley on a silty surface. Note that the surface heating maximum leads the maximum at the lower depths ( $\sim 25$  cm) by 6 hours, and that the damping depth of the diurnal heating is about 50 cm. Both features are fairly typical of most soils.

The soil moisture measurements were obtained by the gravimetric method as follows. Samples are removed from the soil by an extractor, usually a cylindrical coring device. The moist soil is placed in a container, sealed, and later dried in an oven at about  $60^\circ\text{C}$ . The sample is weighed before and after drying to determine the moisture content. The soil moisture content can then be expressed in either of two ways: 1) as a percentage of the dry weight,  $(\text{wet weight} - \text{dry weight})/\text{dry weight}$ , or 2) as a percentage of the volume, % moisture by weight multiplied by the bulk density of soil (dry

ORIGINAL PAGE IS  
OF POOR QUALITY

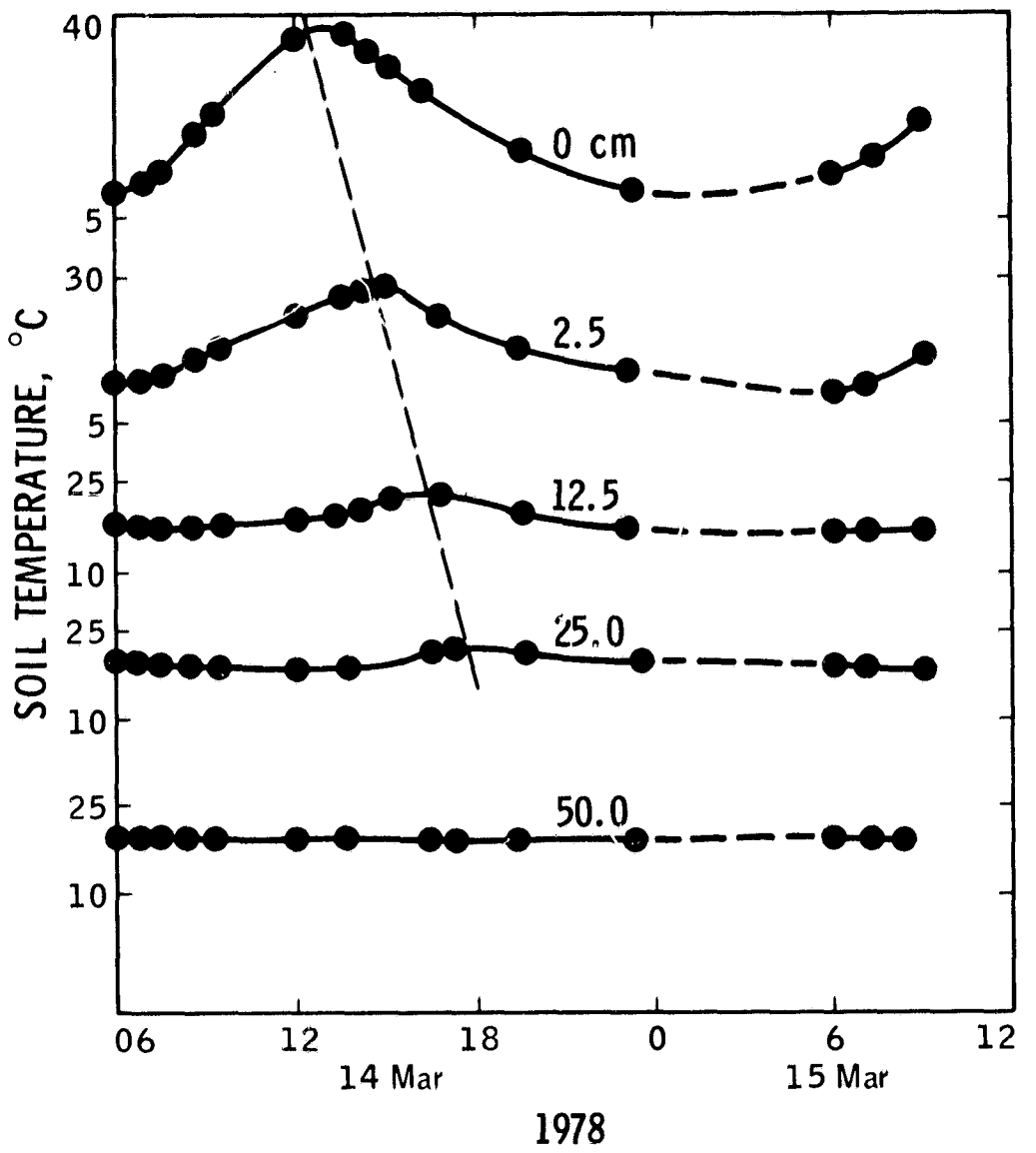


Figure 5. Soil temperature variation with depth and time for Death Valley on March 14 and 15, 1978.

weight/field volume of soil sample). Figure 6 shows an example of volumetric soil moisture measurements for different depths on the floor of Death Valley opposite Desolation Canyon. The ordinate is a scale indicating per cent of moisture content by volume. The abscissa denotes site locations starting at (10) which is furthest from the center of the Valley floor and ending at (6) which is nearest. Sites (10) and (9) are on the gravel fan beneath the canyon, (5) is on the silt past the fan, and (6) is on the salt pan which covers most of the valley floor. Sites (8) and (7) are located on transition zones between the silt and the fan, and the silt and the salt, respectively. The diagram shows the dryness of the fans, and the increase of moisture with distance along the silty surface until the salt pan is reached.

## 2. Meteorological Measurements

Meteorological measurements are needed to specify upper (or surface energy) boundary conditions for the soil thermal model. As an example, Figure 7 shows the surface energy balance for a day in July, 1978 at Stonewall playa which is located near Goldfield, Nevada. These are typical diurnal patterns in solar radiation (S), soil heat conduction (G), net thermal (longwave) radiation (R), and sensible heat flux (H) for a dry, desert surface. The methods used to calculate these values from periodic near-surface measurements are discussed in Kahle (1977).

Radiation measurements, S and R, consist of net shortwave, and longwave flux densities. Net radiation flux densities are obtained by use of a Thornthwaite Model 602 radiometer and strip chart recorder. The radiometer is a flat, circular, black plate (thermal transducer) that is shielded by two clear plastic hemispheres, and has a detection range of about -280 to  $\pm 1110 \text{ w/m}^2$  where positive refers to a net radiant flux directed toward the ground and negative vice-versa. The shortwave component (0.28 - 2.80  $\mu\text{m}$ ) is

ORIGINAL PAGE IS  
OF POOR QUALITY

DEATH VALLEY - DESOLATION CANYON FAN TRAVERSE

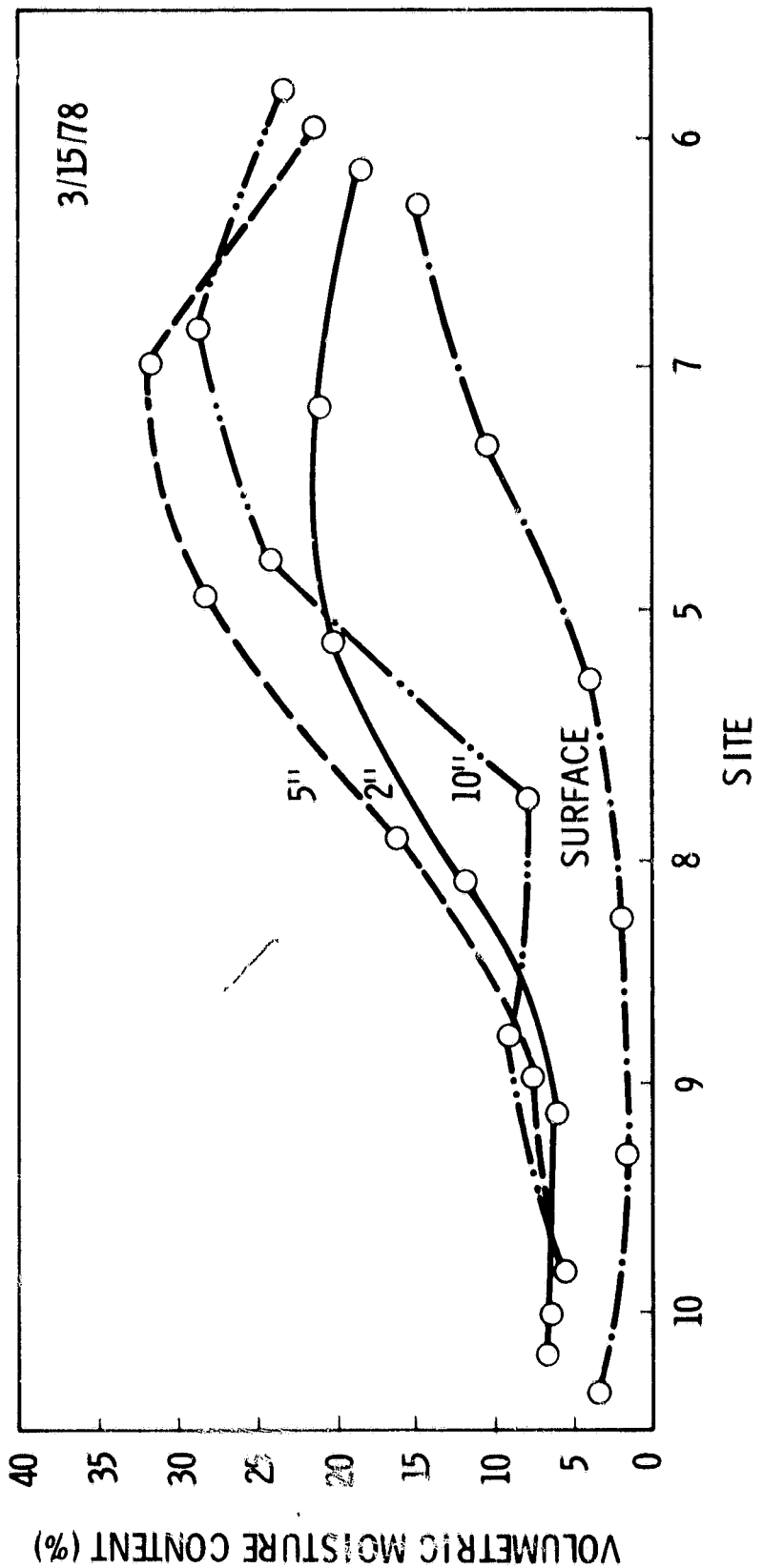


Figure 6. Volumetric soil moisture variation with depth at Death Valley on March 15, 1978.

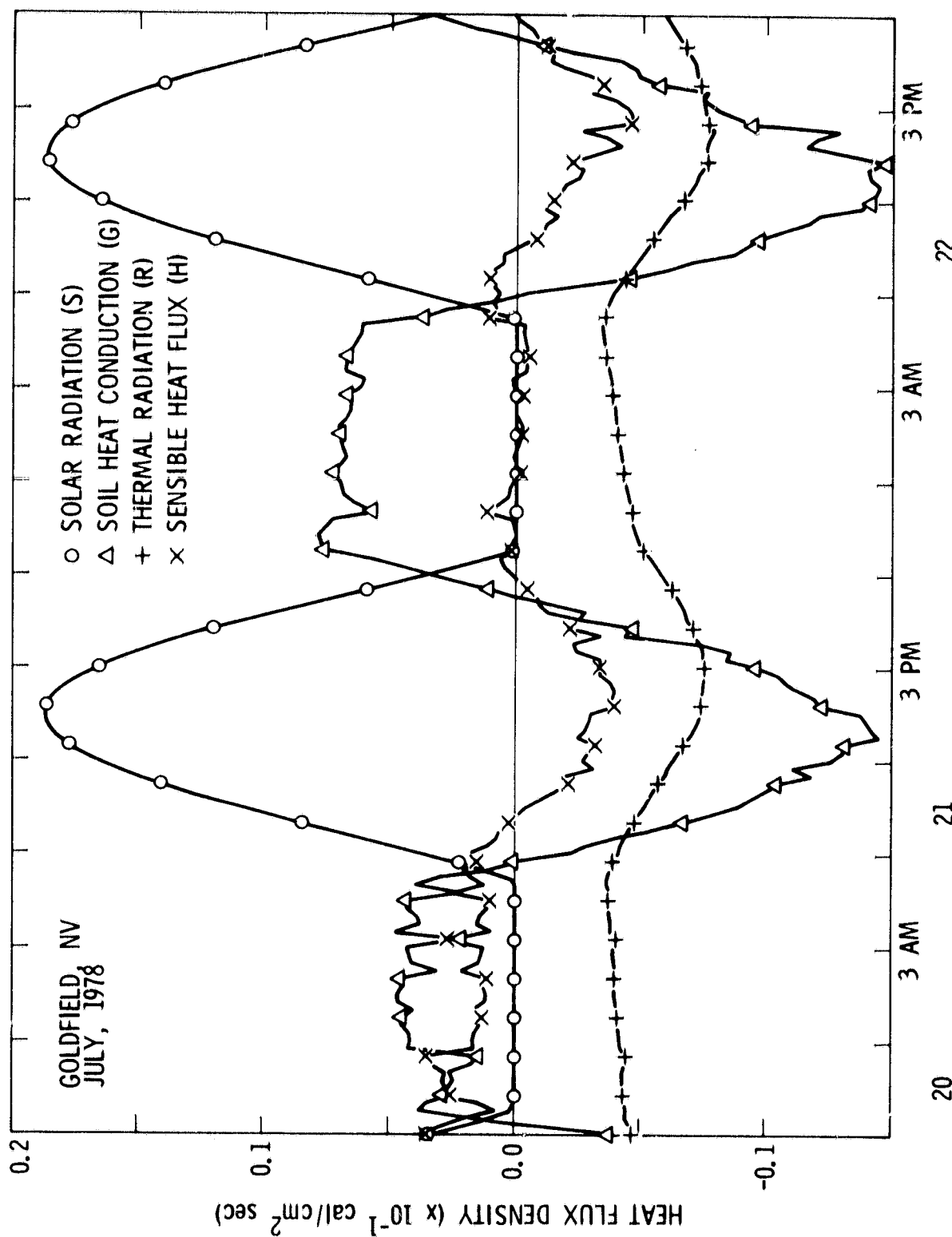


Figure 7. Surface heat flux density at Stonewall Playa, near Goldfield, Nevada - for a day during July, 1978.

measured with an Eppley Precision Spectral Pyranometer (PSP) and the longwave component (3-50  $\mu\text{m}$ ) with an Eppley Precision Infrared Radiometer (PIR). All radiometers are mounted at a height of 1/2 to 1 meter above the ground, and the PSP or PIR can be used to measure either upward or downward radiative flux densities.

Soil heat flux densities ( $G$ ) are measured with a Soil Heat Flux Recording System, Model 310. The sensor is a Thornthwaite thermopile enclosed in a thin, flat disk - 25 mm in diameter and 2.6 mm thick. The disk is placed just below the soil surface and parallel to it and the temperature difference across its upper and lower faces is proportional to the soil heat flux. The data are entered on a strip chart recorder.

Sensible ( $H$ ) and latent ( $L$ ) heat flux densities are computed from weather observations of wind speed, air temperature, and air humidity. In situ weather data are obtained at each site from two systems. The first system is a Meteorology Research, Inc. (MRI) mechanical weather station. This is a self-contained instrument powered by four 1.5 V flashlight batteries, and is equipped to measure wind speed and direction, air temperature, and relative humidity at a single level above the ground (~ 1 or 2 m). Data are recorded on a strip chart. The second system is a micrometeorological station - designed and built at JPL - that collects data at 7 levels above the ground (1/8, 1/4, 1/2, 1, 2, 4, 8 m). A psychrometer-anemometer pair are mounted at each level at the end of a 1 m rod that is attached to a mast a little over 8 m tall (Figure 8). The anemometers are three-cup type about 9 cm high, 5 cm in diameter, and with rotor arms 7.5 cm long. The rotation rate, in RPM, of the cup assembly is related to the wind speed ( $U$ ) by the formula  $U = 0.026 \times \text{RPM} + 0.118 \text{ m/s}$  which was obtained by wind tunnel tests. The relation between  $U$  and RPM - obtained by fitting a least squares line through

ORIGINAL PAGE IS  
OF POOR QUALITY

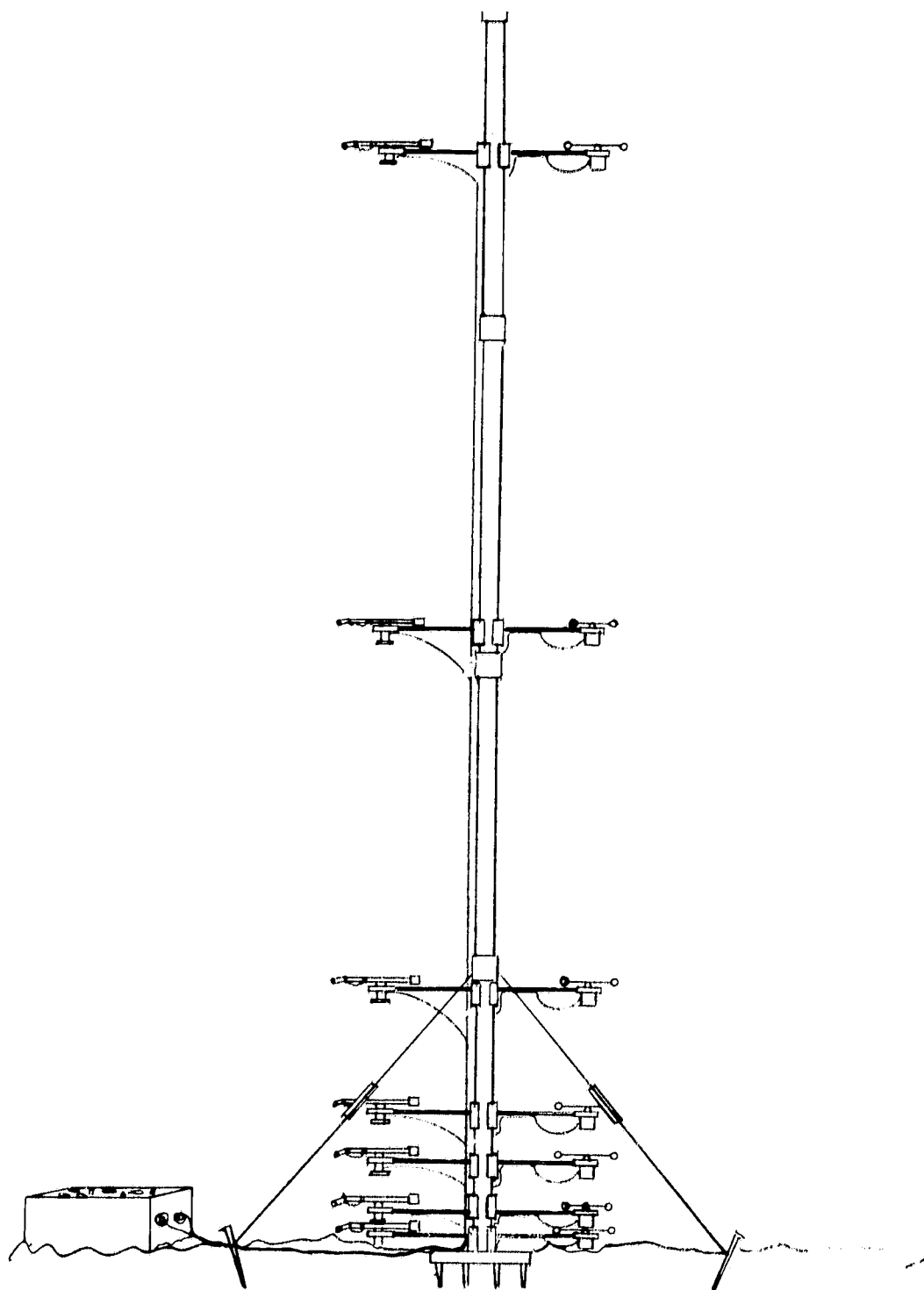


Figure 8. Schematic of the JPL micrometeorological station.

the data - is almost perfectly linear,  $r^2 = 0.992$  (where  $r$  is the correlation coefficient and  $r^2 = 1.000$  denotes perfect linearity). The psychrometers are a dry-bulb and wet-bulb arrangement of paired thermistors, Yellow Springs Instrument Model #44202, which are accurate to within  $\pm 0.15^\circ\text{C}$  over a range of  $-5$  to  $+45^\circ\text{C}$ . The wet-bulb thermometer is covered by a cotton wick that is supplied with water from a small reservoir attached to the bottom of the psychrometer case. A small fan set in front of the case ventilates the thermistor couple. The entire system is powered by a 6 volt battery. Data are printed in digital form on paper tapes, and can be averaged over several time intervals from 30 seconds to 16 minutes.

#### D. Thermal Inertia Meter

The paucity of laboratory measurements of the thermal inertia components (conductivity, density, and specific heat) for rocks and soils found in natural field conditions is apparent after review of the heat conduction literature. The vast majority of these measurements have been of engineering or insulating materials and not geologic materials in the field. For example, the Handbook of Physical Constants (Clark, 1966), presents approximately 75 rock type conductivity values, only a few density values, and no specific heat values.

Several methods of laboratory or direct in situ measurement of thermal inertia have been developed. For example, Brennan (1971) has developed a laboratory method of determining thermal diffusivity ( $\kappa = K/\rho c$ ). It utilizes an instrument having a transistor heated base plate which remains at a constant temperature through thermostatic control. A small rock core is placed on the plate and a thermistor monitors the temperature at the opposite end of the core. Thermal diffusivity is inversely proportional to the time taken by the unheated end of the core to rise an increment of temperature.

Because the instrument is calibrated, the diffusivity can then be calculated when the temperature increment is small with respect to the temperature difference between the base plate and the initial core temperature. Brennan (1971) has published approximately forty measurements of thermal diffusivity and thermal inertia.

A laboratory method has been developed by Schultz (1968) for non-destructively determining the thermal inertia of materials at ambient temperatures. The method involves the radiant heating of an unknown sample and a standard. The temperature history of the sample and standard are monitored with an infrared radiometer and comparison of their temperature histories yields the local thermal inertia of the sample.

In this study, the surface temperature rise of the materials is used to calculate the thermal inertia of the sample. This calculation is based upon the following assumptions: 1) the compositions of the standard and sample materials are homogeneous, 2) the heat flux density at the surface of each material is constant and equal for each material, and 3) the materials are thick enough to be approximated as semi-infinite bodies. This allows us to calculate the thermal inertia of the sample from a simple, algebraic equation adapted by Schultz from Carslaw and Jaeger (1959),

$$P_t = \frac{\Delta T_s}{\Delta T_t} \times P_s \times (\epsilon_t / \epsilon_s)^2 . \quad (1)$$

where:

$P_t$	=	target thermal inertia
$P_s$	=	standard thermal inertia
$\Delta T_s$	=	standard change in temperature
$\Delta T_t$	=	target change in temperature
$\epsilon_t$	=	target emissivity
$\epsilon_s$	=	standard emissivity

A critical point is whether the net flux density at the surface is constant. Even under laboratory conditions, the actual surface boundary condition is non-linear because the surface is emitting radiant energy at a rate proportional to the fourth power of the surface temperature,  $T_{\text{surf}}$ . Under controlled circumstances, i.e. in the laboratory, the surroundings radiate energy onto the test surfaces by an amount proportional to the fourth power of the room (ambient) temperature,  $T_{\text{amb}}$ , so that the net energy loss from the surface depends upon the difference,  $T_{\text{surf}}^4 - T_{\text{amb}}^4$ . Since  $T_{\text{amb}}$  usually changes slowly, it can be considered constant and the non-linearity of the boundary condition depends almost entirely on the  $T_{\text{surf}}$  component. Provided the magnitude of the constant flux from the heat source is large and the duration of heating is not too long, the net flux density at the surface will be approximately constant and the heating history of the materials will be represented by a parabolic curve (cf. Carslaw and Jaeger, 1959, pg. 75). Schultz has achieved these results by heating materials at  $6 \text{ cal cm}^{-2} \text{ s}^{-1}$  for 5 seconds. Any attempt to employ this technique in the field must deal with a more complicated set of environmental conditions, viz. the most serious difficulty being gusty winds which transfer heat to, or from, the materials by advection or convection.

Nonetheless, the fundamental simplicity of Schultz's technique suggests that this method can be applied to construct a field instrument to measure thermal inertia in situ. The JPL thermal inertia meter (TIM) is designed to heat a target and two standards, with the resulting temperature change of each material monitored with an infrared radiometer.\* This permits

---

\* TIM was designed and tested by Dr. Stuart Marsh during his tenure at JPL as a National Research Council Research Associate.

the relationship expressed by Equation 1 to be used under field conditions. Again, this relationship is valid only if the three assumptions listed above are satisfied. The first two conditions can be satisfied approximately by proper selection of test materials, by calibration of the heat sources, and by monitoring the local environmental conditions-principally the wind gusts. The third condition is satisfied by insuring that the thickness of the standard material and target is greater than the damping depth of the heating wave.

A photograph of the thermal inertia meter and its configuration is shown in Figure 9. The radiant energy sources (A) are 3200 W quartz infrared heat lamps (GE #3200T3/1CL/HT-384V). The lamps are mounted in parabolic, polished aluminum reflectors coated with lacquer to prevent discoloration. Each lamp is pivoted which permits it to be quickly moved into position to heat the surface and removed to allow monitoring of the surface temperature. The lamps are connected to Variac voltage regulators (B) which permit the mutual balancing of the three infrared lamps. The surface temperature rise is monitored using a Barnes Engineering Company Precision Radiation Thermometer (C), model PRT-5. The instrument is specified to be accurate to 0.5° $C$ . The instrument's detector head (D) is mounted in a metal block in such a way as to permit rapid movement from reference standard to target. The detector head is 38.7 cm above the target or standard yielding a circular field of view 1.35 cm in diameter at the center of the area undergoing heating. A portable digital voltmeter (Dynameter)(E) measures the voltage from the PRT-5. The PRT-5 and voltmeter are mutually calibrated against a temperature-controlled blackbody.

The base of the thermal inertia meter consists of three compartments. Their interiors are painted with flat-black, and are surrounded by 5 cm of styrofoam insulation. Compartments 1 and 3 hold the thermal inertia standards. These standards are placed within plywood boxes, also painted with

ORIGINAL PAGE  
BLACK AND WHITE PHOTOGRAPH

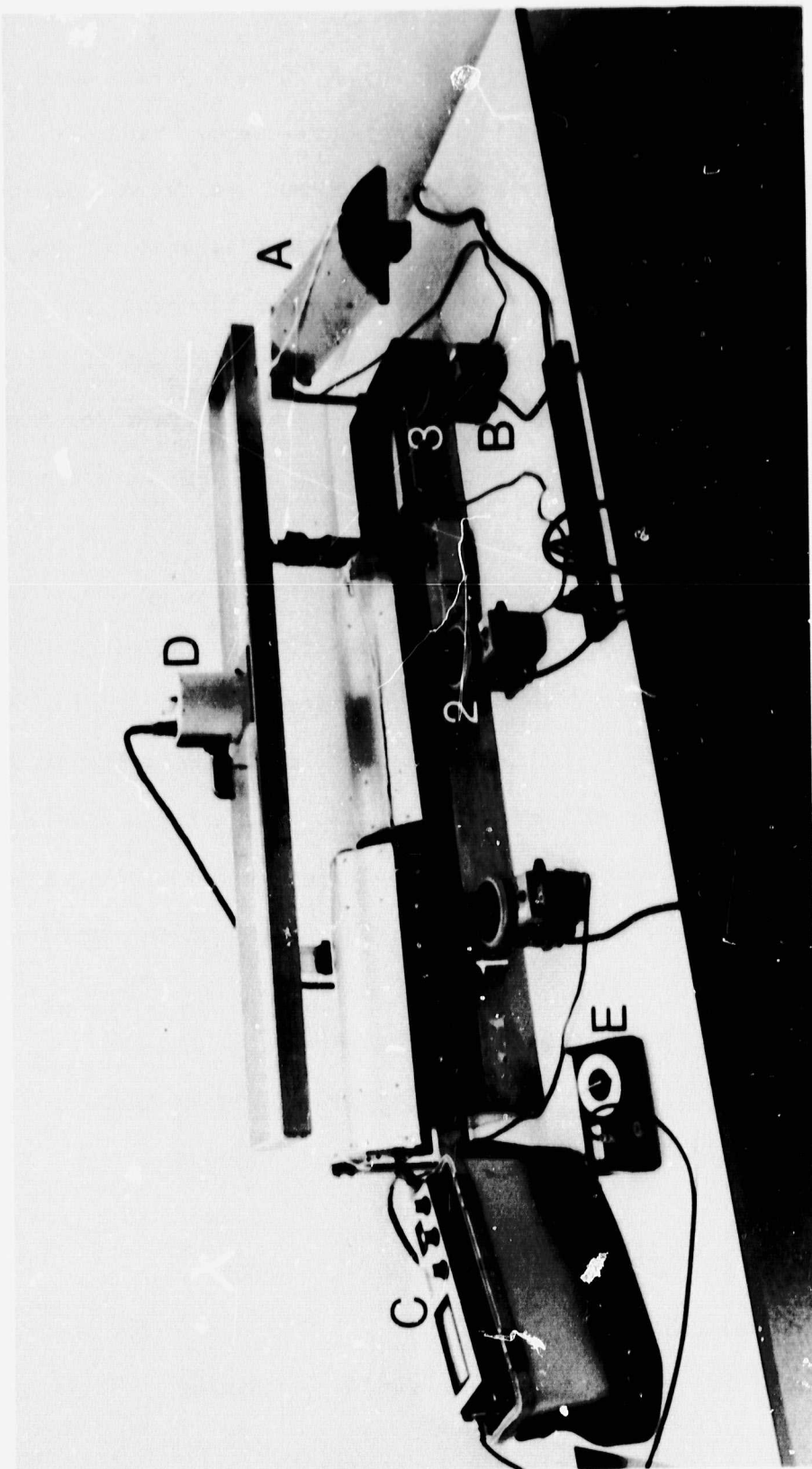


Figure 9. Thermal Inertia Meter (TIM) with quartz infrared heat lamps (A), voltage regulators (B), PRT-5 (C), and detector head (D), digital voltmeter (E), compartments for thermal inertia standards (1 and 3), compartment open to the surface to be measured (2).

flat-black, and then positioned into the compartments. Compartment 2 is left open to the surface which is to be measured by the TIM.

A dolomite block (30 x 18 x 5 cm) and 20/30 mesh Ottawa sand (quartz) were acquired for use as thermal inertia reference standards. These materials were selected in order to have both high and low thermal inertia references. Both materials were sent to an independent laboratory<sup>1</sup> for determination of their respective thermal conductivity, specific heat, and density. The specific heat of both standards was determined by the method of mixtures, the density by a Beckman air pycnometer, and the conductivity by the American Society of Testing Materials (ASTM) method. Results of these determinations are given in Table 3.

Laboratory testing insured that each lamp was heating evenly across the surface of the standard or target. PRT-5 measurements indicated that the surfaces were being evenly heated within the accuracy of the PRT-5 (0.5°C). The radiative energy outputs of the three infrared lamps were balanced by adjusting the settings of the voltage regulators so that after a four minute heating period the temperatures of a given standard recorded during cooling differed by no more than 0.5°C for each lamp. This calibration procedure was

TABLE 3  
THERMAL INERTIA STANDARDS

	<u>DOLOMITE</u>	<u>OTTAWA SAND</u>
Conductivity (k) cal $\text{cm}^{-1}\text{s}^{-1}\text{°C}^{-1}$	0.01182	0.00081
Density ( $\rho$ ) g $\text{cm}^{-3}$	2.97	1.74
Specific Heat (c) cal $\text{g}^{-1}\text{°C}^{-1}$	0.20	0.25
Thermal inertia (P) cal $\text{cm}^{-2}$ $\text{s}^{-1/2}\text{°C}^{-1}$	0.0838	0.0188

<sup>1</sup>(Geosciences LTD., Solana Beach, California 92075)

performed with both the Ottawa sand and the dolomite standards to insure accuracy.

Solution of Equation 1 requires a knowledge of the infrared emissivities of the standards and target. The range of infrared emissivities found among natural terrain materials is generally between 0.89 and 0.99. If no correction is made for emissivity of target and standard in Equation 1, given a possible range of 0.89 - 0.99, an error of 35% could arise in the value of thermal inertia. We did not have the capability to measure the emissivity of the dolomite and Ottawa sand and on a practical basis it would be impossible to measure the emissivity of each target in the field. However, by employing published values (Buechner and Kern, 1965) for dolomite (0.96) and quartz sand (0.92), and by assuming a median value of 0.92 for the target, the potential error in calculated thermal inertia is less than about 14%.

Further testing of the TIM under laboratory conditions disclosed a number of problems. The chief difficulty was determining the nature and magnitude of the heat flux density ( $F_0$ ) at the surface of the standards and target. Use of Equation 1 in the analysis required that  $F_0$  be constant and the same for each material (cf. assumption 2 in the previous discussion). Attempts to measure  $F_0$  with the Eppley precision IR radiometer under controlled, laboratory conditions proved difficult. A warm-up run of approximately seven minutes was necessary before  $F_0$  attained a constant value, about  $0.022 \text{ cal cm}^{-2}\text{s}^{-1}$  for each lamp.

This value of  $F_0$  was compared with numerical calculations of  $F$  derived from measurements of the heating and cooling rates of dolomite and Ottawa sand based on detailed laboratory studies. The surface temperature histories of the two materials were calculated from a finite difference approximation to the one-dimensional heat conduction equation. Next, the

surface boundary condition was adjusted until the calculated surface temperature at the end of the heating phase matched the observed temperature at this point, and then the surface temperature was calculated for a three minute period of cooling following the removal of the heat source. Calculated values of the cooling history were compared with the observed temperature decreases (Figures 10 and 11) in order to infer the nature of the surface boundary condition. In these calculations, the surface boundary condition was comprised of two parts, a constant flux  $F_0$  and a term accounting for radiative heat loss at the surface,  $\sigma (T_a^4 - T^4)$ , where  $\sigma$  is the Stefan-Boltzmann constant. Other trials were made with only the  $F_0$  term included in the calculations, but the results were no better than those shown here. Even so, the calculated values of  $F_0$  in Figures 10 and 11 were both larger (0.025 and 0.030  $\text{cal cm}^{-2}\text{s}^{-1}$  respectively) than the measured value of 0.022  $\text{cal cm}^{-2}\text{s}^{-1}$ , and furthermore, the calculated values were not equal. At first, it was thought that some heat loss due to convection could be occurring at the surface, but incorporation of an empirical expression (Hampton, 1946) to account for this effect did not appreciably alter the results. The calculated results for the heating phase were even more inconsistent than those for the cooling phase. This is shown in Figure 12 in which the observed increase in surface temperature for Ottawa sand is compared with the calculated increase for three different boundary conditions. Values of  $F_0$  ranged from 0.042 to 0.057  $\text{cal cm}^{-2}\text{s}^{-1}$ , about a factor of 2 more than the measured value. A similar calculation for dolomite produced an even larger value of  $F_0$ , 0.070  $\text{cal cm}^{-2}\text{s}^{-1}$ .

Despite this difficulty, there is some merit in using the TIM in the field to distinguish different materials from each other based on relative differences in the estimated thermal inertia. As long as wind speeds are low,

ORIGINAL PAGE IS  
OF POOR QUALITY

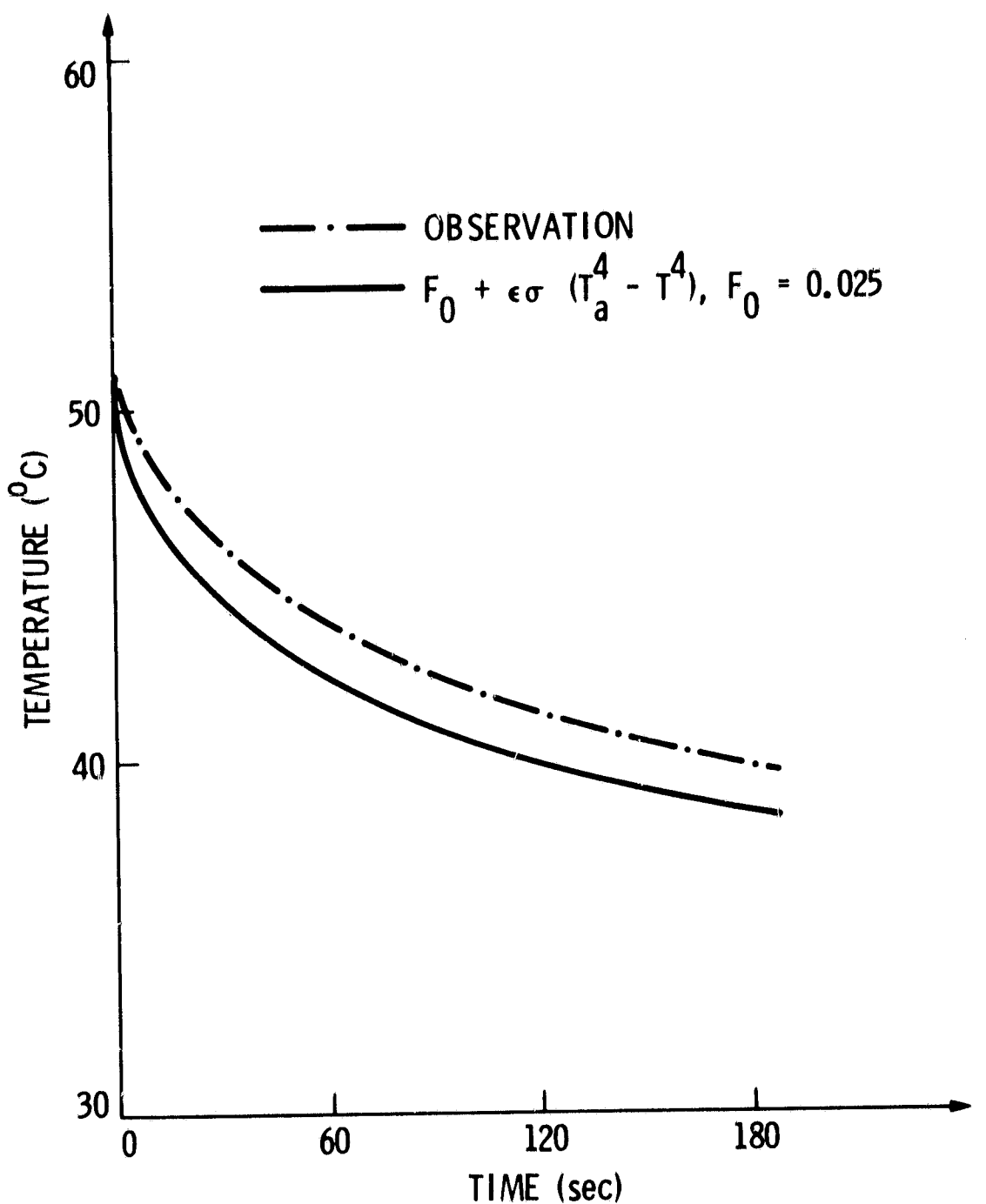


Figure 10. Model calculation for Ottawa sand.  $F_0$  is chosen to predict the correct temperature at the end of the heating period.

ORIGINAL PAGE IS  
OF POOR QUALITY

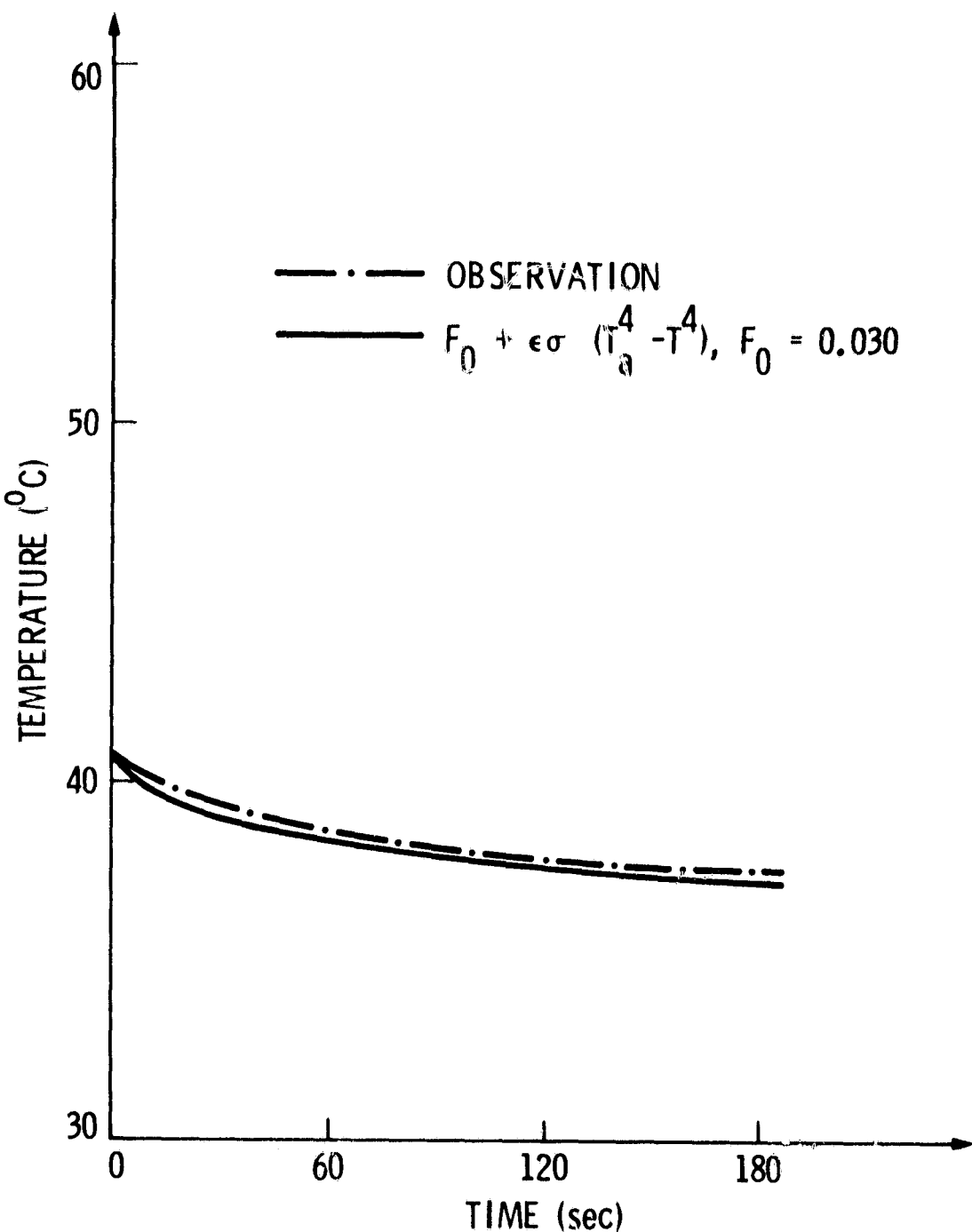


Figure 11. Model calculation for dolomite.  $F_0$  is chosen to predict the correct temperature at the end of the heating period.

ORIGINAL PAGE IS  
OF POOR QUALITY

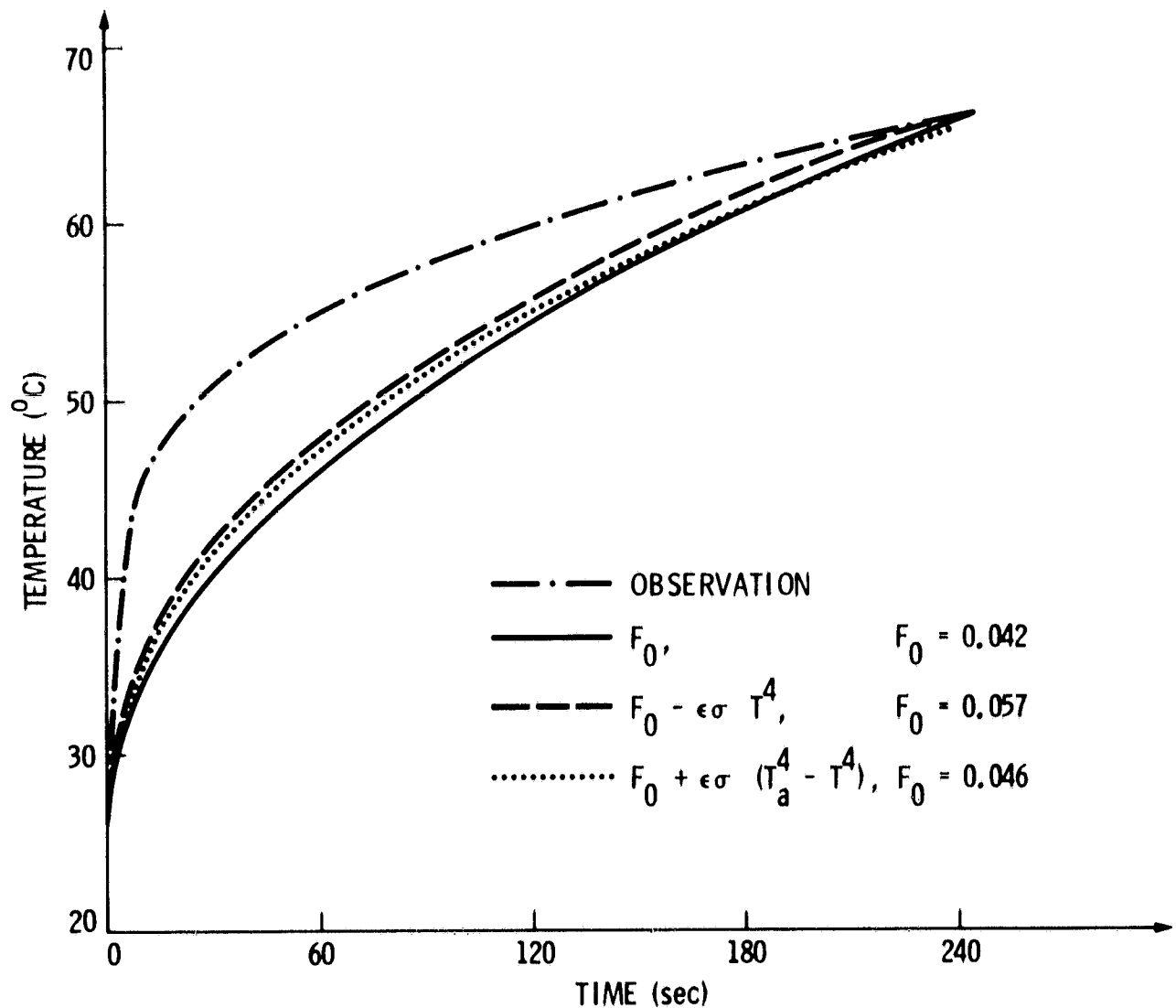


Figure 12. Calculated heating curves for Ottawa sand compared with observed heating after a warm-up period of ten minutes.

so that convective heat loss from the surface is minimized, the assumption of a constant flux at the surface under each lamp may be warranted. To test this hypothesis, we have used the TIM on field trips in the western United States.

Measurements were obtained during two field trips to selected test sites in western Nevada and eastern California in August and December 1979. The field sites in and around Goldfield, Hawthorne, and Elko, Nevada, and Pisgah Crater, California, were chosen because thermal modeling or thermal inertia mapping either had been performed or was planned over these sites. During field trips to these sites, approximately 60 measurements with the thermal inertia meter were recorded. As thermal inertia is very sensitive to soil moisture variations (Quiel, 1975), soil moisture samples of all alluvial material were taken. All sites were located in arid climates and the soils were quite dry (less than 10% moisture content per unit volume near the surface). Of these 60 measurements, approximately 20% were unusable due to equipment malfunction or strong gusts of wind during the heating or cooling cycle.

Table 4 shows the results of this investigation. The value of the calculated thermal inertia and the error are given for several rock and soil types based upon both the Ottawa sand and dolomite measurements. The error limits are only meant to indicate the effect of the 0.5°C inaccuracy in the PRT-5 measurement. A previously published value for a similar material is also given when available. Note that the dolomite-based values are consistently larger (about 21% on average) than the Ottawa sand-based values. Part of this discrepancy is due to the different heating histories of both materials. Both samples and targets were heated for less than seven minutes so that the heat flux density at the surface was still changing. Another factor is that we used typical values of emissivity for both standards. Any

TABLE 4  
 THERMAL INERTIA DERIVED FROM IN SITU THERMAL  
 INERTIA METER MEASUREMENTS

<u>Material</u>	<u>P Relative to Ottawa Sand</u>	<u>P Relative to Dolomite</u>	<u>Published Value</u>
Olivine Basalt	0.032 $\pm$ 0.003	0.042 $\pm$ 0.005	0.053 (Janza)
Pahoehoe Basalt	0.027 $\pm$ 0.002	0.039 $\pm$ 0.004	
Aa Basalt	0.032 $\pm$ 0.002	0.042 $\pm$ 0.003	
Barite	0.038 $\pm$ 0.003	0.043 $\pm$ 0.005	
Chert	0.042 $\pm$ 0.005	0.053 $\pm$ 0.005	
Andesite	0.033 $\pm$ 0.003	0.044 $\pm$ 0.005	0.055 (Brennan)
Rhyolite Ash Flow Tuff	0.016 $\pm$ 0.001	0.022 $\pm$ 0.003	
Silicified Rhyodacite	0.040 $\pm$ 0.004	0.048 $\pm$ 0.005	
Aeolian Sand	0.012 $\pm$ 0.001	0.015 $\pm$ 0.002	
Clay-Silt Playa	0.018 $\pm$ 0.001	0.024 $\pm$ 0.002	
Sandy Alluvium	0.010 $\pm$ 0.001	0.014 $\pm$ 0.002	0.014 (Clark)

deviation from the actual emissivities would cause a consistent difference between the P value based on the dolomite standard and that based on the Ottawa sand standard. For example, an error of 5% in either standard will introduce a consistent error of 10% between the two calculations. Nonetheless, the table shows that it is possible to discriminate materials like sands and silts from barites and basalts. Also, the ratio of P values for olivine basalt and andesite, versus sandy alluvium is nearly the same ( $\sim 3.5$ ) for both published and calculated values.

The TIM field tests indicate that the instrument is useful in a relative sense. As long as very accurate measurements of thermal inertia are

not required, it is adequate for discriminating among different materials. For example, our measurements of thermal inertia near Elko were to test the premise that exploration for barite might be feasible because of barite's very high density and hence high thermal inertia. We used the TIM to measure the thermal inertia of some very high grade barite deposits and the surrounding rock materials. Somewhat surprisingly the chert, which was commonly in the same area as the barite, in all cases had a higher thermal inertia than the barite. This was true both for outcrops and rubble. While barite has a higher density than chert, chert must have a higher thermal conductivity. Regardless of any error in the absolute value of thermal inertia of these two materials, the use of the TIM demonstrated that the chert consistently had a higher thermal inertia than the barite. Both had higher thermal inertias than most of the surrounding rocks, so thermal inertia images could probably be used to trace the extent of the chert-barite units.

The TIM is not useful in discriminating between materials whose  $P$  values are nearly the same nor for absolute measurements of thermal inertia, yet the need for such a field instrument is recognized. For this use, the precision of the instrument must be enhanced. Further study and testing is required, particularly in the following areas: 1) rapid application ( $\sim 1$  min or less) of a large, uniform and constant heat flux to the standard and target surfaces, 2) a detailed study of the best kinds of materials for use as standards, and 3) the effect of convective heat loss in the calculations.

#### IV. DATA PROCESSING

The remote sensing and ground truth data are used in the JPL thermal model as elements of a digital algorithm to compute thermal inertia values. The model is a one-dimensional heat conduction equation which is solved by finite difference techniques, subject to a specific set of initial and boundary conditions. In its original form, the model describes changes in temperature with depth and time for dry soils - an application that is reasonable for arid climates. A second version of the model has been developed (Njoku et al., 1980) to account for moisture transport in the soil so that it also predicts the spatial and temporal variations of volumetric soil water content. This involves a numerical process more complicated than the dry model calculation, since it requires the simultaneous solution of a pair of coupled, parabolic differential equations for heat and moisture flow.

All the aircraft and HCMM data sets have been evaluated to ensure a sufficiently good ensemble of data in order to produce a set of high quality thermal inertia images suitable for analysis. This includes eliminating cases with excessive noise in the thermal or albedo data. The daytime thermal, nighttime thermal, and albedo data sets were coregistered for each individual data set before they were used in the model: once without accounting for topographic corrections, and in the case of the HCMM data, again with the corrections included. Topographic information (for slope azimuth and orientation), in the form of digitized values from the National Cartographic Information Center (NCIC), is added to the processing in the latter case.

## A. Aircraft Data Processing

### 1. M<sup>2</sup>S Aircraft Scanner Data Processing

Included in this study were ten sets of flight lines using the Bendix Modular Multispectral Scanner (M<sup>2</sup>S). The M<sup>2</sup>S was mounted in either a NP-3A or a NC-130B aircraft (Table 1). The M<sup>2</sup>S is an eleven channel scanner, with ten narrow bandwidth channels in the visible to near infrared range and one broad bandwidth thermal channel (Table 5). When operating at night, only the eleventh (thermal) channel is activated.

TABLE 5

#### M<sup>2</sup>S WAVELENGTH BANDS

<u>Channel Number</u>	<u>Bandwidth (Micrometers)</u>		<u>Detector</u>
1	.33	~ .44	Silicon
2	.44	~ .48	Silicon
3	.49	~ .54	Silicon
4	.54	~ .58	Silicon
5	.58	~ .62	Silicon
6	.62	~ .66	Silicon
7	.66	~ .70	Silicon
8	.70	~ .74	Silicon
9	.76	~ .86	Silicon
10	.97 ~ 1.065		Silicon
11	7.95 ~ 13.5		HgCdTe

For the thermal channel, there is an internal calibration to reference blackbodies. Once during each scan line the thermal sensor monitors two blackbodies, one warmer, the other cooler than the anticipated ground temperature. The actual temperatures of these two blackbodies are independently monitored by thermistors and automatically recorded with the scanner data.

The channel 11 DN value ( $DN_{11}$ ) for a pixel is assumed to be linear with thermal radiance ( $r_t$ ) rather than temperature, but since radiance of a blackbody is given by

$$r_t = \epsilon\sigma T^4, \quad (2)$$

the temperature can be found from

$$T^4 = \frac{r_t}{\epsilon\sigma} = aDN_{11} + b \quad (3)$$

where  $a$  and  $b$  are determined by solving Equation 3 for the two blackbodies of known  $T$  and  $DN_{11}$ . The emissivity ( $\epsilon$ ) is assumed constant.

There is no corresponding internal calibration for channels one through ten. As a result, calibration of these channels required on-site ground measurements, taken at the time of the flight. The calibration used for the March, 1975 flights has been previously reported by Gillespie and Kahle (1977). The calibration process was repeated for the October, 1976 flights and is described below. This second calibration was used for all subsequent flights.

Spectral reflectance was measured at seven sites within the Cuprite district during October, 1976, using the Jet Propulsion Laboratory

Portable Field Reflectance Spectrometer (PFRS) (Goetz et al., 1975). These seven sites were chosen for their diverse spectral characteristics and for their ability to be located on the digital images.

It was assumed that the response of each sensor is linear with respect to the reflectivity of the observed region. That is, for each M<sup>2</sup>S channel  $n$ ,

$$DN_n = m_n R_n + b_n \quad (4)$$

where  $R_n$  is the average reflectance within the bandpass of channel  $n$ . Plots of  $DN_n$  vs.  $R_n$  for the seven calibration sites are shown in Figure 13. Channel 1, whose bandpass is outside the range of the PFRS and represents a relatively minor portion of solar power, was not calibrated. The coefficients  $m_n$  and  $b_n$  were computed from these data, using a least-squares fitting algorithm.

Since the value of interest is the amount of energy absorbed by the surface, the desired overall albedo is an average of the channels, weighted by the amount of solar energy incident upon the surface within each bandpass. That is, the weighted albedo,  $A_w$ , is represented by

$$A_w = \frac{\sum_{n=2}^{10} W_n R_n}{\sum_{n=2}^{10} W_n} \quad (5)$$

where the weighting factor  $W_n$  is computed as

$$W_n = \int_0^{\infty} F_n(\lambda) S_n(\lambda) d\lambda \quad (6)$$

ORIGINAL PAGE IS  
OF POOR QUALITY

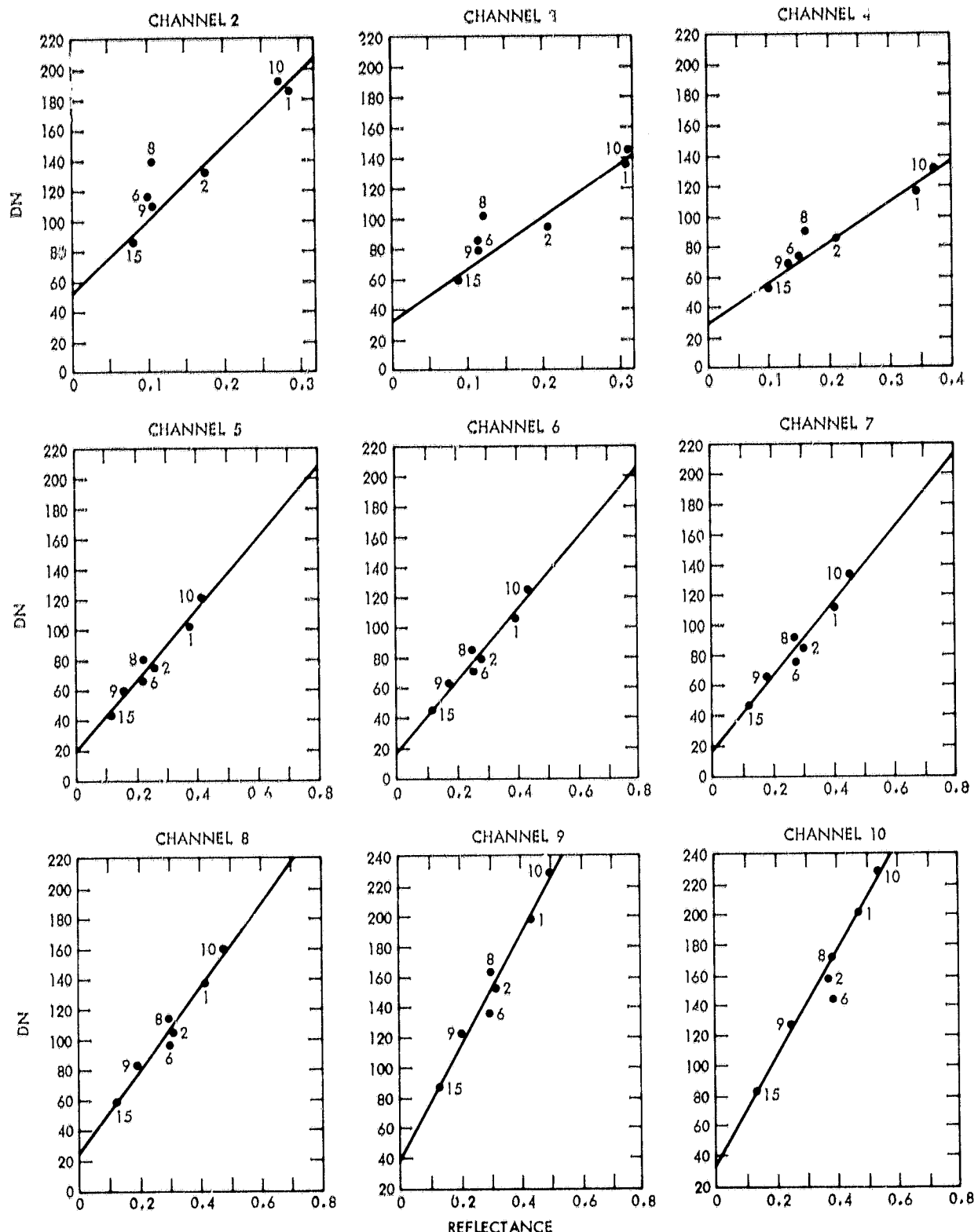


Figure 13. M<sup>2</sup>S calibration plots.

In Equation 6  $F_n(\lambda)$  is the product of the filter transmittance and scanner detector sensitivity (overall sensor response),  $S_n(\lambda)$  is the solar irradiance, and  $\lambda$  is the wavelength. Combining Equations 4 and 5 yields

$$A_w = C + \sum_{n=2}^{10} U_n DN_n \quad (7)$$

where,

$$C = - \frac{\sum_{n=2}^{10} \frac{W_n b_n}{m_n}}{\sum_{n=2}^{10} W_n} \quad (8)$$

and

$$U_n = \frac{W_n}{m_n \sum_{n=2}^{10} W_n} \quad (9)$$

The computed values for  $C$  and  $U_n$  are listed in Table 6.

After a day-night pair of images has been calibrated, the images must be geometrically rectified. Each image was resampled (using a linear interpolation) to remove the distortions originating from the panorama effect and from a non-unity aspect ratio. The roll, pitch, and yaw of the aircraft carrying the scanner introduce additional geometric distortions. While these distortions were sometimes quite noticeable, no attempt was made to remove them.

In order to generate a night-to-day temperature difference image, the nighttime image must be registered to the daytime image. Day-night registration has sometimes proven quite difficult. The primary problem in aircraft image registration arises from the roll, pitch, and yaw distortions within the images. These distortions are often local in nature and completely

TABLE 6  
CALIBRATION COEFFICIENTS FOR  $M^2S$  SCANNER

<u>U Coefficient</u>	<u>Value</u>
2	.000273
3	.000333
4	.000324
5	.000363
6	.000324
7	.000341
8	.000347
9	.000502
10	.000388
C	-.0946

uncorrelated from day to night. A secondary registration problem is that the features visible in a nighttime thermal image are not necessarily conspicuous in a daytime image, visible or thermal. The techniques used to determine a registration transformation fall into two general classes: 1) polynomial fitting, and 2) triangulation.

In a polynomial fit, the transformation from the old coordinates to new coordinates is described by a simple polynomial in two variables (line and sample). With a first order polynomial fit, even a slight deviation from a straight flight line yields substantial misregistration of most of the image. Higher order polynomial fits (up to third order have been tried) are somewhat better at tracking non-linear and local distortions, but tend to work very poorly near the edges and corners of an image.

In a triangulation scheme, the image is divided into a grid of numerous rectangular cells. The transformation for each cell is a linear transformation, but the transformation is independently recomputed for each cell, using only the nearest tiepoints that enclose the corners of the cell. This technique yields a generally closer registration than the polynomial fit, but there may be unpleasant artifactual features along cell boundaries. There is no guarantee that the transformations are continuous across cell boundaries and, as a result, such a boundary may appear as an apparent tear, crimp, or fold in the transformed image. The triangulation method may also lead to poor registration of corners and edges (though not to the extent of the high-order polynomial fits). Most images were registered using the triangulation technique.

## 2. HCM and DMS Aircraft Scanner Data Processing

Computer compatible tapes of nine sets of day-night flights using scanners mounted on a U-2 aircraft were received (Table 1). Seven sets utilized the HCM scanner, while two sets used a modified Daedalus model DEI-1260 multispectral scanner (DMS).

The HCM scanner simulates the two sensors used in the HCMM satellite. The DMS scanner contains eleven channels, ten with visible and near IR bandpasses, and one channel in the thermal range. The characteristics

of these two scanners are summarized in Table 7. In all cases, the calibration information was provided by the operators of the scanner. A more detailed description of the HCM scanner characteristics may be found in Murphy *et al.* (1978).

TABLE 7  
CHARACTERISTICS OF U-2 BORNE SCANNERS

	HCM	DMS
Nominal Altitude	65,000 ft.	65,000 ft.
Angular Resolution (IFOV)	2.8 mr	2.5 mr
Spatial Resolution (at Nadir)	55 meters	50 meters
FOV	90°	85°
Samples Per Scan Line	400	715
Bandpasses		
1	10.5-12.5 $\mu$ m	0.38-0.42 $\mu$ m
2	0.51-0.89	0.42-0.45
3		0.45-0.50
4		0.50-0.55
5		0.55-0.60
6		0.60-0.65
7		0.65-0.69
8		0.70-0.79
9		0.80-0.89
10		0.90-1.10
11		10.40-12.50

Noise (both coherent and random), missing segments of data, severe geometric distortions, and cloud cover combined to make most of these day-night pairs unusable (Figure 14). Only the March, 1978 and April, 1979 data of Death Valley were adequate for generation of thermal inertia images.

The 1:250,000 NCIC digital elevation data were used as the basis for registering daytime and nighttime images (Figure 15). With the images associated with elevation data, topographic data could be used to gain a more sophisticated estimate of the thermal inertia. (At a resolution of 63.4 meters, the NCIC data are comparable to the U-2 images, but inadequate for the higher resolution images from the M<sup>2</sup>S scanner).

The registrations were performed in the following sequence: 1) the nighttime image was registered to the daytime image; 2) the daytime albedo image was used to find a transformation to the elevation image; 3) this transformation was applied to both the day and night (registered to day) images.

This two-stage registration of night to map base implies a summation of errors from each transformation. The alternative, a direct registration of the nighttime image to the NCIC data was less satisfactory, due to a lack of distinct features common to both images (compare Figures 15b and 16c).

#### B. HCMM Satellite Data Processing

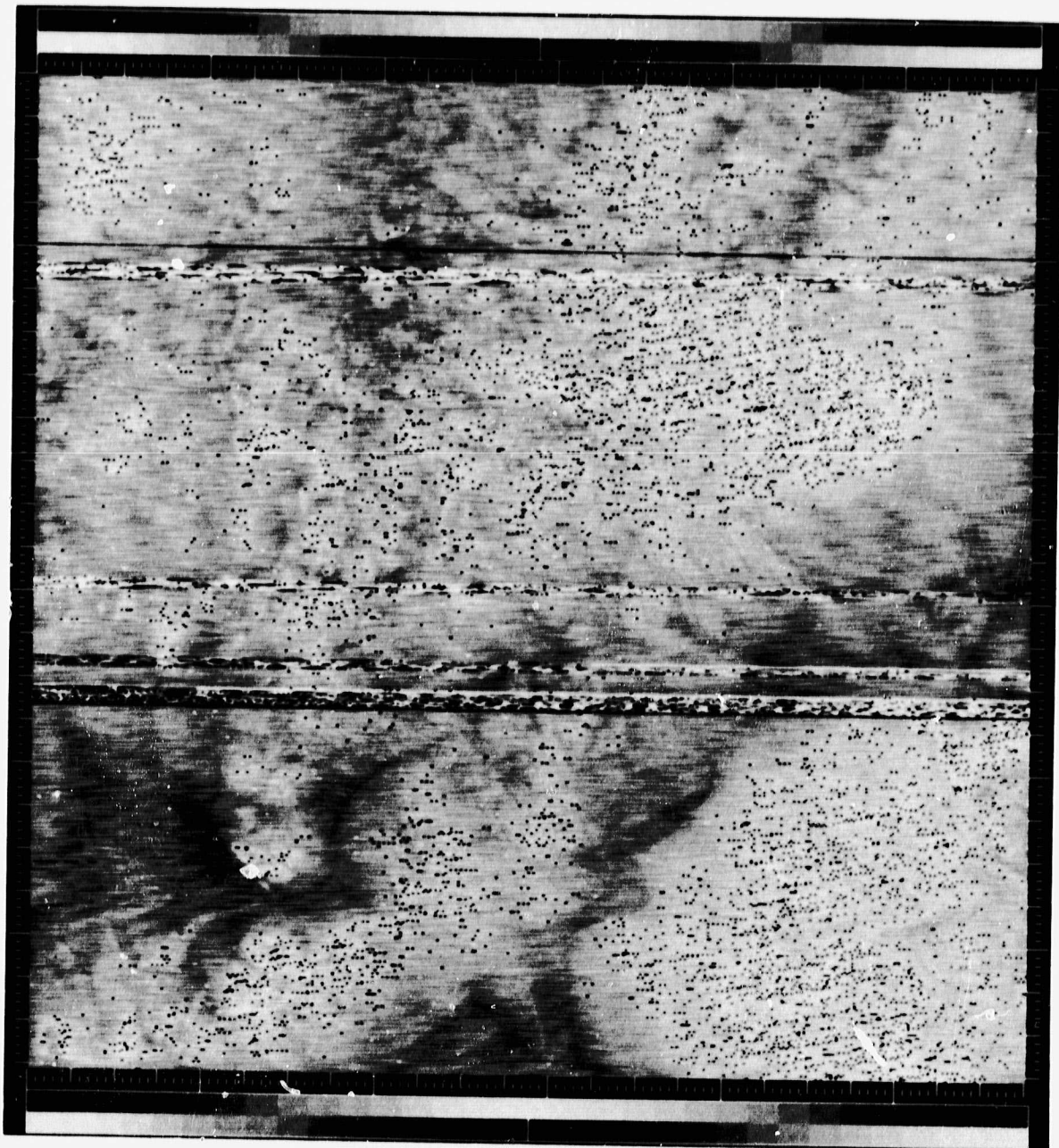
Nine sets of HCMM overpasses were included in this study (Table 2). In general, a set consists of two nighttime scenes, one day apart, and two daytime scenes, also one day apart, with the first daytime scene following the second nighttime scene by twelve hours. That is, the scenes are in the order night-night-day-day (NNDD). In several cases, the test site data

ORIGINAL PAGE  
**BLACK AND WHITE PHOTOGRAPH**



Figure 14a. Example of coherent noise and severe geometric distortion.

**ORIGINAL PAGE  
BLACK AND WHITE PHOTOGRAPH**



**ORIGINAL PAGE  
BLACK AND WHITE PHOTOGRAPH**

Figure 14b. Example of random noise.

ORIGINAL PAGE  
BLACK AND WHITE PHOTOGRAPH



Figure 14c. Example of missing data segments.

ORIGINAL PAGE  
BLACK AND WHITE PHOTOGRAPH



Figure 15a. Shaded topographic relief image of Walker Lane, Nevada.

ORIGINAL PAGE  
BLACK AND WHITE PHOTOGRAPH



Figure 15b. Shaded topographic relief image of Death Valley, California.

ORIGINAL PAGE  
BLACK AND WHITE PHOTOGRAPH

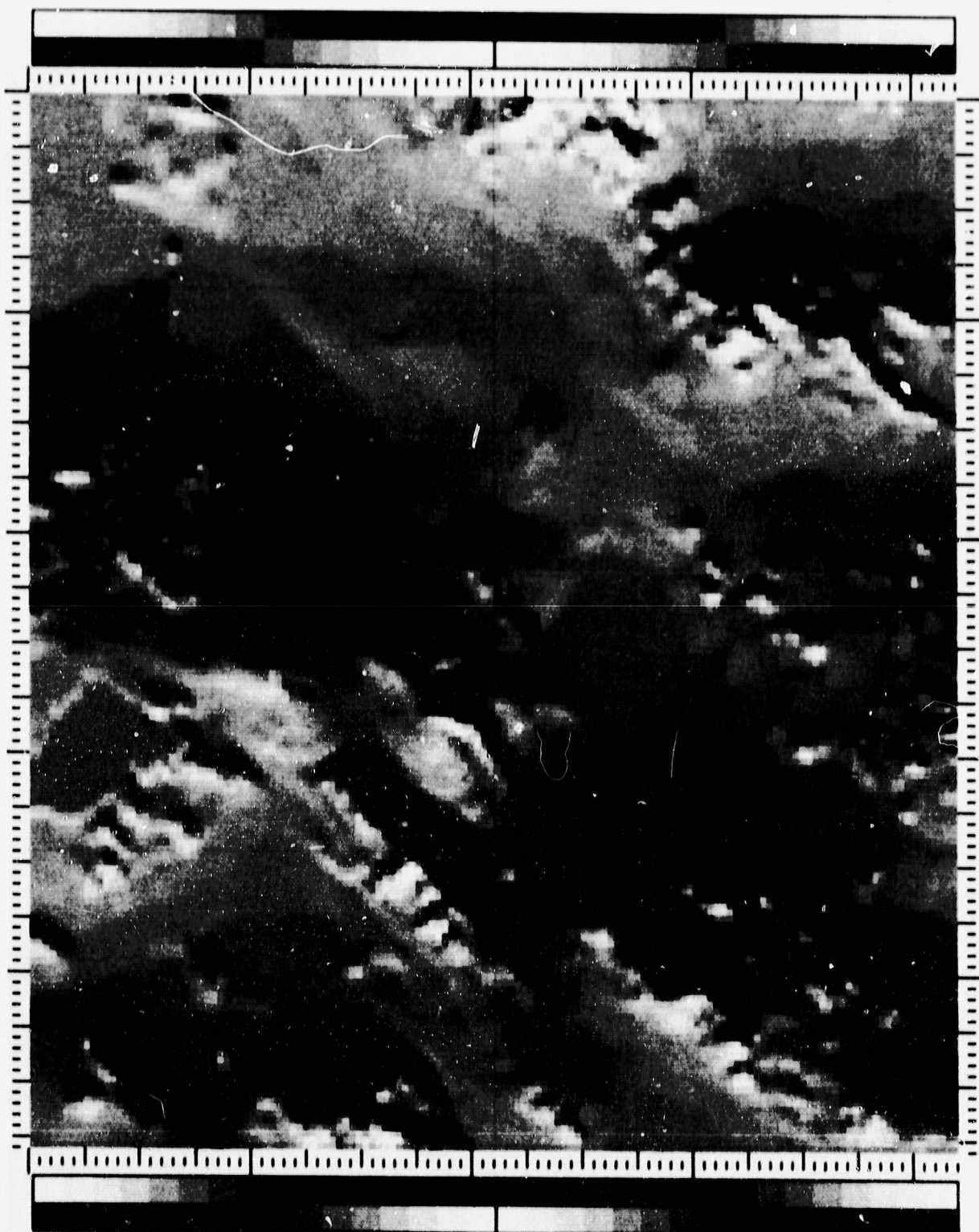


Figure 15c. Shaded topographic relief image of Pisgah, California.

ORIGINAL PAGE  
BLACK AND WHITE PHOTOGRAPH



Figure 16a. Death Valley March 1978 registered visible image.

ORIGINAL PAGE  
BLACK AND WHITE PHOTOGRAPH



Figure 16b. Death Valley March 1978 registered day thermal image.

ORIGINAL PAGE  
BLACK AND WHITE PHOTOGRAPH



Figure 16c. Death Valley March 1978 registered night thermal image.

were contained on two tapes; these data were mosaicked together before any other processing was performed.

The characteristics of the HCMM satellite and its sensors are reported in detail elsewhere (Bohse, et al., 1979). The data received at JPL were calibrated data for both channels, and geometrically rectified to a Hotine Oblique Mercator base. The spatial resolution was approximately 500 meters. Registration was a multi-step operation, and involved the following steps for each set:

1. For the entire scene, both nighttime images and the second daytime image were registered to the first daytime image of the set. In a typical registration, about 25 points common to both images would be located and used to find a geometric transformation. The transformation used was a first order, unconstrained polynomial, i.e.,

$$\begin{aligned}x' &= Ax + By + C \\(10)\end{aligned}$$

$$y' = Dx + Ey + F$$

where the coefficients A, B, C, D, E and F are determined by a least-squares fit. The average residual to the fitted surface was usually under 2.0 pixels.

2. For each of the test sites, a day-night pair was chosen for generation of thermal inertia images. Whenever possible, a pair separated by 12 hours was chosen, but if a site was missed by one of those passes, a 36 hour pair was chosen.

3. The local area surrounding each test site was re-registered, night to day. These corrections were limited to simple offsets, i.e.,

$$X' = x + A$$

(11)

$$Y' = y + B$$

The relative scale and rotation of the images were not allowed to change for these smaller scenes, since the overall registration was expected to yield a better estimate of these values. Offsets varied from 0 to 2 pixels.

4. Except for the San Rafael pair, for which topographic information was not readily available, all pairs were then registered to the 1:250,000 NCIC digital elevation data. A first order unconstrained fit was used, with typical residuals of about one pixel.

As a result of this technique, all pairs were registered to a common Universal Transverse Mercator (UTM) map base at each site.

#### C. Generation of Thermal Inertia Images

A model has been developed at JPL for the purpose of predicting the temperature of the Earth's surface as a function of albedo, topographic orientation, and meteorological conditions. Using this model at each site and date, day-night temperature differences were predicted for a range of albedos and (when topographic information was available) ground slopes and slope azimuths. These predicted  $\Delta T$ 's were then used to generate a table that expressed thermal inertia as a function of albedo,  $\Delta T$ , slope, and slope azimuth. To generate a thermal inertia image, each pixel was referred to this table and assigned the value that corresponded to each of those variables.

The theoretical basis and method of application of this model have been described in detail elsewhere (Kahle, 1977). In brief, the model works

in the following manner. An explicit finite difference scheme is used to approximate a solution to the one-dimensional heat flow equation

$$\frac{\partial T}{\partial t} = \kappa \frac{\partial^2 T}{\partial z^2} \quad (12)$$

where  $T$  is temperature,  $\kappa$  is thermal diffusivity,  $t$  is time and  $z$  is depth. A one centimeter vertical grid is used from the surface to a depth of  $z = 50$  centimeters, and temperature values are recomputed at each depth for each twenty second time interval. Initial temperature profile values are estimates (derived from on-site measurements when available); the importance of these values is minimized by initializing the model to several hours prior to the time interval of interest. The lower boundary condition is that the temperature at 50 cm depth is constant. The upper surface boundary condition is that the heat flux is continuous across the boundary.

In order to compute the fluxes at the surface, some meteorological and geographic data are needed. The date, latitude, and surface elevation are needed to compute solar radiation. Air and ground temperatures and wind speed are used to compute the sensible heat flux. If the latent heat flux is included, the air and ground specific humidities are also used.

Thermal inertia images were then created for each date at each site, with and without the topographic corrections. Some selected full frame thermal inertia images were also produced. Histograms of the distribution of numerical values of thermal inertia in each scene were also generated during this process. Examples are discussed in subsequent sections.

## V. DATA AND TECHNIQUE EVALUATION

We have worked entirely with digital HCMM data in an effort to produce quantitatively meaningful thermal inertia images. In this section we discuss and assess many of the elements involved in a numerical study of the data, the problems encountered, and the resulting thermal inertia products. Specifically we discuss atmospheric transmission and emission effects, problems of HCMR data calibration, the dependence of thermal inertia calculations on meteorological and soil moisture conditions, and model sensitivity studies. We discuss the numerical values of thermal inertia which we obtain, as a function of site, material and time, and finally, we compare modeled thermal inertia with apparent thermal inertia.

### A. Atmospheric Effects

In order to determine the temperature of the surface of the Earth from radiance measurements obtained with a satellite sensor, there are several factors which must be taken into account. These include the emissivity of the surface, atmospheric attenuation of the upward radiation, atmospheric emission of radiation upward into the sensor and downward to be reflected upward to the sensor, and finally the calibration of the sensor, relating received radiance to apparent brightness temperature. The sensor calibration is discussed in a later section. We will discuss the other factors here.

The spectral radiance received by the satellite sensor can be expressed by

$$L_S(\lambda) = [\epsilon_\lambda L_{BB}(\lambda, T_g) + (1-\epsilon_\lambda)L_{A\uparrow}(\lambda)]\tau_\lambda + L_{A\uparrow}(\lambda). \quad (13)$$

Here the ground temperature,  $T_g$ , is the quantity we wish to determine, from the measurement of  $L_S(\lambda)$ . Therefore it is necessary to measure, model, or

ignore the rest of the terms in Equation 13, as defined and discussed below.

The spectral radiance emitted by the ground is given by

$$L_g(\lambda) = \epsilon_\lambda L_{BB}(\lambda, T_g) \quad (14)$$

where  $\epsilon_\lambda$  is the emissivity of the surface material and  $L_{BB}(\lambda, T_g)$  is the black-body spectral radiance at wavelength  $\lambda$  and temperature  $T_g$ . In the 10.5 to 12.5  $\mu\text{m}$  range, most natural surface materials have emissivities between about 0.90 and 0.98. Our lack of knowledge of the emissivity of the surface material will thus introduce an error of a few percent if we assume an average value around 0.95.

The reflected portion of the downward atmospheric radiation  $(1-\epsilon_\lambda) L_{A\downarrow}(\lambda)$  is small because the reflectivity of the surface  $(1-\epsilon_\lambda)$  is small, on the order of 0.05, and the atmospheric downward radiation  $L_{A\downarrow}(\lambda)$  is also small in this window region compared to the radiance from the surface. Therefore, we can ignore this term.

The remaining quantities which we need to determine from models, measurements or some combination of these, are the atmospheric transmission,  $\tau_\lambda$ , and the upward atmospheric radiation  $L_{A\uparrow}(\lambda)$ . These two terms are related. In these wavelengths, contributions to both are due almost entirely to the presence of water vapor and aerosols. As the concentrations of these absorbers-emitters and scatterers increase, the contribution of the ground signal to the radiation received at the satellite will decrease and the contribution of the atmospheric signal will increase. We turn to the theory of radiative transfer in order to understand the effects.

The basic problem of radiative transfer is to determine how a radiation field is altered on passing through and interacting with a medium

(Chandrasekhar, 1960). If we consider a pencil of radiation of intensity  $I_\nu$  (in a frequency interval  $\nu$  to  $\nu + d\nu$ ) propagating through a medium in a specified direction, then we can consider the various ways this intensity will be altered in traveling a distance  $ds$ .

The radiation can be weakened by two processes: true absorption by the medium; and, scattering of the radiation into another direction. In practice, both of these processes are combined into a mass attenuation coefficient, defined as  $\kappa_\nu$  in

$$dI_\nu = -\kappa_\nu \rho I_\nu ds \quad (15)$$

where  $\rho$  is the mass density of the medium. This attenuation coefficient can be due to true absorption only, scattering only, or a combination of both.

As with the weakening of our pencil of radiation in traversing an element of mass, there are two similar processes enhancing the radiation: scattering of radiation into the direction of the pencil, and emission by the mass element. Again, the two are treated together, this time with a single emission coefficient  $j_\nu$  defined such that the element of mass  $dm$  emits into the solid angle  $d\omega$  an amount of radiation in the frequency range  $\nu$  to  $\nu + d\nu$  equal to  $j_\nu dm d\omega d\nu$  in unit time.

The source function is defined as

$$J_\nu \equiv \frac{j_\nu}{\kappa_\nu} \quad (16)$$

For scattering only, this is given by

$$J_v(\theta, \phi) = \frac{1}{4\pi} \int_0^\pi \int_0^{2\pi} p(\theta, \phi; \theta', \phi') I_v(\theta', \phi') \sin \theta' d\theta' d\phi' \quad (17)$$

where  $p$  is the phase function of scattering, when we are considering the scattering from direction  $\theta', \phi'$ , into direction  $\theta, \phi$ .

For no scattering and an atmosphere in thermal equilibrium, the emission coefficient according to Kirchhoff's Law can be given in terms of the absorption coefficient

$$j_v = \kappa_v B_v(T) \quad (18)$$

where  $B_v(T)$  is the black body radiation. Thus the source function  $J_v$  for atmospheric emission is just  $B_v(T)$ . In general the source term will be the sum of the scattering and emission source terms.

The basic equation of radiative transfer sums up the contribution of the various processes which we have just discussed

$$\frac{dI_v}{ds} = -\kappa_v \rho I_v + j_v \rho \quad (19)$$

or

$$-\frac{dI_v}{ds} = \kappa_v \rho I_v - \kappa_v \rho J_v \quad (20)$$

The solution to the equation of radiative transfer is

$$I(s) = I(o) e^{-\tau(s,o)} + \int_o^s J(s') e^{-\tau(s,s')} \kappa \rho ds' \quad (21)$$

where now  $\tau$  is the optical thickness defined by

$$\tau(s, s') = \int_{s'}^s \kappa \rho ds \quad (22)$$

Thus the intensity of radiation at the satellite,  $I(s)$ , is given by the intensity at ground level,  $I(o)$ , reduced by  $e^{-\tau(s,o)}$  plus the radiation from the atmospheric sources reduced by  $e^{-\tau(s,s')}$ . While this solution is easy to write, the evaluation of the atmospheric absorption, scattering and emission parameters is not easy.

In the middle infrared wavelength region in which HCMR operates (10.5-12.5  $\mu\text{m}$ ) both scattering and absorption-emission occur. Rayleigh scattering occurs when the particle size is small compared to the wavelength. Hence, Rayleigh scattering from the atmospheric gas molecules is primarily confined to the visible portion of the spectrum. The scattering in the middle infrared wavelengths of concern here is by aerosols -- liquid water, ice and other particulates.

The major atmospheric constituents,  $\text{N}_2$  and  $\text{O}_2$ , being symmetrical homonuclear diatomic molecules, without a permanent dipole field, do not have vibrational and rotational absorption features, and are essentially transparent to visible and infrared radiation. The absorption and emission in the middle infrared wavelengths is caused by the minor polyatomic gases in the atmosphere, primarily  $\text{H}_2\text{O}$ ,  $\text{CO}_2$  and  $\text{O}_3$ . Even though the 10.5 to 12.5  $\mu\text{m}$  region is considered a good atmospheric window, there is significant absorption and emission by the water vapor. Unfortunately, the water content of the atmosphere is quite variable and the radiation effects are extremely sensitive to these changes. Contrary to the statements in the HCMM Data Users Handbook (Goddard Space Flight Center, 1978), these effects are much more sensitive to

water vapor amount than to atmospheric temperature, as can be inferred from the source term in the radiative transfer equation.

Various numerical solutions to the problem of atmospheric radiative transfer exist. They vary in complexity and accuracy from those giving a single value of total radiation based on one or two average atmospheric parameters, to numerical models which follow every known absorption line, as a function of measured pressure, temperature and atmospheric gas profiles. For the HCMM problem we required a model of intermediate complexity.

A good example of a calculation of the radiation emerging from the top of the atmosphere, developed to study the atmospheric effects on the satellite measurement of surface temperature can be found in the work of Anding et al. (1971). One of their figures, reproduced here as Figure 17, illustrates many of the important effects. The atmospheric model shown in this figure represents a mean atmosphere for 30°N latitude. The solid curves show the spectral radiance emerging from the top of the atmosphere as a function of surface temperature. The dashed curves show the black body radiation which would reach the satellite if there were no intervening atmosphere. The solid curve labelled 0°K represents the atmospheric component of the upward radiation. The magnitude of atmospheric effects in the 10.5 to 12.5  $\mu\text{m}$  wavelength region of interest is readily apparent. Because this model was developed for studies of sea surface temperatures, it assumes the surface to be at sea level.

Another model, which we have been using in our numerical studies of HCMM data and which gives results similar to those of Anding et al. (1971), is the LOWTRAN 5 model, developed at the Air Force Geophysical Research Laboratory. The source code for this versatile computer model is available to the public. The model includes a choice of six standard atmospheres: U.S.

ORIGINAL PAGE IS  
OF POOR QUALITY

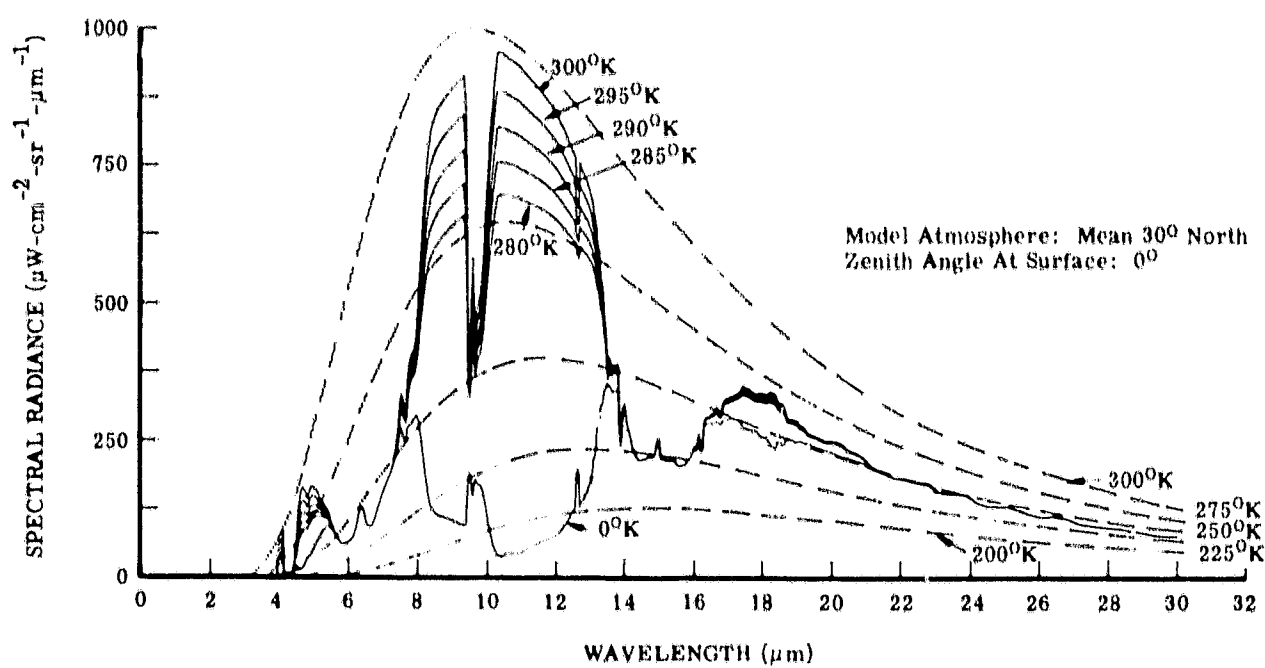


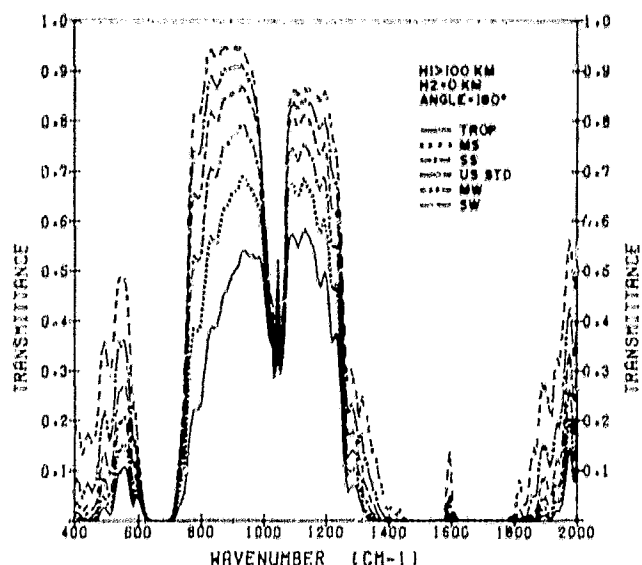
Figure 17. Upward spectral radiance at 100 km, with surface temperature as a parameter, after Anding et al. (1971).

Standard Atmosphere, tropical, midlatitude summer, midlatitude winter, subarctic summer and subarctic winter. Alternatively, it also allows the user to enter his own atmospheric model or measurements. Figure 18, after Kneizys *et al.* (1980), shows some LOWTRAN 5 results. The top figure illustrates the extreme sensitivity of atmospheric transmission to the particular atmospheric model selected. Note that the atmospheric transmittance in the HCMR wavelengths varies from approximately 50% to 95%, primarily as a function of water vapor content. Another important feature of the LOWTRAN 5 model is that it allows the surface elevation to vary. In our running of the model over the range of elevations present at our test sites (- 73 m at Badwater in Death Valley to 3400 m at Telescope Peak only a few miles away), it became apparent that meaningful atmospheric corrections must include surface elevation.

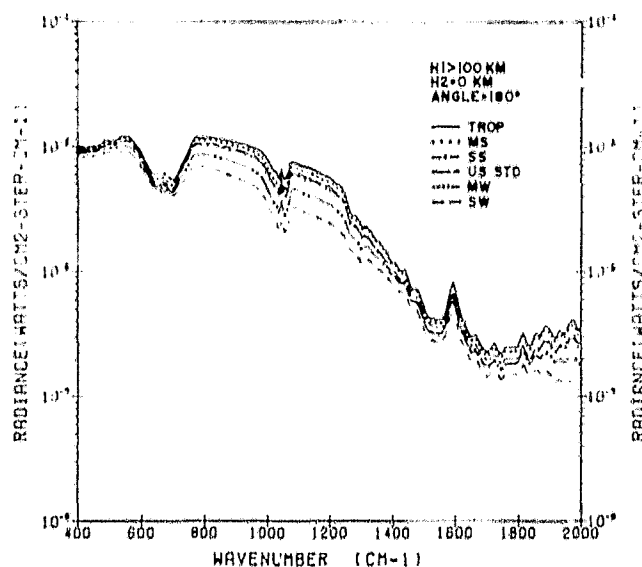
In order to determine the magnitude and variability of the atmospheric corrections required for HCMM data interpretation, we have made several runs with LOWTRAN 5. Assuming a given surface temperature, elevation and atmospheric model, we used LOWTRAN to compute the atmospheric transmission, and the upward radiance at the top of the atmosphere from both the ground and atmospheric emission. This radiance was converted to the effective temperature which would be sensed by the satellite, and the difference between surface temperature and effective temperature was noted. Also the percentage of upward radiance originating in the atmosphere rather than at the surface was calculated. We then allowed the parameters to vary, one at a time. These results are presented in Tables 8-12.

In Table 8 we used the rawinsonde data for July 18, 1978 at 2300 Z (1500 PST) and an assumed ground temperature of 300°K and allowed ground elevation to vary from 1 km to 3 km. The atmospheric effect was to make the ground appear colder than it actually was by from 4°K at an elevation of 1 km

ORIGINAL PAGE IS  
OF POOR QUALITY



a.



b.

Figure 18. (a) transmittance, and (b) radiance spectra for a vertical path looking at the ground from space, for the six model atmospheres of LOWTRAN 5, after Kneizys et al. (1980).

to only 1°K at an elevation of 3 km. In Table 9 we show the result when elevation is constant at 1 km, and the surface temperature is allowed to vary from 260°K to 340°K. There is a striking variation in the atmospheric effect, with the apparent temperature of the surface varying from 3°K warmer for the coldest surface to 11°K colder than the actual surface temperature for the hottest surface. This strong surface-temperature dependence of the atmospheric effects is in good agreement with effects noted by both European investigators and by us in comparisons of measured surface temperature and satellite data. Table 10 shows the results for several different rawinsonde observations over an eight day period in July, 1978; ground elevation and temperature are held constant. Only very small differences are noted. Finally in Tables 11 and 12, we repeat the conditions of Tables 8 and 9, only now using the LOWTRAN midlatitude summer atmospheric model. This model, unlike the rawinsonde data, is available down to sea level. There is somewhat more atmospheric water vapor in this model than in the rawinsonde observations so the effects are slightly larger, but quite similar to those noted in Tables 8 and 9.

TABLE 8

## RESULTS FROM LOWTRAN USING RAWINSONDE DATA FOR VARYING SURFACE ELEVATIONS

Atmospheric Model		Surface Elevation	Surface Temperature	Atmospheric Transmission	% Radiance from Atmos.	Effective Temperature	δT
<b>Rawinsonde</b>							
July 18, 1978	1500 PST	1.0	300	.7468	20.00	296	-4
"	"	1.5	"	.8130	13.98	297	-3
"	"	2.0	"	.8650	9.53	297	-3
"	"	2.5	"	.9015	6.61	298	-2
"	"	3.0	"	.9272	4.59	299	-1

TABLE 9

## RESULTS FROM LOWTRAN USING RAWINSONDE DATA FOR VARYING SURFACE TEMPERATURES

Atmospheric Model		Surface Elevation	Surface Temperature	Atmospheric Transmission	% Radiance from Atmos.	Effective Temperature	δT
<b>Rawinsonde</b>							
July 18, 1978	1500 PST	1	260	.7468	31.19	263	3
"	"	"	270	"	27.66	271	1
"	"	"	280	"	24.72	280	0
"	"	"	290	"	22.14	288	-2
"	"	"	300	"	20.01	296	-4
"	"	"	310	"	18.16	304	-6
"	"	"	320	"	16.60	312	-8
"	"	"	330	"	15.20	320	-10
"	"	"	340	"	14.07	329	-11

TABLE 10  
RESULTS FROM LOWTRAN USING RAWINSONDE DATA FOR VARIOUS DATES

Atmospheric Model		Surface Elevation	Surface Temperature	Atmospheric Transmission	% Radiance from Atmos.	Effective Temperature	$\delta T$
<b>Rawinsonde</b>							
July 16, 1978	0300 PST	1	300	.7463	20.04	296	-4
July 16, 1978	1500 PST	"	"	.7463	20.03	"	"
July 17, 1978	0300 PST	"	"	.7453	20.14	"	"
July 17, 1978	1500 PST	"	"	.7471	19.97	"	"
July 18, 1978	0300 PST	"	"	.7471	19.98	"	"
July 18, 1978	1500 PST	"	"	.7468	20.00	"	"
July 21, 1978	0300 PST	"	"	.7485	19.89	"	"
July 21, 1978	1500 PST	"	"	.7459	20.11	"	"
July 22, 1978	0300 PST	"	"	.7478	19.96	"	"
July 22, 1978	1500 PST	"	"	.7469	20.05	"	"
July 23, 1978	0300 PST	"	"	.7476	19.93	"	"

TABLE 11  
RESULTS FROM LOWTRAN USING MIDLATITUDE SUMMER MODEL FOR VARYING SURFACE ELEVATIONS

Atmospheric Model	Surface Elevation	Surface Temperature	Atmospheric Transmission	% Radiance from Atmos.	Effective Temperature	$\delta T$
Midlatitude Summer	0.0	300	.5627	38.37	295	-5
" "	0.25	"	.6167	32.93	295	-5
" "	0.50	"	.6657	28.07	296	-4
" "	0.75	"	.7096	23.76	296	-4
" "	1.0	"	.7488	19.95	296	-4
" "	1.5	"	.8144	13.97	297	-3
" "	2.0	"	.8638	9.55	298	-2
" "	2.5	"	.8986	6.70	298	-2
" "	3.0	"	.9230	4.72	299	-1

TABLE 12  
RESULTS FROM LOWTRAN USING MIDLATITUDE SUMMER MODEL FOR VARYING SURFACE TEMPERATURES

Atmospheric Model	Surface Elevation	Surface Temperature	Atmospheric Transmission	% Radiance from Atmos.	Effective Temperature	$\delta T$
Midlatitude Summer	1	260	.7488	31.11	264	4
" "	"	270	"	27.57	271	1
" "	"	280	"	24.63	279	-1
" "	"	290	"	22.09	288	-2
" "	"	300	"	19.95	296	-4
" "	"	310	"	18.10	304	-6
" "	"	320	"	16.54	313	-7
" "	"	330	"	15.20	320	-10
" "	"	340	"	14.04	327	-11
" "	"	350	"	13.01	338	-12

Elevation data are available for the test sites in digital format, and all the rawinsonde data are on hand. However we have not had time to develop the computer algorithms to apply the atmospheric corrections differentially across the test sites. This has been left for a follow-on study.

B. HCMR Calibration

Our processing of the HCMM thermal data included an experiment designed to help verify the satellite calibration. The effective temperature corresponding to the radiance at the top of the atmosphere is given by the formula for infrared data conversion supplied by the HCMM Project Office at GSFC,

$$T_s(DN) = \frac{K2}{\ln \left[ \frac{K1}{DN-K3} + 1 \right]}, \quad (23)$$

in which DN is the digital number value (0-255) of a pixel;  $T_s$  is the temperature in degrees Kelvin, with  $T(0) = 260.0^{\circ}\text{K}$  and  $T(255) = 340.0^{\circ}\text{K}$ ; and  $K1 = 14421.587$ ,  $K2 = 1251.1591$ ,  $K3 = -118.21378$ .  $T_s$  differs from the surface temperature  $T_g$  due to the atmospheric effects discussed earlier. Post-launch HCMR calibrations were performed by the HCMM Project Office, based on comparisons of the satellite-measured radiance (and hence temperature) and the "effective temperature" at the top of the atmosphere calculated from ground measurements at White Sands, New Mexico and a GSFC atmospheric correction program. Based on such calculations during the first sixty days after HCMM launch, a  $+5.2^{\circ}\text{K}$  offset was noted, with the HCMR data warmer than the surface data. The project office decided to adjust the calibration constants to offset all data by  $+5.2^{\circ}\text{K}$ , to match the surface "truth," and investigators were so notified. A second "validation" calibration was undertaken by GSFC a

few months later, using the same technique, and again using White Sands data, and with the HCMM data now offset by  $+5.2^{\circ}\text{K}$ . This time a  $5.5^{\circ}\text{K}$  offset in the other direction was noted (or actually only a  $-0.3^{\circ}\text{K}$  offset from the original calibrations). However, the  $+5.2^{\circ}\text{K}$  offset was now being routinely added to all data. At the time that investigators were informed of this problem by GSFC personnel, they also discussed two other possible sources of error due to noise and drift of up to  $0.4^{\circ}\text{K}$  and  $1.0^{\circ}\text{K}$  respectively. Finally the HCMM project office sent a memo stating that both of the above calibration studies were based on their incorrect atmospheric model. Their latest estimate, using their new atmospheric model, showed that the above offsets should have been  $+4.0^{\circ}\text{K}$  and  $-5.7^{\circ}\text{K}$  (instead of  $+5.2^{\circ}\text{K}$  and  $-5.5^{\circ}\text{K}$ ). Meanwhile, several European investigators were stating that they found surface temperature dependent offsets in the data ranging from about 5 to  $10^{\circ}\text{K}$ , increasing with higher surface temperature.

The above information continued to arrive from GSFC during our attempts to put our data analysis on a sound quantitative basis. Recognizing that there appeared to be several uncertainties in the data, we first chose to compare effective temperature measured by the satellite with our measured surface temperatures, with no atmospheric corrections. From this study we hoped to establish at least an estimate of the magnitude of the calibration-offset and the atmospheric correction problems. Our goals in this experiment were to estimate the size of this temperature difference and to determine roughly how much it varied from day to day.

For this investigation we used ground truth data from two sources. The primary source was field data taken by JPL personnel near Goldfield, Nevada in July, 1978. Temperatures were measured with the Precision Radiation Thermometer, model PRT-5 of the Barnes Engineering Company, at eight different

sites at approximately the time of the satellite overpass. These sites were located on the HCMM albedo image with the aid of air photos, and DN values were taken from both day and night thermal images which had been registered to the albedo image. Temperatures computed from these DN values using the conversion formula, Equation 23, were then compared with the recorded temperatures.

In order to compare measurements over a wider temperature range, recorded temperatures were obtained from additional sources. National Weather Service offices in Las Vegas, Nevada and Los Angeles, California provided shoreline water temperatures at, respectively, Lake Mead and six beaches in the Los Angeles-San Diego area. Offshore water surface temperatures for Lake Tahoe were obtained from Professor Charles R. Goldman of the University of California at Davis. Ground surface temperatures were provided by the National Park Service at Death Valley National Monument in California and by the United States Army at the Yuma Proving Ground in Arizona. Measurements from the latter two sources were subsequently excluded from the test as, on the dates under consideration, the temperatures recorded were outside the range of the HCMR. An attempt was made to include the melting temperature of snow as additional ground truth data but the resolution of the HCMM images was too poor to locate accurately the edge of any snow masses.

We sought a functional relationship between the satellite measurements,  $T_s$ , and the temperatures recorded at the surface,  $T_g$ , using a linear least squares analysis. Several data pairs, with  $x = T_g$  and  $y = T_s$  were used to compute the constants  $a$  and  $b$  which would give the best least squares fit to three different functions: linear,  $y = a + bx$ ; power,  $y = ax^b$ ; and exponential,  $y = ae^{bx}$  (or logarithmic,  $y = a + b\ln x$ ). The result,  $T_s = T_s(T_g)$ ,

which was obtained from the best fit to the data was then compared with the assumption  $T_s = T_g$ , which pertains to a dry atmosphere.

Initially  $T_s - T_g$  pairs for three different dates were examined separately as shown in Figure 19. The difference in  $T_s = T_s(T_g)$  between the two dates, July 17, 1978 and July 22, 1978 - both clear, windy days as observed during the acquisition of the field data near Goldfield - ranged from 0 to 3°C. For both dates, the satellite-derived temperature was lower than the recorded ground temperature. No curve is plotted for the 19 August 1978 data because the fit to each of the three trial functions resulted in a very low correlation. These data points are in good agreement with the other two curves. Because field data, the primary source of data used in this calibration experiment, were available only for summer months, possible seasonal effects were not examined.

Because the daily variation in  $T_s$  was small we combined all the data pairs for temperatures measured during the day. The result is shown in Figure 20. A corresponding result for the nighttime data pairs could not be derived due to poor correlation of the data. A final comparison of  $T_s$  and  $T_g$  was made by combining all the data pairs. As shown by the dashed line in Figure 21, the addition of the nighttime temperatures did not greatly affect the form of  $T_s = T_s(T_g)$ .  $T_s$  is seen to be 5-6°C lower than  $T_g$  near 20°C and 8-9°C lower at higher temperatures of 50-60°C. These differences are fairly consistent with the atmospheric effects we calculated in the previous section. The offset for lower temperatures agrees with that found by the HCMM Project Office in their second calibration experiment in October 1978 although they had included atmospheric effects in their calculations, and the temperature dependence agrees with the effects noted by the European investigators.

ORIGINAL PAGE IS  
OF POOR QUALITY

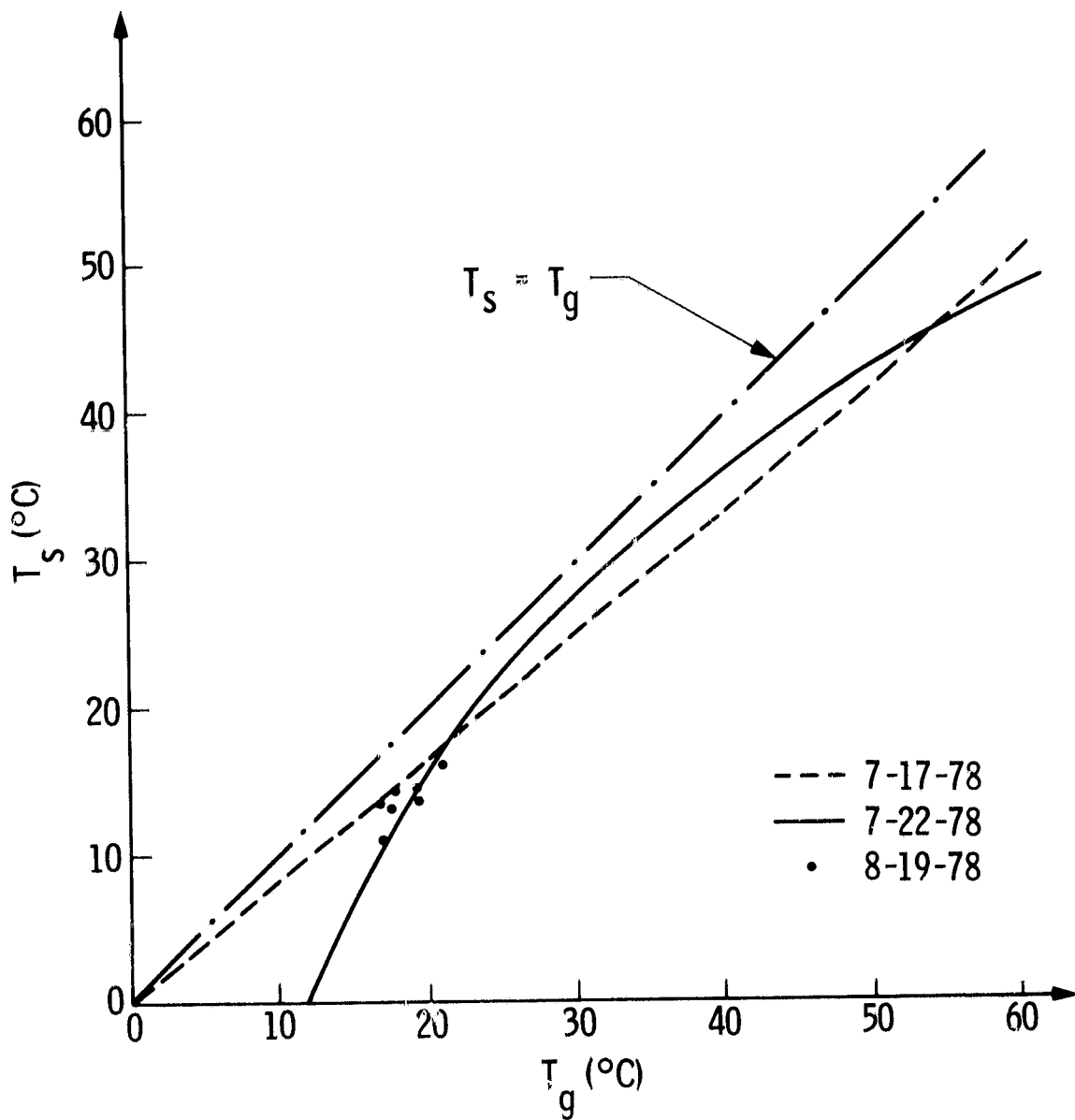


Figure 19. Best fit curve for  $T_s$ - $T_g$  data pairs for different dates. The ideal case is shown by the line labeled  $T_s = T_g$ .

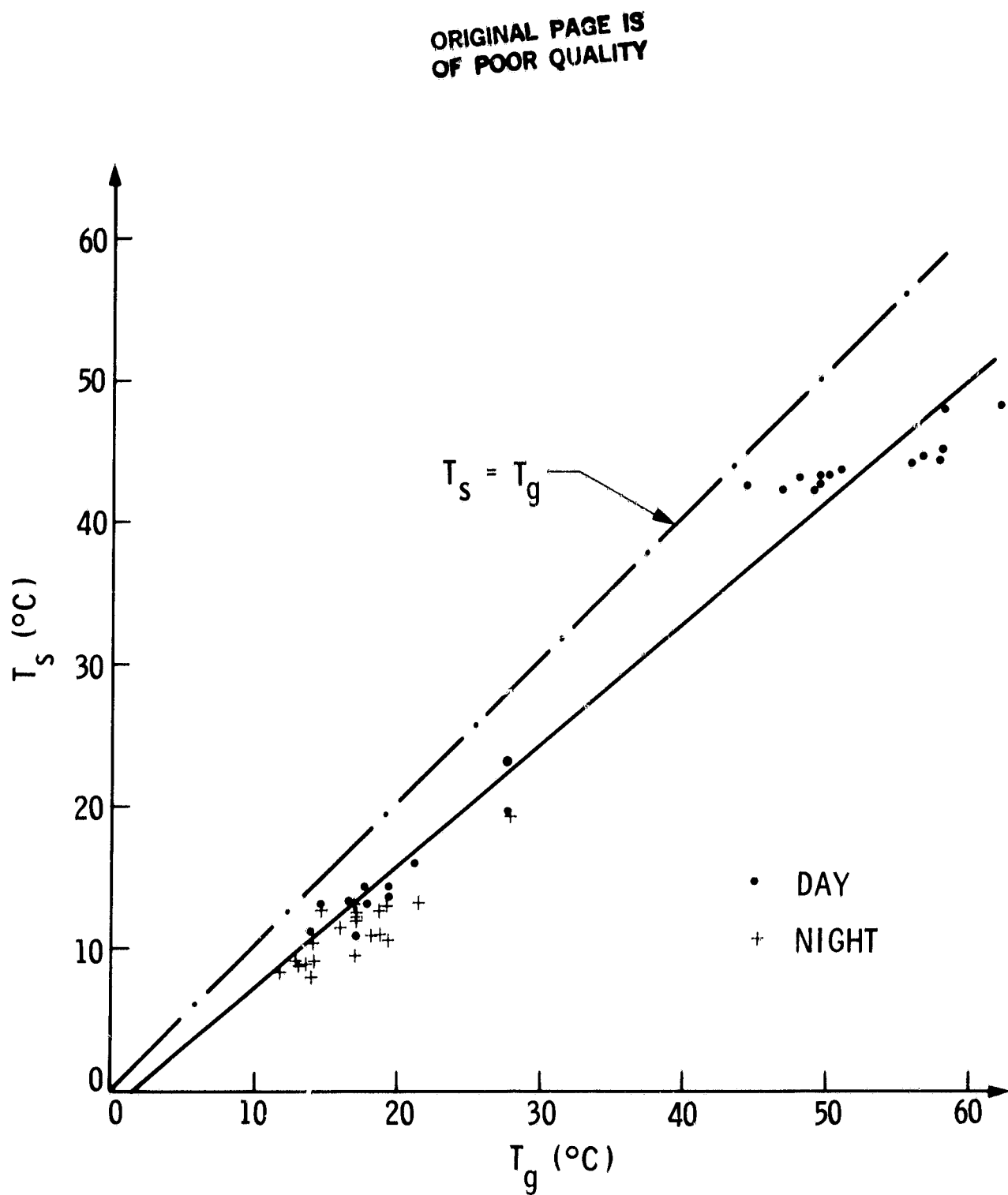


Figure 20. Best fit curve for daytime  $T_s$ - $T_g$  data pairs for all dates. Nighttime data pairs are denoted by crosses. The ideal case is shown by the line labeled  $T_s = T_g$ .

ORIGINAL PAGE IS  
OF POOR QUALITY

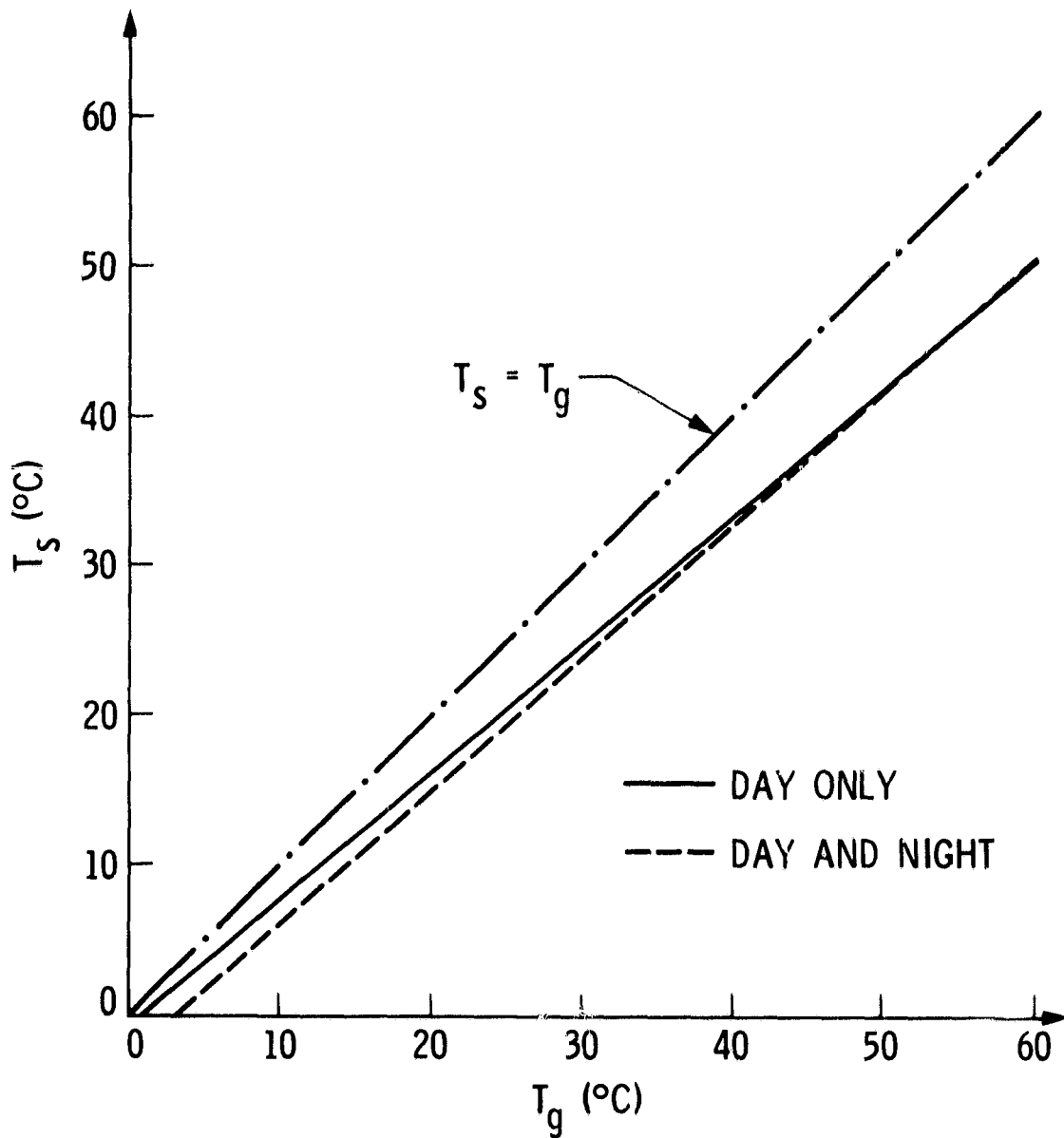


Figure 21. Best fit curves for all  $T_s$ - $T_g$  data pairs (broken line) and for daytime data pairs only (solid line). The ideal case is shown by the line labeled  $T_s = T_g$ .

After receiving notification by GSFC on August 18, 1980 of the error in the radiative transfer program used in their calibration we decided to use only the formula for infrared data conversion, Equation 23, in our processing for this study. It is our intent in a follow-on study to use our atmospheric programs, along with digital elevation information and the ground data discussed above, to better test the HCMR calibration.

C. Dependence of Thermal Inertia Calculations on Meteorological Conditions

Heat and mass fluxes between the ground and air are required when calculating the thermal inertia of surface materials. In particular, sensible and latent heat flux densities are often the predominant terms in the equation for the surface energy balance. Moreover, evaporation from moist soils changes the thermal inertia of the near surface soil layers with depth and time.

The problem of computing sensible and latent heat flux densities for use in thermal inertia calculations requires a knowledge of the mesoscale variability of meteorological conditions over the area covered by the image, on the order of tens to hundreds of square kilometers. Such detailed information is prohibitively costly to obtain and process, even for a single image, since it would require an observational network on a scale of about one station per square kilometer. Furthermore, theoretical analysis of the variation of turbulent heat flux densities over heterogeneous surfaces is still relatively undeveloped. The usual and only practical way around these difficulties is to assume that one or two point measurements are sufficiently representative of the area. This is a fairly good assumption when surface winds are moderate to strong, i.e. more than about 5 m/s, because strong mixing of the air tends to produce uniform conditions everywhere. On the

other hand, large differences in surface meteorological fields can exist on a microscale when surface winds are light, i.e., less than about 1 m/s. Despite this complexity, sensible and latent heat flux densities are often calculated from parameterization methods that employ observations obtained at one point in an area (cf. Bhumralkar, 1976). In the following, we describe the methods used to calculate the turbulent heat flux densities at the ground for use in the JPL thermal model. We include discussions on the details of the formulation, the types of meteorological data used in the calculations, and the limitations of the methods.

In this study, the turbulent heat flux densities are calculated from either of two methods: 1) the bulk aerodynamic method, or 2) the profile method. The chief difference between the two methods is that the first employs meteorological data obtained at a single height above the ground, while the second employs data obtained at two or more heights.

The bulk aerodynamic method also requires that the ground temperature and moisture content be known. For the bulk aerodynamic method, the sensible heat flux density ( $H$ ) is given by the expression (Kahle, 1977),

$$H = \rho_a c_p C_D W (T_a - T_g) \quad (24)$$

where  $\rho_a$  is the surface air density,  $c_p$  is the specific heat of dry air at constant pressure,  $C_D$  is an altitude dependent drag coefficient [= 0.002 + 0.0006(Z/5000)],  $Z$  is elevation in meters,  $W$  is a wind speed factor corrected for gustiness (wind speed plus 2 m/s),  $T_a$  is the air temperature at a height just above the ground (~ 2 m), and  $T_g$  is the ground temperature. The latent heat flux density ( $L$ ) is given by the expression,

$$L = \rho_a C_D W \ell (q_g - q_a) \quad (25)$$

where  $\ell$  is the latent heat of evaporation,  $q_g$  is the specific humidity at the ground, and  $q_a$  is the specific humidity of the air above the ground. The specific humidity is calculated from the standard formula (cf. Saucier, 1955),

$$q = 0.662 \left( \frac{Re_s}{P} \right) \quad (26)$$

where  $R$  is the relative humidity of the air,  $P$  is atmospheric pressure at the ground in millibars, and  $e_s$  is the saturation vapor pressure in millibars expressed as a function of air temperature,  $T$  in  $^{\circ}\text{C}$ ,

$$e_s = 6.11 \times 10^{7.5T/(237.3+T)} \quad (27)$$

The major problem in calculating  $L$  is that  $q_g$  is difficult to determine. ( $T_g$  for the calculation of  $H$  can usually be estimated fairly accurately from remote sensing data.) One method of computing  $q_g$  is to assume that it is a fraction ( $M_g$ ) of the saturation specific humidity ( $q_{\text{sat}} = 0.622 e_s/P$ ).  $M_g$  is a ground moisture factor that ranges from 0 for completely dry soil to 1 for saturated soil. When moisture transport in the soil is included in the thermal model,  $M_g$  is obtained from the model calculations as the ratio,  $\theta/\theta_{\text{sat}}$ .  $\theta$  is the volumetric soil moisture content ( $\text{cm}^3$  of water/ $\text{cm}^3$  of total soil) at the surface and  $\theta_{\text{sat}}$  is its value at saturation.  $\theta_{\text{sat}}$  has a fixed value for each type of soil (Clapp and Hornberger, 1978). If moisture transport is not included in the model,  $\theta$  may be computed from a rate equation along the lines developed by Deardorff (1978).

The profile method is a means of calculating turbulent heat fluxes at the ground from the mean values of simultaneous measurements of wind speed, temperature, and humidity made at several levels in the atmospheric surface layer. The surface layer is the lowest part of the atmospheric boundary layer and usually extends to about 10 m (at night) or 100 m (at mid-afternoon) above the surface. Here the vertical fluxes of momentum, heat, and water vapor are assumed to be independent of height so this region is also called the constant flux layer. A portable micrometeorological system has been developed at JPL (Kahle *et al.*, 1977) to obtain measurements in the constant flux layer over an 8 meter altitude. Seven levels of instrumentation - measuring wind speed, dry-bulb air temperature, and wet-bulb air temperature - are spaced logarithmically (base 2) in the vertical direction from 1/8 m to 8 m. The geometric mean height (GMH) of the array is 1 m. The data are recorded continuously and averaged over 16 minute intervals.

In the profile method, the similarity hypothesis of Monin and Obukhov (cf. Monin and Yaglom, 1971) is used to calculate the heat flux densities. It describes the vertical gradients of wind ( $U$ ), temperature ( $T$ ) and humidity ( $Q$ ) in the constant flux layer as functions of a set of non-constant, nondimensional parameters and constant scale factors,

$$\begin{aligned}\frac{\partial U}{\partial Z} &= \frac{U_*}{\kappa Z} \phi_m(\zeta) \\ \frac{\partial T}{\partial Z} &= \frac{T_*}{\kappa Z} \phi_h(\zeta) \\ \frac{\partial Q}{\partial Z} &= \frac{Q_*}{\kappa Z} \phi_q(\zeta)\end{aligned}\tag{28}$$

where  $Z$  is height above the surface,  $\kappa$  is von Karman's constant ( $\approx 0.35$ ),  $\phi_m$ ,  $\phi_h$ , and  $\phi_q$  are the nondimensional parameters, and  $U_*$ ,  $T_*$ ,  $Q_*$  are the constant scale factors. The parameter  $\zeta$  is equal to  $Z/L$  where  $L$  is the Monin - Obukhov scale length - which is approximately equal to the vertical thickness of the constant flux layer. Ordinarily,  $\zeta$  is  $< 0$  during the day (unstable conditions) and  $\zeta > 0$  at night (stable conditions). The surface layer is called unstable when the ground is warmer than the air above it so that the temperature of the air decreases with height in the surface layer, and stable when the opposite condition exists.  $L$  can be obtained from meteorological observations because  $\zeta$  is proportional to the bulk Richardson number ( $Ri_B$ ) for the height interval (cf. Yaglom, 1977); viz., in our studies the height interval is 8 m and  $Ri_B$  is computed at the GMH ( $\approx 1$  m) of the observations. Finally,  $U_*$ ,  $T_*$ ,  $Q_*$  are calculated by the least-squares fit of the observations to the integrated forms of Equations 28. (The parameters  $\phi_m$ ,  $\phi_h$ , and  $\phi_q$  are given as a function of  $\zeta$  in Table 13.) Then,  $H$  and  $L$  are calculated from,

$$H = \rho_a c_p U_* T_* \quad (29)$$

$$L = \rho_a \kappa U_* Q_* \quad (30)$$

Figure 22 is an example of  $H$  and  $L$  calculated from profile data obtained at Death Valley in January, 1977.

How representative are the turbulent heat flux densities calculated from these two methods? The bulk aerodynamic method is often used to provide surface values for use in atmospheric general circulation models (e.g. Gates et al., 1971). The profile method is more often used to determine momentum, mass, and heat transfer on level fields (e.g. Morgan et al., 1971). Ostens-

ORIGINAL PAGE IS  
OF POOR QUALITY

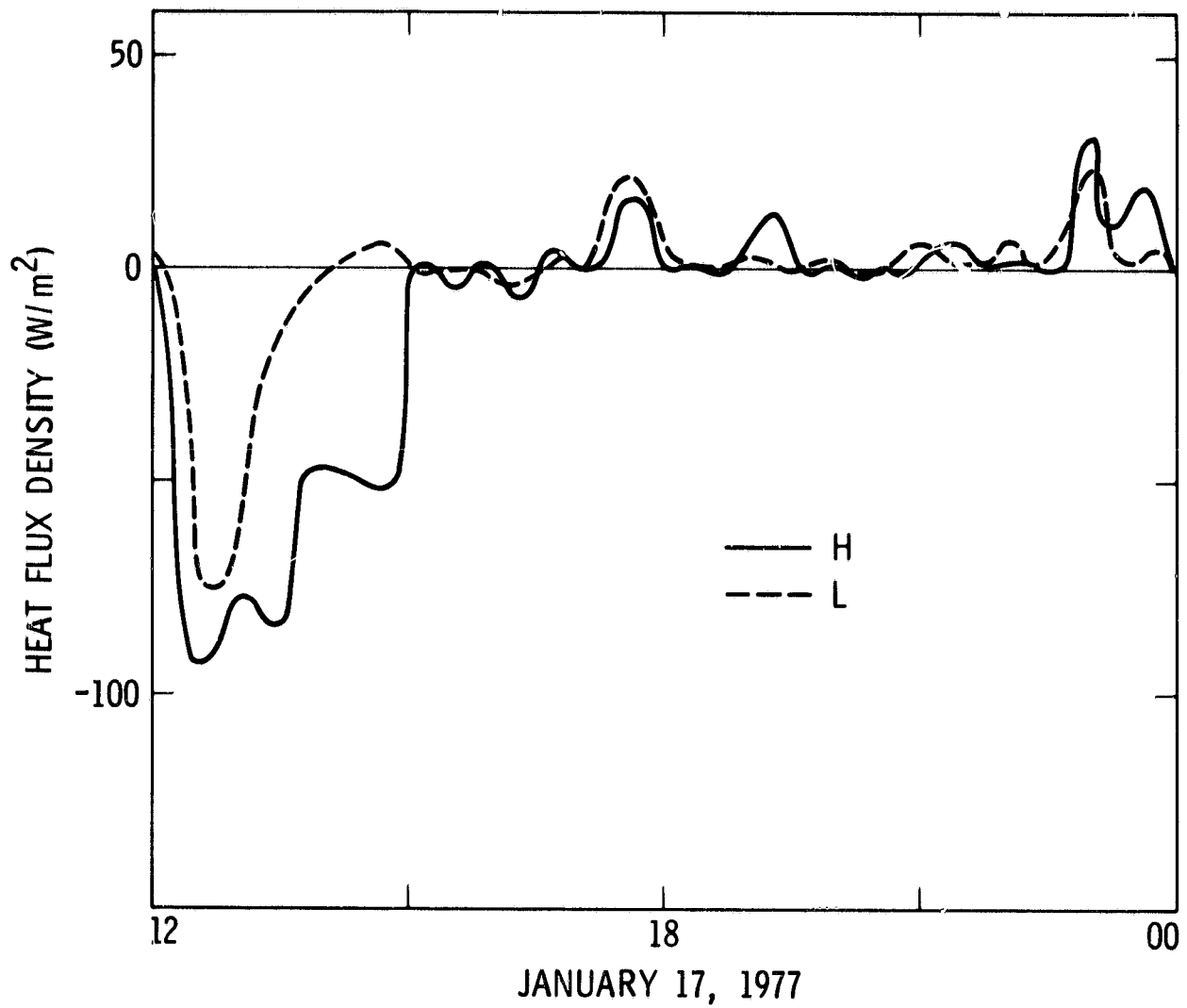


Figure 22. Sensible (H) and latent (L) heat flux densities calculated for Death Valley for January 18, 1977.

TABLE 13  
ATMOSPHERIC STABILITY PARAMETERS

<u>Condition</u>	<u>Parameter</u>	<u>Expression<sup>a</sup></u>
1. Unstable ( $\zeta < 0$ )	$\phi_m$	$(1-15\zeta)^{-1/4}$
	$\phi_h$	$0.74(1-9\zeta)^{-1/2}$
	$\phi_q$	$0.74(1-9\zeta)^{-1/2}$
2. Neutral ( $\zeta = 0$ )	$\phi_m$	1.0
	$\phi_h$	0.74
	$\phi_q$	0.74
3. Stable ( $\zeta > 0$ )	$\phi_m$	$1 + 4.7\zeta$
	$\phi_h$	$0.74 + 4.7\zeta$
	$\phi_q$	$0.74 + 4.7\zeta$

<sup>a</sup> Businger et al. (1971)

ibly, the profile method should give a closer representation of the surface turbulent flux densities at a point since it utilizes not one, but many measurements over the thickness of the surface layer. This is particularly relevant at night when the thickness of the surface layer is often no more than the height of the profile system ( $\sim 8$  m). Furthermore, profile calculations have been found to correspond quite well with direct measurements of turbulent fluxes by the eddy correlation method (Miyake et al., 1970). Practically, the bulk aerodynamic method is more convenient than the profile method. The latter, unlike the former, requires data derived from a complex array of observational equipment that is not always easy to calibrate, transport, or maintain. Figure 23 shows sensible heat flux densities

ORIGINAL PAGE IS  
OF POOR QUALITY

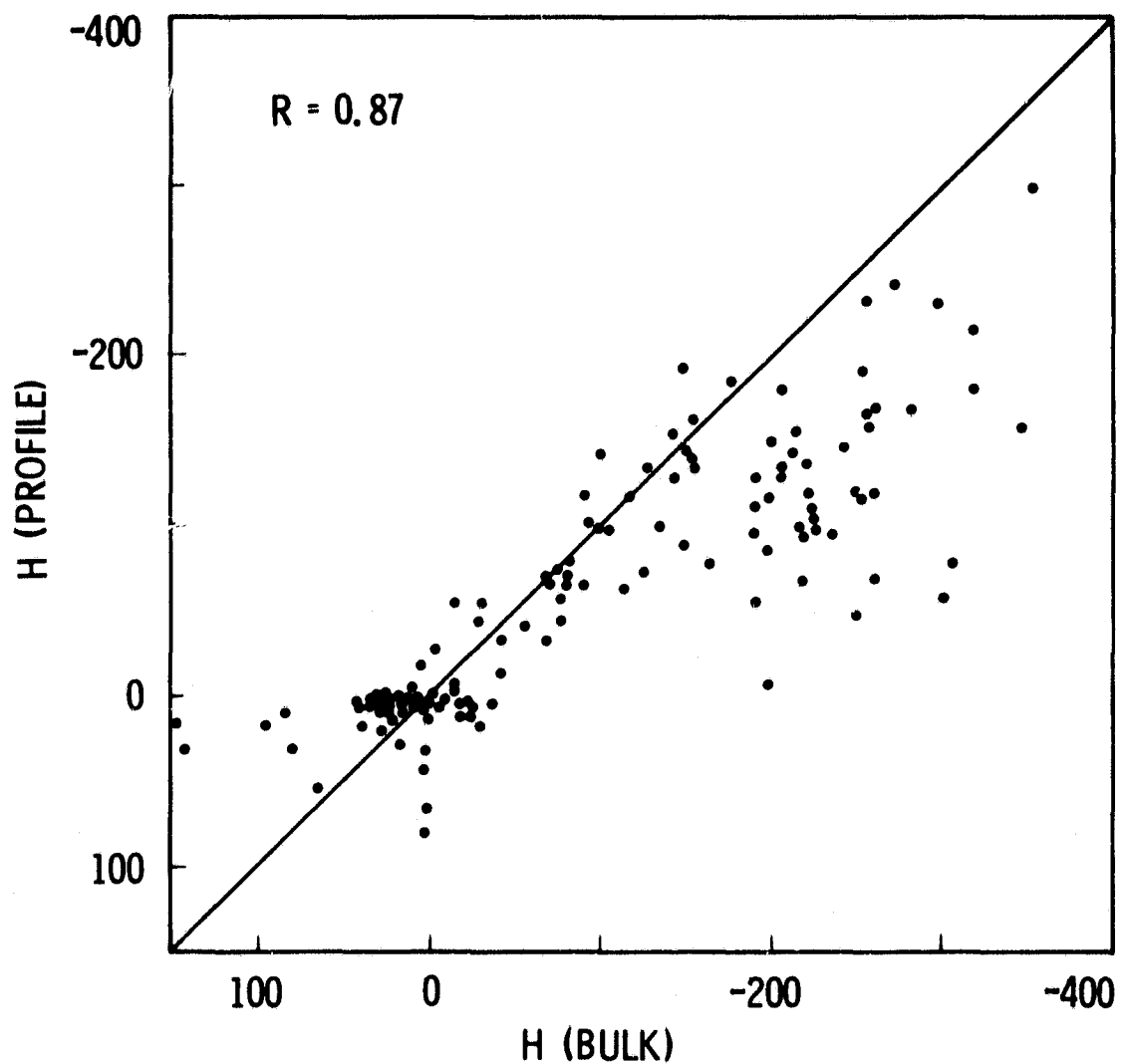


Figure 23. Scatterplot of sensible heat flux densities ( $H$ ) calculated from the bulk aerodynamic method and the profile method for Stonewall Playa, July, 1978.

calculated from both the bulk aerodynamic and the profile methods for a common data set collected in July, 1978 at Stonewall playa near Goldfield, Nevada. The bulk calculations have been made from observations at 2 m. Although the overall correlation between the two methods is good, there are some notable differences. Nighttime values (positive) of  $H(\text{bulk})$  are larger than  $H(\text{profile})$  values. Daytime values (negative) of  $|H(\text{bulk})|$  greater than about  $200 \text{ W/m}^2$  show the same result.

These discrepancies occur primarily because in the bulk method the drag coefficient,  $C_D$ , 1) is not a function of stability, 2) is equal for both momentum and heat transfer, and 3) pertains strictly to moderate or strong wind conditions (cf. Burke, 1943; Rossby and Montgomery, 1935). The latter point is particularly relevant to the nighttime differences because nighttime winds are often light in strength, and one would expect the bulk method to overestimate  $H$ . This is not a serious discrepancy because nighttime flux densities tend to be small. On the other hand, daytime flux densities calculated from the two methods are relatively large and differ by as much as a factor of two. The net effect will be an overestimation of the value of the thermal inertia calculated from the model.

Different kinds of meteorological data can be used in the model. For example, the National Weather Service (NWS) has a large network of weather stations in the continental United States that routinely record weather observations at least once an hour. This is an attractive source of data since an HCMM pass is usually over at least one NWS station. Unfortunately, the NWS data may not be entirely representative of the weather everywhere in an area. Figure 24 shows two curves representing the diurnal variation of sensible heat flux density at two sites in the Walker Lane area of Nevada. The solid line depicts  $H$  calculated from NWS hourly observations in June, 1976

ORIGINAL PAGE IS  
OF POOR QUALITY

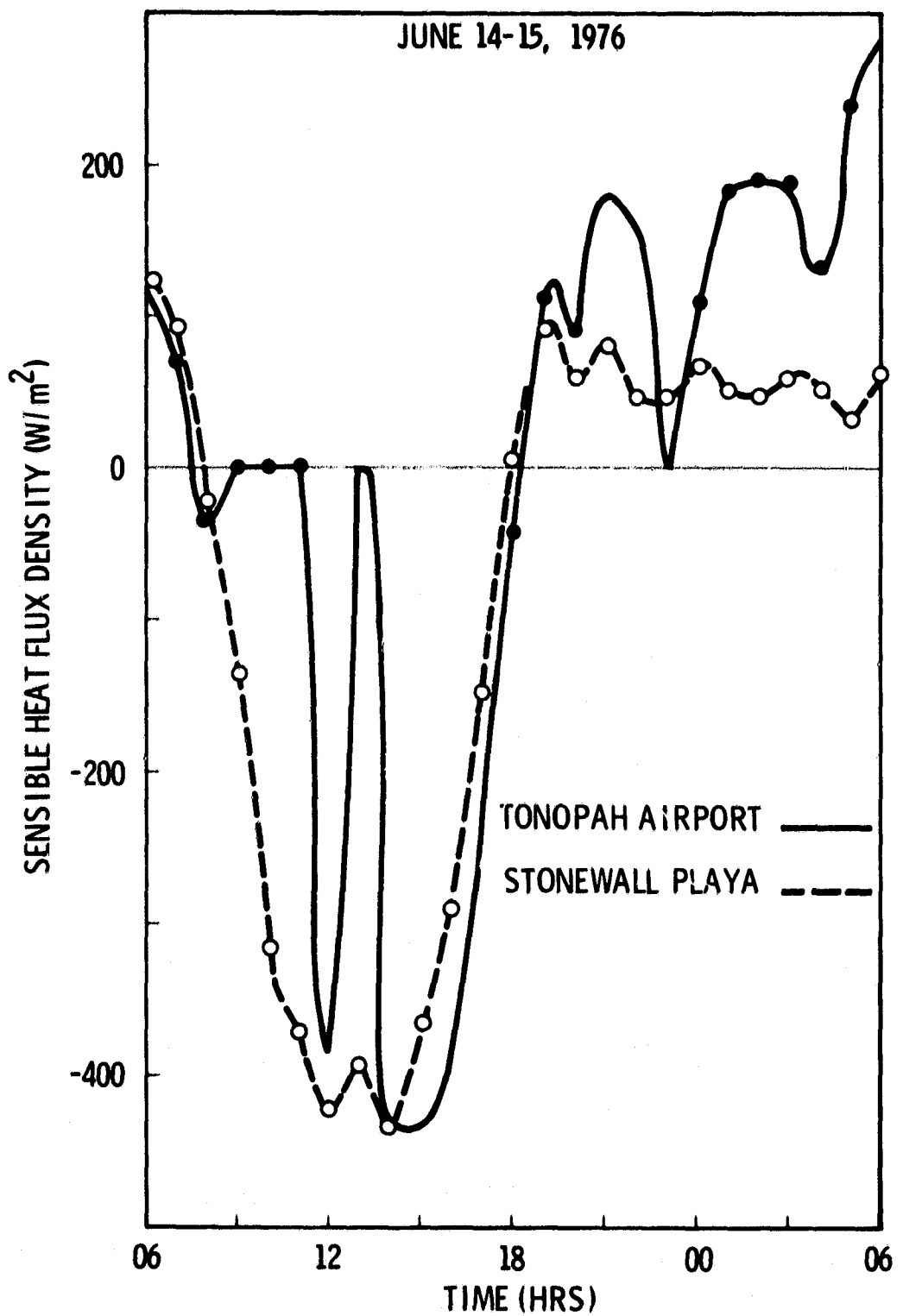


Figure 24. Sensible heat flux densities calculated from bulk aerodynamic method with data sets from two sites: Tonopah airport and Stonewall Playa, June 14-15, 1976.

at the Tonopah airport and the dashed line represents calculations derived from in situ observations for the same time at Stonewall playa, a dry lake about 60 km south of Tonopah. Both calculations were made from the bulk aerodynamic formulations. Note several major differences. Although both curves have the same magnitude at their daytime peaks, they are not conformable in general. Nighttime values of  $H$  are the most disparate. The  $H$  values from the NWS data are about twice as large as the  $H$  values from the in situ data. This pair of curves illustrates the problem encountered when applying microscale measurements to mesoscale models.

Our calculation of thermal inertia values from the HCMM data included only the effects of sensible heat transfer in the JPL model and not the effects of latent heat transfer because most of the areas of interest are semi-arid. The sensible heat flux densities have been calculated by the bulk aerodynamic formulation in all cases. This formulation is sufficiently accurate for the calculation of thermal inertia values from the JPL model in view of the intrinsic difficulties in modeling mesoscale meteorological fields, and the practical difficulties of employing more complicated methods such as the profile or eddy-correlation techniques.

#### IV. The Effect of Soil Moisture on Thermal Inertia

Thermal inertia varies with the amount of water present in the soil. This is because the thermal inertia of moist soil is typically about  $0.040 \text{ cal cm}^{-2}\text{s}^{-1/2}\text{C}^{-1}$  which is comparable to thermal inertia values for many rocks (cf. Kahle, 1980). As soil water content varies, the thermal properties of the soil also vary. The difference between the daytime maximum and the nighttime minimum in temperature is greater in the near surface layers of dry soils than it is in wet ones. The consequences of water transport on the soil

thermal regime can be studied with the use of an appropriate mathematical model.

With support from the AgRISTARS program, the JPL thermal model has been modified to describe heat and moisture transport in soils. This version of the model has not been used in analysis of the HCMM data for this report; however, it may be employed in future studies. A few results from this model are shown here because they illustrate the magnitude of the effect of changing soil moisture on the thermal history of surface materials.

The modifications to the model include an additional term (Q) in the heat conduction equation to describe heat transfer by vapor diffusion under moisture gradients, an additional partial-differential equation to describe moisture changes, a set of initial conditions for the volumetric soil moisture profile, and boundary conditions to specify the moisture variation at the surface and at the lower boundary (~ 1 m) of the model. The result is a set of coupled, diffusion-type equations,

$$C \frac{\partial T}{\partial t} = \frac{\partial}{\partial z} \left( \lambda \frac{\partial T}{\partial z} \right) + Q \quad (31)$$

$$\frac{\partial \theta}{\partial t} = \frac{\partial}{\partial z} \left( D_\theta \frac{\partial \theta}{\partial z} \right) + \frac{\partial}{\partial z} \left( D_T \frac{\partial T}{\partial z} \right) + \frac{\partial K}{\partial z}, \quad (32)$$

where T is soil temperature,  $\theta$  is volumetric moisture content, z is depth,  $\lambda$  is thermal conductivity,  $D_\theta$  is moisture diffusivity,  $D_T$  is thermal diffusivity, K is hydraulic conductivity, C is volumetric heat capacity, and Q is a term due to heat transfer by distillative effects. The pair of equations is solved numerically by a finite difference technique. Complete details of the model are given in Njoku et al. (1980).

As a test, the model was used to simulate temperature and moisture profiles for a bare field near Bakersfield, California during May, 1978. Figures 25 and 26 show soil temperature and volumetric moisture variations with depth and time. The results of the modeling are shown in Figures 27 and 28 for comparison. The computed temperature and moisture curves agree in general with observations although there is less conformity between the moisture curves. This is not unexpected since soil moisture measurements are more difficult to make than temperature measurements and also, model results represent discrete levels in the soil while the observations are obtained from soil layers of finite thickness.

The variability of thermal inertia with changing moisture content can be inferred from these results. Initially, the soil is quite moist ( $\theta \geq 0.25 \text{ cm}^3/\text{cm}^3$ ) to a depth of about 30 cm and the difference,  $\Delta T$ , between the daytime maximum and nighttime minimum in temperature at the surface is about  $24-29^\circ\text{C}$ . As the soil dries, which it does quite rapidly near the surface,  $\Delta T$  increases until it reaches about  $34^\circ\text{C}$  at the end of the record. This amounts to a change in  $\Delta T$  of about 20%. The effect this change has on the thermal inertia can be estimated by considering the expression for apparent thermal inertia (AP) in its approximate form (see section V-G),

$$AP \approx (1-A)/\Delta T \quad (33)$$

where  $A$  is soil albedo. Ignoring changes in  $A$  and taking the partial derivative of AP with respect to  $\Delta T$ , one obtains

$$\frac{\partial(AP)}{\partial(\Delta T)} = -\frac{1}{\Delta T} \quad (34)$$

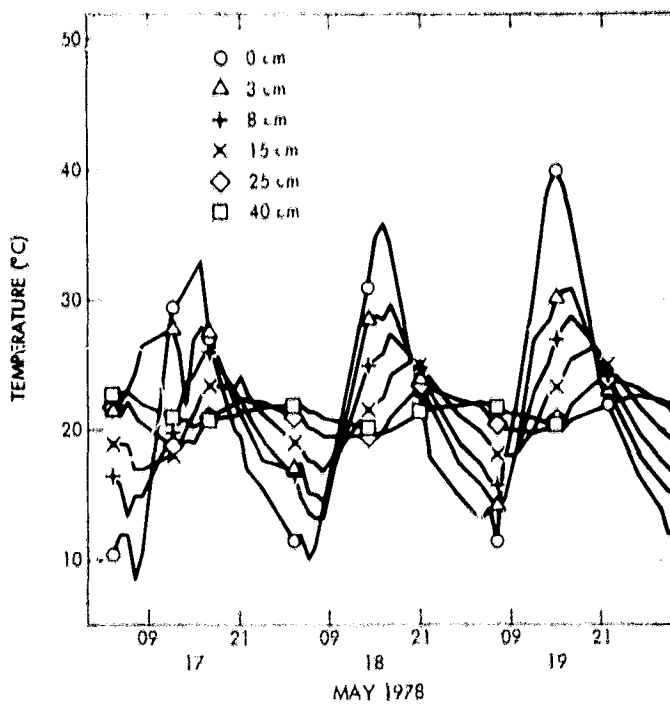


Figure 25. Observed soil temperature variations at a six different depths on a bare field near Bakersfield, California for the period May 17-19, 1978.

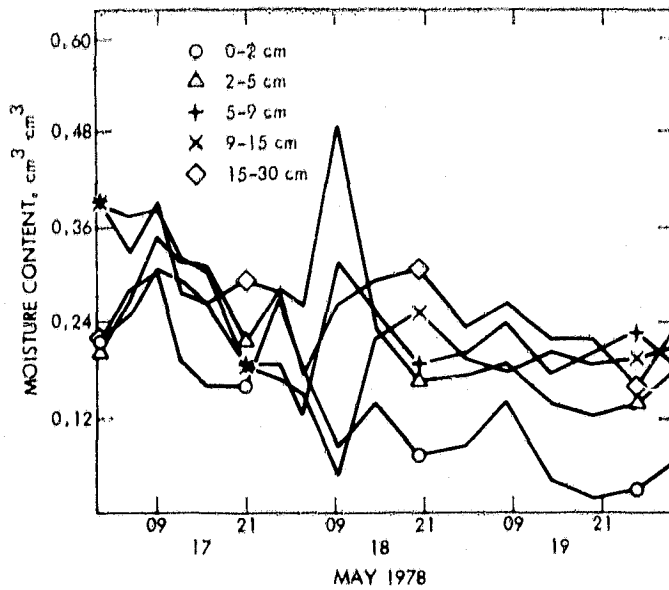


Figure 26. Observed soil moisture content at six different depths on a bare field near Bakersfield, California for the period May 17-19, 1978.

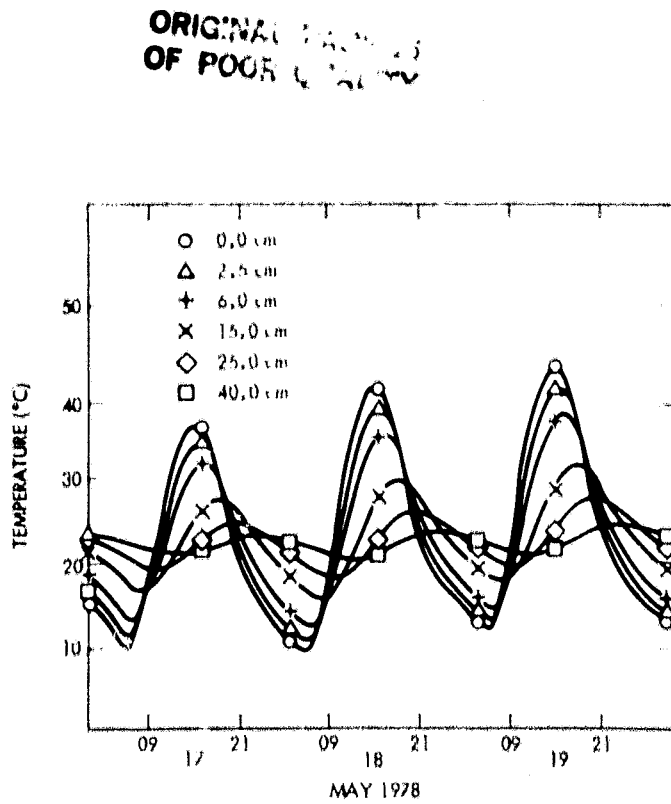


Figure 27. Calculated soil temperatures obtained from the numerical model for the May 17-19, 1978 period.

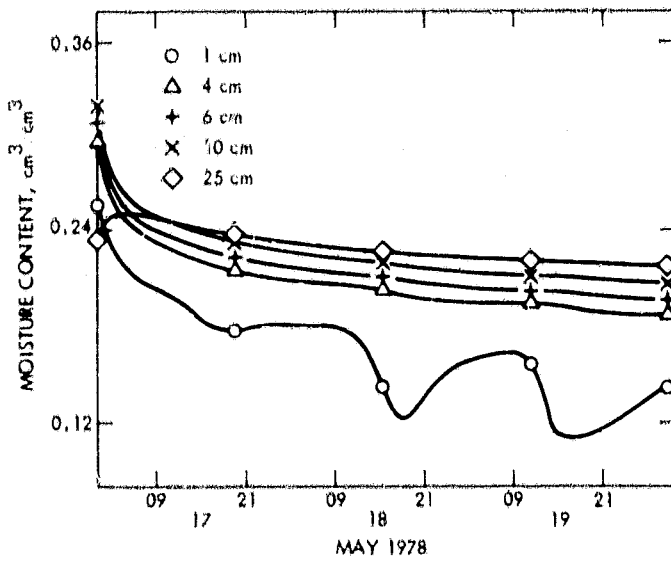


Figure 28. Calculated soil moisture obtained from the numerical model for the May 17-19, 1978 period.

which implies that a 20% increase in  $\Delta T$  causes a 20% decrease in AP. In reality, A also decreases with surface wetness, and this additional effect on AP is given by

$$\frac{\frac{\partial(AP)}{\partial A}}{AP} = -\frac{1}{1-A}. \quad (35)$$

For the range of  $\theta$  shown in both Figures 26 and 28, this gives an increase in A of about 10 to 30% as the soil dries according to Janza (1975), and implies a further decrease in AP by about the same magnitude. Therefore, in this case, the thermal inertia of the soil can be reduced by nearly a half in just a few days due to the effects of evaporation and internal drainage.

Spatial and temporal variations in soil moisture can be ascertained from HCMM thermal images. For example, Figures 29 to 39 show how these changes appear at different scales for the Death Valley site. The first set, Figures 29 to 31, are full-frame, daytime IR images of a part of the western United States. Death Valley is located south of the letters "DV" on the images of May 14, 1978, August 18, 1978, and September 19, 1978. The elongated feature is the valley floor, the ring-shaped feature at the north end is Cottonball Basin designated with a "C", south of this is Middle Basin shown with an "M", and further south the Badwater area is designated with a "B". The dark (cooler) areas in the valley coincide with the moist part of the salt pan. Seasonal and spatial variations in the area's ground moisture are evident from one frame to the next. In May, the valley is barely perceptible, particularly the Cottonball Basin area; in August, it is more distinct and Cottonball Basin is seen as a faint quasi-circular area; in

ORIGINAL PAGE  
BLACK AND WHITE PHOTOGRAPH

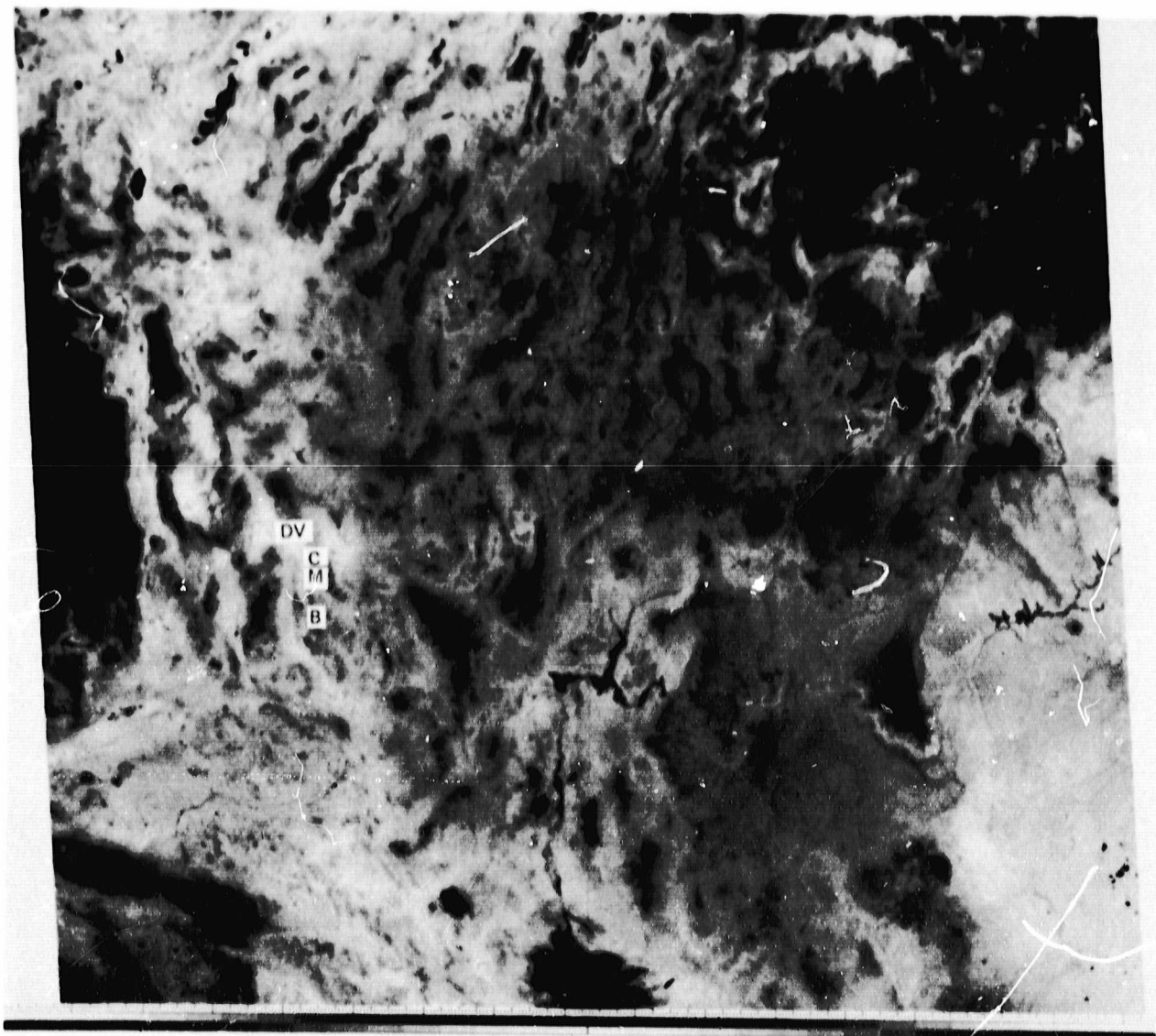


Figure 29. Full-frame HCMM day IR image of part of the western United States for May 14, 1978. Death Valley is located south of the "DV." Test site locations within the valley are indicated by C (Cottonball Basin), M (Middle Basin), and B (Badwater).

ORIGINAL PAGE  
BLACK AND WHITE PHOTOGRAPH

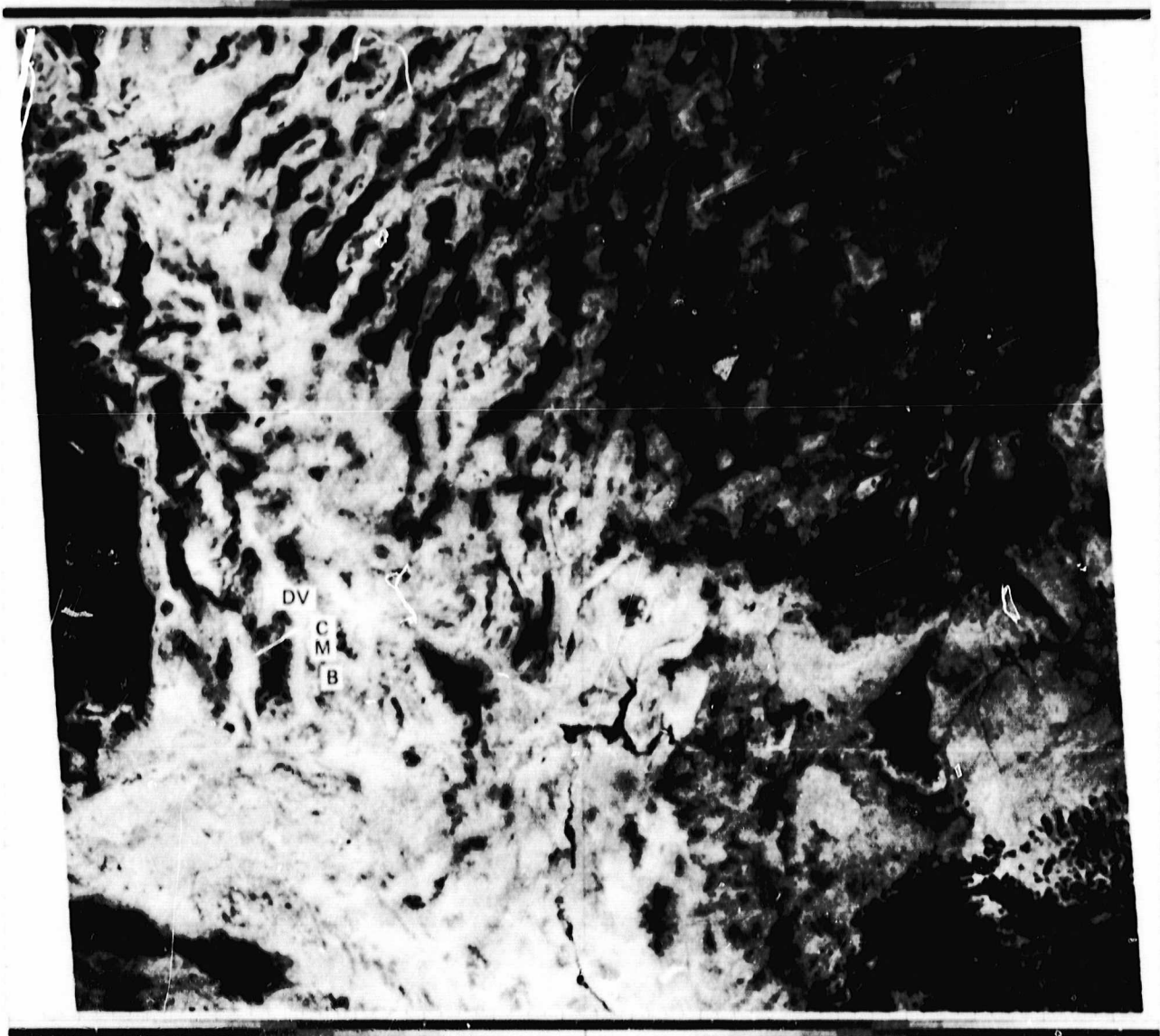


Figure 30. Full-frame HCMM day IR image of part of the western United States for August 18, 1978. Death Valley test sites are indicated.

ORIGINAL PAGE  
BLACK AND WHITE PHOTOGRAPH

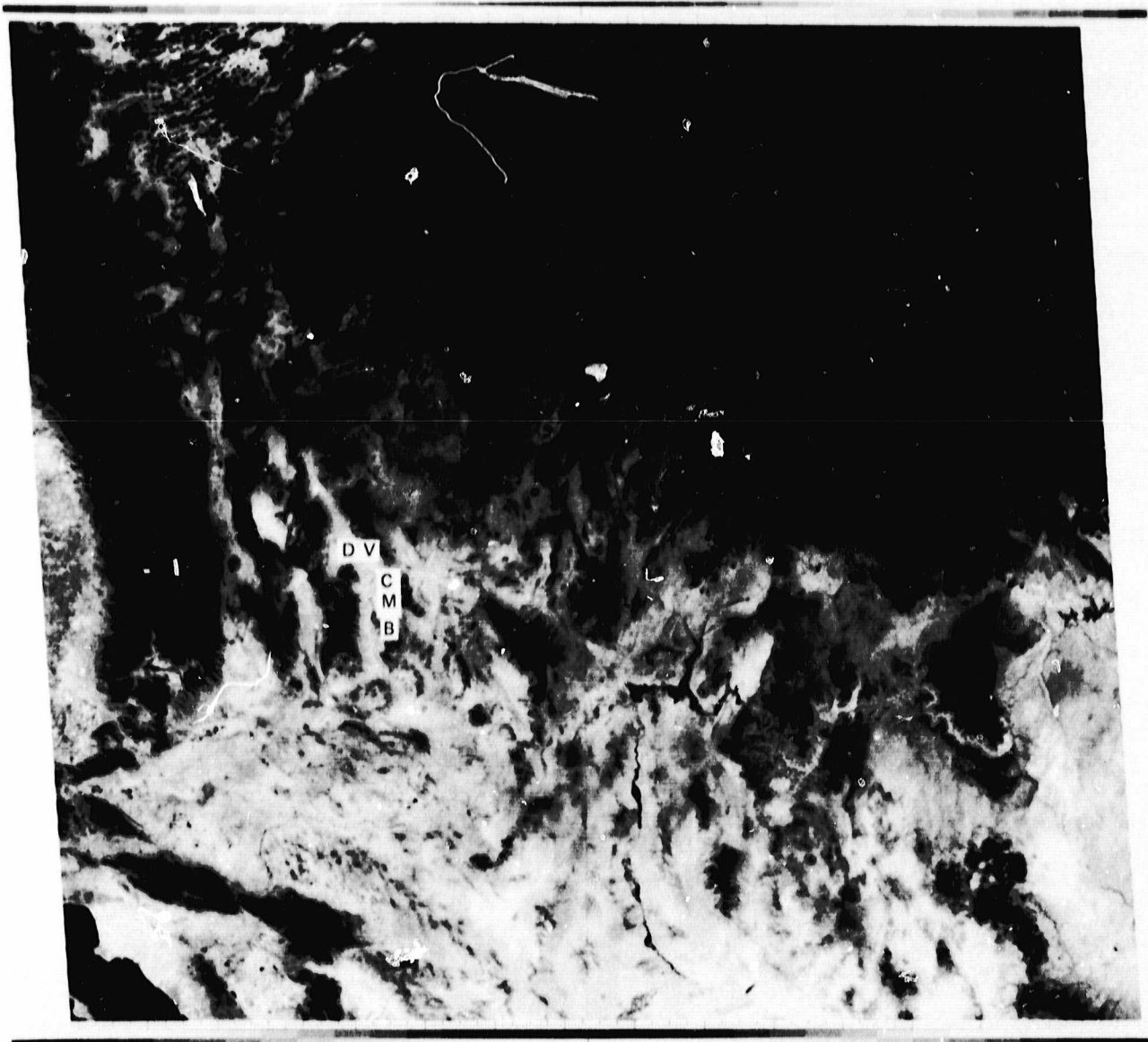


Figure 31. Full-frame HCMM day IR image of part of the western United States for September 19, 1978. Death Valley test sites are indicated.

September, the three areas (G, M and B) are quite visible, particularly the Badwater area.

Figures 32 to 35 are subareas of the HCMM data that have been processed at JPL to display thermal inertia of Death Valley on a larger scale. This processing has been done with the dry version of the JPL thermal model. Some of these images are incomplete because of a lack of overlapping HCMM data on successive passes; nonetheless, the valley is discernible on all images. Four days are shown: May 30, 1978, July 22, 1978, August 18, 1978, and April 4, 1979. On the May image, Cottonball Basin is indicated by the ring-shaped feature near the center of the image, the Middle Basin is the light area at the end of the filament protruding some distance from the bottom of the ring, and Badwater Basin is located by the bright, quasi-triangular feature an equal distance below the Middle Basin. These areas can be similarly identified on the other images. Each of these areas undergoes changes in size and brightness, visible on the separate images, and each area is a region of significant moisture variability. Increased moisture content results in higher thermal inertia, hence wetter areas appear lighter in the images. Parts of all these basins are subject to seasonal flooding, and Badwater Basin contains regions where the ground is nearly always saturated. It is unfortunate that the delay in distribution of HCMM data made it impossible to identify areas of significant change on images, and then undertake field measurements in key areas during subsequent satellite overpasses, as had been originally planned.

The detail in the HCMM images is good enough to identify regional changes in ground moisture but is not good enough to delineate small features of special interest. Aircraft data are more useful for this task. Figures 36 through 39 show visible and thermal inertia images of Death Valley obtained

**ORIGINAL PAGE  
BLACK AND WHITE PHOTOGRAPH**



Figure 32. HCMM thermal inertia image of Death Valley for May 30, 1978.

ORIGINAL PAGE  
BLACK AND WHITE PHOTOGRAPH



Figure 33. HCMM thermal inertia image of Death Valley for July 22, 1978.

ORIGINAL PAGE  
BLACK AND WHITE PHOTOGRAPH



Figure 34. HCMM thermal inertia image of Death Valley for August 18, 1978.

ORIGINAL PAGE  
BLACK AND WHITE PHOTOGRAPH

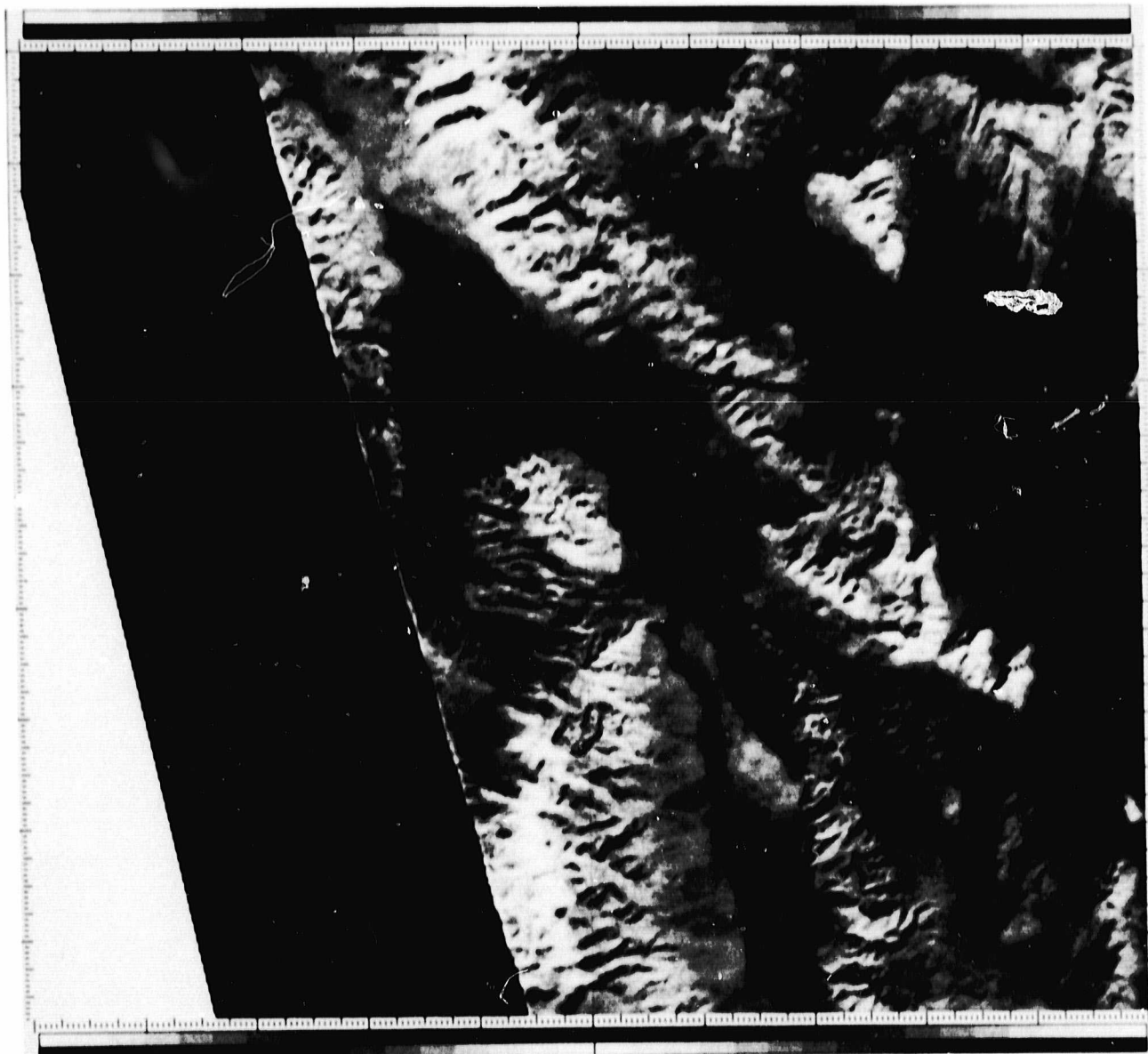


Figure 35. HCMM thermal inertia image of Death Valley for April 4, 1979.

from aircraft data. The images portray the northern and southern halves of Death Valley.

The visible image of the northern half (Figure 36) is distinguished by Cottonball Basin. The Furnace Creek area is located in the lower right-hand corner and the building complex and airstrip can be seen in dark, gray tones. Cottonball Basin is a salt-encrusted portion of the valley floor and is subject to flooding by the rise of ground water during wet periods and by runoff. The most notable feature in the image is the bright area north of Furnace Creek on the east side of the Basin. This feature is a very moist area, which also appears on the thermal inertia image (Figure 38) as a bright spot (indicating high thermal inertia values). On the visible image of the southern half (Figure 37), the most conspicuous feature is the dark quasi-triangular area known as the Devil's Golf Course. It is an elevated massive rock salt formation which is nearly saturated, and the surface is extremely rough. The thermal inertia image (Figure 39) shows this as an area of relatively high thermal inertia as would be expected of a wet area. An unusual feature does appear in the Middle Basin at the top, left-hand side of both images. This is a strip of salt-encrusted sand and silt shaped like the letter Y. The bottom leg and the right-hand fork of the Y show a uniform brightness on the visible image. In the thermal inertia image, however, only the bottom half of the leg indicates high thermal inertia. The difference between the two representations indicates the effectiveness of thermal inertia techniques for differentiating materials with similar surface properties but apparently different bulk properties. Field checking will be required to ascertain the nature of features in both the northern and southern halves of the valley.

ORIGINAL PAGE  
BLACK AND WHITE PHOTOGRAPH



Figure 37. M<sup>2</sup>S visible image of the southern half of Death Valley obtained from NP-3A flight on March 11, 1977.

ORIGINAL PAGE  
BLACK AND WHITE PHOTOGRAPH

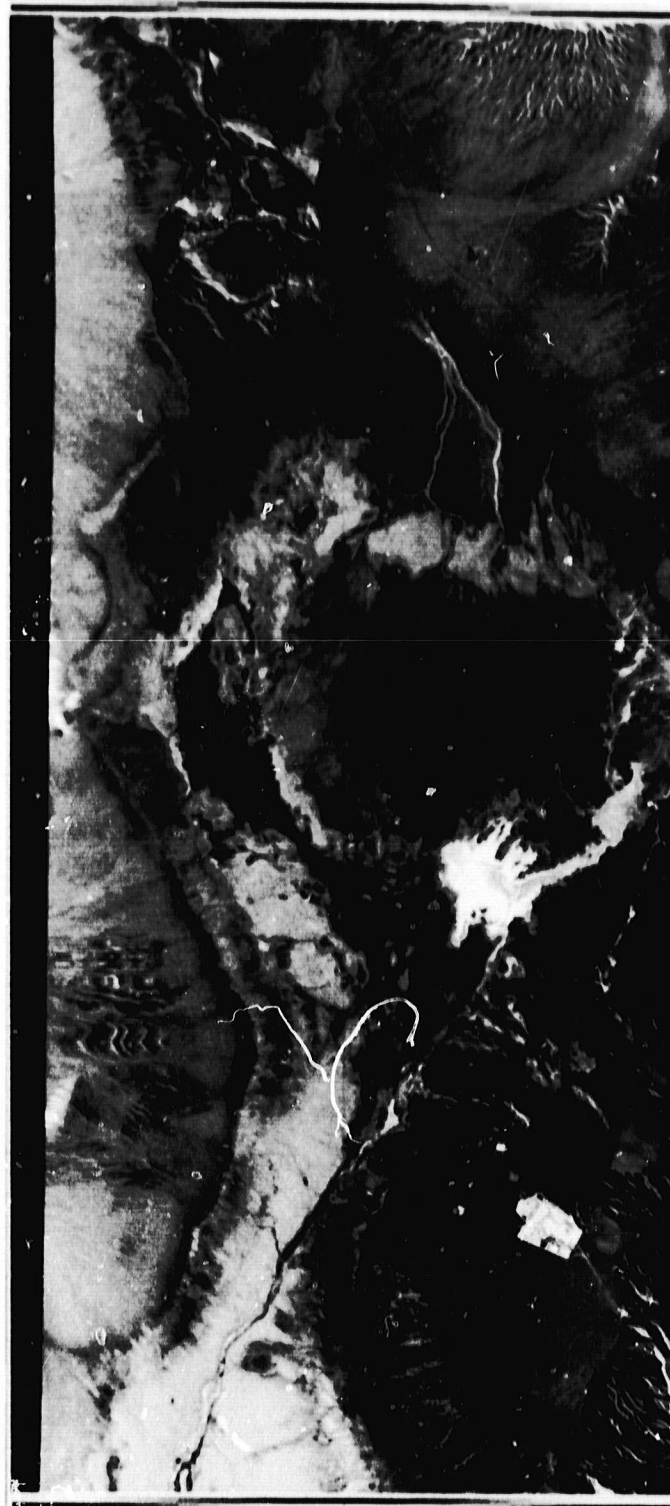


Figure 38. Thermal inertia image of the northern half of Death Valley produced from data obtained during the NP-3A flight on March 11, 1977.

ORIGINAL PAGE  
BLACK AND WHITE PHOTOGRAPH



Figure 39. Thermal inertia image of the southern half of Death Valley produced from data obtained during the NP-3A flight on March 11, 1977.

#### E. Model Sensitivity Studies

Thermal inertia calculations depend upon many factors. The model results are sensitive to variations in such parameters as day-night temperature difference ( $\Delta T$ ), albedo, topography, sky radiance, cloudiness, vegetative cover, and ground-level meteorology. These and other related topics are discussed in this section. In particular, Table 14 presents the results of a study to determine the magnitude of these effects on thermal inertia calculations based on data for the Goldfield, Nevada and Pisgah, California test sites. Goldfield is about  $3^{\circ}$  of latitude north of Pisgah Crater. The results are somewhat dependent upon the site because of the difference in initial and boundary conditions in the calculations. Changes in  $P$  are given in  $\text{cal cm}^{-2}\text{s}^{-1/2}\text{ }^{\circ}\text{C}^{-1}$ .

The simulations for Goldfield and Pisgah have been carried out with data from the October, 1976 experiments. The effects represent perturbations upon a standard value of  $P$  for each site. As noted above, the initial and boundary conditions -- which include factors such as local meteorological conditions, albedo, and topography -- are different for each site and therefore the same amount of change in a source parameter can produce effects of different magnitudes. For example, a  $1^{\circ}\text{C}$  error in measured day-night temperature difference ( $\Delta T$ ) produces an effect about four times greater at Goldfield than at Pisgah. Nonetheless, these are typical results and are indicative of the relative strengths of these effects in introducing errors into the analysis.

Most of the sources of errors listed in the table are due to the way energy flux densities are partitioned at the upper boundary, or surface. For instance, the albedo, ground slope and azimuth, atmospheric radiance (a.k.a. sky temperature component), and cloud cover all affect the composition of the

TABLE 14  
PERTURBATIONS UPON THERMAL INERTIA MODELS

<u>Source</u>	<u>EFFECT</u>	
	<u>GOLDFIELD</u>	<u>PISGAH</u>
1°C Error in Measured ΔT	.012	.003
2°C Error in Measured ΔT	.023	.006
8% Error in Measured Albedo	.011	.007
4° Error in Measured Ground Slope	.005	.002
45° Error in Measured Ground Slope Azimuth	.013	.005
20°C Error in Estimated Sky Temperature	.001	.003
Effect of 20% Vegetation Cover	.014	.006
Effect of Morning Cloudiness	.001	.002
Effect of Noon Cloudiness	.008	.007
Using Ely, Nevada Weather Station Data		
Wind Speed Only	.009	
Air Temperature Only	.047	
Both Wind and Temperature	.026	

net radiative flux density at the surface. Errors due to subsurface factors such as water transport in soils are not considered here. Cloud cover is simulated by eliminating the direct solar heating for a short time during early (morning) and late (afternoon) phases in the diurnal cycle. Only the diffuse component of radiation incident at the surface is included in the calculations. The cumulative effect of errors in the radiative factors is considerable both at Goldfield ( $0.053 \text{ cal cm}^{-2} \text{s}^{-1/2} \text{ }^{\circ}\text{C}^{-1}$ ) and at Pisgah ( $0.026 \text{ cal cm}^{-2} \text{s}^{-1/2} \text{ }^{\circ}\text{C}^{-1}$ ), and they rival the sum of the remaining effects.

Vegetative cover is important because it not only affects the areal albedo, but also the near surface micro-climate and turbulent heat transfer. However, in our analysis, we have only considered the effects of temperature modification by assuming that the ground temperature of the vegetated areas was equal to the air temperature. The final entry under the Goldfield column indicates the important role that sensible heat flux plays in redistributing energy at the surface. Sensible heat flux is proportional to the product of the wind and the air-ground temperature difference. We conclude that although errors in both wind and temperature seriously affect the calculation of  $P$ , an erroneous measurement in the air temperature is particularly damaging. Over natural surfaces this can be a major problem because air temperatures often vary substantially on a regional basis, as discussed earlier. Errors in the measured temperature also create large uncertainties in calculating  $P$ . Those errors are multiplicative; i.e. a  $2^{\circ}\text{C}$  error in  $\Delta T$  produces about twice as much error as a  $1^{\circ}\text{C}$  error. Their size is brought into perspective if you consider the inherent error of  $0.5^{\circ}\text{C}$  in an IR radiometer like the PRT-5.

The results in this table indicate that errors can be introduced into the thermal inertia modeling through measurement (e.g. temperature, albedo, topography) or parameterization (e.g. sensible heat flux, cloud cover) and that these errors can account for spurious contributions to  $P$  of significant magnitude. Despite the effect of these errors, the model gives results that are accurate enough to discriminate among many different kinds of geologic materials. Improvements in the model's accuracy will depend upon further research in technical and theoretical areas related to measurement and parameterization techniques.

#### F. Numerical Values of Thermal Inertia

Table 15 is a list of thermal inertia values and their standard deviations for selected small areas of fairly uniform composition at the four test sites. All the data pertain to model calculations of  $P$  obtained from the July 6, 1978 data sets. Also listed are thermal inertia values for some of these materials as published in the Manual of Remote Sensing (Reeves, 1975) in the column headed MRS. In an absolute sense, our values of  $P$  do not always agree closely with the limited published values for the materials. In general our results are larger in magnitude. However, in a relative sense within a given site at a given time and within the limits of error, the values of  $P$  in Table 15 are useful in discriminating among many rock and soil types. For example, at Goldfield, altered and unaltered materials are readily distinguishable from each other, but almost all values appear to be too high. At Pisgah, different kinds of basalt can be separated one from another, while at Death Valley, dolomite is separable from other materials. It is interesting to note the wide range of values of thermal inertia among the sandstone units at San Rafael. These differences appear to be real and are ascribed primarily to the different weathering properties and resultant soil development on the various units.

The fact that our thermal inertia values are in general larger than published values can be ascribed to our not yet included atmospheric corrections. Because of the surface temperature dependence of these corrections, the warmer daytime temperatures will be more affected than the cooler nighttime temperatures. It is apparent from Table 9 that the measured  $\Delta T$ , with no atmospheric corrections, will be smaller than the actual  $\Delta T$ . For instance, an actual daytime surface temperature of  $320^{\circ}\text{K}$  and nighttime temperature of  $290^{\circ}\text{K}$  ( $\Delta T = 30^{\circ}$ ) would result in a satellite measured  $\Delta T$  of only  $24^{\circ}$ . This smaller

TABLE 15

## THERMAL INERTIA VALUES AND THEIR STANDARD DEVIATIONS AT FOUR TEST SITES

		$\bar{P}$	$\sigma$	MRS Value
7/6 Goldfield	1 Playa	30.95	5.00	42 (Clay soil-moist)
	2 Basalt	37.84	5.09	53
	3 Silicified Volcanics	54.67	2.58	
	4 Argillically Altered Volcanics	35.50	1.06	
	5 Unaltered Volcanics	44.31	1.86	
7/6 Pisgah	1 Playa	53.96	3.48	42 (Clay soil-moist)
	2 Aa	81.47	2.63	
	3 Basalt	76.73	1.77	53
	4 Basalt	74.62	3.65	53
	5 Biotite Quartz Monzonite	77.33	3.43	
	6 Alluvium	61.22	1.13	
	7 Dacite	55.87	1.78	
	8 Granite	74.13	1.02	52
7/6 Death Valley	1 Dolomite, Qtz, LS	104.93	6.17	75, 74, 45
	2 Dolomite, Qtz, LS	107.04	6.15	75, 74, 45
	3 Quartz Monzonite	99.74	5.84	
	4 Alluvium, Pleistocene	78.87	2.18	
	5 Q Lake	60.62	2.40	
	6 Alluvium, Recent	86.01	1.79	
	7 Sand	61.26	1.72	24 (sandy soil)
	8 Basalt	82.05	4.07	
San Rafael	1 Navajo SS	72.76	4.20	54
	2 Entrada SS (soil)	9.22	2.30	54
	3 Kaibab LS	70.64	8.86	45
	4 Moenkopi Silt	49.56	4.22	
	5 Cedar Mtn Fm	31.56	1.95	
	6 Carmel Fm	18.39	1.89	
	7 Mancos Shale	20.49	3.46	34
	8 Ferron SS	27.33	2.27	54
	9 Salt Wash SS	40.24	5.37	54
	10 Dunes	27.02	2.06	24 (sandy soil)

$\Delta T$  would result in erroneously larger values of calculated thermal inertia. As seen in Table 14, even a  $1^{\circ}$  error in  $\Delta T$  can result in an error in thermal inertia of from .003 to .01  $\text{cal cm}^{-2} \text{s}^{-1/2} \text{C}^{-1}$  or more. This clearly demonstrates the importance of the atmospheric corrections which we will be incorporating into these calculations.

Large variations in calculated values of thermal inertia occur at all sites, as a function of time. Table 16 shows the average values of thermal inertia ( $\bar{P}$ ) and the standard deviations ( $\sigma$ ) for the HCMM overflights of 1978. The top set of numbers is calculated from the JPL thermal model and the bottom set from apparent thermal inertia calculations (cf. section G for a discussion of apparent thermal inertia). Values of  $\bar{P}$  refer to the entire image and are obtained from calculations of the frequency distribution of  $P$  over the scene. The bottom three rows in the table give the values for all days of the range of  $\bar{P}$ , the average value of the ratio of  $\sigma$  to  $\bar{P}$ , and the average value of  $\bar{P}$ , respectively. Goldfield displays the greatest amount of variability for both cases. This list gives some idea of seasonal changes in  $\bar{P}$ . Both Death Valley and Pisgah data show increases or decreases in  $\bar{P}$  with time, and there is also some indication of an increasing trend in  $\bar{P}$  in the Goldfield data although this is not explicitly clear because of the variability in the results. The model results show the changes in  $\bar{P}$  at Goldfield from one date to the next are almost as great as the range in  $\bar{P}$  over the entire sample.

Note that the model values of  $\bar{P}$  are larger than the apparent thermal inertia values in all cases although the general form of the variations in  $\bar{P}$  is similar throughout.

Seasonal changes in the calculated value of thermal inertia can be attributed to a number of factors, e.g., variations in meteorological condi-

TABLE 16  
 AVERAGE VALUES ( $\bar{P}$ ) AND STANDARD DEVIATIONS ( $\sigma$ )  
 OF THERMAL INERTIA ( $\times 1000$ ) FOR 1978 HCMM FLIGHTS

MODEL CALCULATIONS

<u>Date</u>	<u>Goldfield</u>	<u>Death Valley</u>	<u>Pisgah</u>
May 14	NA***	89.5 $\pm$ 21.5	64.7 $\pm$ 10.4
May 30	NA	81.6 $\pm$ 14.4	65.6 $\pm$ 9.1
July 6	50.0 $\pm$ 17.6	76.6 $\pm$ 13.4	63.8 $\pm$ 8.0
July 17	45.0 $\pm$ 15.5	76.7 $\pm$ 13.5	71.0 $\pm$ 9.4
July 22	62.5 $\pm$ 15.2	77.4 $\pm$ 16.3	69.5 $\pm$ 20.2
August 18	36.5 $\pm$ 14.5	73.1 $\pm$ 13.9	72.6 $\pm$ 9.1
September 19	67.5 $\pm$ 13.2	NA	84.3 $\pm$ 7.4
Range	17.5	16.4	20.5
$\langle \sigma/\bar{P} \rangle *$	0.31	0.19	0.15
$\langle \bar{P} \rangle **$	52.3	79.1	70.2

APPARENT THERMAL INERTIA

<u>Date</u>	<u>Goldfield</u>	<u>Death Valley</u>	<u>Pisgah</u>
May 14	NA	53.1 $\pm$ 12.8	38.8 $\pm$ 4.6
May 30	NA	45.1 $\pm$ 8.4	38.7 $\pm$ 4.2
July 6	39.8 $\pm$ 8.4	46.2 $\pm$ 9.3	38.2 $\pm$ 3.6
July 17	36.5 $\pm$ 5.5	46.8 $\pm$ 8.5	45.0 $\pm$ 5.0
July 22	38.9 $\pm$ 9.2	47.8 $\pm$ 10.7	44.3 $\pm$ 8.1
August 18	35.1 $\pm$ 5.1	47.5 $\pm$ 8.8	42.6 $\pm$ 4.9
September 19	44.9 $\pm$ 10.3	NA	47.4 $\pm$ 5.6
Range	9.8	8.0	9.2
$\langle \sigma/\bar{P} \rangle$	0.19	0.20	0.12
$\langle \bar{P} \rangle$	39.0	47.7	42.1

\*  $\langle \sigma/\bar{P} \rangle$  = average of  $\sigma/\bar{P}$ 's

\*\*  $\langle \bar{P} \rangle$  = average of  $\bar{P}$ 's

\*\*\* NA = not analyzed because of incomplete data

tions, in ground moisture, in surface albedo, in vegetation cover, and in the emission and transmission properties of the atmosphere along the IR signal path length). Some of these factors cause true changes in the thermal inertia, and some only introduce errors into the calculations.

We have investigated the effect of two factors, local wind speed and atmospheric water vapor content. We first considered variations in the local winds. We have calculated the correlation coefficient ( $r$ ) for the average daily wind speed and the values of  $\bar{P}$  for each day at each site listed in Table 16. For both model and apparent values of thermal inertia, no significant correlation ( $r \sim 0.1$ ) exists between wind strength and  $\bar{P}$ . This result is partly due to the fact that the wind speeds used in the analysis were measured at one location for each site whereas the mesoscale variability of winds over an entire site should be considerable.

Second, we have compared values of  $\bar{P}$  with the amount of water vapor present in the atmosphere. This analysis has only been done for the Goldfield data because Goldfield is the only test site located near a rawinsonde station. Rawinsonde data were obtained from the Mercury, Nevada National Weather Service upper air station which is about 160 km southeast of Goldfield. The upper air data consist of pressure, temperature, and dew point measurements for a number of heights from near the surface to about 30 km. The amount of precipitable water ( $W$ ) in a column of air of unit cross-section can be calculated from the upper air data (Saucier, 1955) and, therefore,  $W$  is a measure of the amount of water vapor present in the atmosphere.  $W$  is an important parameter to consider because water vapor absorption is the principal mechanism for attenuating the IR signal strength along its path of propagation. Nonetheless, we did not find any significant correlation ( $r = 0.10$ )

between  $\bar{P}$  and  $W$  from the Goldfield and Mercury data for either the model or apparent thermal inertia calculations.

Ground moisture is another factor of importance when considering variations in  $\bar{P}$  between images of the same site. A few measurements of soil moisture content are available from the sites, but the areal and temporal coverage during the aircraft and HCMM overflights was not sufficient for detailed study. Furthermore, most of the measurements pertain to very dry conditions -  $\theta \lesssim 0.05 \text{ cm}^3/\text{cm}^3$  - and so a statistical analysis of the data would not be meaningful.

The simple correlations in the preceding text may not be appropriate because the many variations in  $\bar{P}$  interact in an intricate way. Soil moisture effects undoubtedly play a role in the variability of  $\bar{P}$ , but they may be modified by other conditions. In complex terrain, changes in  $\bar{P}$  due to soil moisture compete with changes engendered by warm or cold air advection. The latter effects are different than the turbulent transport of heat between the ground and air which is accounted for in the model calculations of  $P$ . Those calculations are made under the assumption that advection is unimportant. In reality, mesoscale wind systems often advect air of different thermal properties from one place to another. Of particular importance in our analysis are drainage winds which usually occur during the night, and are also known as slope or valley winds. These winds frequently result in cold-air ponding on valley floors and in isolated hollows in open country. The calculated thermal inertia of materials that are located in depressions and are subject to cold-air ponding may be underestimated because the day-night temperature difference is increased above the value it would obtain in the absence of these conditions.

As an example, consider a circular basin of uniform material subject to cold-air ponding. The calculated value of  $P$  at the center will be lower than that at the edges so that after processing, the corresponding image will show an annular band of high  $P$  surrounding a central core of low  $P$ . This result is complicated by the fact that water collects in depressions, and this has the opposite effect on  $P$ .  $P$  at the bottom, or center, is then higher with respect to its value at the drier edges, and so a thermal inertia image would show a light center enclosed by a dark ring. This is illustrated in Figures 40 and 41 which are thermal inertia images of the Goldfield area. The upper right-hand corner of each image shows a quasi-circular playa known as Mud Lake. This appears as a bright disk surrounded by a dark annular ring on the April, 1979 image. This is indicative of the latter condition discussed in which the outer edges of the basin are dry and the center is moist. The same feature is visible on the July, 1978 image except a small dark area is superimposed upon the center of the bright disk. This is circumstantial evidence of cold-air ponding in a moist depression. This view is supported by a review of wind measurements that were made on nearby Stonewall playa. Steady, moderate winds (more than 2 m/s) occurred in the early morning hours of April 4, 1979 in the area and intermittent, weak winds (less than 1 m/s) occurred for the same time on July 6, 1978. The latter winds usually indicate drainage wind in this kind of terrain.

#### G. Comparison of Apparent and Modeled Thermal Inertia Images

Apparent thermal inertia (AP) is defined by Price's (1977) formula,

$$AP = \frac{2 \cdot SVC}{\sqrt{\omega[1 + \alpha^2 + \sqrt{2}\alpha]}}^{1/2} \cdot \frac{(1-A)}{\Delta T} \quad (36)$$

ORIGINAL PAGE  
BLACK AND WHITE PHOTOGRAPH

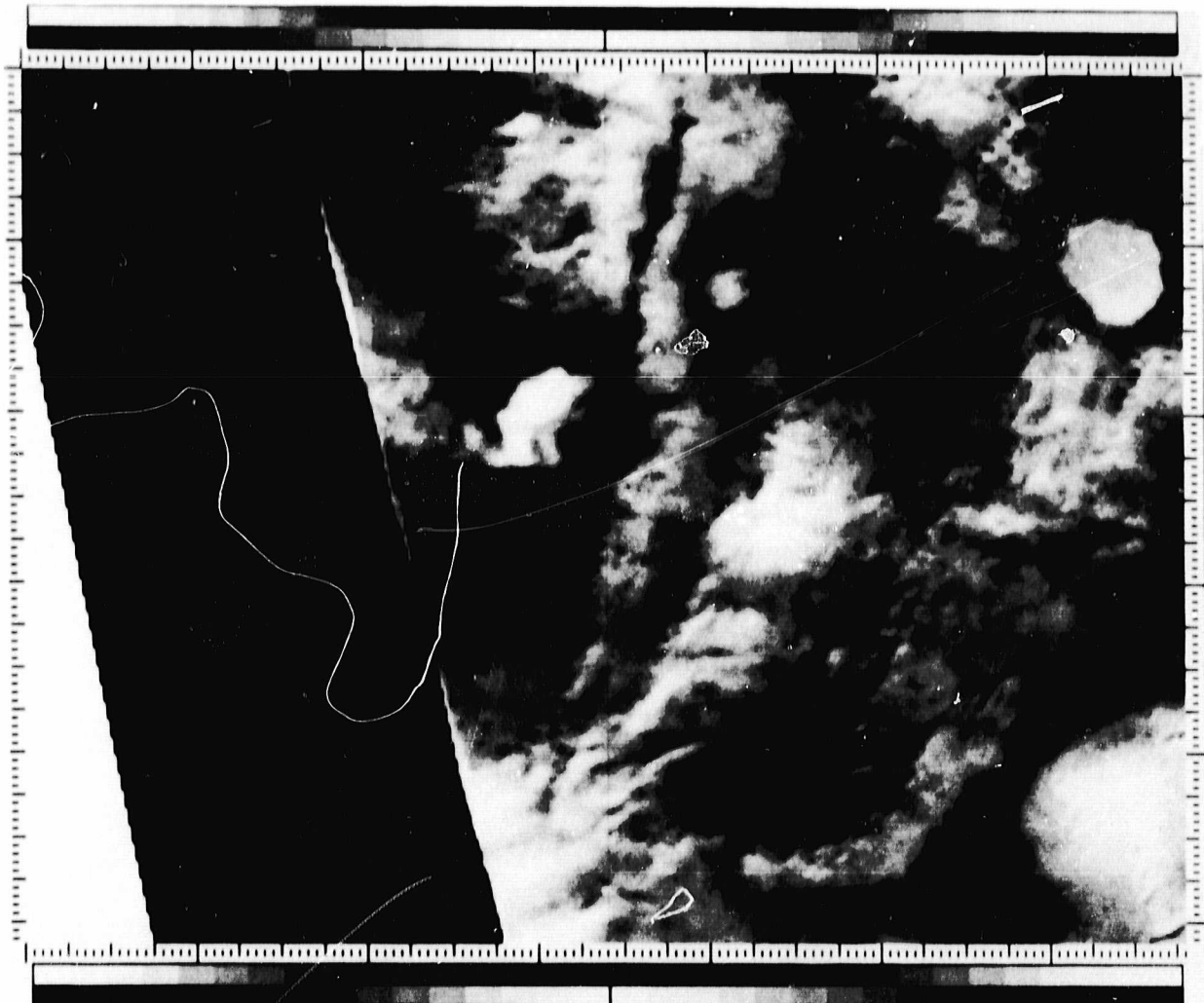


Figure 40. Thermal inertia image obtained from HCMM data for April 4, 1979 in the Walker Lane area near Goldfield, Nevada.

ORIGINAL PAGE  
BLACK AND WHITE PHOTOGRAPH

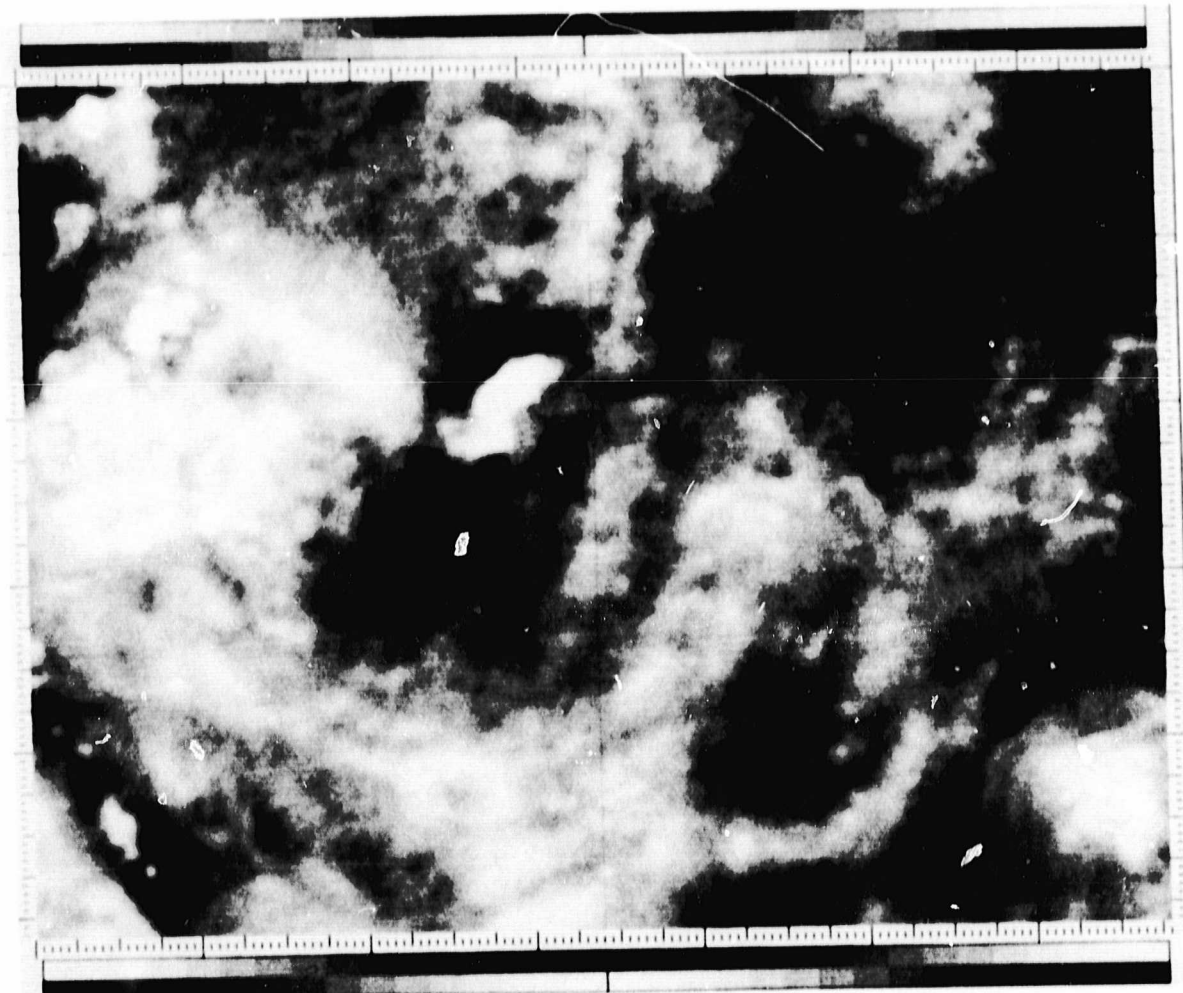


Figure 41. Thermal inertia image obtained from HCMM data for July 6, 1978 in the Walker Lane area near Goldfield, Nevada.

where  $S$  is the solar constant ( $\approx 1.98 \text{ cal cm}^{-2} \text{ min}^{-1}$ ),  $V$  is atmospheric transmittance at visible wavelengths (a value of 0.75 is used in the calculation),  $A$  is albedo,  $\Delta T$  is the day-night temperature difference (taken between 1330 LT and 0230 LT),  $\omega$  is the angular speed of the earth's rotation ( $\approx 4.363 \times 10^{-3}$  radians/min),  $\alpha$  is a parameter which is proportional to the ratio of the heat flux density transferred by the surface to the air to that transferred into the ground, and  $C$  is a parameter which varies with solar declination ( $\delta$ ) and latitude ( $\phi$ ) according to

$$C = \frac{1}{\pi} [\sin \delta \sin \phi \arccos (-\tan \delta \tan \phi) + \cos \delta \cos \phi (1 - \tan^2 \delta \tan^2 \phi)^{1/2}] . \quad (37)$$

Table 17 shows the result of a linear least squares fit of  $P$  values calculated from the JPL thermal model versus  $AP$  values calculated from Equation 36. Meteorological data from four midlatitude NWS locations - Ely, Nevada and three Arizona stations, Yuma, Winslow, Tucson - have been fit to the linear equation,

$$P(\text{model}) = mAP + b. \quad (38)$$

The last column in the table gives standard deviations ( $\sigma$ ) for each calculation. The seasonal values refer to solar declinations of  $\delta = 23.5^\circ$  (June 21),  $\delta = 0^\circ$  (March 21, September 21),  $\delta = -23.5^\circ$  (December 21). The model calculations pertain to dry conditions (no soil moisture or latent heat flux components) for 96 cases: four stations  $\times$  four seasons  $\times$  three  $P$  values ( $0.02, .05, .08 \text{ cal cm}^{-2} \text{ s}^{-1/2} \text{ }^\circ\text{C}^{-1}$ )  $\times$  two albedo values (0.1, 0.4). Values

TABLE 17  
LINEAR LEAST-SQUARES FIT OF P(MODEL) TO AP

	m	b	$\sigma$
ALL CASES	2.09	-0.026	0.012
Ely, Nevada	1.61	-0.008	0.017
March	3.06	-0.055	0.005
June	2.92	-0.080	0.008
Sept	3.12	-0.048	0.004
Dec	4.29	-0.057	0.009
Yuma, Arizona	2.61	-0.044	0.006
March	2.78	-0.052	0.004
June	2.69	-0.052	0.003
Sept	2.54	-0.042	0.003
Dec	2.77	-0.043	0.005
Winslow, Arizona	2.31	-0.032	0.012
March	3.02	-0.048	0.004
June	2.87	-0.065	0.004
Sept	2.98	-0.062	0.007
Dec	3.09	-0.041	0.005
Tucson, Arizona	2.64	-0.050	0.006
March	2.81	-0.053	0.005
June	2.49	-0.048	0.003
Sept	2.76	-0.059	0.006
Dec	2.91	-0.054	0.005

of  $\Delta T$  are computed for each case and, along with other data, are used to compute AP values which are used with the given P values as data in the regression analysis. Different values of  $m$ ,  $b$ , and  $\sigma$  occur for similar seasons (e.g. March, September where  $\delta = 0$ ) because the model calculations employed climatological data for each station, and these data differ from one month to the next. The values of  $m$  and  $b$  for all cases are 2.09 and -0.026 respectively and the table shows that P(model) is larger than AP in all cases.

It is interesting to apply this result to the P(model) and AP calculations of the HCMM flights listed in Table 1. The AP values of the HCMM data are also lower than the corresponding P(model) values. If the HCMM data for AP are used in the formula

$$P(\text{model}) \approx 2.09 \text{ AP} \approx 0.026 \quad (39)$$

then the values of P(model) calculated from this formula agree, for the most part, within 5 to 15% of the P(model) values listed for the HCMM data.

Two versions of the modeled images of P are used: one with and one without corrections for topography. The topographic corrections are obtained from NCIC data which include information on elevation in digital format. Figures 42, 43, and 44 show topographic images derived from the NCIC data of the Goldfield, Nevada area. These are respectively a shaded relief map, a slope azimuth map, and a slope orientation map. For reference, the Goldfield mining district is in the upper right of each image, Stonewall Mountain is in the lower right corner of each and Clayton Valley is in the left central portion.

The next set of figures, 45 through 47, show HCMM data for July 6, 1978. In order, they are apparent P, modeled P without topographic correc-

ORIGINAL PAGE  
BLACK AND WHITE PHOTOGRAPH

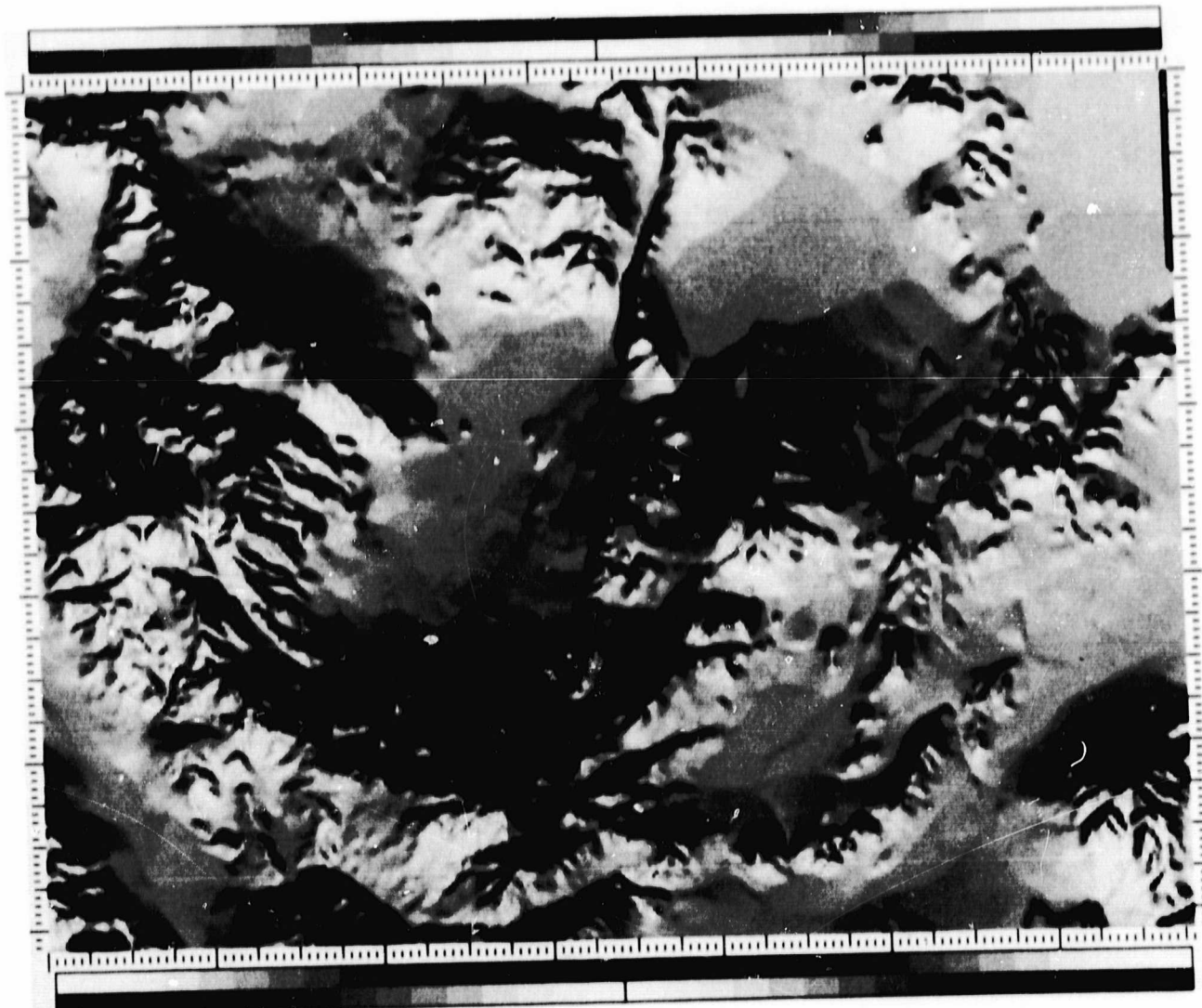


Figure 42. Shaded relief map of the Walker Lane, Nevada area.

ORIGINAL PAGE  
BLACK AND WHITE PHOTOGRAPH

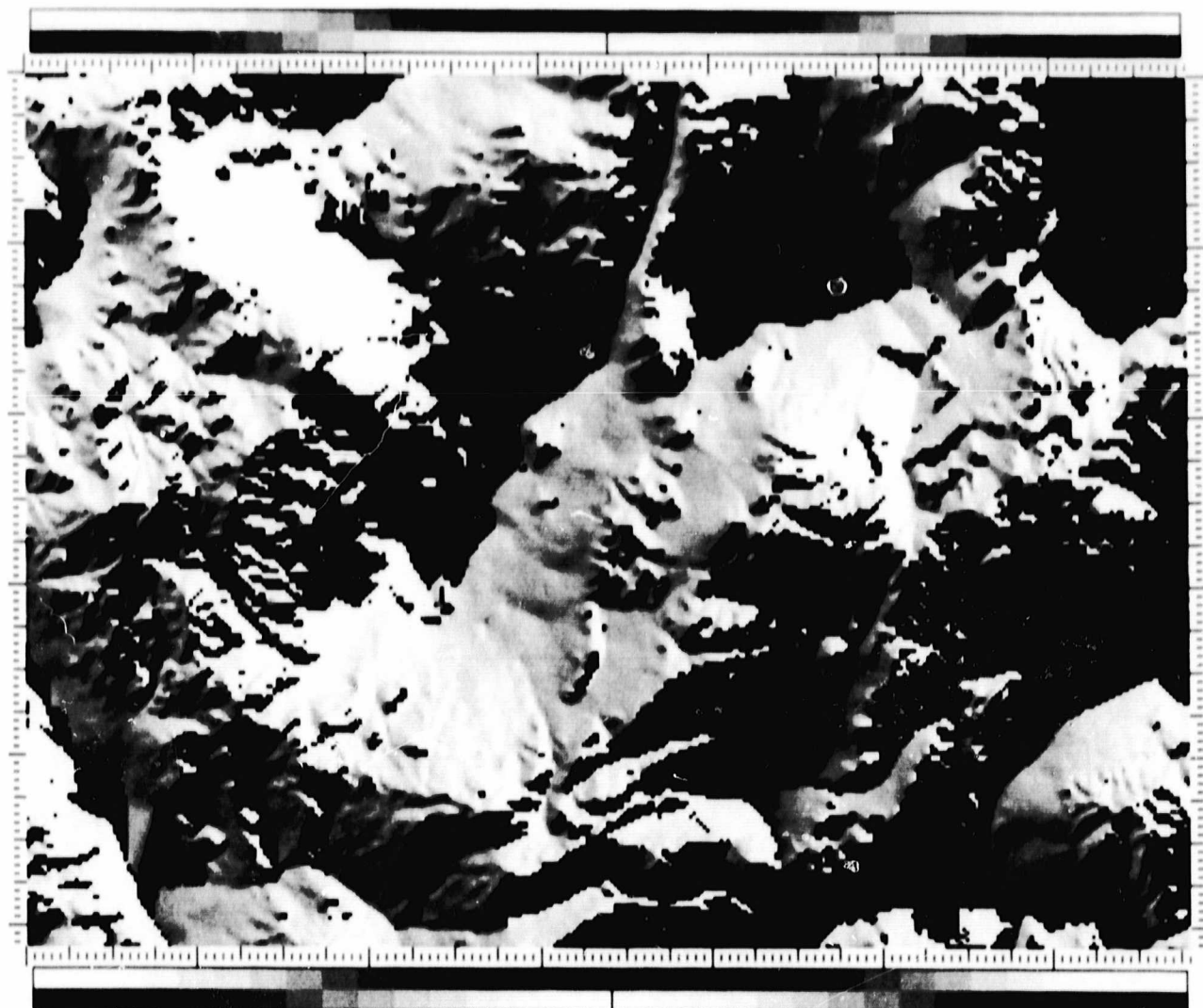


Figure 43. Slope azimuth map of the Walker Lane, Nevada area.

ORIGINAL PAGE  
**BLACK AND WHITE PHOTOGRAPH**



Figure 44. Slope orientation map of the Walker Lane, Nevada area.

tions, and modeled P with topographic corrections. The large, white area in Clayton Valley is a body of standing water. There are no significant differences between the modeled images. Evidently, the NCIC scale ( $\sim 60$  m) for the topography is too fine-grained to be useful on the scale ( $\sim 500$  m) of the HCMM data. Furthermore, the apparent P image also displays little variation from the other two images. This also holds true for the other HCMM data products that were processed but not shown here. The one exception noted is at Mud Lake which is seen as a dark or gray disk-like feature in the upper right on each image. The dark area around the perimeter of the disk is more extensive on the apparent P image than on the modeled one. The reason for this difference is not clear but it may be related to the ground moisture distribution.

This study indicates the benefits of constructing apparent thermal inertia images. The quality of the images is comparable to that attained by the more sophisticated model products without the extra labor and cost involved. This advantage is restricted to image interpretation in a relative sense, i.e. discriminating among geologic materials with different thermal inertia values. In an absolute sense, neither the apparent nor model thermal inertia images faithfully reproduce exact thermal inertia values of the geologic units depicted. However, the model products are more likely to approach the actual values since model calculations make provision for some of the factors (e.g. atmospheric effects, ground-level meteorological conditions) that cause discrepancies between calculated and actual values. This does not minimize the importance of the apparent thermal inertia products. For many geologic applications, the use of thermal inertia images that are valid in a relative sense is quite appropriate, and in this context, apparent thermal inertia products are considerably useful.

ORIGINAL PAGE  
BLACK AND WHITE PHOTOGRAPH

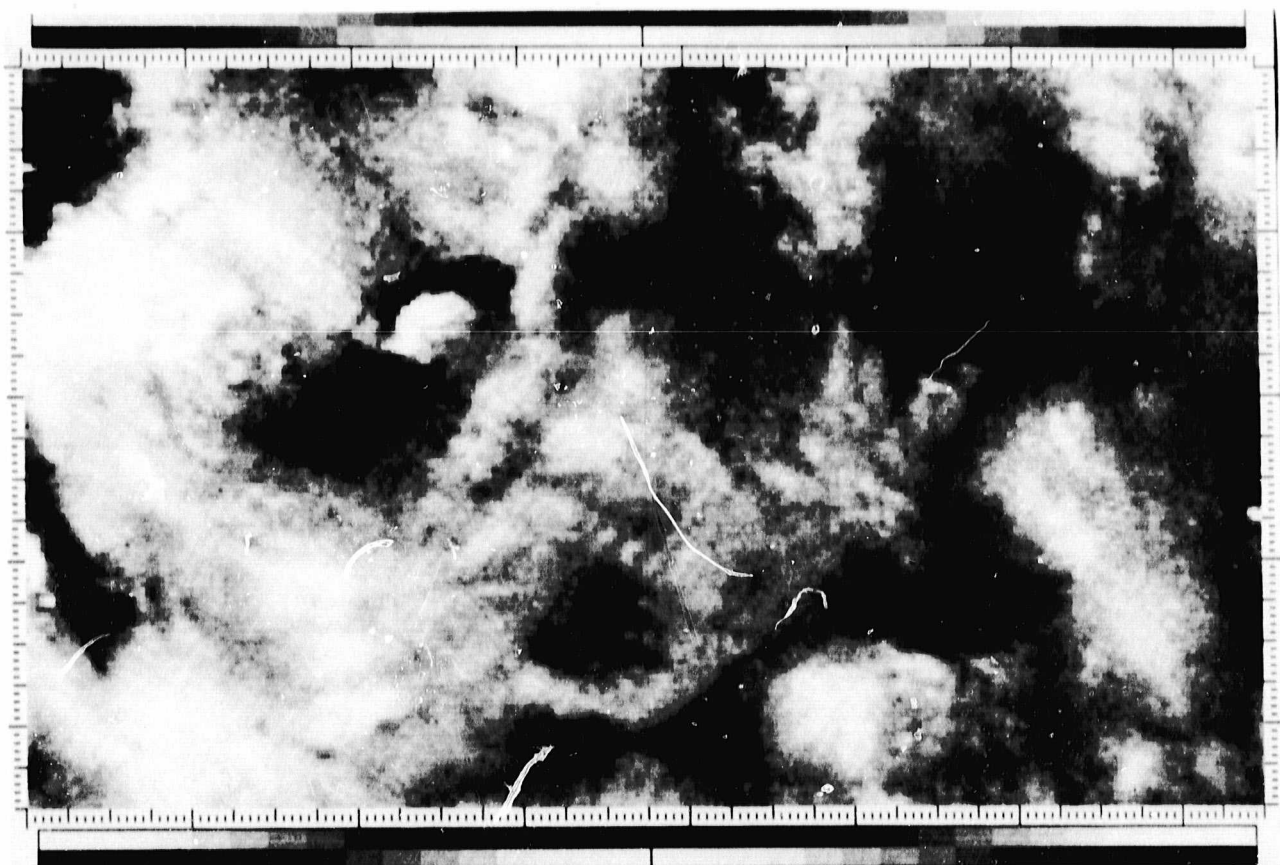


Figure 45. Apparent thermal inertia image obtained from HCMM data for Walker Lane on July 6, 1978.

ORIGINAL PAGE  
BLACK AND WHITE PHOTOGRAPH

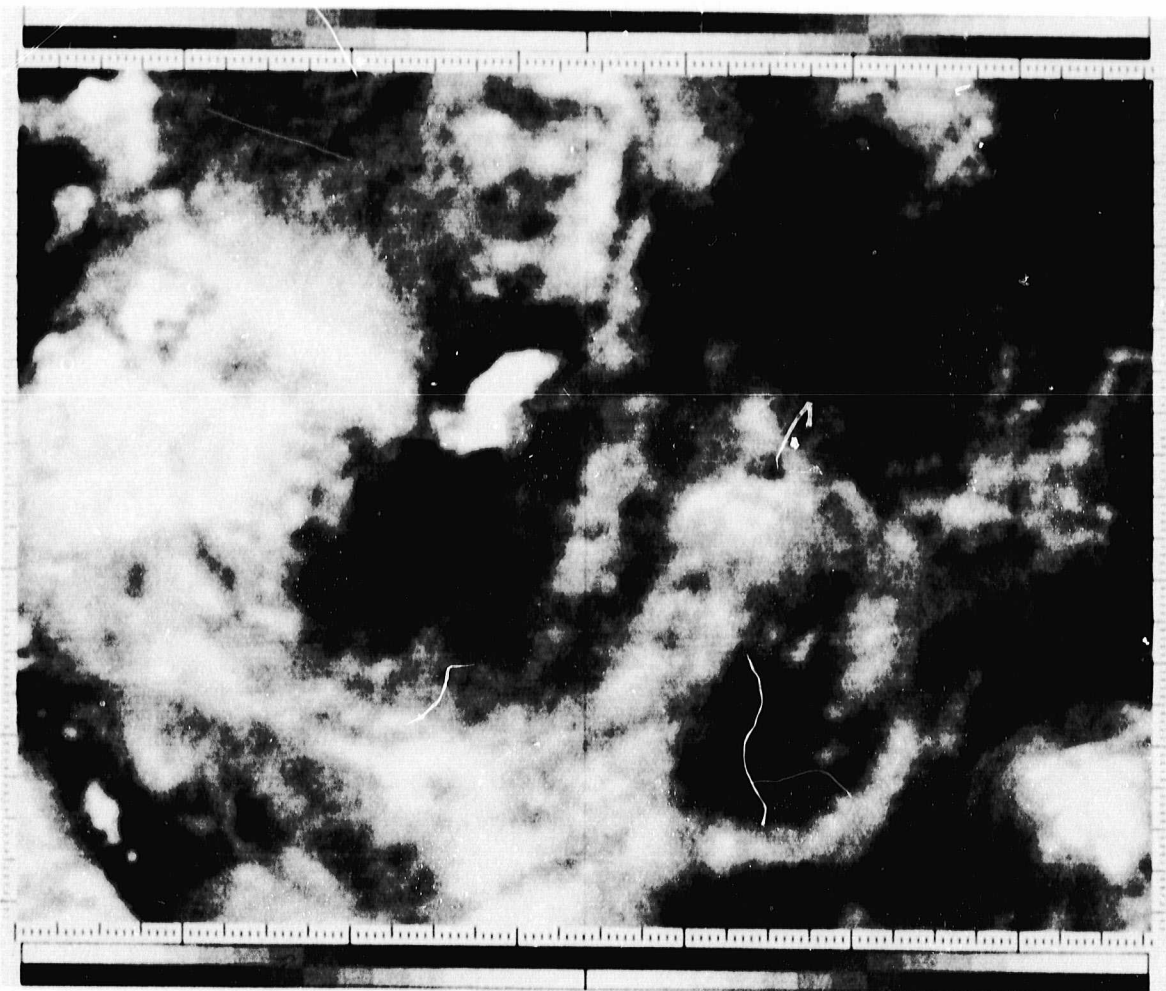


Figure 46. Calculated thermal inertia image obtained from HCMM data for Walker Lane on July 6, 1978. Topographic corrections not included.

ORIGINAL PAGE  
BLACK AND WHITE PHOTOGRAPH

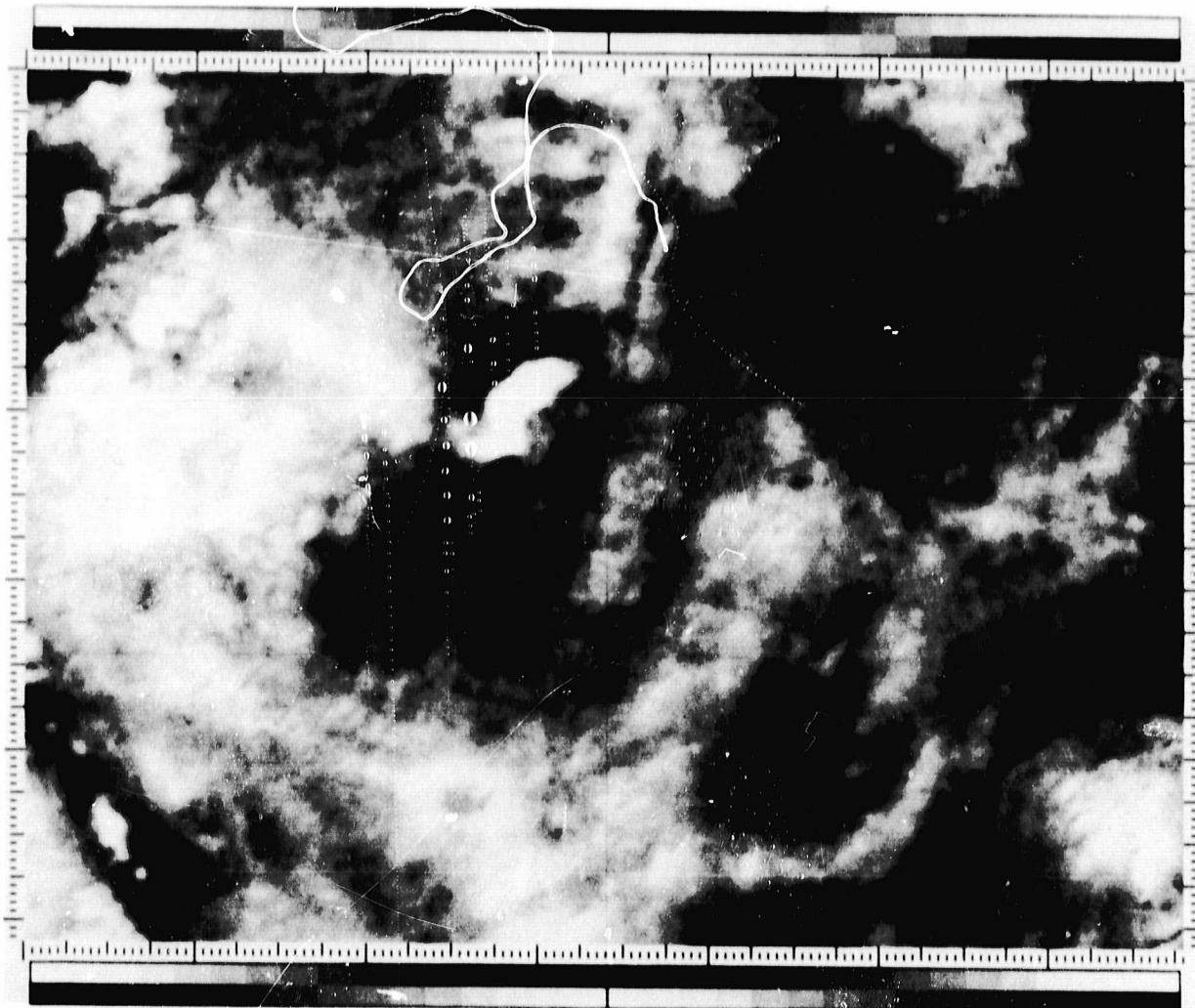


Figure 47. Calculated thermal inertia image obtained from HCMM data for Walker Lane on July 6, 1978. Topographic corrections included.

## VI. GEOLOGICAL INTERPRETATION

### A. Walker Lane

#### 1. Geologic Description

The Walker Lane test site is in Esmeralda County, southwestern Nevada, (Figure 48), in the Basin and Range province. The overall topography is dominated by arcuate ranges and intervening valleys. The general relief between valley bottoms and the crests of adjacent ranges is on the order of 1000 m.

The climate is arid to semi-arid with an average annual precipitation of about 10 cm. Vegetation on the lower slopes and valleys consists of sagebrush and other desert plants; average cover is less than 15%. At higher elevations pinon or juniper predominate.

Rocks exposed in the area include sedimentary, volcanic, and intrusive rocks. Sedimentary rocks consist of dolomite, limestone, shale, valley alluvial fill derived from the adjacent mountains, and playa deposits. Plutonic rocks are of Mesozoic and Tertiary age, and are dominantly quartz monzonitic in composition. Volcanic rocks include welded and non-welded ash flow tuffs, lava flows and volcanic breccia, ranging in composition from rhyolitic to basaltic, with quartz latite composition being the most common (Albers and Stewart, 1972) (Figure 49, geologic map).

The Walker Lane test site area is famous for its precious metal deposits. The Goldfield and Tonopah gold and silver deposits have produced major tonnages of ore since 1890. Hydrothermal alteration associated with the Goldfield deposit includes silicification and argillization. To the south, the Cuprite mining district is characterized by silicification and opalization.

ORIGINAL PAGE IS  
OF POOR QUALITY

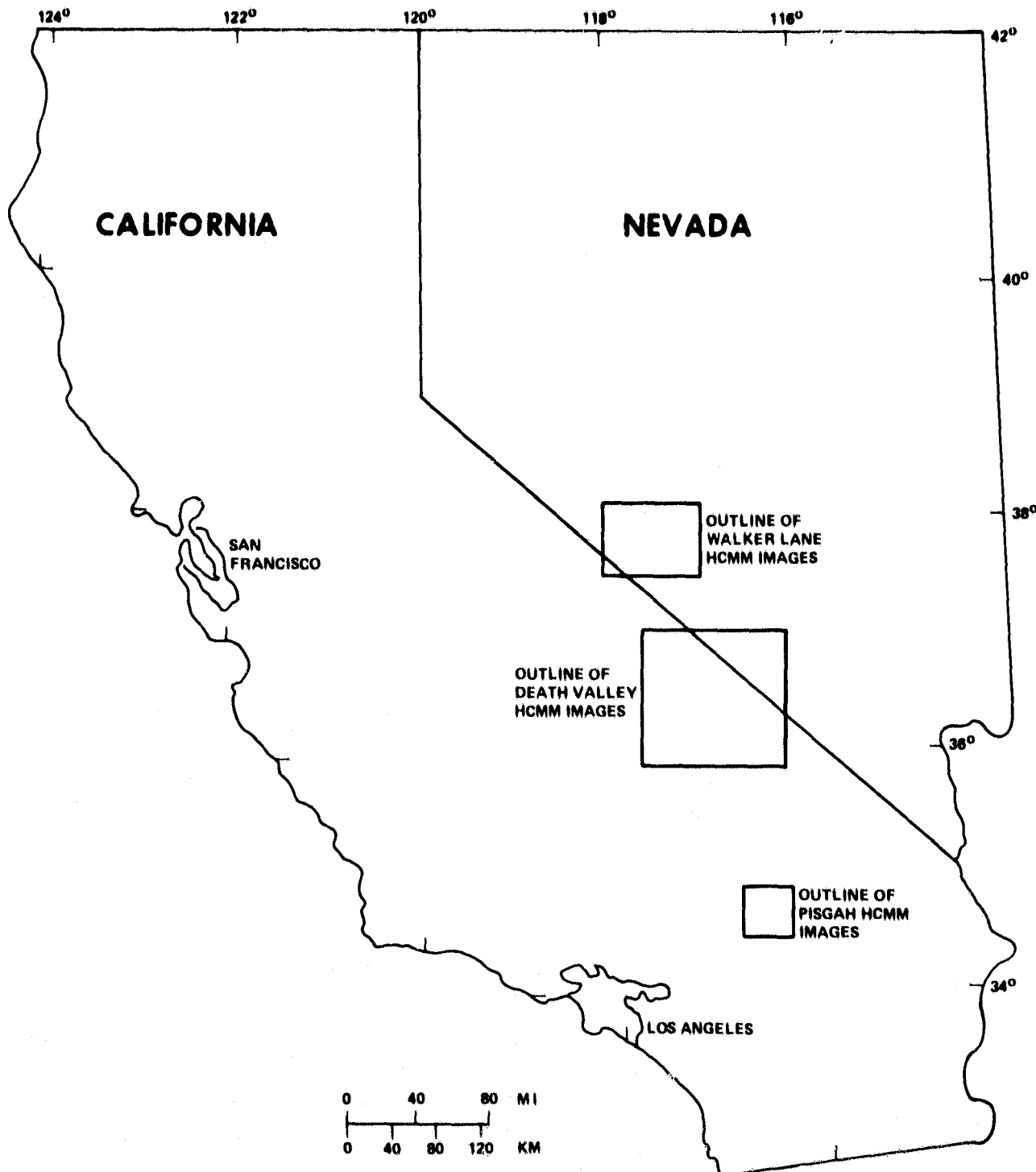


Figure 48. Location map of Walker Lane, Pisgah and Death Valley sites.

**ORIGINAL PAGE  
COLOR PHOTOGRAPH**

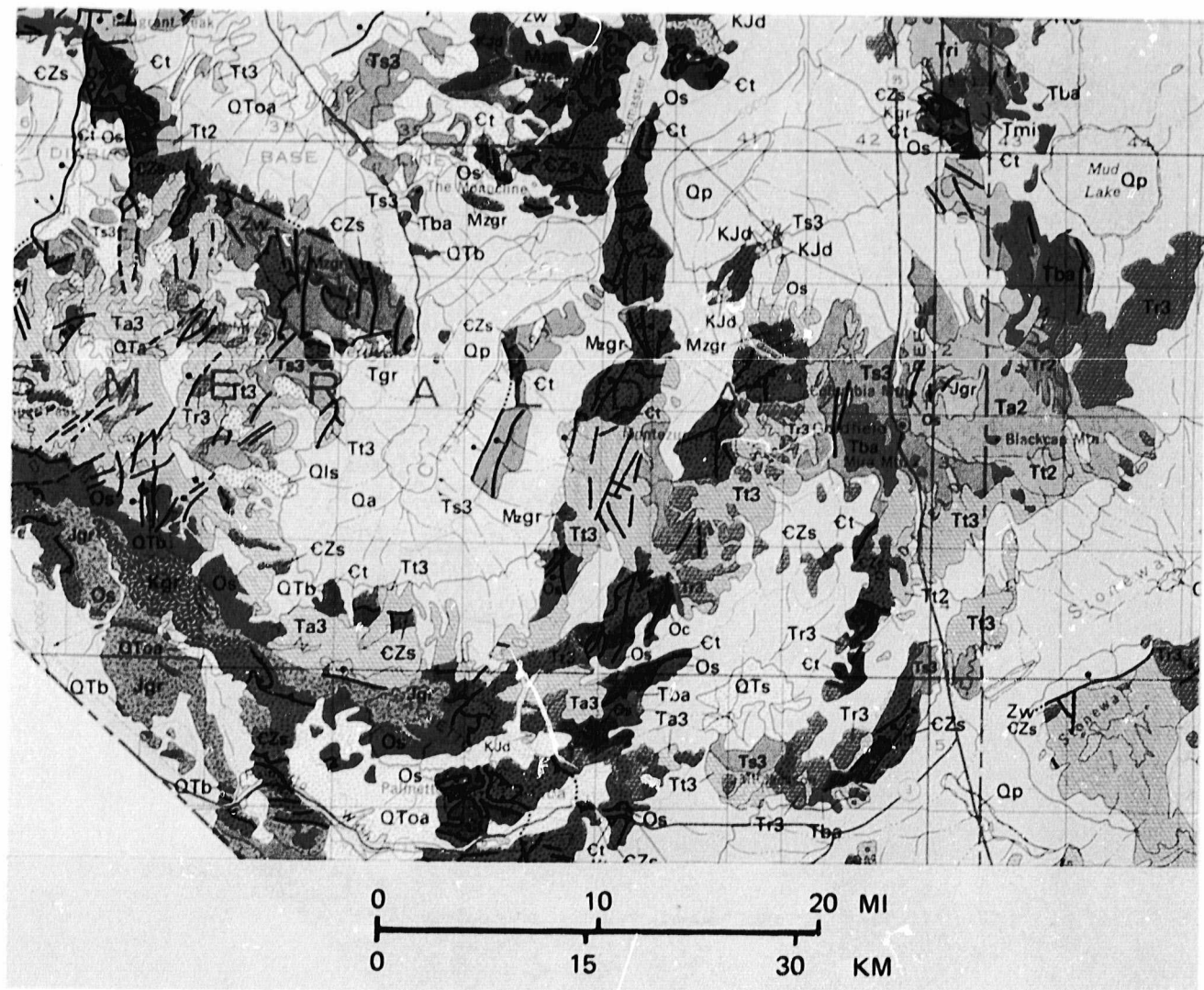


Figure 49. Geologic map of Goldfield, Nevada and vicinity.

## 2. HCMM Images

An HCMM day visible image for the Walker Lane test site is shown as Figure 50. (This and all subsequent HCMM scenes for Walker Lane, Death Valley, and Pisgah are from the 6-7 July 1978 data set.) The very bright areas are playas and a few clouds (in the northwest corner). The darkest areas are basalts and other volcanic rocks. At high elevations, vegetation cover also appears dark.

The day IR image (Figure 51) has Clayton Valley playa and the small clouds displayed as the coldest areas in the scene. There is probably standing water on the playa, as the other playas in the scene appear much warmer. Other cold areas include Stonewall Mountain, and other high elevations. Both the altitude and vegetation cover cause the cooler temperatures. Alluvial valleys appear very warm, with low to moderate elevation bedrock regions appearing cooler. Very little, if any, lithologic information can be interpreted from this presentation.

The tonal patterns on the night IR image (Figure 52) correspond closely to the pattern of outcrop areas vs. alluvial areas, with the former generally colder than the latter. Clayton Valley has a very warm area in the north (water) and a cold area to the south (dry).

The thermal inertia image (Figure 53) has more geologic information than the previous three data types. The highest thermal inertia areas (white) correspond to outcrops of sedimentary rocks of dolomitic, quartzitic, and limestone composition. Low thermal inertia areas include alluvial fans and dry playa deposits. The area around Goldfield is mixed; a high thermal inertia area corresponds to an area of basalt and silicification; moderate thermal inertia areas are rhyolites and andesites; low thermal inertia areas are alluvium.

ORIGINAL PAGE  
BLACK AND WHITE PHOTOGRAPH

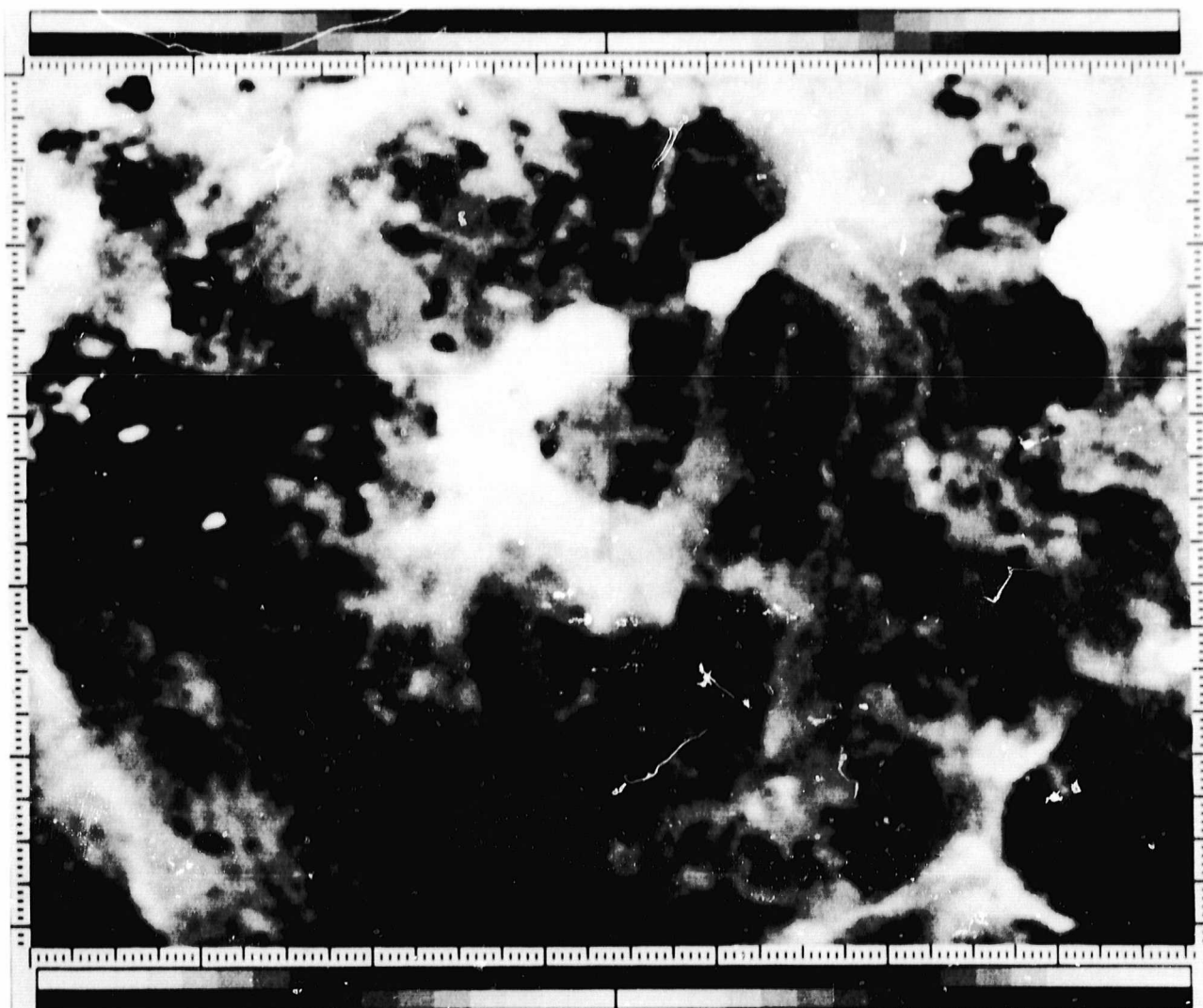


Figure 50. HCMM day visible image of Walker Lane site. Image size is 65 x 85 km.

ORIGINAL PAGE  
BLACK AND WHITE PHOTOGRAPH

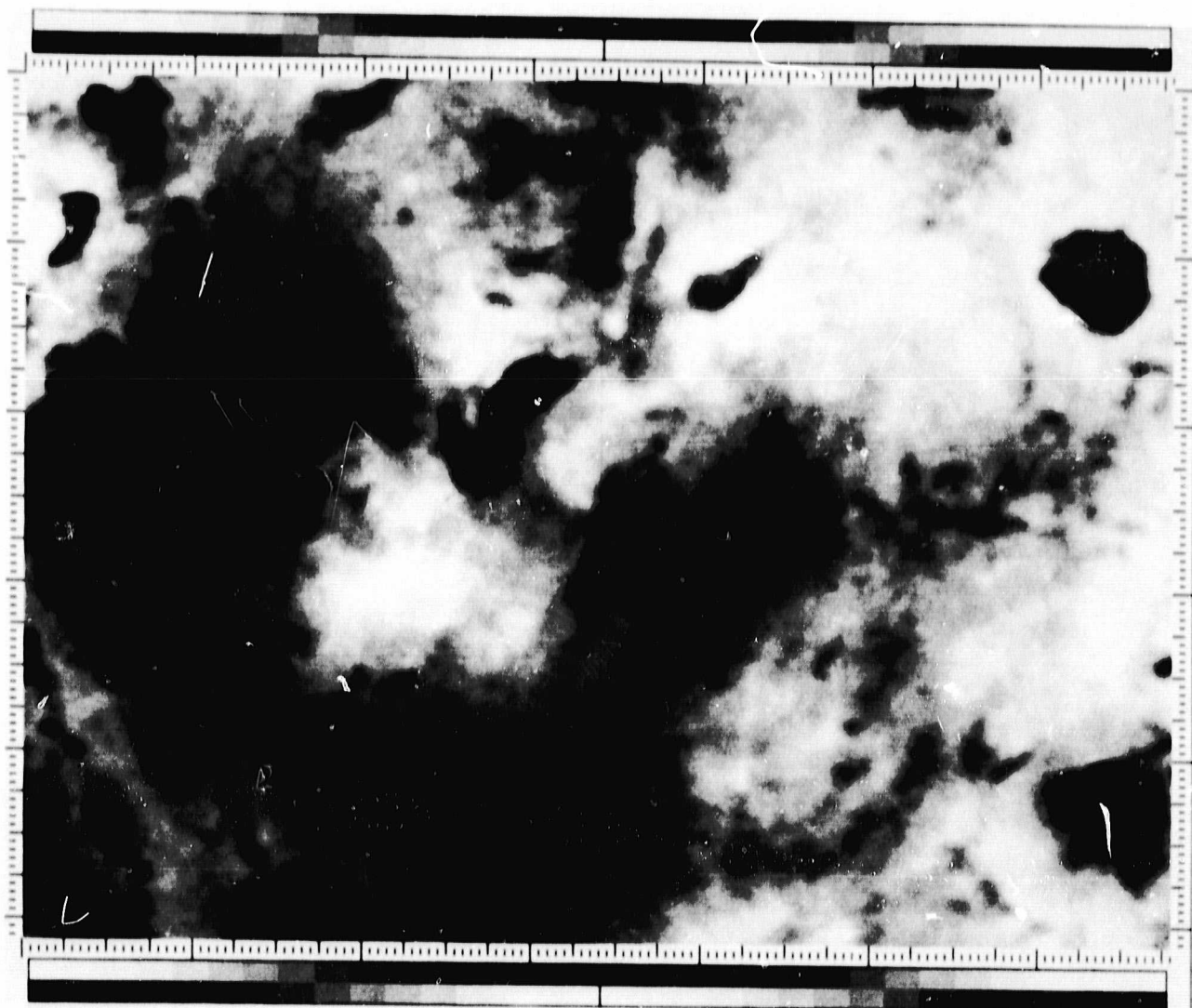


Figure 51. HCMM day IR image of Walker Lane site. Image size is 65 x 85 km.

ORIGINAL PAGE  
BLACK AND WHITE PHOTOGRAPH

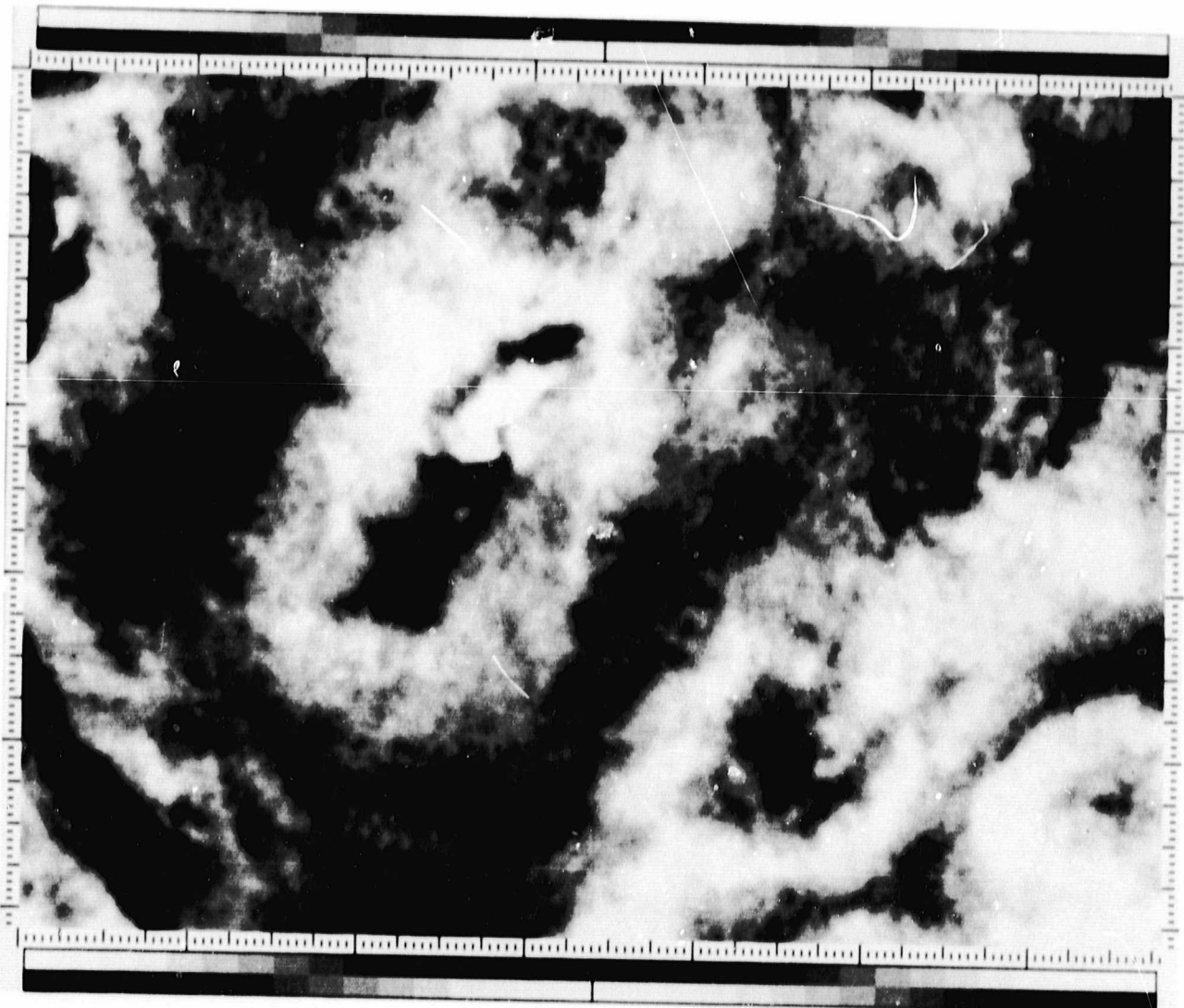


Figure 52. HCMM night IR image of Walker Lane site. Image size is 65 x 85 km.

ORIGINAL PAGE  
BLACK AND WHITE PHOTOGRAPH

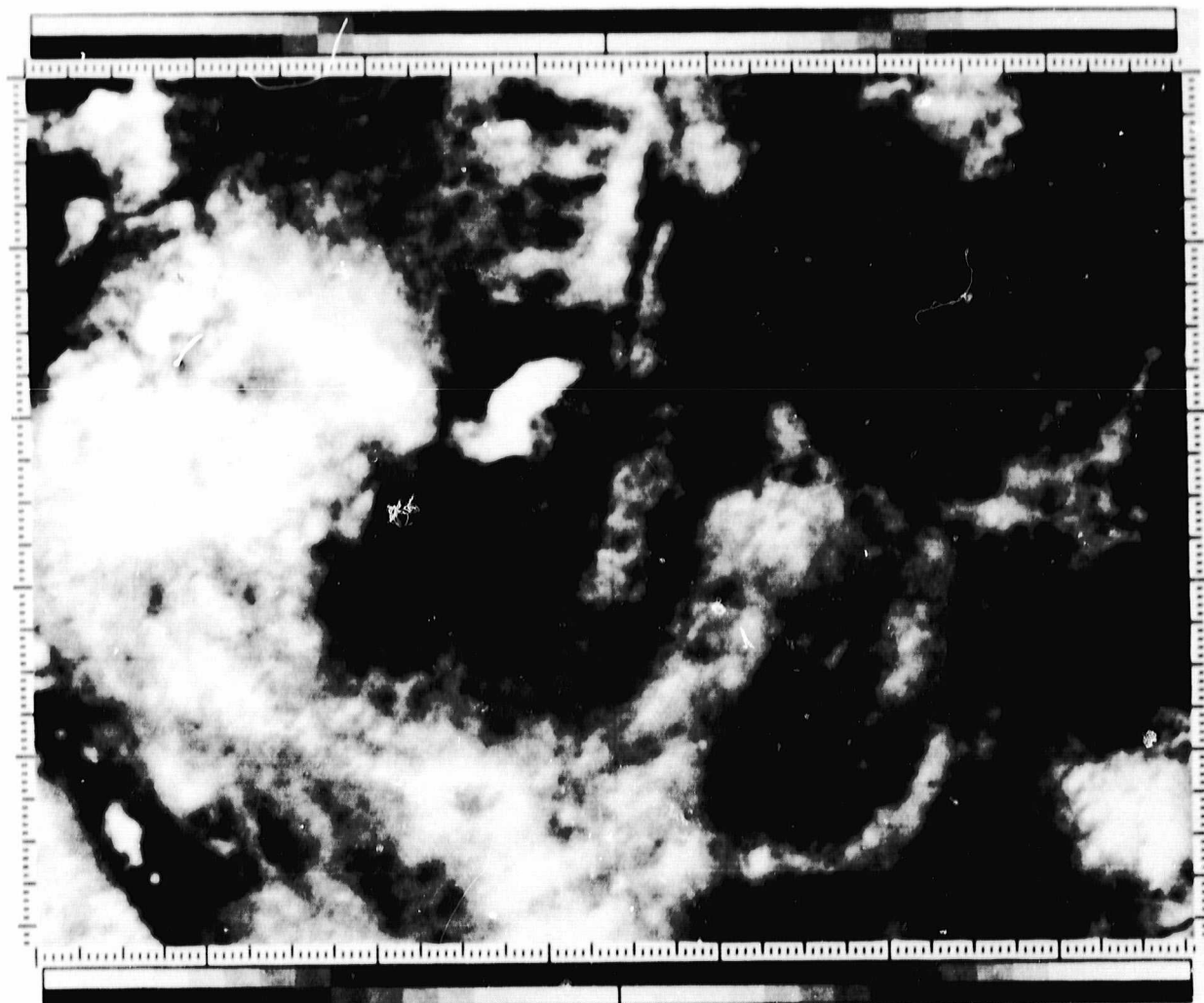


Figure 53. HCMM thermal image of Walker Lane site. Image size is 65 x 85 km.

A far more effective display of the HCMM data is shown in Figure 54. The color composite was produced by combining the visible, day IR, and night IR images, displayed as green, red, and blue, respectively. The visible and night IR images were also complemented. Complementing the data is the same as changing a photographic positive to a negative. Black areas become white, white areas become black. The algorithm used is:

$$DN_o = 255 - DN_1$$

where  $DN_o$  is the digital number or brightness value of the new picture,  $DN_1$  is the value of the original picture. The brightness values range from 0 (black) to 255 (white). Areas which have low albedo, are cold at night, or are warm in the day, appear brightly colored in the composite picture. An interpretation map produced from this picture is shown in Figure 55. Table 18 is a description of the symbols used for the interpretation.

The playas are dark blue (#1) as are the altered rocks at Goldfield (#16) and the altered rocks at Cuprite to the south. At Goldfield, alteration consists of both silicification along faults, and more widespread argillization. It is the latter that probably stands out. The similar appearance of playa material is due to their similar albedos and thermal properties (low thermal inertia).

Basalts are yellow or green; other volcanic rocks are yellow-green. However, some outcrops of alluvium and phyllitic siltstone (#14) also appear the same color. Red to pink areas are alluvial valleys. There are a great many areas where the different lithologies cannot be separated (#15). These appear in various colors. Overall, some lithologic separations could be made; more information is displayed than on any of the separate black-and-

ORIGINAL PAGE  
COLOR PHOTOGRAPH

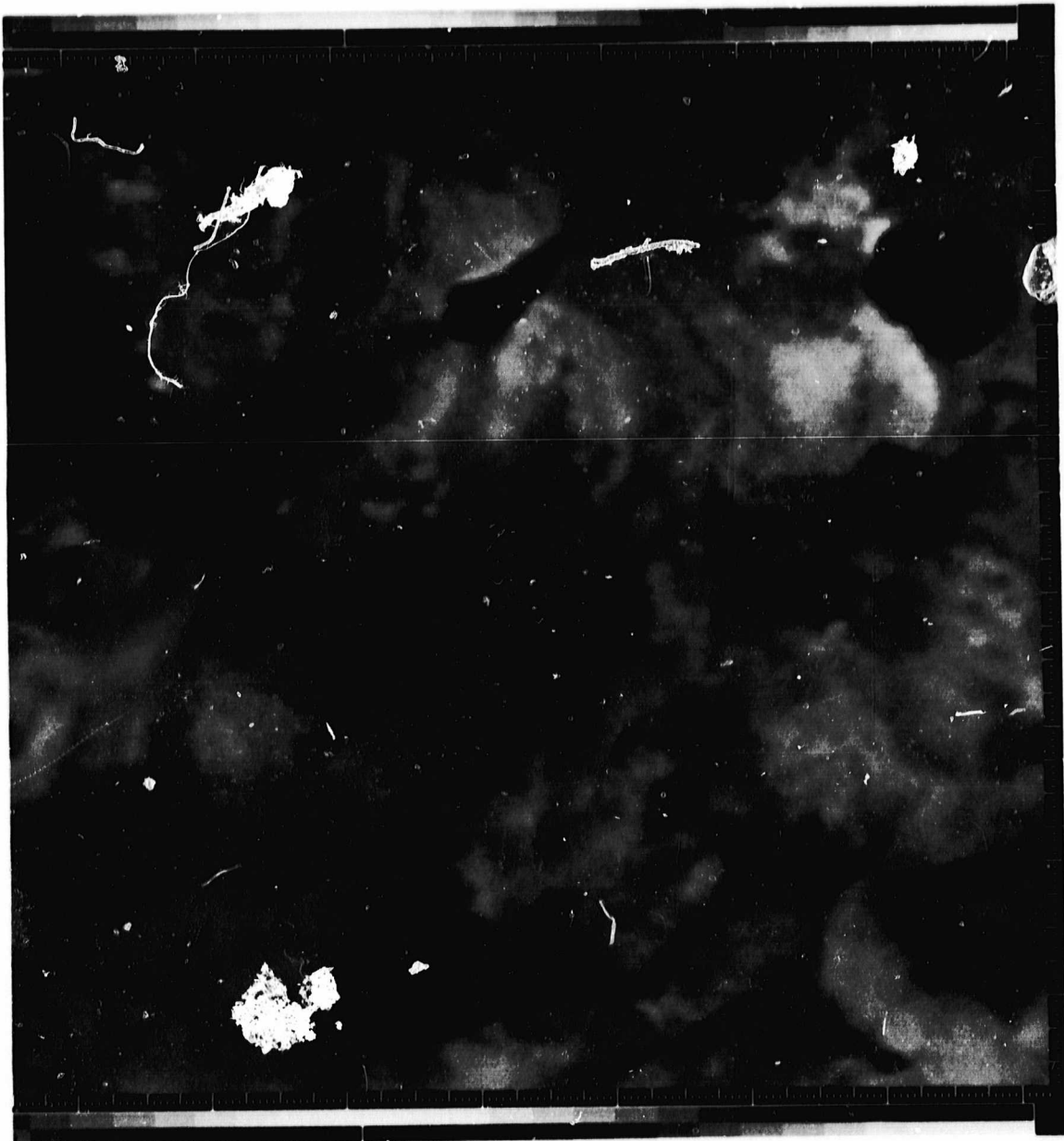
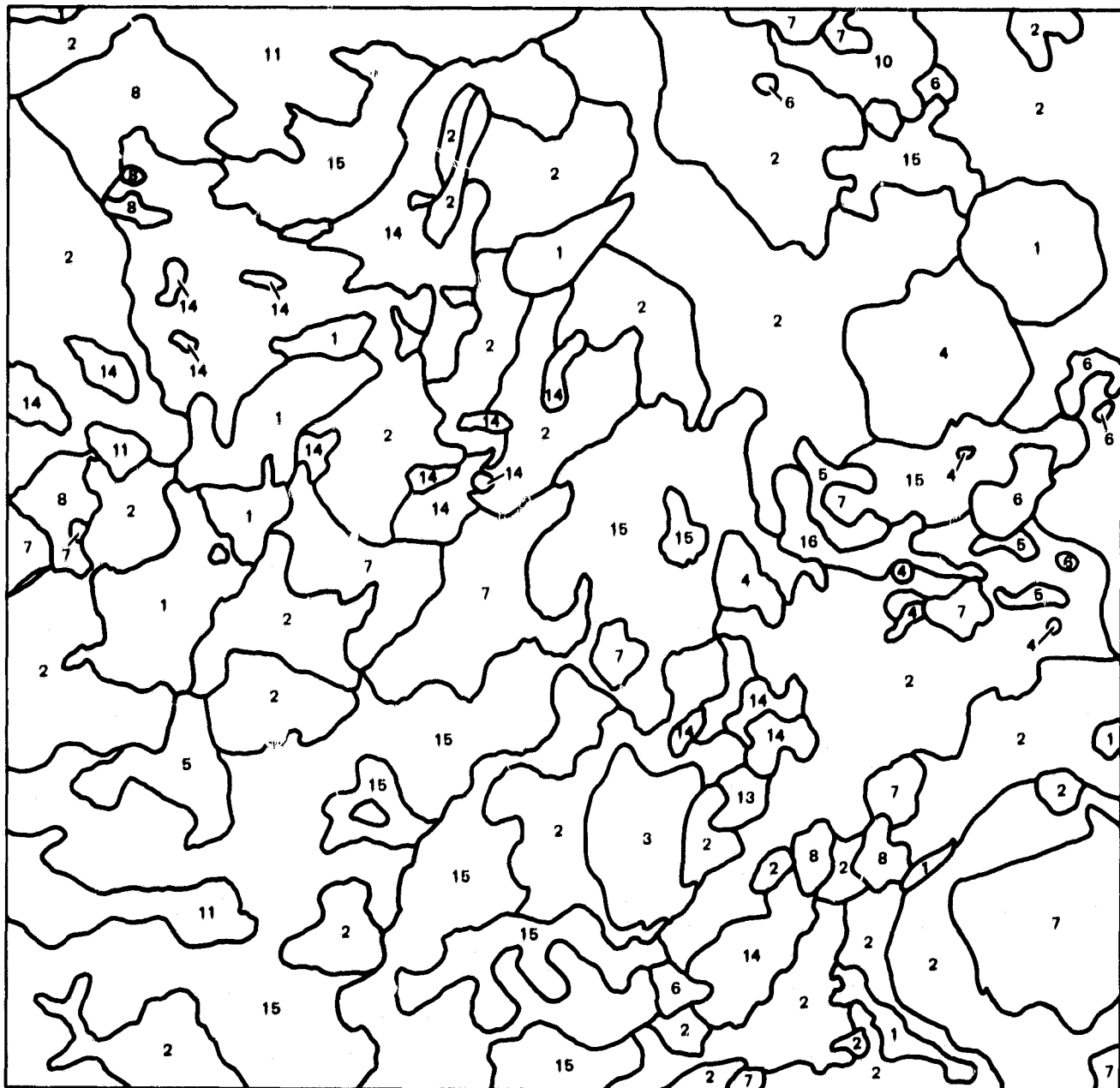


Figure 54. HCMM color composite of Walker Lane. Day IR, night IR, and visible images displayed as red, blue, and green respectively. Visible and night IR images were complemented.

ORIGINAL PAGE IS  
OF POOR QUALITY

GOLDFIELD, NEVADA TEST SITE: HCMM



INTERPRETATION OF HCMM COLOR COMPOSITE: DAY VISIBLE + DAY IR +  
NIGHT IR. FOR SYMBOLS, SEE ACCOMPANYING CHART

Figure 55. Interpretation map produced from Figure 54.

TABLE 18

## DESCRIPTION OF SYMBOLS FOR WALKER LANE HCMM INTERPRETATION

<u>Unit</u>	<u>Geologic</u> <u>Map Symbol</u>	<u>Material</u>
1	Qp	Playa
2	Qa, QToa	Alluvium
3	QTs	Lake deposits
4	QTb, Tba	Basalt
5	Qta, Ta3, Ta2	Andesite
6	Tr3, Tr2	Rhyolite
7	Tt3, Tt2	Silicic ash flow tuff
8	Ts3	Tuff sediments
9	Tri	Rhyolite intrusive
10	Tmi	Mafic intrusive
11	Tgr, Jgr, KJd, Mzgr	Granite
12	OC	Limestone, dolomite, shale
13	OS, Et	Shale, limestone, chert
14	EZs, Zw	Phyllitic siltstone
15		Mixed
16		Alteration at Goldfield

white images. However, other work using Landsat data was far superior for lithologic mapping in this area (Rowan et al., 1974).

### 3. Aircraft Images

High resolution aircraft data were acquired over the Goldfield and Cuprite mining areas. A thermal inertia image for the Goldfield site appears as Figure 56. The same image with the mapped alteration zones superimposed (Ashley and Keith, 1976) appears as Figure 57. The alteration zones include areas of high thermal inertia (silicified) and low thermal inertia (argillized). Other high thermal inertia areas are unaltered volcanic rocks (basalts, andesites); other low thermal inertia areas are unaltered rocks and alluvium. Unique identification of the alteration zone is not possible from the thermal inertia data. The circular distribution of high thermal inertia material, however, would alert the geologist to the possible existence of a structural feature. In this area, this feature reflects control of the alteration by a caldera boundary. Alteration fluids were channeled along fractures at the boundary, producing the circular pattern.

The geology and alteration maps for the Cuprite district to the south of Goldfield are shown in Figures 58 and 59. An aircraft thermal inertia image of the area is shown in Figure 60. The silicified area in the eastern half of the district appears as a region of high thermal inertia on the image. On the western half of the image, high thermal inertia areas correspond to opalized and silicified rocks. The playa on the right edge of the image appears dark (low thermal inertia). The appearance of the silicified and opalized rocks is consistent with the appearance of similar rocks in the Goldfield aircraft thermal inertia image.

In order to better evaluate the contribution of thermal data for rock type/alteration discrimination, the thermal inertia data were regis-

ORIGINAL PAGE  
BLACK AND WHITE PHOTOGRAPH



Figure 56. Thermal inertia image of Goldfield, Nevada from aircraft data.  
Image size is 15 x 15 km.

ORIGINAL PAGE  
BLACK AND WHITE PHOTOGRAPH



Figure 57. Mapped alteration zones superimposed on Figure 56.

ORIGINAL PAGE  
COLOR PHOTOGRAPH

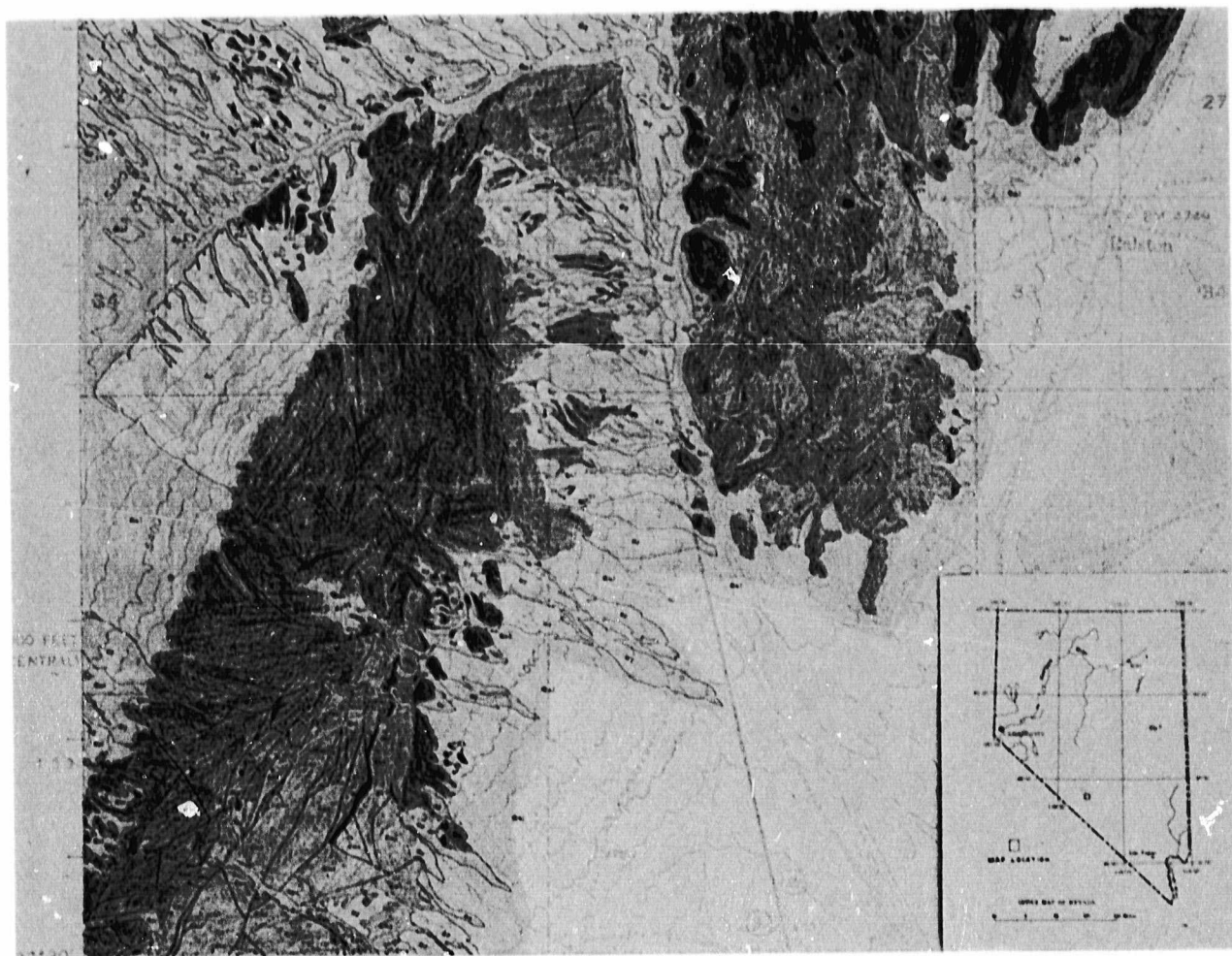


Figure 58. Geologic map of Cuprite Mining District, Nevada.

**ORIGINAL PAGE  
COLOR PHOTOGRAPH**



Figure 59. Alteration map of Cuprite Mining District, Nevada.

ORIGINAL PAGE  
BLACK AND WHITE PHOTOGRAPH



Figure 60. Thermal inertia image of Cuprite Mining District, Nevada from aircraft data. Image size is 8 x 12 km.

tered to an earlier aircraft data set, obtained with NASA's 24-channel scanner. This data set included data in the 0.5 to 2.5  $\mu\text{m}$  region. A color ratio composite picture produced from this visible and near-infrared data (Figure 61) allowed discrimination of the three mapped alteration types (Abrams *et al.*, 1977). The visible and near-infrared data were combined with the thermal inertia data, and processed using a principal components analysis (Blodget *et al.*, 1978). A color composite produced from the analysis is shown in Figure 62. Silicified rocks appear yellow, argillized rocks deep blue, and opalized rocks green. No additional alteration information was produced. However, after inclusion of the thermal data, at least three separate units can be discriminated in the unaltered volcanic rocks in the north-central part of the scene (brown on the geologic map, Figure 58), which are not shown on the geologic map or on the color composite produced from the visible and near-infrared data above. Field work is necessary to identify the causes of the image distinctions. It is probable that the image processing brings out sub-units of the volcanic rocks which either were not recognized or were combined on the map as a single unit.

#### B. Death Valley

##### 1. Geologic Description

Death Valley is in southeastern California (Figure 48) at the south edge of the Great Basin. The valley trends north-south between block-faulted mountains. In the main part of the valley, the floor is a flat playa, crusted with salts, and covering more than 500 square kilometers. The mountains bordering the valley rise to more than 3400 m only 7 km from the edge of the salt pan, 80 m below sea level.

Death Valley is a desert area, receiving an average of 4.2 cm of rainfall annually. Below about 1500 m, Death Valley is part of the lower

ORIGINAL PAGE  
COLOR PHOTOGRAPH

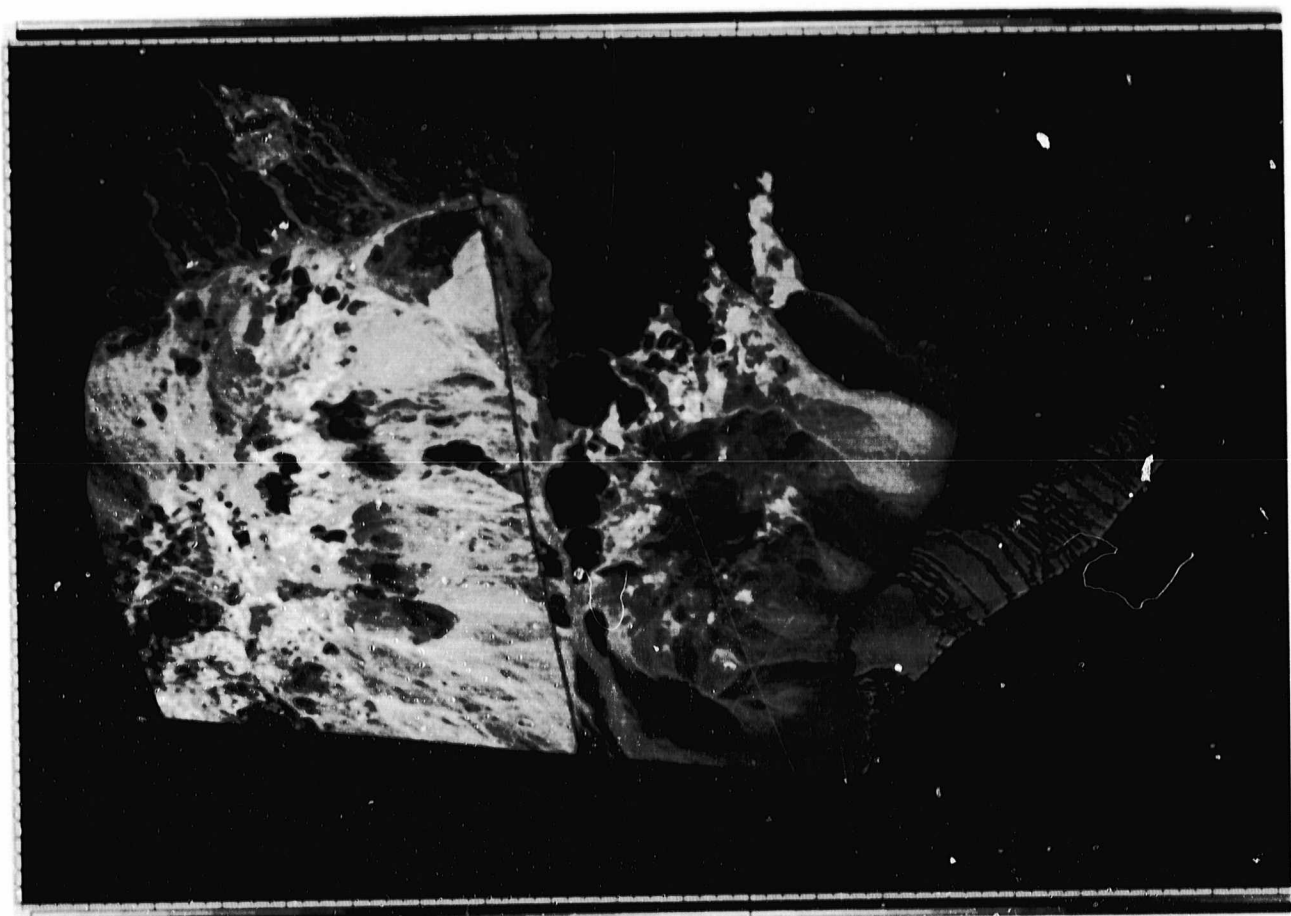


Figure 61. Cuprite Mining District, Nevada. Color ratio composite from visible and near-infrared aircraft multispectral scanner data.

ORIGINAL PAGE  
COLOR PHOTOGRAPH

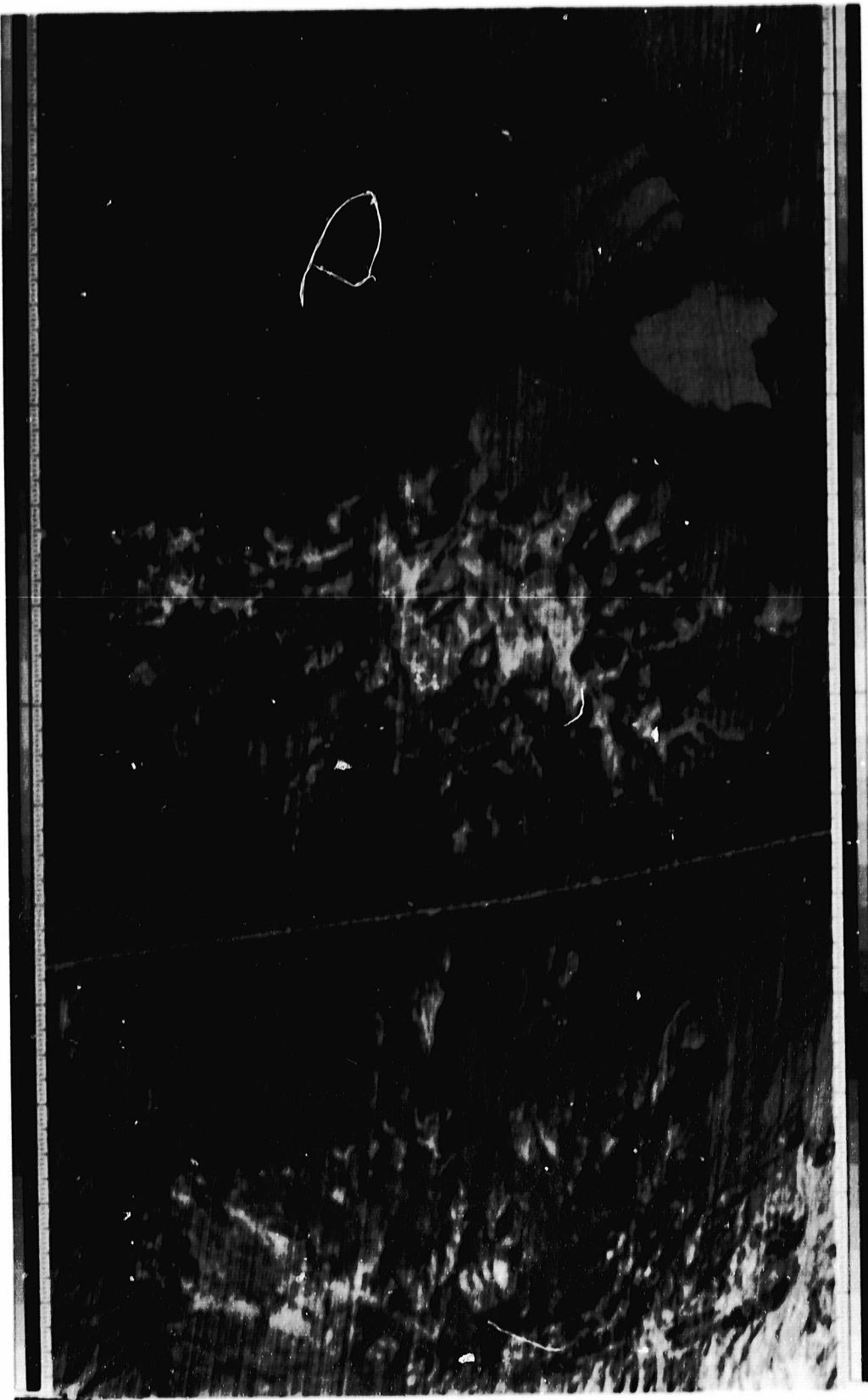


Figure 62. Cuprite Mining District, Nevada. Principal components composite from visible, near-infrared, and thermal inertia aircraft data.

Sonoran zone, characterized by creosote bush. Vegetation is scanty or absent, except along the valley floor where spring-fed areas locally support mesquite, salt bush, and pickleweed. Overall, vegetation density is no more than 5%. Above 1500 m pinon-juniper become prevalent.

Rocks exposed in the Death Valley area range in age from Precambrian to Quaternary. They include metasediments; dolomites, limestones, sandstones, shales, quartzites of marine origin; granitic intrusives; volcanic rocks of basaltic, andesitic, and pyroclastic composition; continental sediments and fanglomerates; evaporite deposits of varying saline and gypsiferous composition; and sand dunes.

Structural features are dominated by Quaternary normal Basin and Range faults which formed the trough that is Death Valley, and northwest trending right-lateral/normal faults. Older thrust faults and normal faults in the mountain ranges produced a structurally complex exposure pattern of the Precambrian to Mesozoic rocks (Hunt and Mabey, 1966) (Geologic map, Figure 63).

## 2. HCMM Images

An HCMM thermal inertia image for the Death Valley test site is shown in Figure 64. Bright areas have high thermal inertia and dark areas have low thermal inertia. The brightest features in the scene correspond to areas underlain by dolomite, limestone, quartzite, or granite. These rock types stand out distinctly on the thermal inertia image and are quite easy to map. The darkest features correspond to areas of young alluvium in the mountain valleys while the floor of Death Valley is bright to medium gray; the former areas are those that are probably more moist than the other areas (cf. Section V-D).

The thermal inertia image also allows accurate delineation of

ORIGINAL PAGE  
COLOR PHOTOGRAPH

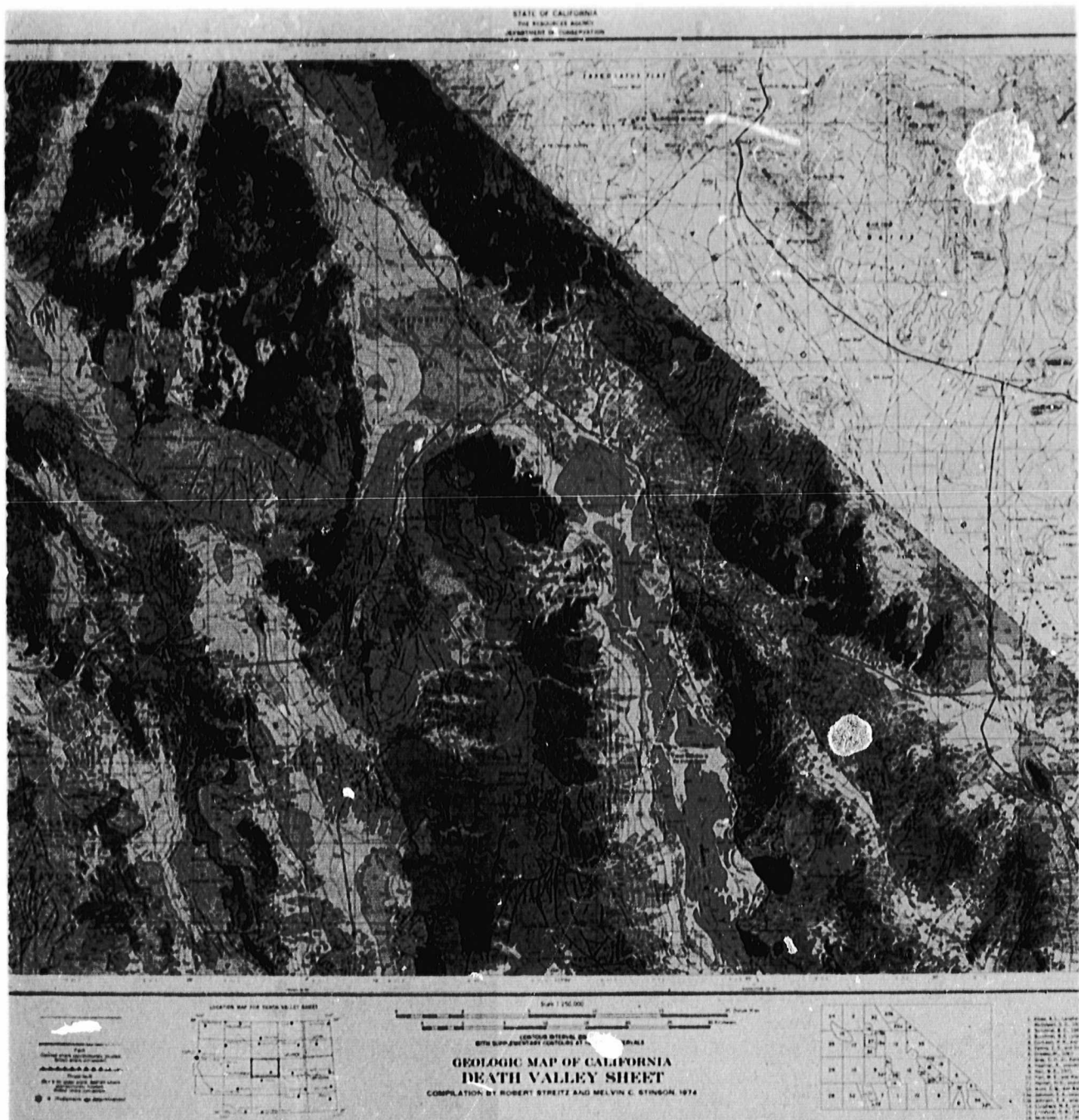


Figure 63. Geologic map of Death Valley, California area.

ORIGINAL PAGE  
**BLACK AND WHITE PHOTOGRAPH**



Figure 64. HCMM thermal inertia image of Death Valley area. Image size is 110 x 126 km.

the bedrock-alluvium contact. This differentiation is often difficult to make on visible or reflected IR images, particularly when moderate to low spatial resolution prevents the use of textural information.

Examination and comparison of eight thermal inertia images produced from different dates of HCMM data indicates that there are no differences in the appearance of the mountains and alluvial areas. Some change was observed in the playas, as previously described.

Color composites created from the HCMM data produced the best overall images for displaying lithologic differences. Figure 65 is a combination of night IR, day IR, and visible displayed as red, blue, and green, respectively. The three components have been complemented, so areas that are cold or have low albedos are brightly colored.

The Death Valley salt pan is deep blue, indicating it has high albedo, is cold in the day and warm at night. This is consistent with a composition of clay, silt and salt that is also moist. A detailed interpretation of boundaries that are delineable on the image, and the mapped geologic units they correspond to, is shown in Figure 66. A description of the symbols is listed in Table 19.

Light blue areas (#13) are outcrops of limestone, dolomite and quartzite. These materials have medium albedos, are cold in the day and warm at night; these are also the areas which had the highest thermal inertia values on the previous image (Figure 65). Green areas are underlain by older alluvial fans. Yellow-green areas (#5, 7, 8) are underlain by fanglomerates, loosely consolidated volcanic rocks and basalts. Orange and red areas correspond to young alluvial deposits (cold at night, warm in the day, moderate to low albedo) and are the areas with the lowest thermal inertia values in Figure 65.

ORIGINAL PAGE  
COLOR PHOTOGRAPH

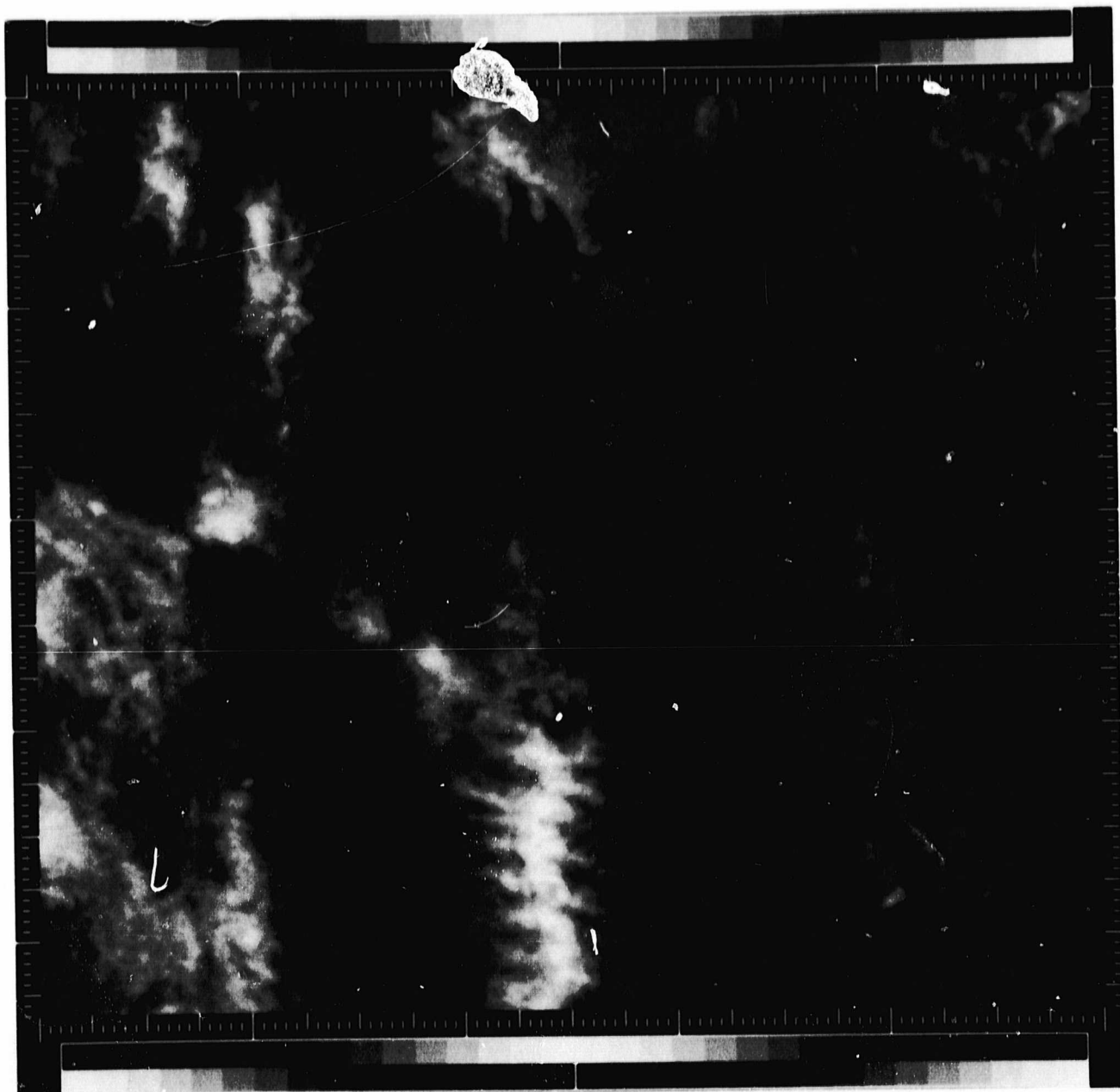
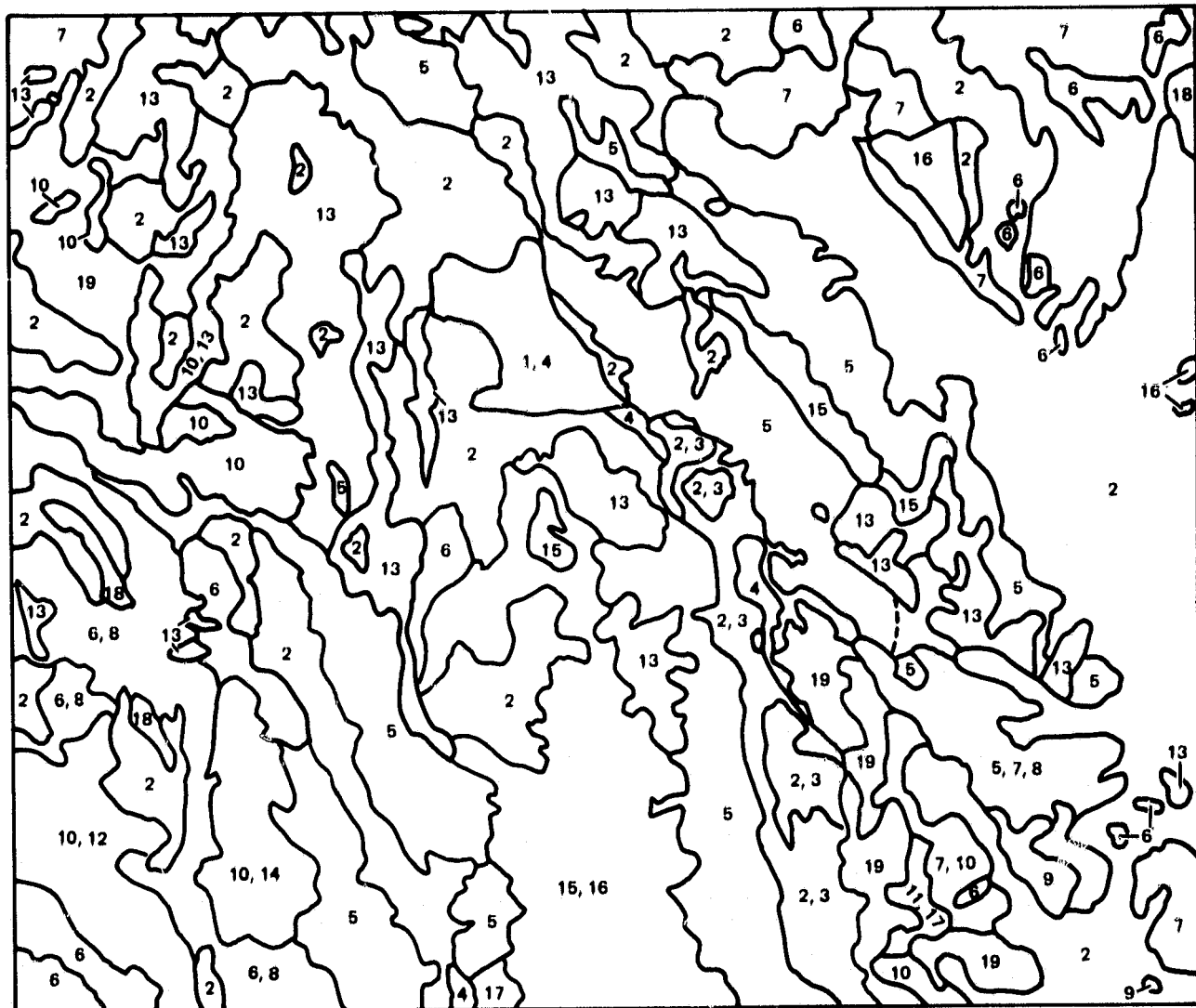


Figure 65. HCMM color composite of Death Valley. Day IR, night IR, and visible images displayed as blue, red, and green, respectively. The three images were also complemented.

ORIGINAL PAGE IS  
OF POOR QUALITY

DEATH VALLEY, CALIFORNIA: HCMM



INTERPRETATION OF HCMM COLOR COMPOSITE: BLUE = DAY IR (-),  
GREEN = DAY VISIBLE (-), RED = NIGHT IR (-)

Figure 66. Interpretation map of Figure 65.

TABLE 19

## DESCRIPTION OF SYMBOLS FOR DEATH VALLEY HCMM INTERPRETATION

<u>Unit</u>	<u>Geologic Map Symbol</u>	<u>Material</u>
1	Qs	Sand
2	Qa1	Alluvium
3	Qst	Salt
4	Q&	Lake beds
5	Qc, QP, P <sub>c</sub> , T <sub>c</sub>	Conglomerate, Fanglomerate
6	QPvb, Pvb	Basalt
7	Pvr, Tvr	Rhyolite
8	Pvp, Tvp	Pyroclastic
9	Tir	Rhyolite Intrusive
10	Tgr, gr	Granite
11	bi	Basic Intrusive
12	m	Metamorphic
13	R, D, S, O, E	Limestone, Dolomite, Quartzite
14	Rm	Quartzite, Sandstone, Limestone
15	E?	Limestone, Shale, Quartzite
16	spE	Conglomerate, Quartzite, Granite, Gneiss
17	epE	Granite, Gneiss
18	CP, CM	Shale, Limestone
19		Mixed

The distinction between alluvial areas and bedrock is particularly well defined. In addition, some separations can be made between different lithologies.

A second color composite for the test site is presented in Figure 67. The same three components and color assignments as the last figure were used, except that the uncomplemented visible image was used for the green component (spectrally dark areas are dark, bright areas have a high green content). The accompanying interpretation map (Figure 68) is very similar to Figure 67, with a few exceptions. Differences are now discernible in the Death Valley salt pan - some areas are green, others are cyan. The intermountain valleys and playas also display differences not previously discernible. These differences are attributable to changes in material (salt vs. clay vs. sand) and to moisture content.

### C. Pisgah

#### 1. Geologic Description

The Pisgah test site is located in the Mojave Desert region of southeastern California (Figure 48). Topography is variable: flat alluvial fans and dry lake beds surround rugged mountains with relief in excess of 700 m. Vegetation is either sparse or absent owing to the minimal annual precipitation.

Rocks exposed in the area are igneous intrusives and extrusives, and sediments derived from these sources. The intrusive rocks include quartz monzonite, biotite quartz monzonite, felsite, and mafic and felsic dikes. Extrusive rocks include basalt, andesite, dacite porphyry, and pyroclastic assemblages of variable lithology. Sedimentary rocks are dominated by fanglomerates and fan gravels derived from adjacent mountains and deposited as

ORIGINAL PAGE  
COLOR PHOTOGRAPH

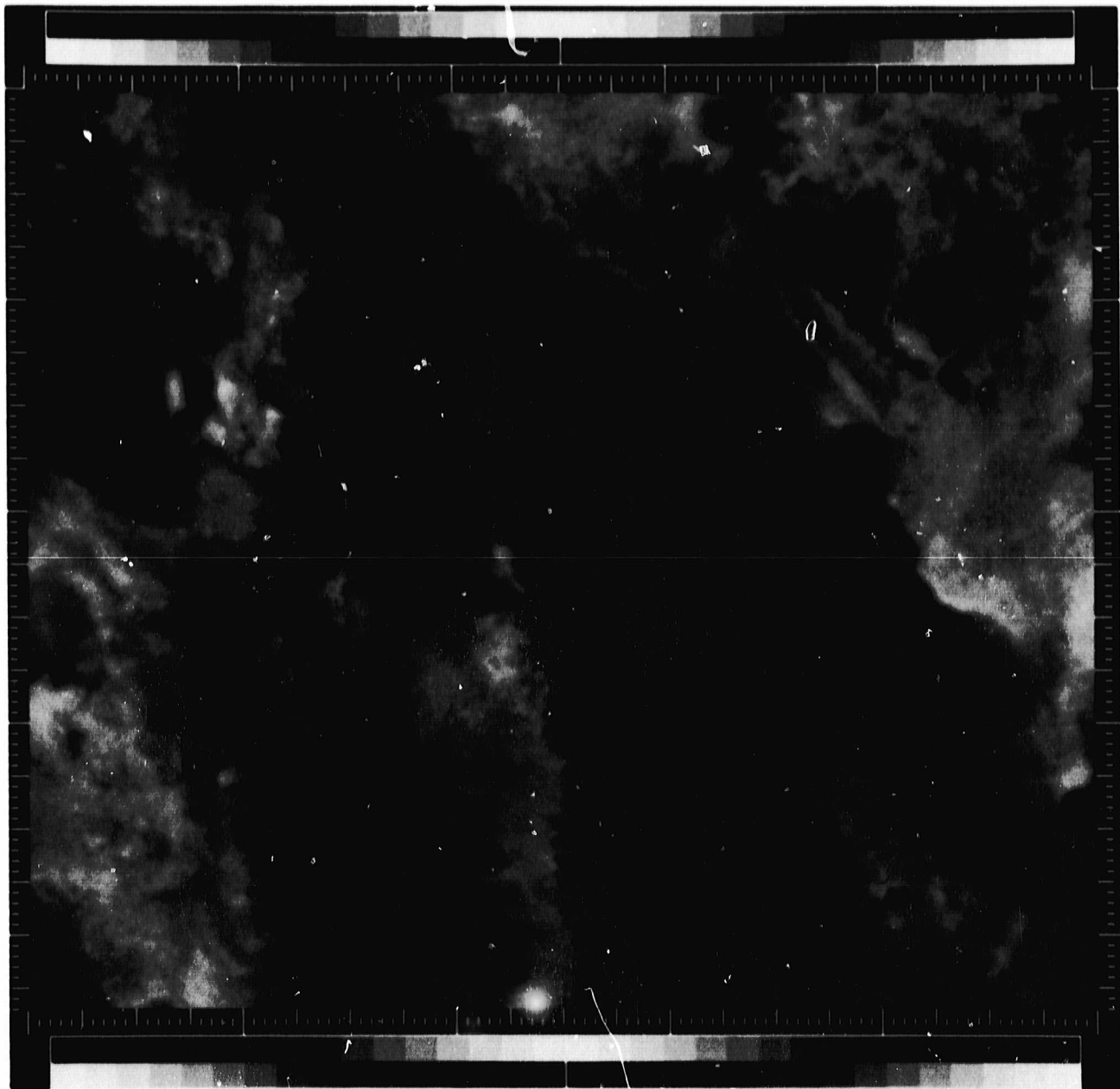
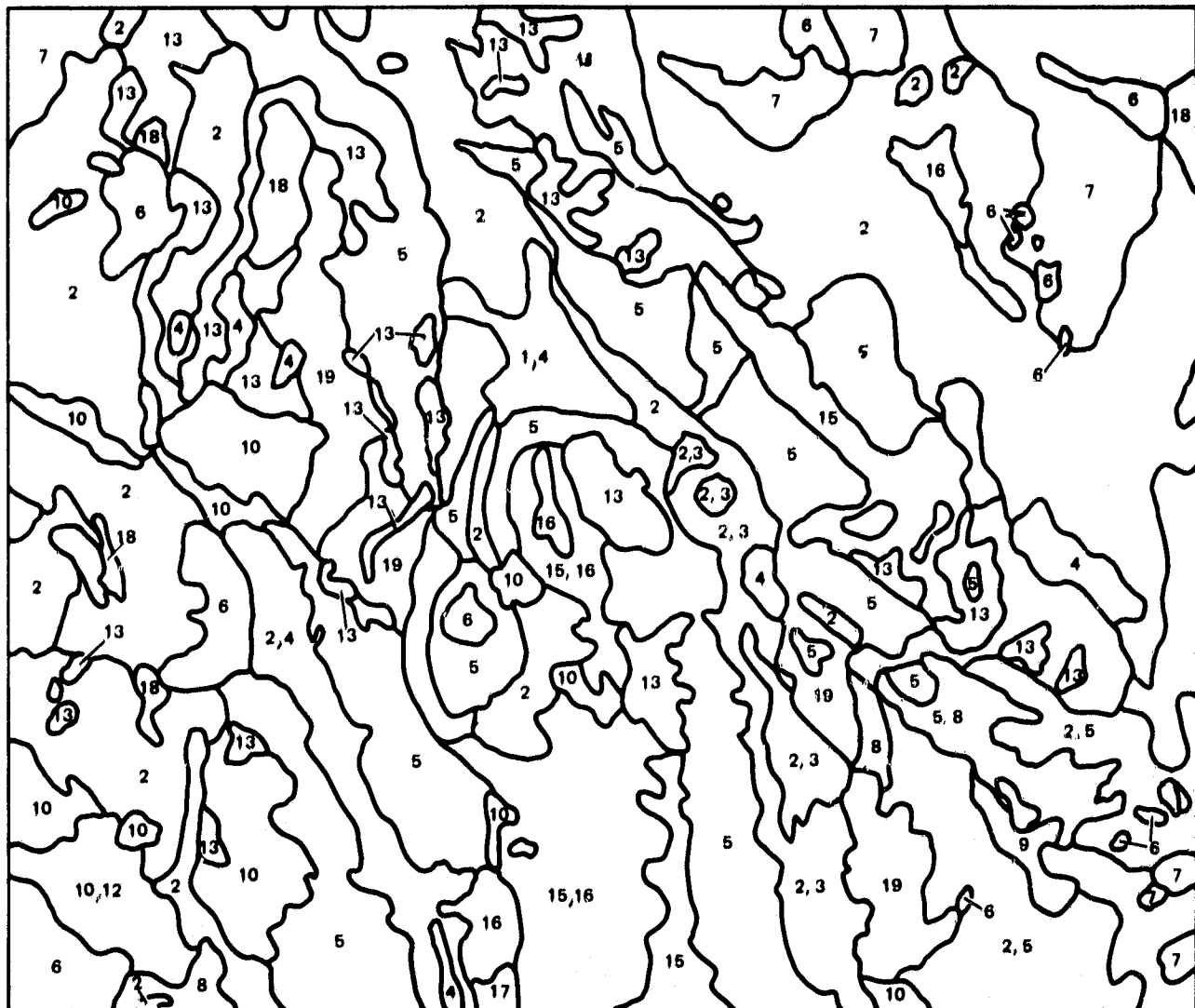


Figure 67. HCMM color composite of Death Valley. Day IR, night IR, and visible images displayed as blue, red, and green, respectively. Day and night IR images were complemented.

ORIGINAL PAGE IS  
OF POOR QUALITY

## **DEATH VALLEY, CALIFORNIA: HCMM**



**INTERPRETATION OF HCMM COLOR COMPOSITE: BLUE = DAY IR (-),  
GREEN = DAY VISIBLE (+), RED = NIGHT IR (-)**

Figure 68. Interpretation map of Figure 67.

alluvial fans. Alkaline clay occurring in the dry lake beds and windblown sand deposits form surficial sediments of non-volcanic origin.

Structures in the area are dominated by northwest trending right-lateral strike-slip faults with some normal displacement, and minor normal faults of various trends (Geologic Map, Figure 69).

## 2. HCMM Images

The HCMM day IR image is shown as Figure 70. The cold areas (dark) correspond to Lavic Lake playa, and outcrops of pyroclastics, andesite, some basalts, dacite, biotite granite, and granite. The area of aa at the Pisgah flow is colder than the pahoehoe, though the flow is not separable from the surrounding alluvial fans. The warmest areas are those corresponding to older fan deposits (north central part of the image).

The night IR image is shown as Figure 71. The warmest areas generally outline bedrock outcrops; alluvial areas are colder; Lavic Lake playa is quite cold. Very little lithologic discrimination is possible based on this image.

The visible image (Figure 72) allows separation of several units. The darkest areas are basalt outcrops, playas are the lightest, medium grays correspond to the rest of the intrusive rocks. Again, very little discrimination is possible, though there appears to be more information present here than on the night IR image.

In order to examine the interrelationship of the three HCMM data types, several color composite images were produced by using various combinations of data types as components of a color additive triplet. One such image is shown in Figure 73 (left). This image is a combination of the day IR, night IR, and visible, displayed as blue, red, and green respectively. All three components were complemented, so areas that are cold or have low

**ORIGINAL PAGE  
COLOR PHOTOGRAPH**

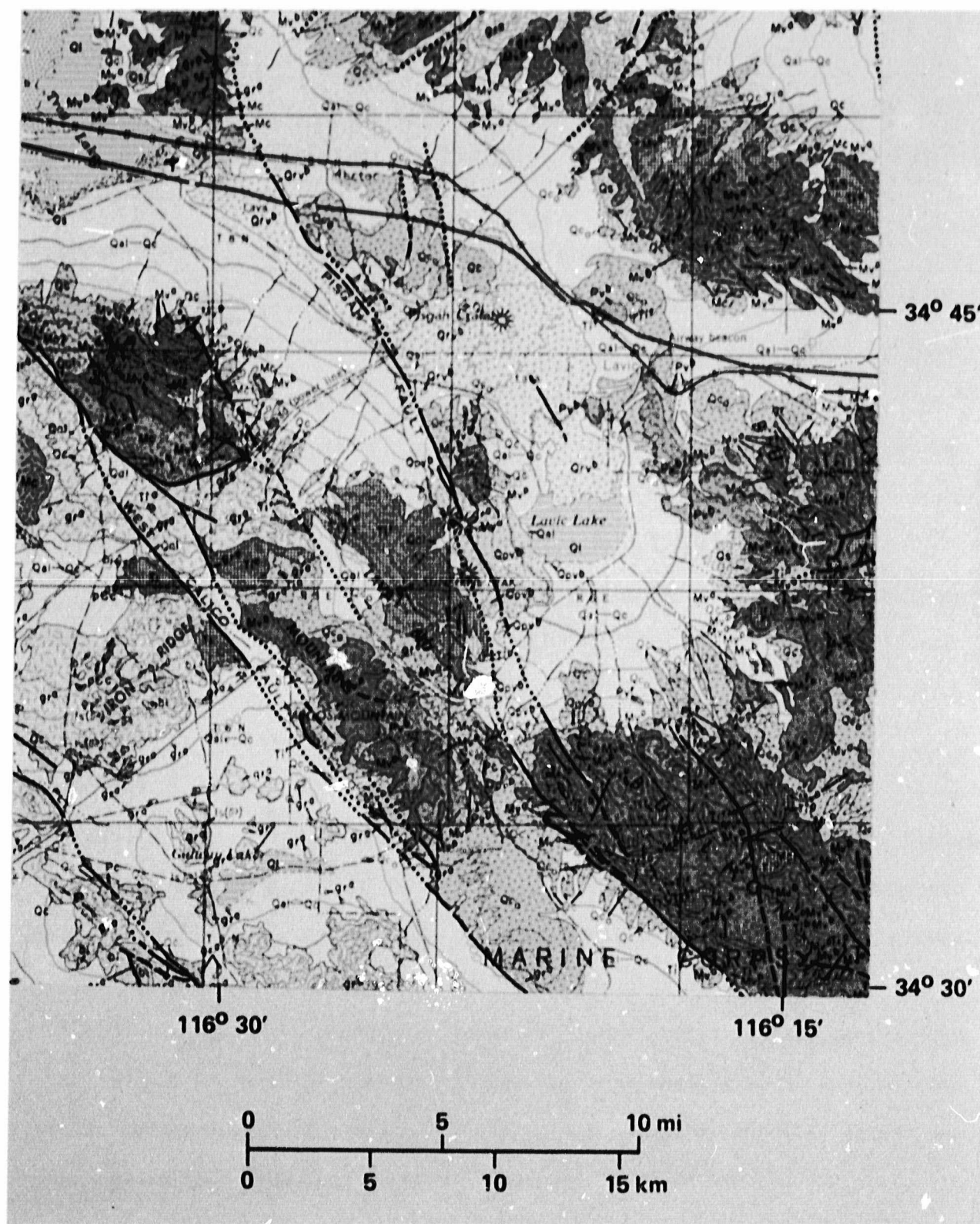


Figure 62. Geologic map of Pisgah, California area.

ORIGINAL PAGE  
BLACK AND WHITE PHOTOGRAPH

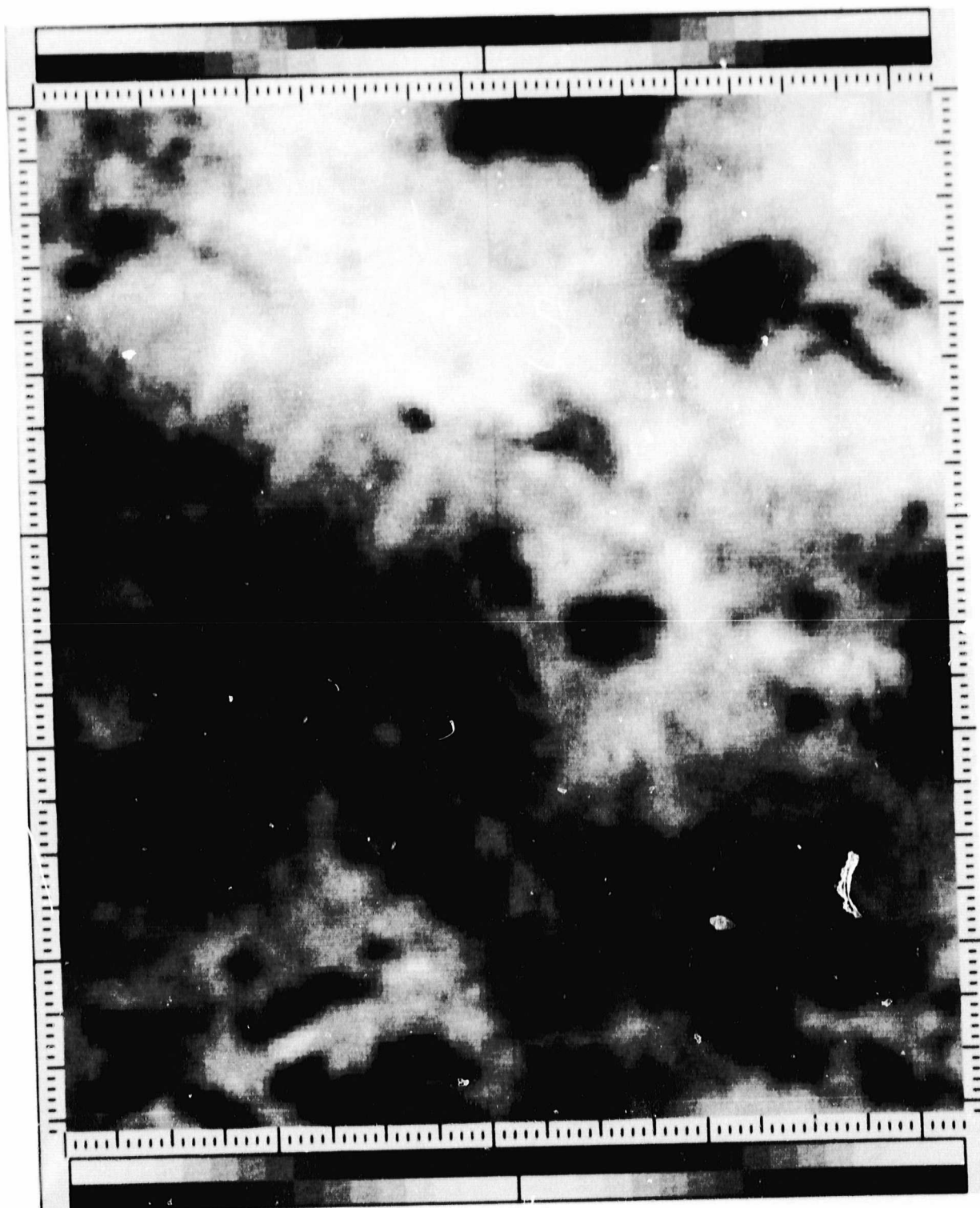


Figure 70. HCMM day IR image of Pisgah area. Image size is 35 x 40 km.

ORIGINAL PAGE  
BLACK AND WHITE PHOTOGRAPH

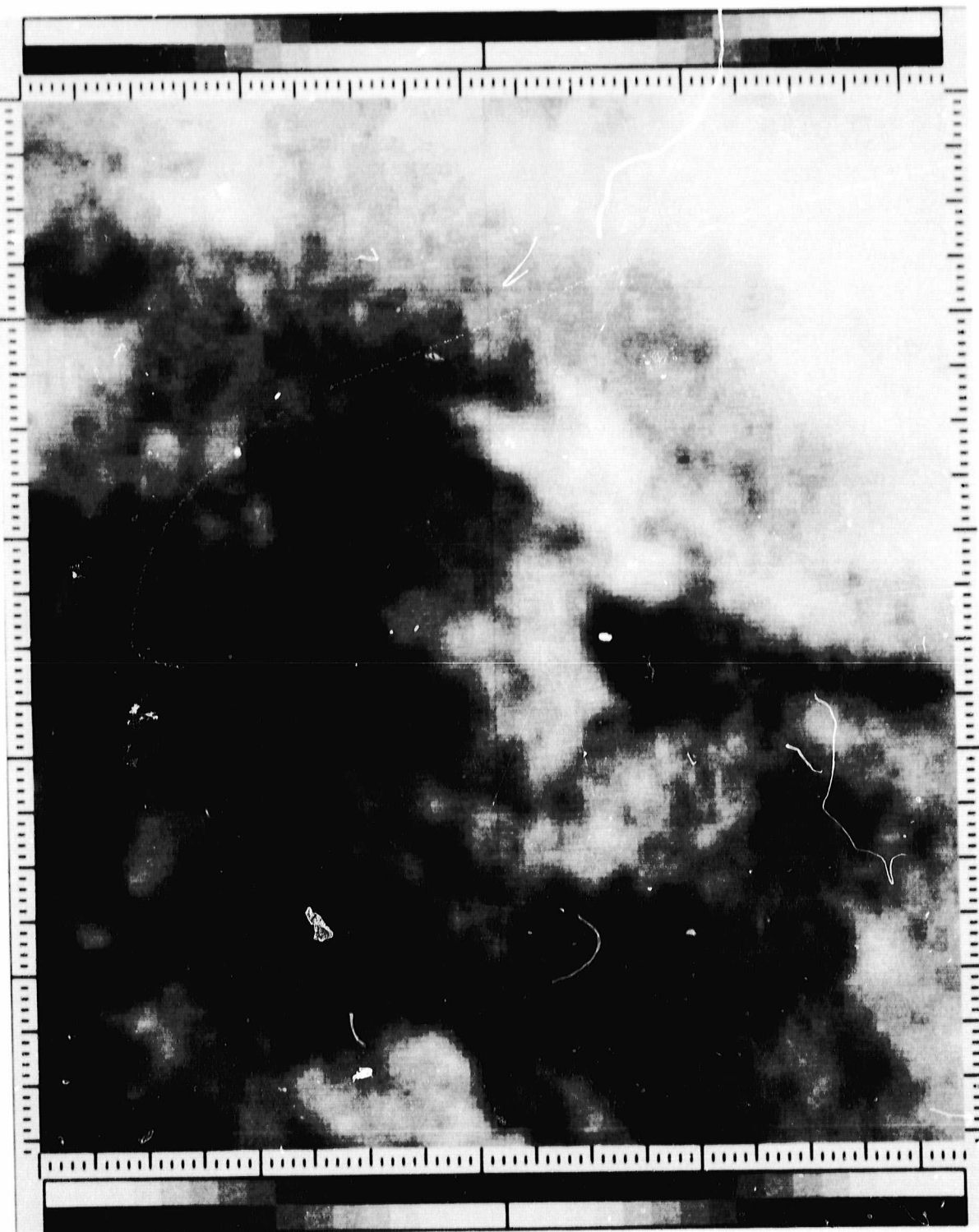


Figure 71. HCMM night IR image of Pisgah area. Image size is 35 x 40 km.

ORIGINAL PAGE  
~~BLACK AND WHITE PHOTOGRAPH~~

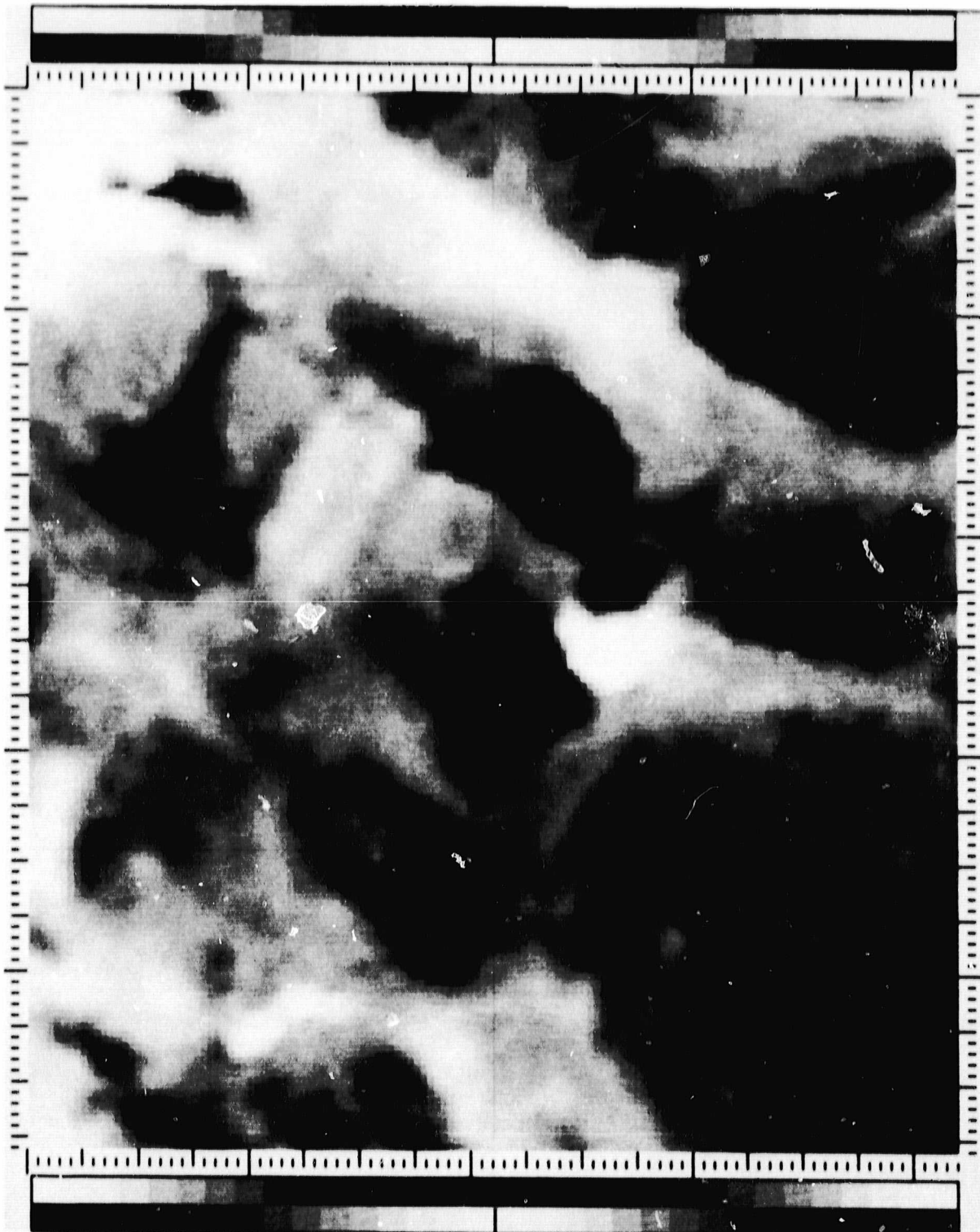


Figure 72. HCMM visible image of Pisgah area. Image size is 35 x 40 km.

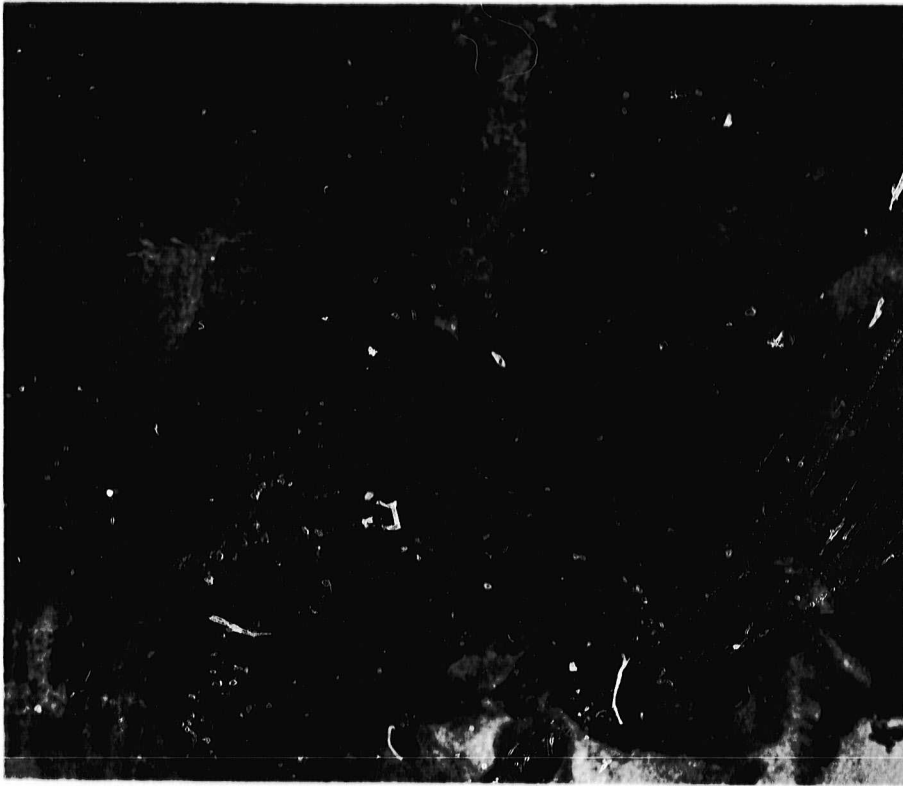
albedo appear as strongly colored in the image. For comparison, a Landsat scene of the same area was computer processed; of several enhancements produced, the best, a principal components transformed image (Blodget *et al.*, 1978), is shown in Figure 73 (right). Interpretation maps of each are presented in Figure 74.

The HCMM image presents a wide variety of different colors for bedrock areas, whereas most of these areas are similarly colored on the Landsat image. Many of the rocks are quite flat spectrally in the Landsat wavelength region, and so cannot be separated. These same rocks, however, appear to have different thermal properties, and so can be separated using HCMM data.

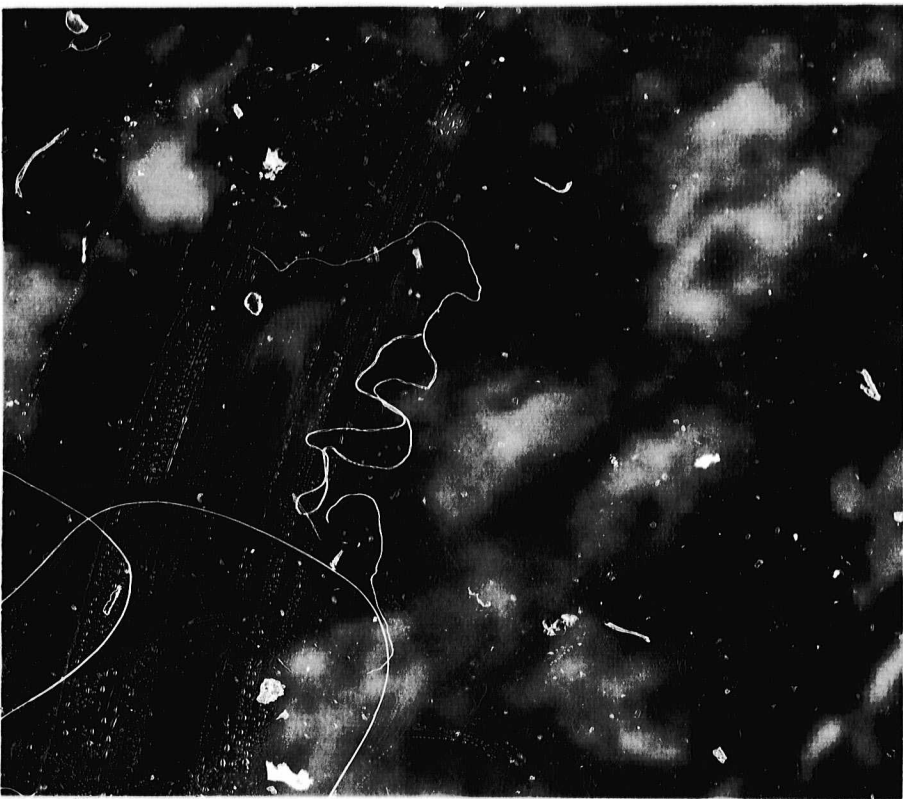
On the HCMM image, basalts are green. The aa flows at Pisgah and west of Pisgah are yellow, and easily separable. They are colder at night than the pahoehoe flows due to their lower thermal inertia. Granitic rocks are generally orange; the biotite quartz monzonites in the south are somewhat redder. The dacite west of Pisgah is the same orange color; compositionally this rock is similar to the granites. The sand dunes in the northwest corner are red (cold at night, warm in the day, high albedo) as is Lavic Lake playa. The other extrusive rocks are orange-yellow in color. The varied colors of the alluvial areas reflect the variation in their source rock composition.

On the Landsat image the bedrock areas are easily distinguishable from the alluvial areas. However, very few separations can be made between the various rock types. The major improvement over HCMM data is the higher spatial resolution which permits mapping of smaller features. Very little other information can be interpreted from the Landsat image.

LANDSAT



HCMM



ORIGINAL PAGE  
COLOR PHOTOGRAPH

PRINCIPAL COMPONENTS  
COMPOSITE  
DAY IR (BLUE) + NIGHT IR (RED)  
+ VISIBLE (GREEN). ALL COMPLEMENTED  
(IMAGE CENTER: 34°40'N, 116°25'W)  
0 10 20 km  
0 5 10 mi

Figure 73. HCMM and Landsat color composites of Pisgah area.

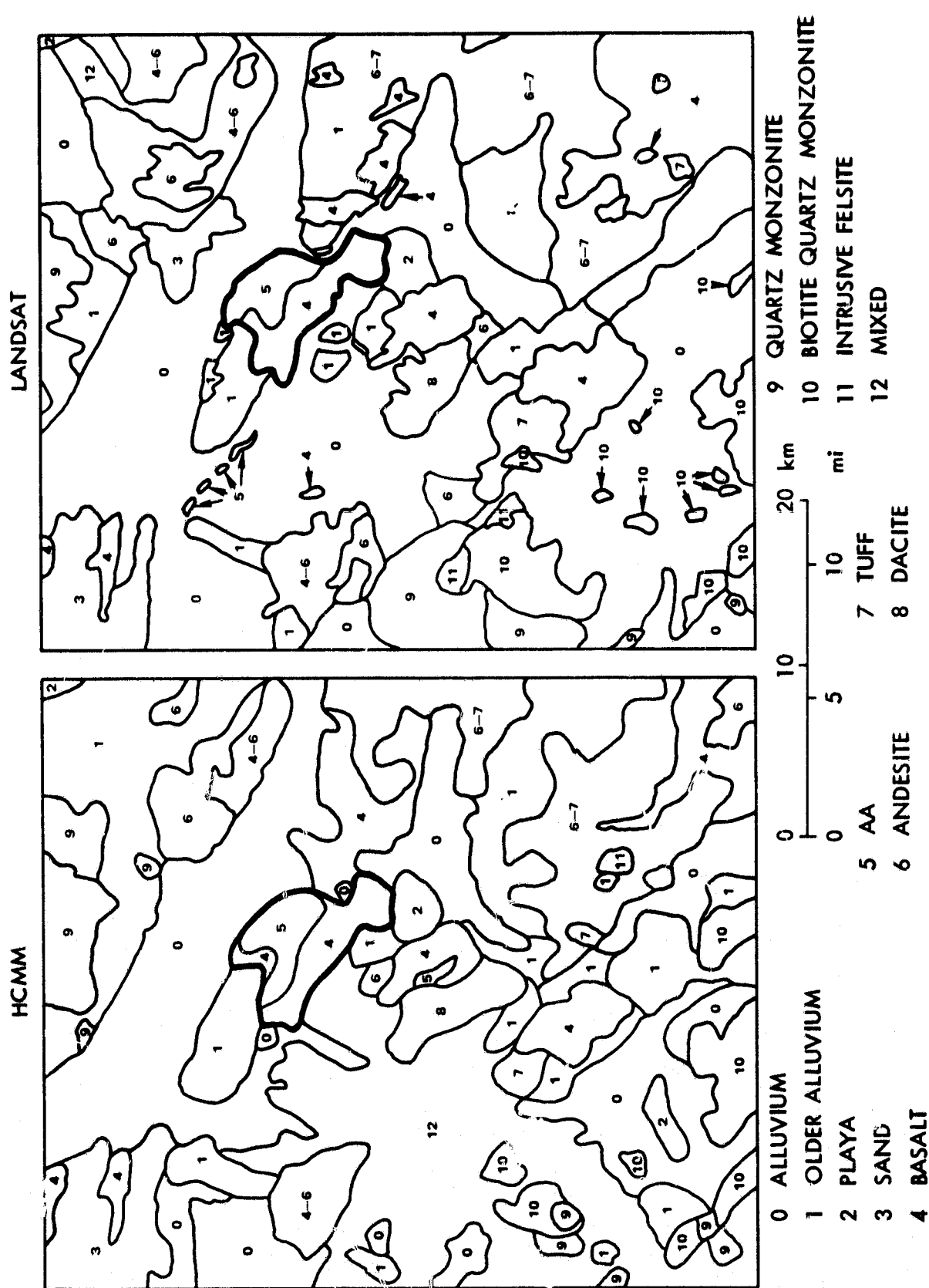


Figure 74. Interpretation map of Figure 73.

### 3. Aircraft Images

The greatly increased spatial resolution provided by aircraft scanners is shown in Figure 75, a thermal inertia image of the Pisgah flow and vicinity. An interpretation map produced from this image (Figure 76) and the description of the symbols (Table 20) are also presented.

TABLE 20

#### DESCRIPTION OF SYMBOLS FOR PISGAH AIRCRAFT INTERPRETATION

<u>Unit</u>	<u>Geologic Map Symbol</u>	<u>Material</u>
1	Qal, Qco	Alluvium
2	Qp	Playa
3	Qb, Tb	Basalt
3a		"Aa"
4	Ti	Rhyolite intrusive
5	Gr	Granite
6	Bm	Biotite quartz monzonite
7	Mvp	Pyroclastics
8	Mva, Mvb	Andesite, basalt

Some thermal inertia differences associated with different rock types are depicted by varying gray tones in the image. The area of aa flows (#3a) is clearly separable from the pahoehoe flows (#3). The low thermal inertia area of Lavic Lake playa in the south central part of the image is also readily apparent. A major characteristic of the terrain, discernible due to the higher resolution, is geomorphology and drainage texture. With the

ORIGINAL PAGE  
BLACK AND WHITE PHOTOGRAPH

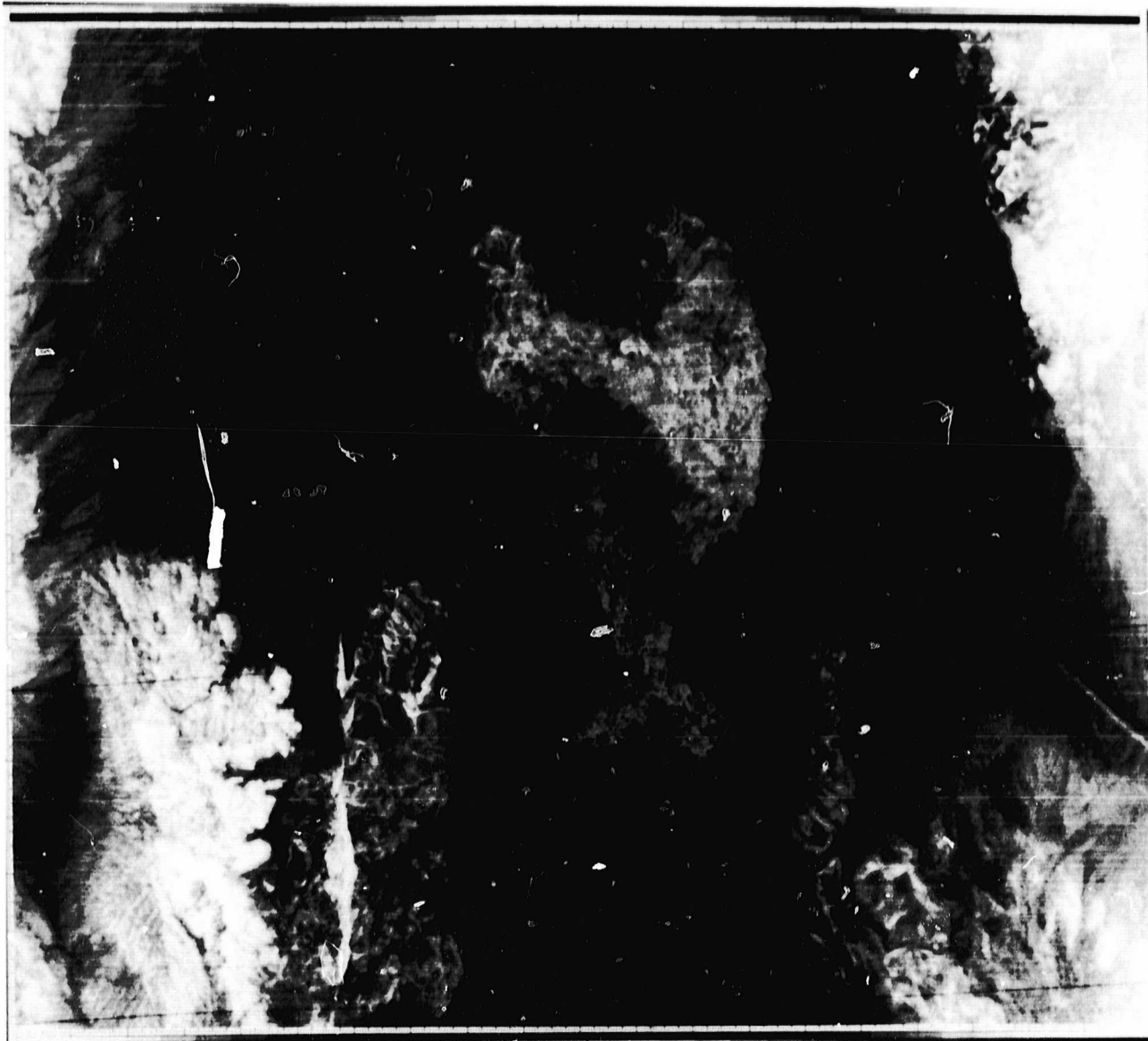


Figure 75. Thermal inertia image of Pisgah from aircraft data. Image size is 18 x 20 km.

ORIGINAL PAGE IS  
OF POOR QUALITY

AIRCRAFT THERMAL INERTIA (JULY 13, 1977)

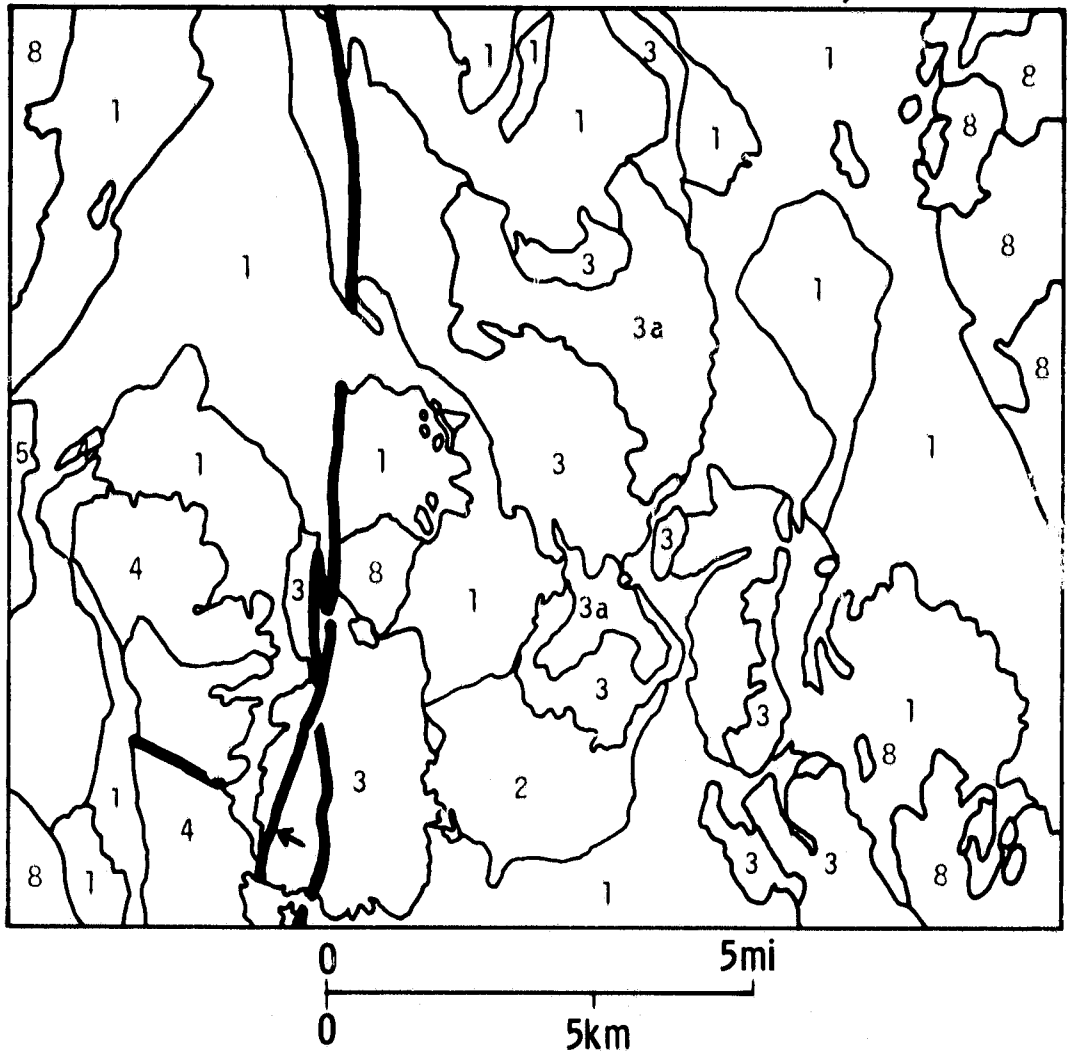


Figure 76. Interpretation map of Figure 7..

addition of this information, several units can be separated. The older fans, for example, have a dissected appearance due to high drainage density. The rhyolite intrusive (#4) appears distinctive due to linear features (dikes) cutting it. Flow features are visible on the Pisgah flows. Alluvial fans appear fairly homogeneous with parallel to braided drainage patterns. This type of information, vital to photointerpreters, is not available from HCMM data.

The north-northeast trending linear feature in the southwest part of the image (indicated by arrows) is interpreted to be a fault, and does not appear on the detailed geologic map of the area. It is easiest to distinguish this feature on the thermal inertia image. It seems to be expressed as a narrow valley or series of low areas covered with alluvium, which have a lower thermal inertia than the surrounding bedrock. Future field work will be necessary to determine the actual cause of this feature.

#### D. San Rafael

##### 1. Geologic Description

The San Rafael Swell is a large asymmetric anticline located in Emery County, Utah. (Figure 77). Rocks ranging in age from Pennsylvanian to Cretaceous are exposed. The Swell is a breached structural feature: the inner part is underlain mainly by Permian and Triassic age rocks; the outer part is formed mainly of Triassic and Jurassic age rocks; younger strata of Jurassic and Cretaceous age ring the structure (Hawley, et al., 1968).

The oldest rocks, of Pennsylvanian and Permian age, are exposed in deep canyons and consist of the Elephant Canyon formation and the Hermosa formation. Younger strata in the inner part are more widely exposed and consist of the Coconino Sandstone and Kaibab Limestone of Permian age, and the Moenkopi and Chinle formations of Triassic age. In the outer part of the

ORIGINAL PAGE IS  
OF POOR QUALITY

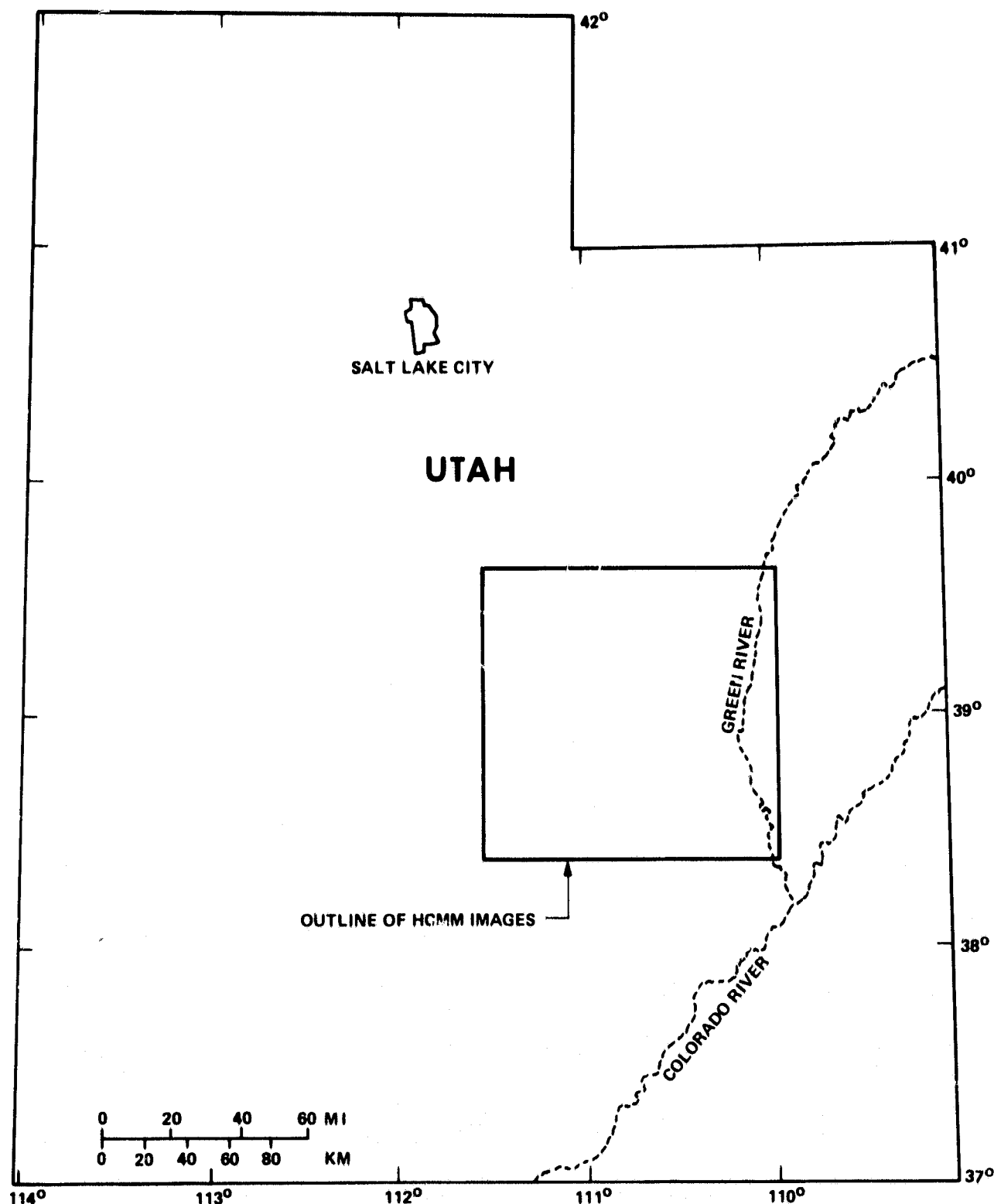


Figure 77. Location map of San Rafael Swell, Utah.

Swell are found exposures of the Wingate Sandstone, Kayenta formation, and Navajo formation of Triassic and Jurassic age. Ringing the Swell are exposures of the Carmel formation, the Entrada Sandstone, the Curtis formation, the Summerville formation, and the Morrison formation of Jurassic age, the Cedar Mountain formation, the Dakota Sandstone, and the Mancos Shale of Cretaceous age (Figure 78).

Vegetation throughout the San Rafael Swell is generally sparse, ranging from nearly 0% to 20% atop limestone and sandstone benches. At higher elevations, in mountains surrounding the Swell, substantial pinon-juniper forests are found with 80-100% vegetative cover.

## 2. HCMM Image

The HCMM day IR image for the San Rafael Swell is shown in Figure 79. An interpretive map derived from this image, and explanation are presented in Figures 80 and 81.

Overall, this image allows separation of only a few geologic units. The most consistently distinct unit is the Entrada Sandstone, a red, fine grained sandstone which weathers to produce sandy/silty flat-lying areas.

The Navajo/Kayenta/Wingate Sandstones are usually separable as a group. They are, in general, cliff-forming, massive, light-colored sandstones, distinct from the overlying Carmel Formation and underlying Chinle Formation.

Separation of most of the other units was difficult or impossible due to the limited spatial resolution of the HCMM data and the relatively narrow outcrop width of many of the geologic units.

The night IR HCMM image (Figure 82) provided some improvement for separating various units (Figure 83). The massive light sandstones appear warm in the image; the Entrada appears cold. Contrast between other, adjacent

**ORIGINAL PAGE IS  
OF POOR QUALITY**

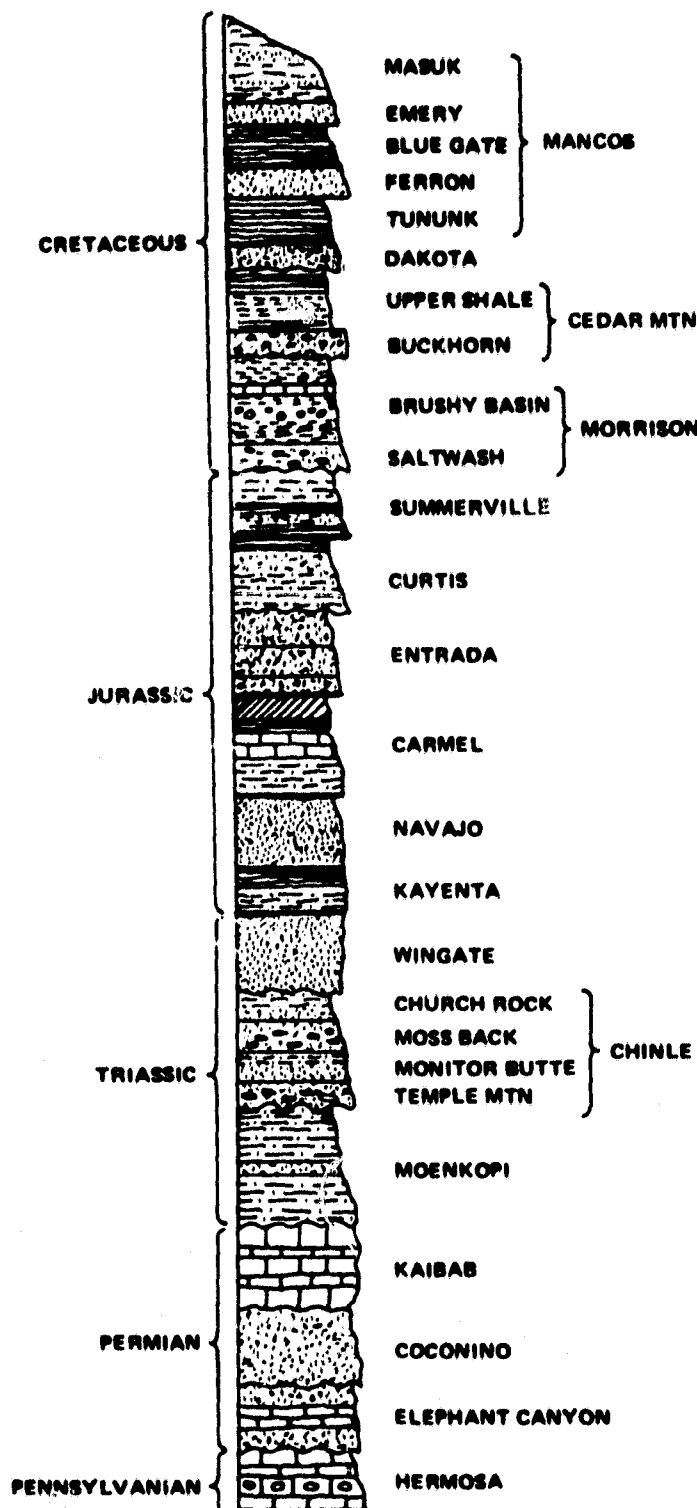


Figure 78. Stratigraphic column of rocks exposed in San Rafael Swell.

ORIGINAL PAGE  
BLACK AND WHITE PHOTOGRAPH

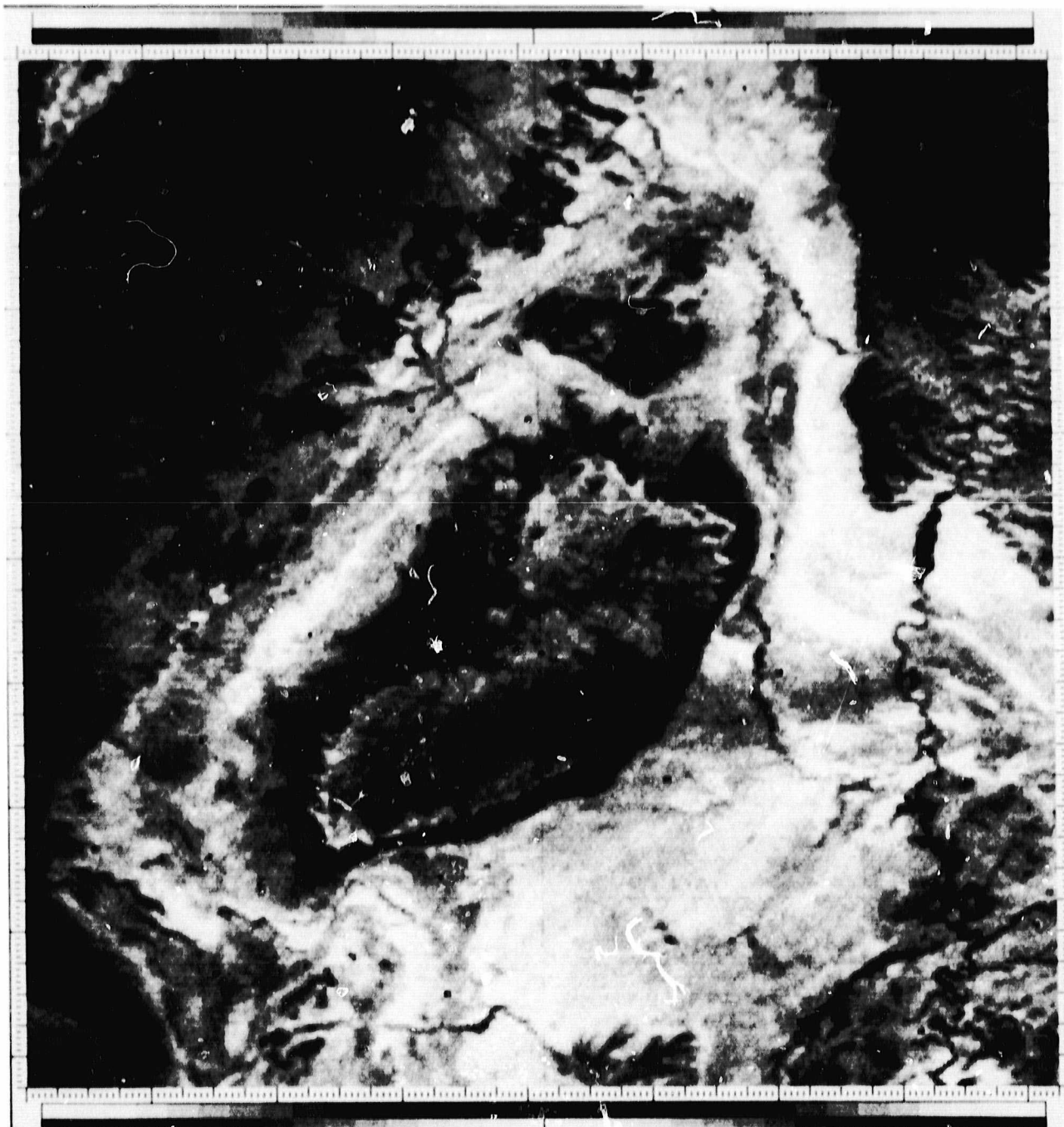


Figure 79. HCMM day IR image of San Rafael Swell. Image size is 140 x 140 km.

ORIGINAL PAGE IS  
OF POOR QUALITY

## SAN RAFAEL SWELL, UTAH

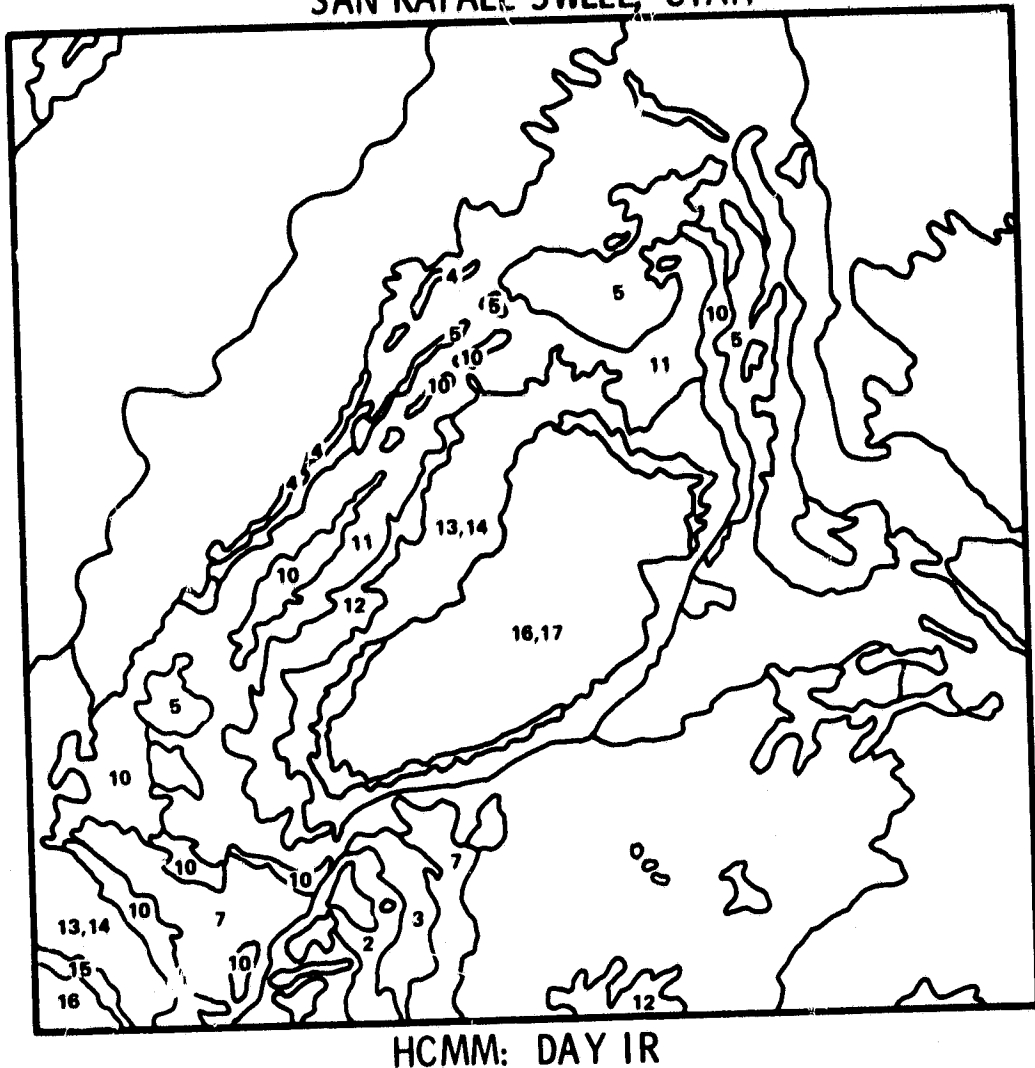


Figure 80. Interpretation map for Figure 79.

## LEGEND

Cretaceous	Tib	1	Basic Intrusive
	Kfe	2	Ferron Sandstone Member of Mancos Shale
	Kmt	3	Tununk Shale Member of Mancos Shale
	Kd	4	Dakota Sandstone
Jurassic	Kcm	5	Cedar Mountain Shale
	Jmbb	6	Brushy Basin Member of Morrison Formation
	Jmsw	7	Salt Wash Member of Morrison Formation
	Jsu	8	Summerville Formation
	Jcu	9	Curtis Formation
	Je	10	Entrada Sandstone
	Jca	11	Carmel Formation
	Jna	12	Navajo Sandstone
	JRK	13	Kayenta Sandstone
	Twi	14	Wingate Sandstone
Triassic	Tc	15	Chinle Formation
	Tm	16,16a	Moenkopi Formation (Red beds on top of bleached)
	DKa	17	Kaibab Limestone

SCALE 1 : 250,000

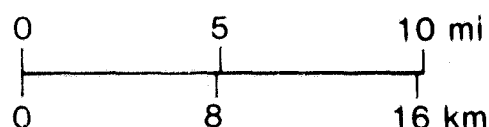


Figure 81. Legend and explanation for Figures 80, 83, 85, 87, 89.

ORIGINAL PAGE  
**BLACK AND WHITE PHOTOGRAPH**

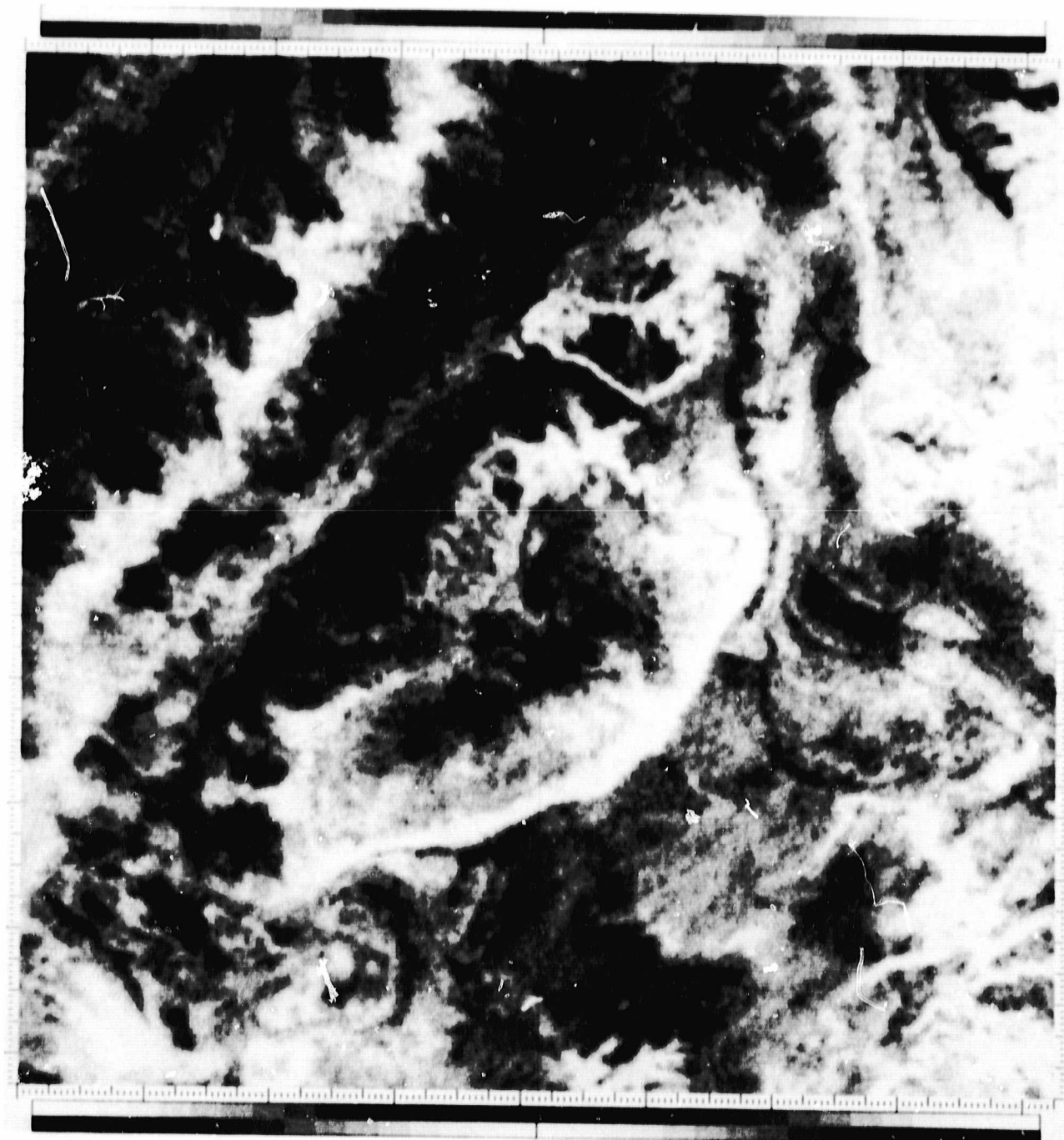


Figure 82. HCMM night IR image of San Rafael Swell.

ORIGINAL PAGE IS  
OF POOR QUALITY

## SAN RAFAEL SWELL, UTAH

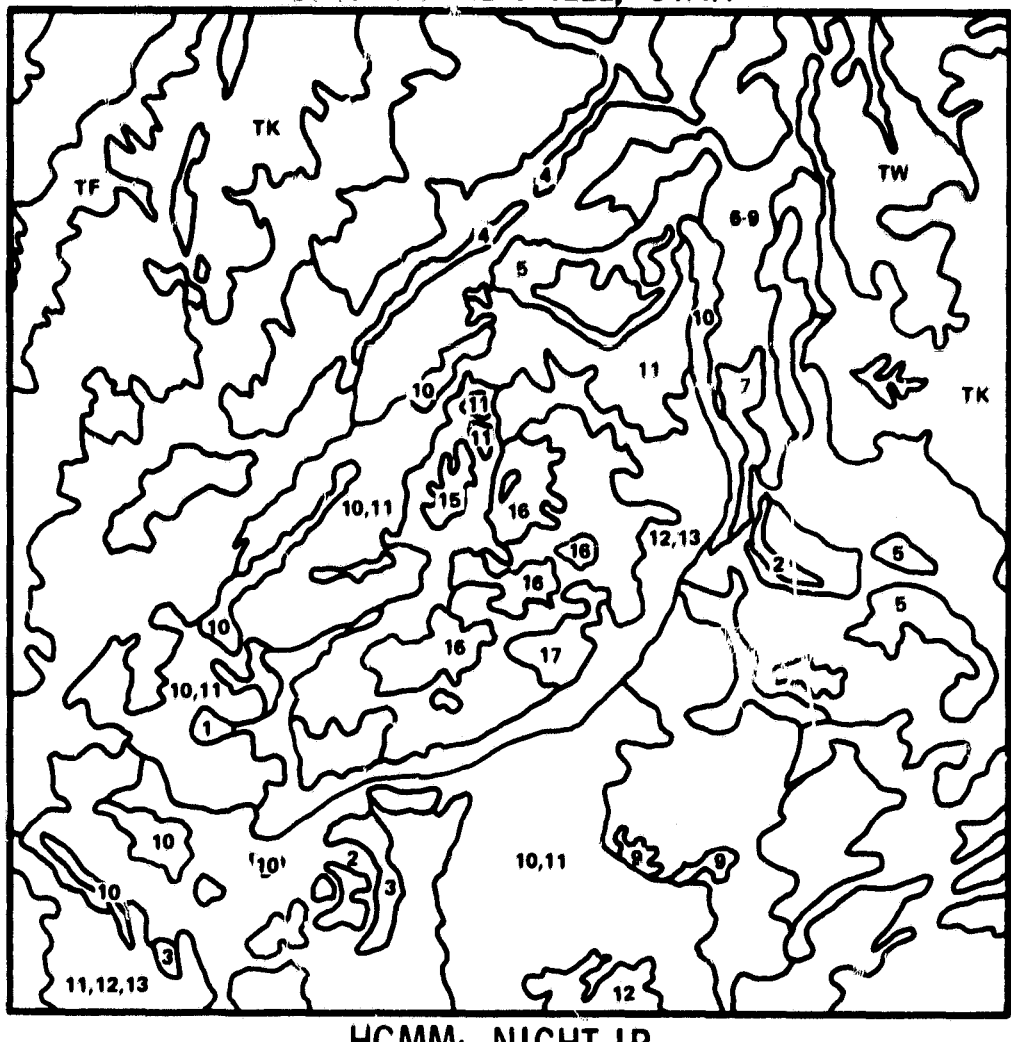


Figure 83. Interpretation map for Figure 82.

stratigraphic units allows them to be separated. In general, warmer areas are those underlain by massive, light sandstones (high thermal inertia), and dark, cold areas are underlain by silty material. The effect of elevation on temperature is indicated by the cold ridges in the northwest corner of the image.

The thermal inertia image (Figure 84) generally provided the same amount of information (Figure 85) as the day or night IR images. Bright areas (high thermal inertia) are underlain by the massive sandstones. In the northwest and northeast corners of the image, the high thermal inertia values are due mainly to high elevations (no corrections for elevation-dependent temperature variations were made) and cold nighttime temperatures. Low thermal inertia areas are underlain by unconsolidated material such as the sand dunes in the southeast part of the image, and the Entrada and Carmel Formation benches.

Comparison of the day and night IR data indicated that there was information on each not shown on the other. In order to combine the data, simple color additive composites were produced. The best one is shown in Figure 86. This composite has as its components day IR, night IR, and visible displayed in red, blue, and green respectively. All three components were complemented: areas that are either spectrally dark, or cold are displayed as brightly colored on the image.

Generally, more units could be separated using the color composite than any of the single images previously described (Figure 87). Along the west side of the Swell, the Tununk shale, Dakota Sandstone, and Cedar Mountain, Brushy Basin, Entrada, Carmel, Navajo and Chinle formations were separable. These units have appropriately large outcrop patterns, varying albedos, and varying thermal properties. The Entrada Sandstone, for

ORIGINAL PAGE  
BLACK AND WHITE PHOTOGRAPH

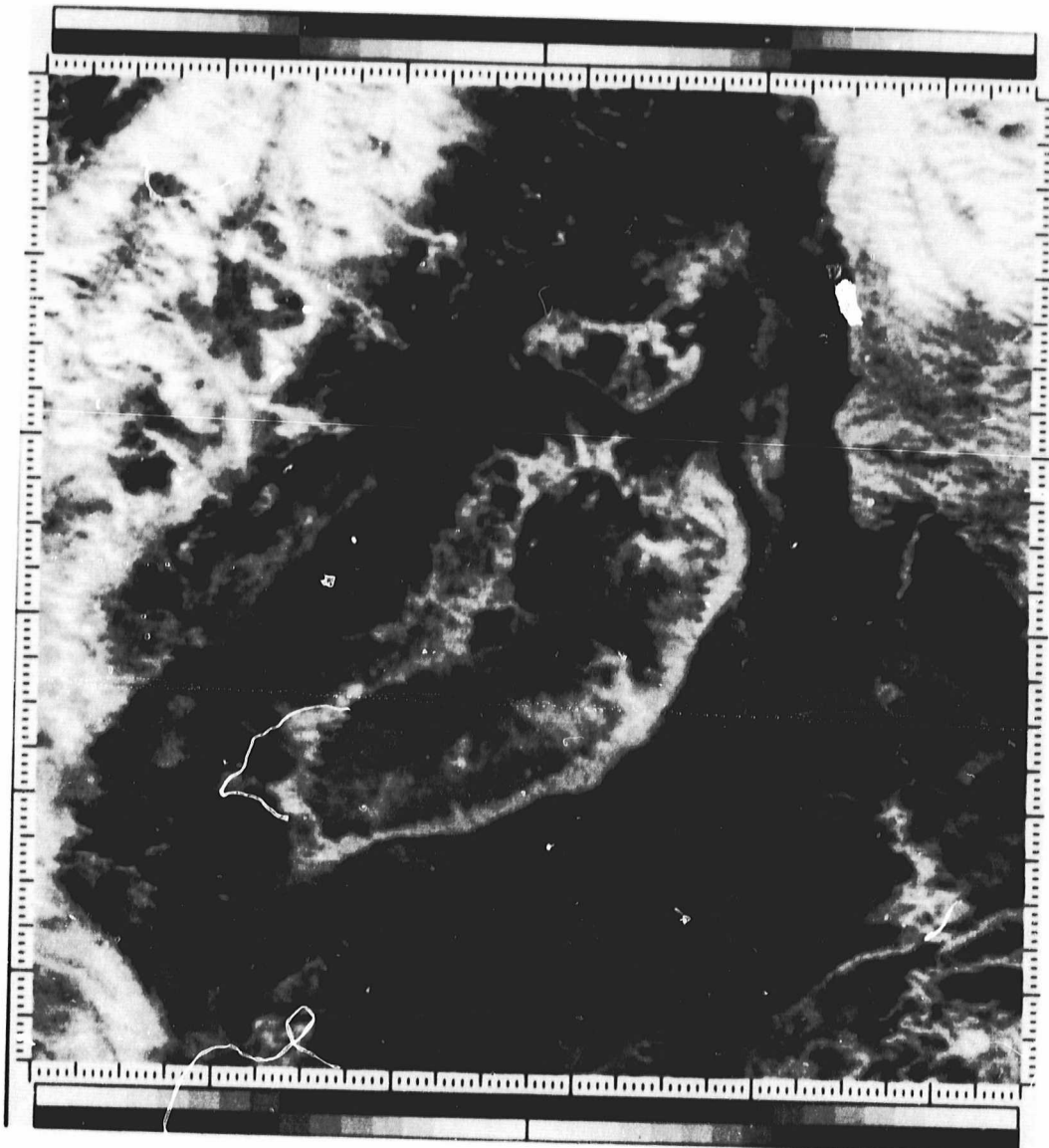


Figure 84. HCMM thermal inertia image of San Rafael Swell.

ORIGINAL PAGE IS  
OF POOR QUALITY

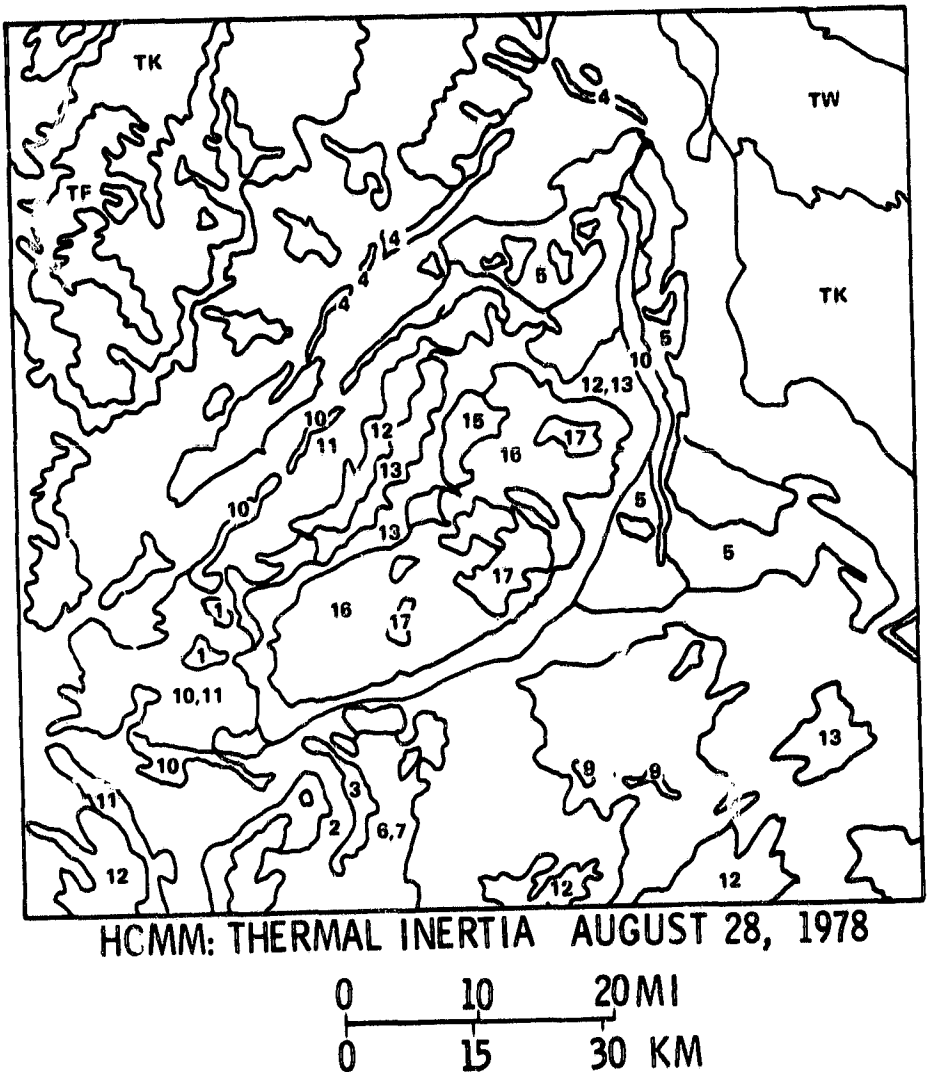


Figure 85. Interpretation map for Figure 84.

ORIGINAL PAGE  
COLOR PHOTOGRAPH

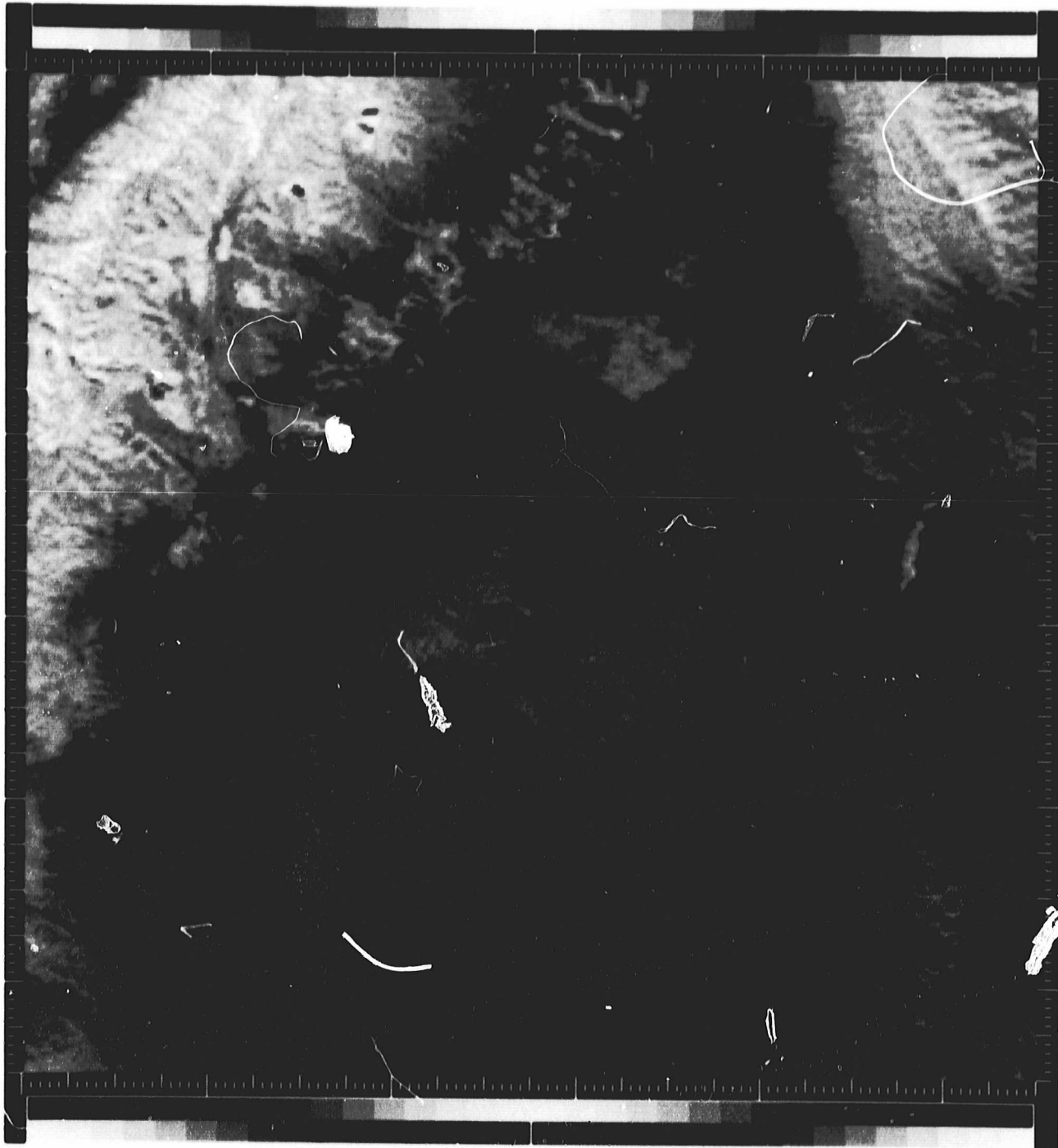
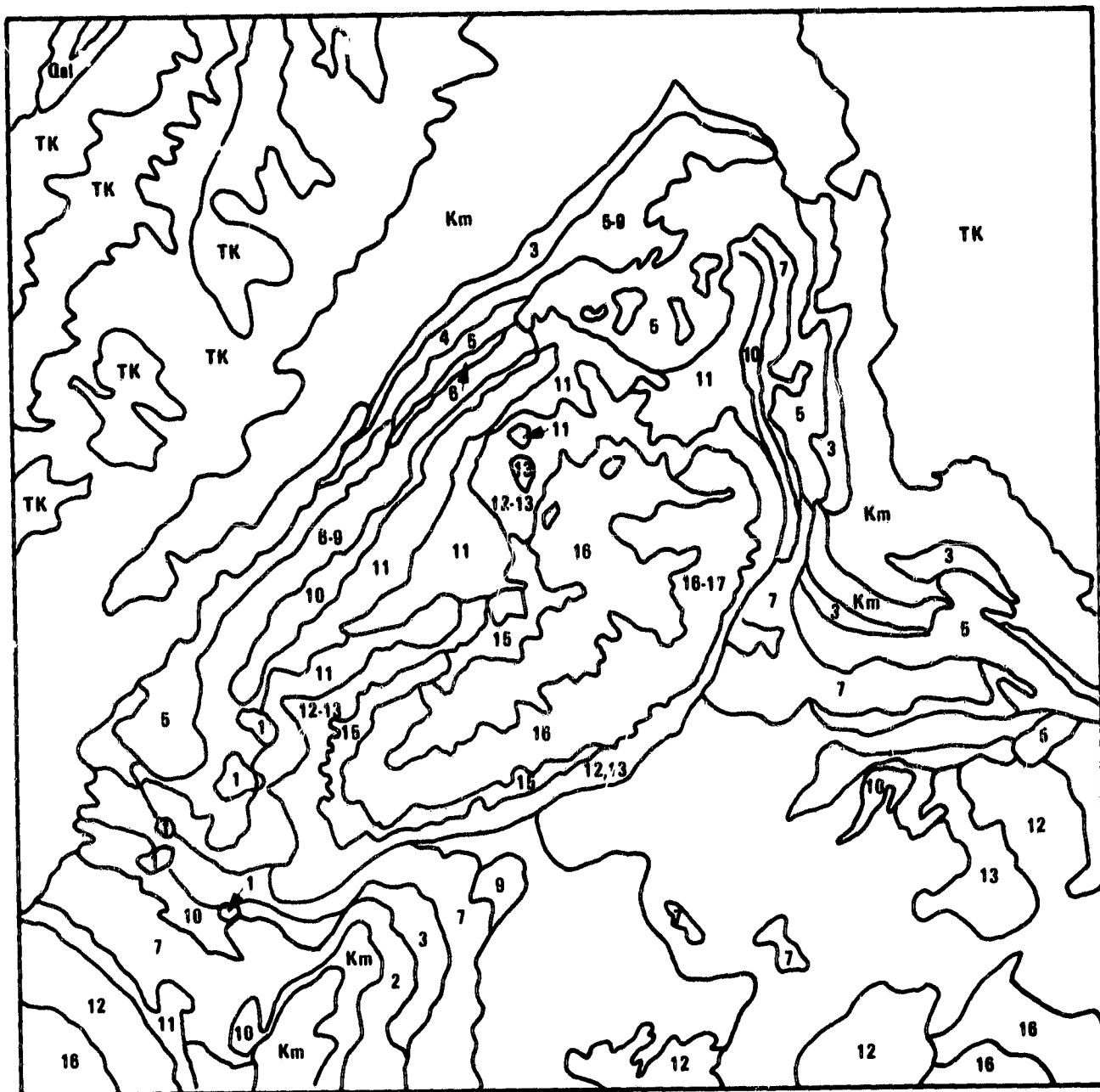


Figure 86. HCMM color composite of San Rafael Swell. Day IR, night IR, and visible images displayed as red, blue, and green, respectively. All three components were complemented.

ORIGINAL PAGE IS  
OF POOR QUALITY



## INTERPRETATION OF HCMM COLOR COMPOSITE

Figure 87. Interpretation map for Figure 86.

example, is dark blue, which indicates it has low albedo, is warm in the day, and relatively cold at night implying a low thermal inertia. The Navajo sandstone is orange on the image, which indicates it has high albedo, is cold in the day, and warm at night. This indicates a high thermal inertia. Similar conclusions can be made about the other units separable on the image. The appearance on the image of the units is consistent with what is known about their characteristics.

The color compositing technique presented here appears to be a simple but effective method of displaying the various HCMM data types acquired by the satellite. The use of color improves the analyst's ability to recognize differences between areas, and allows the simultaneous display of multivariate data.

For comparison purposes, a Landsat-Seasat composite scene covering the same area was obtained and interpreted (Figure 88). This image is a combination of coregistered Landsat and Seasat data. Processing consisted of performing a principal components transformation of the Landsat bands, then using the Seasat radar data to modulate the intensity of each of the three components for the color composite. In this manner the higher resolution of the Seasat data is merged with the Landsat spectral data, with some contribution from Seasat backscatter response folded into the color picture as intensity (brightness). This product was found to be the most effective combination of several examined.

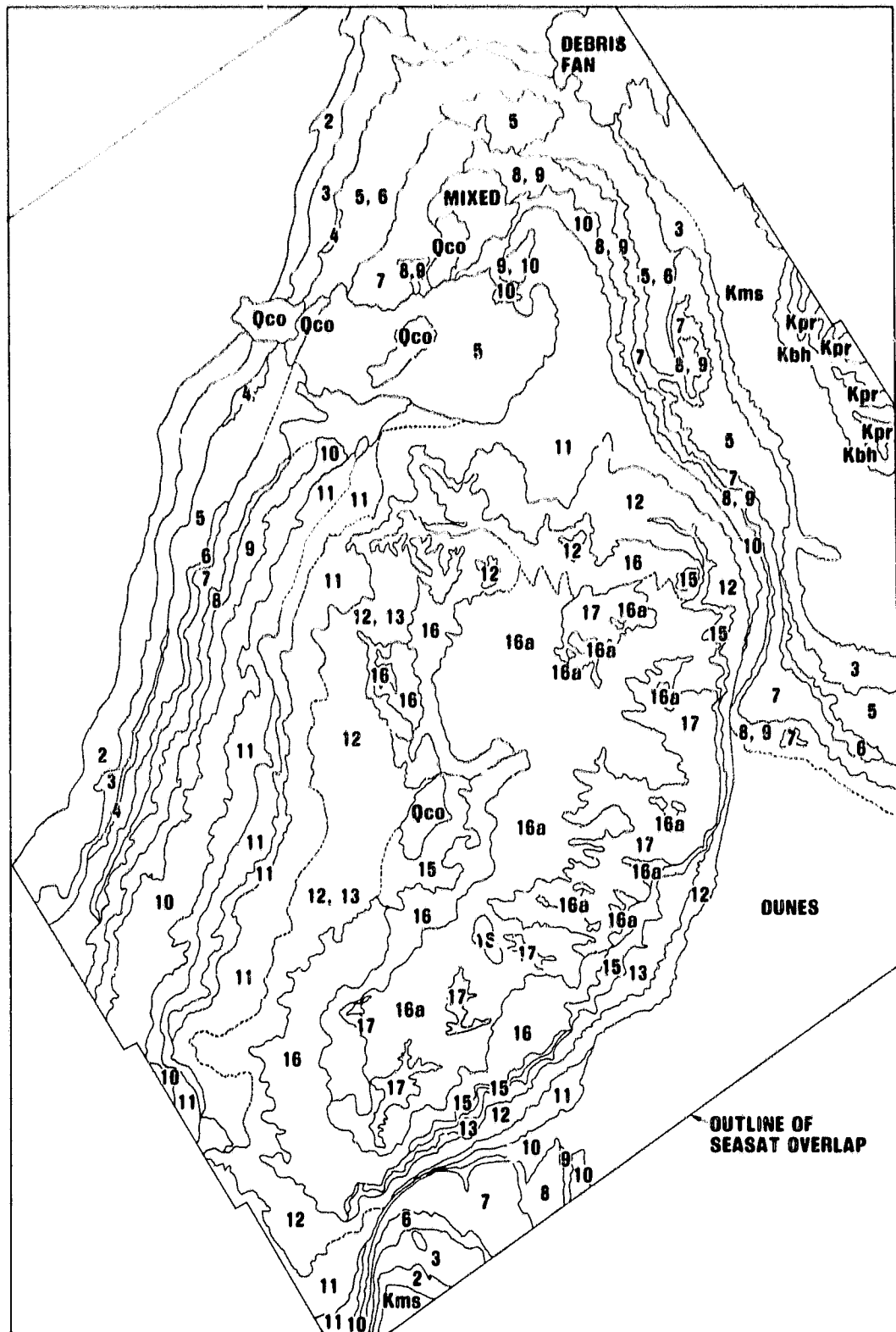
The interpretation map (Figure 89) shows that significantly more lithologic separations can be made using Landsat/Seasat data compared to HCMM data. This is due both to the improved spatial resolution, and to spectral bands of Landsat and the Seasat backscatter response. Contrary to the results from some of the other test sites, no additional information was

ORIGINAL PAGE  
COLOR PHOTOGRAPH



Figure 88. Landsat/Seasat composite of San Rafael Swell, Utah.

ORIGINAL PAGE IS  
OF POOR QUALITY



obtained from the HCMM data that was not already available in the Landsat/Seasat data.

The spectral characteristics of the sedimentary rocks exposed in the San Rafael Swell are sufficiently distinctive to allow their separation in the Landsat wavelength region. In addition, textural information interpretable from the images, also contributes to the separability of the units. However, this critical characteristic cannot be extracted or inferred from the HCMM data due to the poorer spatial resolution.

## VII. SUMMARY AND CONCLUSIONS

Our attempts to determine quantitatively accurate thermal inertia values from HCMM digital data have met with only partial success owing to a variety of factors. Calculations of the atmospheric radiative transfer effects showed that the radiance measured at the satellite was equivalent to a surface temperature of from +3 to -11°C different from the actual ground temperature. These effects were strongly dependent on water vapor content of the atmosphere, surface elevation and surface temperature. These effects could easily produce an error in  $\Delta T$  of 6°C, and perturbation studies with our thermal model showed that even a 1°C error in  $\Delta T$  could cause an error in thermal inertia of  $0.01 \text{ cal cm}^{-2}\text{s}^{-1/2}\text{C}^{-1}$ . Because of the delay in receipt of HCMM data and the continued confusion over the calibration of the HCMM sensor, we were forced to leave incorporation of these important atmospheric effects to a future study. The effects of atmospheric transmission and radiance, instrument calibration, and varying elevations are tractable in future missions and some success should still be attainable upon further work with HCMM data. However, a solution to the problem of varying meteorology across a scene (as it affects the surface heat balance, not as required for atmospheric radiance corrections) may prove to be prohibitively costly and time consuming.

As an adjunct to the satellite and aircraft studies, we built and tested a thermal inertia meter (TIM) in order to obtain in situ thermal inertia values of rock and soil types. The results of laboratory tests indicated that precise thermal inertia values were not possible to achieve principally because of the difficulty in providing a constant heat flux at the surface of the standard and target materials. Nonetheless, field tests in Nevada and California desert regions showed that the TIM was useful in a relative sense.

As long as wind speeds were low, to minimize convective heat loss, TIM measurements were accurate enough to be used to discriminate many different types of geologic materials from one another, e.g. chert and barite.

Spatial and temporal soil moisture effects are evident in the thermal inertia images constructed from both the aircraft and HCMM data. Parts of Death Valley's floor are subject to seasonal flooding and the lower half of the Valley, around Badwater Basin, is nearly always saturated. On the thermal inertia image, these moist areas are bright corresponding to regions of relatively high thermal inertia values. Similar patterns are evident on the dry lakes in the Walker Lane area of Nevada, and some evidence of seasonal change can be seen when comparing images at different times of the year. The details of seasonal moisture changes are important for future studies but have not been treated here in any depth. This requires additional field work and the use of the soil moisture version of the JPL thermal model. This model has not been used to analyze the HCMM data for this study, but it is available now for a future effort.

An important positive result that has come out of this study is the recognition that in most instances apparent thermal inertia is an excellent qualitative representation of true thermal inertia. For many applications this will considerably reduce data processing requirements, with only minimal loss of information. Apparent thermal inertia should prove to be completely adequate for those geological applications where the desire is to use the data as part of a photo-geologic interpretation problem such as to discriminate between units or to examine structural or textural relationships. Little loss of information should be noticeable when using apparent thermal inertia in combination with other data sets, such as Landsat data, in multivariate

analysis algorithms, as long as the analysis is confined to small, local studies.

The spatial resolution of HCMM is considerably less than desirable for the type of geologic investigations which we have undertaken. Nevertheless, considerable success has been achieved in demonstrating the utility of day-night thermal data for geologic applications. For the four sites examined, only limited geological information was interpretable directly from images of individual HCMM data types; i.e., day visible, day IR, night IR, or thermal inertia. Various display enhancement techniques were applied to these data to try to increase the information displayed, with little success. A method of combining HCMM data types to create color composites was developed which: a) was computationally simple; b) allowed simultaneous display of several variables; c) effectively displayed the interrelationship of the HCMM variables; d) provided a useful, interpretable product displaying significantly more lithologic information.

At the Walker Lane site, the color composite of HCMM data provided some lithologic separations. Playas and alluvial areas were generally distinguishable; the alteration zones at Goldfield and Cuprite had similar appearances to the playas; basalts and other volcanic rocks were mappable, though there was a significant proportion of the scene where these rocks were not separable; large areas were found where no useful lithologic distinctions could be made. The high resolution aircraft data allowed identification of the silicified altered rocks at both Goldfield and Cuprite due to their high thermal inertia. A combination of the thermal inertia data with visible and near infrared multispectral data was produced for Cuprite. The thermal inertia data improved the separation of sub-units of unaltered, spectrally dark and flat

volcanic rocks. No other additional information was discernible due to the addition of thermal data.

At Death Valley, HCMM thermal inertia images allowed delineation of areas underlain by dolomite, limestone, quartzite, and granite (all high thermal inertia materials). The boundary between bedrock and alluvium was clearly discernible and easier to recognize than from Landsat images. Examination of color composites of HCMM data allowed separation of various lithologies and alluvial units. Playas, salt pans, sand, sediments, and volcanic rocks were, in places, separable.

At the Pisgah site, the individual HCMM data types provided limited separation of lithologic units. The color composite produced using these data types provided a significant amount of information. The basalt flows of Pisgah could be separated into aa and pahoehoe units; other basalts were distinctive in color; granitic rocks and mineralogically similar volcanic rocks were separable, and had similar appearance on the images; boundaries of various types of alluvium were distinct. A comparison with a computer processed Landsat scene indicated that despite the higher spatial resolution of Landsat data, HCMM data provided more lithological information. This is thought to be due to the featureless spectral properties of the materials in the Landsat wavelength region versus the variable thermal properties in the HCMM wavelength region. Examination of high resolution aircraft thermal data revealed the presence of a previously unrecognized linear feature, interpreted to be a fault. It was most easily discernible on the thermal inertia image.

Finally, at San Rafael Swell a comparison of HCMM data (both individual bands and color composites) with a Landsat/Seasat composite indicated that no additional lithologic information was provided by the HCMM data. The spectral

characteristics of the units and the improved spatial resolution of Landsat and Seasat allowed discrimination of almost all of the mapped geologic units.

First attempts at digitally combining HCMM data with Landsat multispectral data at the various sites show promise for improved rock discrimination. In a future study we intend to continue to evaluate the improvement in geologic remote sensing made possible by this extended multivariate data set.

## VIII. ACKNOWLEDGEMENTS

The authors would like to thank the many people who have helped in one or more phases of this project. All are affiliated with JPL unless noted otherwise. Alexander Goetz originally suggested that we undertake this project and has reviewed this report. Lawrence Rowan of the USGS Reston helped to define the geological problems to be investigated. Alan Gillespie formulated the original thermal inertia computer algorithms, and subsequently helped with the digital topography. Richard Machida and Warren Rachwitz helped design, build, maintain and operate much of the field equipment. Stuart Marsh was responsible for the concept and design of the Thermal Inertia Meter. James Soha was responsible for continuity of computer activites, while Elsa Abbott made the atmospheric calculations. Peter Sanchez of the National Park Service assisted with data acquisition in the Death Valley National Monument. The aircraft managers and personnel from both Ames and Johnson Space Center worked diligently to get as many as possible of the requested aircraft flights and data sets. Helen Paley was responsible for data coordination, quarterly reports, and the careful editing and collation of this manuscript. Numerous other JPL employees have helped at one time or another with field work and data reduction.

The research described in this report was carried out by the Jet Propulsion Laboratory, California Institute of Technology, under contract with the National Aeronautics and Space Administration.

## IX. REFERENCES

Abrams, M. J., R. P. Ashley, L. C. Rowan, A. F. H. Goetz, and A. B. Kahle, Mapping of hydrothermal alteration in the Cuprite Mining District, Nevada, using aircraft scanner imagery for the 0.46 - 2.36  $\mu$ m spectral region, Geology, Vol 5, No. 12, p. 713-718, December 1977.

Albers, J. P. and J. H. Stewart, Geology and mineral deposits of Esmerelda County, Nevada, Nevada Bureau of Mines and Geology, Bulletin 78, 80 pp, 1972.

Anding, D., R. Kauth and R. Turner, Atmospheric effects on infrared multi-spectral sensing of sea-surface temperature from space, Rpt. No. NASA CR-1858, Univ. of Michigan, Ann Arbor, Mich., 1971.

Ashley, R. P. and W. J. Keith, Distribution of gold and other metals in silicified rocks of the Goldfield Mining District, Nevada, U.S. Geological Survey Professional Paper 843-B, 21 pp, 1976.

Bhumralkar, C. M., Parameterization of the planetary boundary layer in atmospheric general circulation models, Reviews of Geophysics and Space Physics, Vol. 14, No. 2, 215-226, 1976.

Blodget, H. W., F. J. Gunther, and M. H. Podwysocki, Discrimination of rock classes and alteration products in southwestern Saudi Arabia with computer-enhanced Landsat data, NASA Technical Paper 1327, Scientific and Technical Information Office, 40 pp, 1978.

Blom, R. G., M. J. Abrams and C. Conrad, Rock type discrimination using Landsat and Seasat image data, IEEE Geoscience and Remote Sensing Soc. Mtg., Wash. D.C., June 8-10, 1981.

Bohse, J. R., M. Bewtra, and W. L. Barnes, Heat Capacity Mapping Radiometer (HCMR), data processing, algorithm, calibration, and flight performance evaluation, NASA Technical Memorandum 80258, Goddard Space Flight Center, Greenbelt, Maryland, April 1979.

Brennan, P. A., Thermal diffusivity: An important parameter in geologic thermal imagery evaluation, NASA Earth Resources Program Technical Letter 17, 23 pp, 1971.

Buettner, K. J. K. and C. D. Kern, The determination of infrared emissivities of terrestrial surfaces, Journal of Geophysical Research, Vol. 70, No. 6, 1329-1337, 1965.

Burke, C. J., Transformation of polar continental air to polar maritime air, Journal of Meteorology, Vol. 2, 94-112, 1945.

Businger, J. A., J. C. Wyngaard, Y. Izumi, and E. F. Bradley, Flux-profile relationships in the atmospheric surface layer, Journal of the Atmospheric Sciences, Vol. 28, 181-189, 1971.

Carslaw, H. S. and J. C. Jaeger, Conduction of Heat in Solids, Oxford Press, London, 1959.

Chandrasekhar, S., Radiative Transfer, Dover, New York, 1960.

Clapp, R. B. and G. M. Hornberger, Empirical equations for some soil hydraulic properties, Water Resources Research, Vol. 14, 601-604, 1978.

Clark, S. P., ed., Handbook of Physical Constants, Geological Society of America Memoir 97, New York, 459-483, 1966.

Deardorff, J. W., A parameterization of ground-surface moisture content for use in atmospheric prediction models, Journal of Applied Meteorology, Vol. 16, 1182-1185, 1978.

Gates, W. L., E. S. Batten, A. B. Kahle, and A. B. Nelson, A documentation of the Mintz-Arakawa two-level atmospheric general circulation model, Rep. R-877-ARPA, Rand Corp., Santa Monica, Calif., 1971.

Gillespie, A. R. and A. B. Kahle, The construction and interpretation of a digital thermal inertia image, Photogrammetric Engineering and Remote Sensing, Vol. 43, No. 8, 983-1000, August 1977.

Goddard Space Flight Center, Heat Capacity Mapping Mission (HCMM) data users handbook for Applications Explorer Mission-A (AEM), NASA Goddard Space Flight Center, Greenbelt, Maryland, December, 1978.

Goetz, A. F. H., F. C. Billingsley, A. R. Gillespie, M. J. Abrams, R. L. Squires, E. M. Shoemaker, I. Lucchitta, and D. P. Elston, Application of ERTS image processing to regional geologic problems and geologic mapping in northern Arizona, Jet Propulsion Laboratory, Technical Report 32-1597, Pasadena, Calif., 1975.

Goetz, A. F. H. and L. C. Rowan, Geologic remote sensing, Science, Vol. 211, pp 781-791, February 20, 1981.

Hampton, W. M., Approximate expression for loss of heat from exposed surfaces, Nature, Vol. 157, p. 481, 1946.

Hawley, C. C., R. C. Robeck, and H. C. Dryer, Geology, altered rocks, and ore deposits of the San Rafael Swell, Emery County, Utah, U.S. Geological Survey Bulletin 1239, 155 pp, 1968.

Hunt, C. B. and D. R. Mabey, Stratigraphy and structure Death Valley, California, U.S. Geological Survey Professional Paper 494-A, 1966.

Janzen, F. J., Interaction mechanisms, Chapter 4, in Manual of Remote Sensing, R. G. Reeves, ed. American Society of Photogrammetry, Falls Church, VA, p. 83, 1975.

Kahle, A. B., A simple thermal model of the Earth's surface for geologic mapping by remote sensing, Journal of Geophysical Research, Vol. 82, No. 11, 1673-1680, 1977.

Kahle, A. B., Surface thermal properties, in Remote Sensing in Geology, B. S. Siegal and A. R. Gillespie, ed., John Wiley and Sons, New York, 257-276, 1980.

Kahle, A. B., A. R. Gillespie and A. F. H. Goetz, Thermal inertia imaging: A new geologic mapping tool, Geophys. Res. Let., 3, 26-28, 1976.

Kahle, A. B. and L. C. Rowan, Evaluation of multispectral middle infrared aircraft images for lithologic mapping in the East Tintic Mountains, Utah, Geology, 8, May, 1980.

Kahle, A. B., J. Schieldge, and H. N. Paley, JPL field measurements at the Finney County, Kansas, test site, October 1976: meteorological variables, surface reflectivity, surface and subsurface temperatures, JPL Publication 80-57, 1977.

Kneizys, F. X., E. P. Shettle, W. O. Gallery, J. H. Chetwynd, Jr., L. W. Abreu, J. E. A. Selby, R. W. Fenn and R. A. McClatchey, Atmospheric transmittance/radiance: Computer code LOWTRAN 5, Rpt. #AFGL-TR-80-0067 Air Force Geophysical Laboratory, Hanscom AFB, MA, 1980.

Miyake, M., M. Donelan, G. McBean, C. Paulson, F. Badgley, and E. Leavitt, Quarterly Journal of the Royal Meteorological Society, Vol. 96, 132-137, 1970.

Morgan, D. L., W. O. Pruitt, and F. J. Lawrence, Analyses of Energy, Momentum, and Mass Transfers Above Vegetative Surfaces, Research and Developmental Technical Report ECOM 68-G10-F, 1971.

Morin, A. S. and A. M. Yaglom, Statistical Fluid Mechanics, Vol. I, The MIT Press, Cambridge, Mass., 769 pp., 1971.

Murphy, C. J. III, W. L. Barnes, and D. Escoe, The Heat Capacity Mapping Experiment Part I, Equipment and Data Calibration, NASA X-940-77-212, Goddard Space Flight Center, Greenbelt, Maryland, January 1978.

Njoku, E. G., J. P. Schieldge, and A. B. Kahle, Joint Microwave and Infrared Studies for Soil Moisture Determination, JPL Publication 80-57, 112 pp, 1980.

Price, J. C., Thermal inertia mapping: A new view of the Earth, Journal of Geophysical Research, Vol. 82, No. 18, 2582-2590, 1977.

Quiel, F., Thermal IR in geology; Some limitations in the interpretation of imagery, Photogrammetric Engineering and Remote Sensing, Vol. 2, 147-158, 1975.

Reeves, R. G., ed, Manual of Remote Sensing, American Society of Photogrammetry, Falls Church, Va, 1975.

Rossby, C. G., and R. B. Montgomery, The layer of frictional influence in wind and ocean currents, MIT and Woods Hole Oceanographic Institute Papers, Vol. 3, No. 3, 101 pp., 1935.

Rowan, L. C., P. H. Wetlaufer, A. F. H. Goetz, F. C. Billingsley, and J. H. Stewart, Discrimination of rock types and detection of hydrothermally

altered areas in south-central Nevada by the use of computer-enhanced  
ERTS images, U.S. Geological Survey Professional Paper 883, 39 pp, 1974.

Saucier, W. J., Principles of Meteorological Analysis, The University of  
Chicago Press, Chicago, 1955.

Schultz, A. W., An infrared transient method for determining the thermal  
inertia, conductivity, and diffusivity of solids, Applied Optics, Vol. 7,  
No. 9, 1845-1851, 1968.

Vincent, R. K., The potential role of thermal infrared multispectral scanners  
in geologic remote sensing, Proc. IEEE, 63, 137-147, 1975.

Yaglom, A. M., Comments on wind and temperature flux-profile relationships,  
Boundary Layer Meteorology, Vol. 11, 89-102, 1977.